Study of chemical reactivity of MAX phase single crystals

Shiqi Zhang

Communauté
UNIVERSITÉ Grenoble Alpes

THÈSE

Pour obtenir le grade de

DOCTEUR DE LA COMMUNAUTE UNIVERSITE GRENOBLE ALPES

Spécialité : **Matériaux, Mécanique, Génie civil, Electrochimie**

Arrêté ministériel : 25 mai 2016

Présentée par

Shiqi ZHANG

Thèse dirigée par **Thierry OUISSE** et
codirigée par **Olivier DEZELLUS**

préparée au sein du **Laboratoire des Matériaux et du Génie Physique**
dans **l`IMEP-2**

Etude de la réactivité chimique des monocristaux de phase MAX

Thèse soutenue publiquement le **26 février 2018**
devant le jury composé de :

Dr. Gilles Hug
Directeur de recherche, ONERA, Président
Dr. Thierry Cabioch
Professeur, Université de Poitiers, rapporteur
Dr. Catherine Journet
Professeur, UCBL Lyon, rapporteur
Dr. Olivier Dezellus
Maitre de conférences, UCBL Lyon, co-directeur de thèse
Dr. Thierry, Ouisse
Professeur, Grenoble-INP, directeur de thèse

General information

The current thesis was elaborated in Laboratoire des Matériaux et du Génie Physique (LMGP) of Grenoble INP and it was financially supported by the Agence Nationale de la Recherche on MAX phase single crystal "MAXICRYST" (March 2014 - 42 months). The core of scientific objective of the MAXICRYST program is aimed to overcome the technological barrier limiting the improvement of large MAX phases single crystals and to get forward in the physical, chemical and mechanical properties.

The work of the current thesis undertakes one part of the project and mainly deals with the chemical reactivity of MAX phase single crystal. Collaborations were mainly achieved with 4 partners involving three laboratories in France and one in the USA. The first part of the thesis of one year and three months took place in the Le Laboratoire des Multimatériaux et Interfaces of university Claude Benard Lyon 1. Synthesis of MXene from MAX phase single crystal is performed there (the results are presented in Chapter 2). A following cooperation of several months is achieved in "Laboratoire de Science et Ingénierie des Matériaux et Procédés" of Grenoble INP in France. Conversion of MAX phase single crystals into highly porous carbides by high-temperature chlorination is elaborated by a CVD reactor (the results are given in Chapter 3) and a journal article was published including an oral presentation in European Ceramic Society Conference. Crystalline orientation dependent electrochemical behaviors of single crystal Cr_2AlC in 1M H_2SO_4 was investigated in "Electrochimie et physicochimie des matériaux et des interfaces" of Grenoble INP in France. A correspondent journal article is being produced now. Results are presented in Chapter 4. At last, a close collaboration took place with Prof. Michel Barsoum of Department of Materials Science and Engineering at Drexel University in the USA. Crucial indirect evidence of ripplocation in polished and electrochemically etched Cr_2AlC single crystals, based on the samples prepared in LEPMI, was discovered, for a better understanding of the ripplocation in layered solids.

This thesis will bring some original viewpoints into the field of chemical reactivity of MAX phase single crystals. The topics that were investigated are 1) Synthesis of MXene from MAX phase single crystal based on the anisotropic chemical reactivity. The aim is to acquire large-scale MXene taking advantage of large size single crystal. This requires a thorough study of etching agent selection and mechanism 2) Chemical reactivity in chlorination: the initial purpose is to obtain MXene as an intermediate product in chlorination. However, we present another attractive derivative of MAX, porous chromium carbides that exhibit several interesting

properties. 3) Anisotropic electrochemical resistance. Large size single crystals are the first time used as electrode for the electrochemical tests. Significant anisotropy is shown by electrochemical polarization and EIS. 4) Ripplocation in MAX phase. A recently discovered new dislocation type, ripplocation is indirectly demonstrated in mechanically polished MAX phase single crystal through polarization.

According to the investigated topics, the structure of the current thesis is as below.

The first chapter starts with an introduction to MAX phase involving research history, structure, physical and chemical property and applications. The most attractive derivative product MXene is emphatically introduced. Then, all the growth techniques of MAX phase are introduced including the method for large single crystals used in the current thesis. At the end, the main contribution of the present thesis to MAX phase world is mentioned.

In the second chapter, we present details of the synthesis of MXene from MAX phase single crystals. Chemical and electrochemical methods are attempted to extract MXene from the MAX phases. Furthermore, based on the results, chemical reactivity is presented in different etching environments.

In the third chapter, we investigate the conversion of MAX phase single crystals into highly porous carbides by high-temperature chlorination. The morphology and structure are characterized by SEM and XRD. The effect of the various crucible parameters such as temperature and time are presented by Raman spectroscopy. We also demonstrate the magnetoresistance of porous Cr-C for the first time and the result shows that it is in the same magnitude with dense bulk one. The reaction mechanism is also investigated by XRD and Raman spectroscopy so as to understand the chemical anisotropic reactivity based on Al.

The fourth chapter is dedicated to exploring the anisotropic behavior of MAX phase single crystals in electrochemical environment. The evidence is given through a combined investigation of experimentally obtained polarization results and EIS analysis coupled with simulated equivalent circuits. Therein, possible mechanisms are discussed concerning the anisotropic reactivity. Furthermore, we show that the shape and morphology of defects created by mechanically polishing large Cr_2AlC single crystals are consistent with the nucleation of recently discovered new dislocation, bulk ripplocations.

At the end, general conclusions and prospective for future research close the presentation of current thesis.

Summary of the thesis

MAX phases are a family of layered ternary carbides and nitrides with chemical formula $M_{n+1}AX_n$, where M is an early transition element, A is an element of groups 13 to16 and X is either C, N or both. These phases combine the merits of ceramics and metals, such as chemical stability, machinability, shock resistance, good electrical and thermal conductivity, etc. However, the investigation of their intrinsic properties and anisotropies has heretofore been limited by a lack of availability of single crystals. This thesis mainly deals with the chemical reactivity of MAX phase single crystals. Owing to the large size single crystals grown at LMGP, it was possible to directly assess the anisotropy of the chemical reactivity and to obtain original data. We showed that the prominent role played by the A element for initiating chemical transformations could lead to the synthesis of original materials, and we focused on four different aspects. First, we tried to synthesize MXenes from MAX phase single crystals: The purpose was to obtain large-scale MXenes by taking advantage of the large size of the single crystals. Effort was put on describing the chemical reactivity of MAX phases dipped in different etchants, focusing on HF. Secondly, we studied the MAX phase reactivity with chlorination: the initial purpose was to obtain MXenes, but we finally developed a method for synthesizing porous chromium carbides which exhibit several interesting properties. Thirdly, we used large size single crystals in order to assess the anisotropy of the electrochemical properties. A significant anisotropy was found, either by measuring the current during electrochemical polarization or by frequency-dependent impedance measurements. Several mechanisms were proposed in order to explain this anisotropy of the corrosion properties. Eventually, we showed that the electrochemical results could be used to indirectly evidence the presence of structural defects recently identified in the literature. Such defects, called ripplocations, are specific to nano-lamellar materials.

Résumé de thèse

Les phases MAX forment une famille de carbures et de nitrures nano-lamellaires de formule chimique $M_{n+1}AX_n$, où M est un métal de transition des premières colonnes, A appartient aux colonnes 13-16 et X est soit C, soit N, ou une combinaison des deux éléments. Ces phases combinent les mérites des céramiques et des métaux, comme une bonne stabilité chimique, l'usinabilité, la résistance aux chocs mécaniques, de bonnes conductivités thermique et électrique, etc. Malgré tout, l'étude de leurs propriétés intrinsèques et de leurs anisotropies a été jusqu'à présent limitée par l'indisponibilité de monocristaux. Cette thèse traite de la réactivité de tels monocristaux de phases MAX. Grâce à la large taille des cristaux produits au LMGP, il a été possible d'évaluer directement l'anisotropie de la réactivité chimique et d'obtenir des données originales. Nous avons montré le rôle prépondérant joué par l'élément A pour initier des transformations chimiques menant parfois à la synthèse de matériaux originaux, et nous nous sommes concentrés sur quatre aspects différents : Tout d'abord, nous avons tenté de synthétiser des MXènes de grande taille, en profitant de la grande taille des cristaux disponibles. Un effort particulier a été porté sur la description de la réactivité chimique de phases MAX plongées dans diverses solutions d'attaque, avec un accent particulier mis sur l'utilisation de HF. En second lieu, nous avons étudié la chloruration de phases MAX : l'objectif initial était de former des MXènes, mais nous avons finalement développé une méthode pour synthétiser des carbures de chrome poreux avec des propriétés intéressantes. Troisièmement, nous avons utilisé des cristaux de grande taille pour évaluer l'anisotropie des propriétés électrochimiques. Une anisotropie significative a été trouvée, soit en mesurant le courant durant la polarisation électrochimique, soit par mesure de spectroscopie d'impédance. Divers mécanismes ont été proposés afin d'expliquer cette anisotropie des propriétés de corrosion. Enfin, nous avons montré que les résultats électrochimiques pouvaient être utilisés pour révéler indirectement la présence de défauts structurels récemment identifiés dans la littérature. De tels défauts, appelés « ripplocations », sont spécifiques aux matériaux nano-lamellaires.

Acknowledgement

First of all, I would like to express my heartfelt gratitude to my supervisor Dr. Thierry Ouisse for his help, strong support, sincere encouragement, and enthusiasm related to my thesis, great tutoring, significant advice and his confidence in me. Hence, all can be concluded in one sentence: THANK YOU!

From the beginning of 2016, I started to work with Thierry at LMGP. He taught me everything in detail, from the preparation of scientific figures to science writing, from theoretical knowledge to experimental operation. Each time I made the unprofessional results, he was always patient and gave me significant advice, which help me to make large progress. Every comment, advice, and discussion could be the precious gift for my future career. I would like to appreciate all the patients and support from him to help me to finish my thesis and grow up in science life.

I would like also to give great appreciation to my co-supervisor, Dr. Olivier Dezellus, for the first-year teaching. With Olivier, I started to learn how to deal with the Ph.D. work and feel enjoyable for the research life.

I think myself very lucky and honored for collaborating with a number of wonderful persons during my Ph.D. in France.

Great appreciation should be given to all the members at LMI in Lyon, Jérôme Andrieux, Bruno Gardiola, Erwann Jeanneau and Nassim Samer for the help and advice in and out of Lab for their friendship.

I would like also to thank the permanents at LMGP, Odette Chaix, Isabelle Gélard, Laetitia Rapenne-Homand, Eirini Sarigiannidou, Herve Roussel for giving me the patient technique training and helping me much for the sample characterizations.

Fortunately, I had the precious opportunity to work with the members of TOP at Lab SIMAP, Fréderic Mercier, Roman Reboud, Raphael Boichot, and Maeva Chen. I should give large appreciation to them for the CVD reactor training and kindly settle with the tense apparatus arrangement schedule.

As well, I should thank another cooperation partners at LEPMI whose support me all the electrochemical devices to extend our study on MAX phase. Dr. Virginie Roche and Dr. Fanny Hilario gave me a systemical training for the electrochemistry and worked a lot for helping me to interpret experimental results, inspiriting discussions, great suggestions. Mr.

Vincent Martin helped to measure the porosity of chromium carbides which provides me important information about our products.

I should also give great appreciation to the research leaders Dr. Didier Chaussende and Dr. Michael Barsoum. The former accompanied me at the beginning of the project and gave me a lot of suggestions. The latter spend time with me for the significant discussion for our work, not only in the investigation of mechanical dislocation of MAX phase but also in all other studies in terms of MAX phases.

I would like also to thank Dr. Franz Bruckert and Dr. Maria Carmen Jimenez Arevalo for giving me very kind encouragement and advice in my thesis and science career. As well, Michèle San Martin and Virginie Charriere help me in solving administrative problems, friendly advice, and support.

Fortunately, I could invite Dr. Catherine Journet-Gauthier and Dr. Thierry Cabioch to review my thesis and to be rapporteurs and juries in my defense committee. The same appreciation is also given to Dr. Gilles Hug as the jury in my defense committee.

I would like also to thank my colleagues Dr. Lu Shi and Dr. Hongjun Liu who helped me a lot to be familiar with the laboratory in the beginning and helped me in and out of Lab. As well, I should appreciate all other Ph.D. student colleagues in group Christallogenese at LMGP, Yun Ji Shin Hoang-Long Le-Tran, Damir Pinek for making my thesis an enjoyable and unforgettable experience.

Finally, I would like to thank my parents and girlfriend, for their comprehension, care and support without reservation. Without their accompanying and care, the thesis would not have been possibly completed. My parents teach me all the life knowledge and bring me up for life. I owe everything to them.

Contents

Chapter 1 Introduction

MAX phase history, background, growth methods and applications

This chapter gives some background information about MAX phases, MAX phase single crystals and growth techniques. First, an overall introduction to the MAX phase development history will be given from the 1960s until now. Then we focus on some important MAX phase properties, and summarize the existing and potential applications proposed by some companies and laboratories. Finally, we describe the techniques of synthesis of MAX phases, and we close this chapter by listing the contributions of this work to the field of MAX phase single crystals.

1.1 History

MAX phase is a family of lamellar, hexagonal carbides and nitrides with the chemical formula $M_{n+1}AX_n$ (n=1, 2 or 3), where M is an early transition metal, A is an element from groups 13 to 16, and X is carbon, nitrogen or both.

MAX phases were discovered in the sixties, but one had to wait until 1996 for the beginning of a systematic and intense research activity. In the 1960s, H. Nowotny and co-workers discovered a large family of ternary lamellar carbides and nitrides, which they called the 'H' phases [1-4] with formula T_2MC, now identified as the M_2AX phases (*i.e.* n = 2), and several M_3AX_2 phases such as Ti_3SiC_2 and Ti_3GeC_2 [5-7]. From then on, it opened the doors of MAX phase investigation. In their studies, the crystalline structures were adequately studied by X-ray diffraction. The crystal structures, with hexagonal atomic arrangement, are given in figure 1.1. M_3X_2 layers are separated by A layers [1]. Then Nickl *et al.* [8] and Japanese scientists T. Goto et al. [9] tried to synthesize polycrystals of Ti_3SiC_2 by chemical vapor deposition from chloride sources. Unlike other transition metal-carbides, Ti_3SiC_2 showed an unusual anisotropic hardness, for the hardness perpendicular to the basal plane is roughly three times larger than that parallel to the basal plane. Other unusual properties were also evidenced, such as high-temperature resistance and stiffness.

However, obtained crystals were always mingled with impurities at an early stage. For example, sintering in system Cr-Al-C does not only produce Cr_2AlC but also contains Cr_7C_3 and Cr_3C_2 [3]. The purity of the best result was limited to 80-90% [10], which influenced the characterization and stability of these novel materials, and prevented their use on potential applications. As a consequence, the discovery of those new lamellar compounds did not attract so much interest. The research was all but active, until it went to a turning point in 1996. Fully dense and pure Ti_3SiC_2 phase was successfully synthesized in the research group of M. Barsoum in Drexel, through the hot-pressing method, and fully characterized for the first time. Analysis revealed this phase to possess a distinct combination of some of the best properties of metals and engineering ceramics [11]. Since 1996, when the seminal paper was published, a significant amount of MAX phases has now revealed to exhibit quite similar attractive properties. Since then, the method of hot pressed sintering has been extensively used for synthesizing MAX phases with different seal crucibles, depending on the A element [1-7].

Moreover, tremendous progress has been made for understanding the properties of these phases. The investigation of oxidation resistance was performed on Ti_3SiC_2 [12] and showed that the oxidation kinetics was importantly influenced by oxygen diffusion and Ti. Then, in 1999, Barsoum's group paid much attention to the Ti-Al-N system [13]. They synthesized Ti_4AlN_3 (413 MAX phase) and realized that they were able to deal with a much larger family of solids that thought initially, which all behaved similarly. During the last 15 years, the researchers recognized that these phases represent a new class of thermodynamically stable Nano-laminated solids. At an early stage, the 211 phases were named M_2BX or H phases. In the 1980s, as the international union of pure and applied chemistry has published a new modified periodic table, accordingly, aluminum and silicon are defined in the A group. So Barsoum *et al*. re-named the H-phases and their counterparts with n>2 as $M_{n+1}AX_n$, or as "MAX" phases. Since 2006 researchers have preferentially focused on the solution of two fundamental problems: manufacturing cost and sample size. Making large parts is still not commercially viable. In 2013, T.Ouisse et al. [14] succeeded to grow MAX phase single crystal Cr_2AlC by the high-temperature solution growth method. After some effort, the size of Cr_2AlC crystals has increased from hundreds of square microns to several square centimeters. Then this technique has been extended to the synthesis of other phases. Many phases can now be obtained in single crystal form, such as V_2AlC and Ti_3SiC_2. The availability of single crystals made possible a detailed investigation of the anisotropic physical properties. Furthermore, new fabrication methods, extensive characterization of all kinds and composites implementation of MAX phase materials have been explored. Doped phases, like aluminum-MAX phase composites, have largely improved mechanical properties like ductility and toughness over pure MAX phase material [15]. More complex multi-M/A phases such as $Ti_3(Si_{0.43}Ge_{0.57})C_2$[16] have been discovered, sometimes possessing additional attractive properties as compared to the simple MAX phases. Research on MAX phases is now a very active field, and more than 100 phases have been discovered.

1.2 Structure and defects

In this section, we summarize some published research results on the crystal structure and related issues, in order to provide the information necessary to understand the reason why and how are established the physical properties.

1.2.1 Atom position and stacking sequences

The usual $M_{n+1}AX_n$ phase compounds have a structure with hexagonal symmetry, which belongs to the space groupD^4_{6h} (P^6_3/mmc), with the repetition of two formula units per unit cell. In each case, adjacent closed packed $M_{n+1}X_n$ layers are separated by a pure A group layer, and X atoms occupy octahedral sites between the M layers [17]. The layered nature of these compounds is visible in Fig.1.1 and 1.2. The M_6X units share their edges and are the same as those observed in the rock salt structure. The A-group atoms are situated at the center of trigonal prisms that are larger than the octahedral sites and thus enable to accommodate big A atoms. The differences between the structures with various n values is illustrated in Figure1.1a-c. The majority of existing compounds belong to the 211 phases and the most usual A element is aluminum, with around 13 compounds including carbides and nitrides.

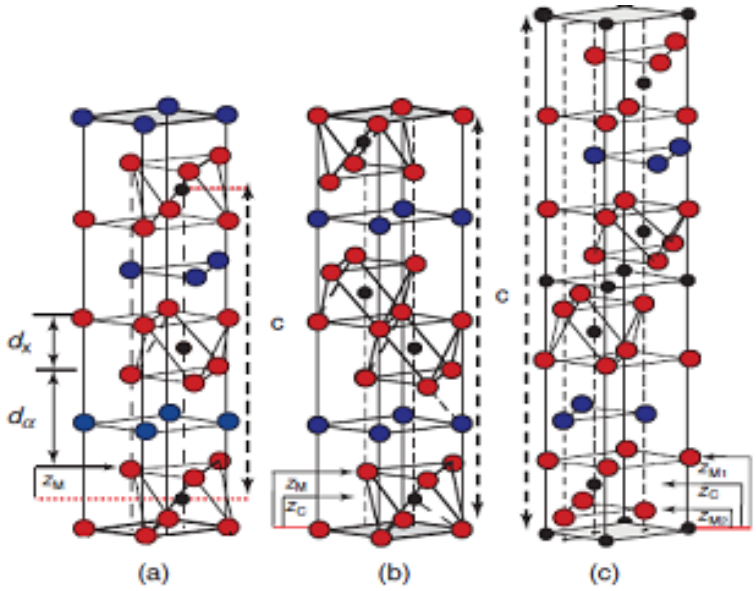

Figure 1.1. Unit cells of (a) 211 (b) 312 and (c) 413 phases. The c lattice parameters are shown by vertical dashed lines. d_x represents the distance from the nearest hcp planes containing the transition metal atoms; d_α is the same parameter but for the A layers. Those distances are connected together by the equation $c= 2\ d_\alpha + 2\ d_x$ for the 211 phases [17].

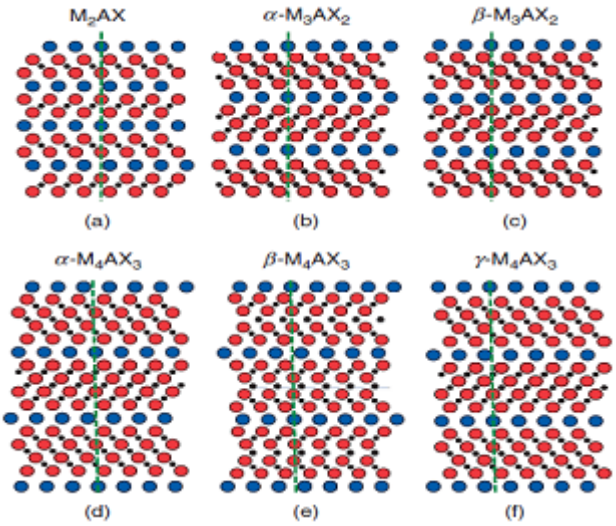

Figure 1.2. Schematics of the (11-20) zone axis for the phases (a) M_2AX, (b) α-M_3AX_2, (c) β-M_3AX_2, (d) α-M_4AX_3, (e) β-M_4AX_3 and (f) γ- M_4AX_3. Note that only in the α-M_3AX_2 structure the A atoms lie on top of each other [17].

The density (D) and lattice parameters (a, c) of MAX phase compounds are listed in Table 1.1 [18-31]. As to the 211 phases, there is just one polymorph (Figure 1.2a). In the 312 phases, there are two polymorphs, α and β, shown in Figures 1.2b and c, respectively. For the 413 cases, there are three polymorphs: α, β, and γ, shown in Figures 1.2d, e and f, respectively. In these arrangements, the capital and lower-case letters depict the M and A layers. The Greek letters represent the X positions corresponding to roman letter counterpart. α is an A site, β is a B site, and so on. These sequences are best appreciated when the (11-20) planes are sketched, respectively (Fig1.2a,b,d). The A element planes are mirror planes, and the MX blocks are zig-zagged, in agreement with the TEM analysis [32].
The stacking sequences for the corresponding α phase are

BγAbAγBaBγAbAγB……M_2AX

AγBaBγAβCaCβAγBaBγA…… α-M_3AX_2

α BcBαCβAγBaBγAβCαBcB.αC….. α-M_4AX_3

The stacking sequences for the corresponding β phase are

AγBcBγAβCbCβAγBcBγA…… β -M_3AX_2

γBcBγAγBγAbAγBγAγBγAγBcBγA ….. β -M_4AX_3

Lastly, the sequence for the γ- M_4AX_3 structure is

αBaBαCβAγBcBγAβCαBaBαC…. γ- M_4AX_3

There have been recent discoveries of MAX phases with n=4 and 5. However, what is currently unclear is whether these compositions can be synthesized as a single phase in mass or whether they are only small regions with high densities of stacking faults. Hybrid structures also exists as well. The earliest ones were reported in the Ti-Si-C system [32].

Table 1.1. Density and lattice parameters of 77 Max phase compounds. **[18-31,33]**

No.	Compounds	Density D, (Mgm-3)	Lattice parameters a
211 Phases			
1	Sc_2AlC	2.99	3.280, 15.373
2	Sc_2GaC	3.93	3.253, 15.813
3	Sc_2InC	4.72	3.272, 16.452
4	Sc_2TlC	6.60	3.281, 16.530
5	Ti_2AlC	4.11	3.051, 13.637
6	Ti_2AlN	4.31	2.989, 13.614
7	Ti_2SiC	4.35	3.052, 12.873
8	Ti_2PC	4.56	3.191, 11.457
9	Ti_2SC	4.62	3.216, 11.22
10	Ti_2GaC	5.53	3.07, 13.52
11	Ti_2GaN	5.75	3.00, 13.3
12	Ti_2GeC	5.30	3.07, 12.93
13	Ti_2AsC	5.71	3.209, 11.925
14	Ti_2CdC	9.71	3.1, 14.41
15	Ti_2InC	6.30	3.134, 14.077
16	Ti_2InN	6.54	3.07, 13.97
17	Ti_2SnC	6.10	3.163, 13.679
18	Ti_2TlC	8.63	3.15, 13.98
19	Ti_2PbC	8.55	3.20, 13.81
20	V_2AlC	4.07	3.1, 13.83
21	V_2SiC	5.20	2.955, 11.983
22	V_2PC	5.38	3.077, 10.91
23	V_2GaC	6.39	2.93, 12.84
24	V_2GaN	5.94	3.00, 13.3
25	V_2GeC	6.49	3.00, 12.25
26	V_2AsC	6.63	3.11, 11.3
27	Cr_2AlC	5.21	2.863, 12.814
28	Cr_2GaC	6.81	2.88, 12.61
29	Cr_2GaN	6.82	2.875, 12.77
30	Cr_2GeC	6.88	2.95, 12.08
31	Zr_2AlC	5.78	3.2104, 14.2460
32	Zr_2AlN	5.83	3.2155, 14.2134
33	Zr_2SC	6.20	3.40, 12.13
34	Zr_2InC	7.1	3.34, 14.91
35	Zr_2InN	7.53	3.27, 14.83
36	Zr_2SnC	6.9	3.3576, 14.57
37	Zr_2TlC	9.17	3.36, 14.78
38	Zr_2TlN	9.60	3.3, 14.71
39	Zr_2PbC	8.2	3.38, 14.66
40	Nb_2AlC	6.50	3.10, 13.8
41	Nb_2PC	7.09	3.28, 11.5
42	$Nb_2SC0.4$	7.01	3.27, 11.4
43	Nb_2SCx	-	-

1.2.2 Lattice parameters, bond length and interlayer thickness

1.2.2.1 Lattice parameters

Fig.1.1 shows the fundamental stacking building blocks of MAX phases with the edge-sharing MX_6 octahedra. A good correlation exists between the a lattice parameters and two adjacent M-M atoms interval distance d_{M-M} in the MX binaries [17]. For other MAX phases, the exception is the Cr-C system because Cr-C compounds do not crystallize in the rock salt structure. The two adjacent M atoms distance d_{M-M} is usually investigated in C-N system that does exist in the rock salt structure. The c lattice dependencies on M atoms interval distance and a element diameter d_A can be summarized as follows: Firstly, for phases with the same A element, the c parameter increases linearly as a function of d_{M-M}. M_3AlX_2 phases follow the same rule [34]. Secondly, the relationship between the c parameter and A atom diameter d_A is complex. A non-linear dependence can be separated into three regimes. For d_A<2.5 Å, the c lattice parameter has small values and increases slightly with increasing d_A. Around 2.5 Å, the c lattice exhibits an almost step like dependence on d_A. For d_A >2.6Å, the c parameter is relatively independent on d_A.

The ratio between c/a for the 211 phases ranges from 3.5 to 4.6, where the P-, S-, and As containing ternaries have the lowest values [17]. Accordingly, we can assume that the ternary phases are filled with A and X atoms in interstitial sites between M atoms. In this case, the c parameter, including four M layers per unit cell, could reasonably be around four times the a parameter, which is equal to d_{M-M}. By such analogy, the 312 and 413 phases are predicted to exhibit a ratio around 6 and 8 respectively [17].

1.2.2.2 Bond length

Once the canonical position z_i values and lattice parameters are known, all the bond lengths and bond angles in the structures can be calculated. For example, for the 211 phases, the following applies [35]:

$$R_{M-X} = \sqrt{\frac{a^2}{3} + z_M^2 c^2}$$

$$\boldsymbol{R_{M-A} = \sqrt{\frac{a^2}{3} + (\frac{1}{4} - z_M)^2 c^2}}$$

$$R_{M1-M2} = a \text{ (In plane M atoms)}$$

For the out-of-plane atoms:

$$R_{M-X} = \sqrt{\frac{a^2}{3} + 4z_M^2 c^2}$$

Table 1.2. Summary of experimental bond distance (Å), deduced from the lattice parameters and the z_i parameters for select Ti-containing MAX and MX phases. [42]

MAX	M_1-A	M_1-X_1	M_1-M_2	M_1-M_1	M_2-M_1	M_2-X_2	**Reference**
Ti_2AlC	**2.846**	**2.116**	**2.905**	**3.064**	**-**	**-**	**[35] at 10K**
	2.855	**2.119**	**2.942**	**3.058**	**-**	**-**	**[41] at 400K**
Ti_2AlN	**2.823**	**2.087**	**2.910**	**2.994**	**-**	**-**	**[3]**
	2.837	**2.086**	**2.0905**	**2.995**	**-**	**-**	**[35] at 10K**
Ti_3SiC_2	**2.696**	**2.135**	**2.971**	**3.068**	**2.135**	**-**	**[36]**
	2.693	**2.085**	**2.963**	**3.066**	**2.181**	**-**	**[37]**
	2.681	**2.088**	**2.963**	**3.058**	**2.176**	**-**	**[38]**
$Ti_4AlC_{2.9}$	**2.818**	**2.087**	**2.913**	**2.988**	**2.093**	**2.141**	**[39]**
TiC	**-**	**2.165**	**-**	**3.062**	**-**	**-**	**[40]**
TiN	**-**	**2.120**	**-**	**2.997**	**-**	**-**	**-**

Table 1.2 compares the various bond lengths of selected Ti-containing MAX phases with those in MX binaries TiC and TiN. In general, the bond length in the MX compound is relatively similar to those in the MAX phase. However, there are still some significant differences and trends. Based on table 1.2, the M_1-X bonds in 211 and 312 phases are all shorter than those in MX binaries.

The rule for 413 phases becomes slightly different in comparison with the 211 and 312 phases, because two M layers are solely bonded to X atoms. For example, the Ti_1-N_1 bondings in the octahedral nearest the A layer, are significantly shorter that those Ti_2-N_2 in the center of the unit cell [39].

1.2.2.3 Interlayer thickness

Based on the results in the literatures [23,42], the compression of the layer along [0001] orientation of the octahedra increases as the latter are closer to an A layer. This is proved by the fact that in all cases, the interlayer distance follows the trend: Ti_1-$C_1(d_1)$<Ti_2-$C_2(d_2)$<Ti_3-$C_3(d_3)$. Furthermore, the M-A interlayer distance-D is a relatively independent of the number n. Besides, the M_1-X_1 interlayer distance-D_1 is less than the corresponding distance in the binary. An opposite trend applies to D_2. The Ta-C distance in the binary is roughly the average of the Ta-C distances in the ternaries. This is only valid in both Ti-Al-C and Ta-C systems. [23].

1.2.3 Defects

1.2.3.1 Vacancies

The vacancies exist in all solid materials, both for thermodynamic and process reasons. In some cases, their role is extremely important. However, it is really difficult to determine the chemical stoichiometry by wavelength dispersive spectroscopy (WDS) or energy dispersive x ray spectrometry (EDS). By EDS, the carbon quantity is difficult to assess, due to the light atomic mass. WDS often gives unclear results. Some assumptions bring up that the clear XRD diffractograms can confirm the formal ratio of the elements of the MAX phases [43,44]. However, this is not always true. For example, the actual stoichiometric chemistry of Ti_4AlN_3 is $Ti_4AlN_{2.9}$ with a N sub-stoichiometry verified by clear WDS measurements [45].

Therefore, we have to admit our poor knowledge about vacancies in MAX phase materials, especially the defect energy and occurring positions. Until now, Ti_3SiC_2 is one of the most stoichiometric phases, and appears to be significantly stable.

As mentioned above, the actual chemistry of Ti_4AlN_3 is $Ti_4AlN_{2.9}$. This investigation prompted further investigations which simulated the vacancies in Ti_4AlN_3 through ab-initio calculations [46]. This study reveals that the N 2a sites in $Ti_4AlN_{2.75}$ to be the most probable vacancy sites, as controlled by the energy of vacancy formation. Moreover, the ab-initio calculations have been employed by Medvedeva et al. to study the defects in MAX phases [43]. The 2a sites at the center of the unit cell is the most probable carbon vacancy location in the case of Ta_4AlC_3 [47]. Other Density Functional Theory (DFT) calculations showed that in Ti_2AlC the Ti vacancies had higher formation energies than that of Al and C[44].

1.2.3.2 Stacking faults

Stacking faults, SFs, have been firstly investigated in MAX phases in 1998 [48], and they were evidenced in Ti_3SiC_2. Then, as observed by HRTEM, the Si mirror plane at the center of the basal plane may be lacking, and the remaining six close compact Ti plane containing thin lamellae with five carbon planes in between indicate the same stacking as for the {111}TiC plane [49]. This is shown by the vertical blacklines added on Si planes (Fig.1.3). This thin lamella with three Ti and two C basal planes is indicated by the black lines in Fig.1.3, and the region around the stacking fault center is emphasized by the white line. It is important to note that these basal plane stacking faults are certainly growth faults, because they could not be created by a simple shear force.

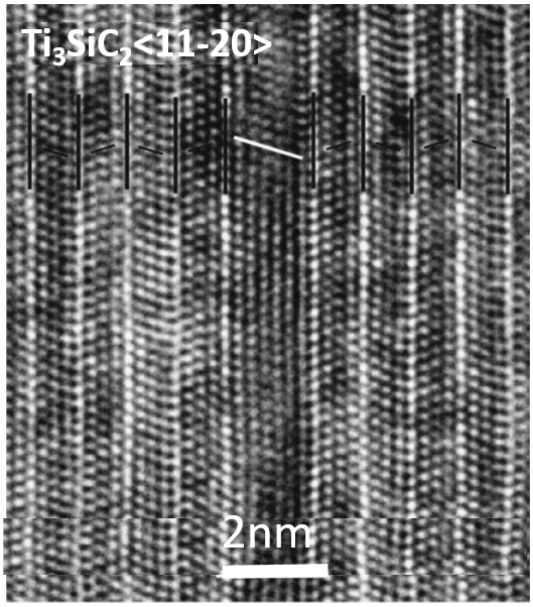

Figure 1.3. HRTEM image of a basal plane Stacking fault in Ti_3SiC_2. The viewing direction is [11-20,49]

1.2.3.3 Dislocations

Dislocations in MAX phases were firstly investigated in 1996 [50]. According to this study, the dislocations in the basal plane have a Burgers vector equal to the **a** lattice parameter. For those lying in the non-basal plane, one would have Burgers vectors greater than the lattice parameter **c**, which is nevertheless less important than those in the basal plane [45,49,51].

The MAX phases also possess a "super tolerance" to mechanical damage. When a stress is loaded in the direction parallel to the plane, "kink bands" can be observed. With a

critical shear stress, pairs of dislocations of opposite signs, moving in opposite directions, are created. The appearance of kink bands is due to the formation of these dislocations, which under stress are organized and form a wall which constitutes the boundary of the kink band (Figure 1.4) [12,52-54]. In most cases, this phenomenon results in an alteration of the mechanical properties of the material, but this is not the case for the MAX phases. For a delamination crack to propagate beyond the kink band, it must displace all the dislocations that constitute its boundary, which is a very energetic process. Kink bands boundaries can, therefore, be seen as containers or reflectors of damage.

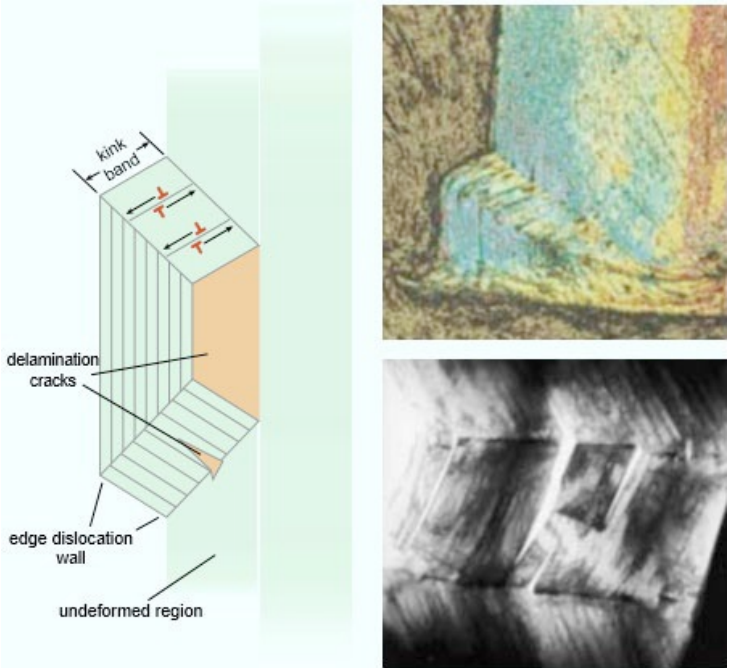

Figure 1.4. The Kink bands form in the crystalline solid when the dislocations form and move in the opposite direction. The fissures, when created, delaminate the layers, but are stopped by the boundaries of the Kink bands. Two layers can always slip to each other, and the material stays ductile. The macroscopic and microscopic Kink bands with boundaries can be observed by optical microscopy and TEM, respectively. It is worth noting that the fissures only propagate in the areas defined by Kink bands boundaries, and not beyond [54].

1.3 Characteristics

In the following we chose Cr_2AlC as a representative example of the MAX phase family and of some of their common characteristics.

1.3.1 Surface morphology

Single crystals of MAX phases have a morphology which depends on the phase and growth process. Cr_2AlC single crystals are obtained in the form of platelets with an area varying from several mm^2 to some cm^2. They exhibit silver metallic luster. Due to the final solidification stage (cf section devoted to growth), the surface of MAX phase raw single crystals is generally not perfect. As shown in Fig.1.5a by optical microscopy, crystal surface exhibit step bunching and dendrites. Depending on the growth conditions, crystals may also exhibit a relatively smooth surface (Fig.1.5b).

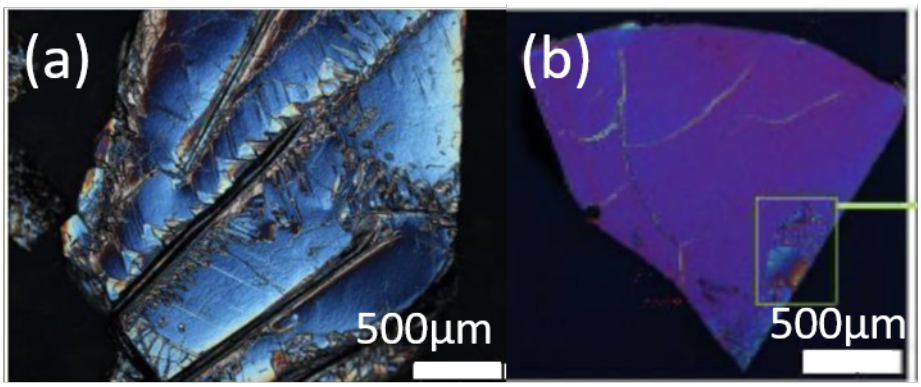

Figure 1.5. Cr_2AlC single crystal (a) with interlocking trace (b) relatively smooth

Fig. 1.6 shows an SEM image of a Cr_2AlC crystal cross-section after mechanical bending, and the morphology of the platelet top surface. Less tightly bound planes of the A elements allow such crystals to perform in a very particular way, since buckling is the main answer to stress and preferentially happens in the ab-plane. Hence, bending the crystal spectacularly highlights its lamellar structure (Fig.1.6a). Due to the latter, layer delamination and buckling is extensively studied. Fig.1.7 shows a cleaved crystal with a smooth surface, which is particularly suited to or demanded for measurement techniques such as Raman spectroscopy and ARPES (Angular Resolved Photoemission Electron Spectroscopy).

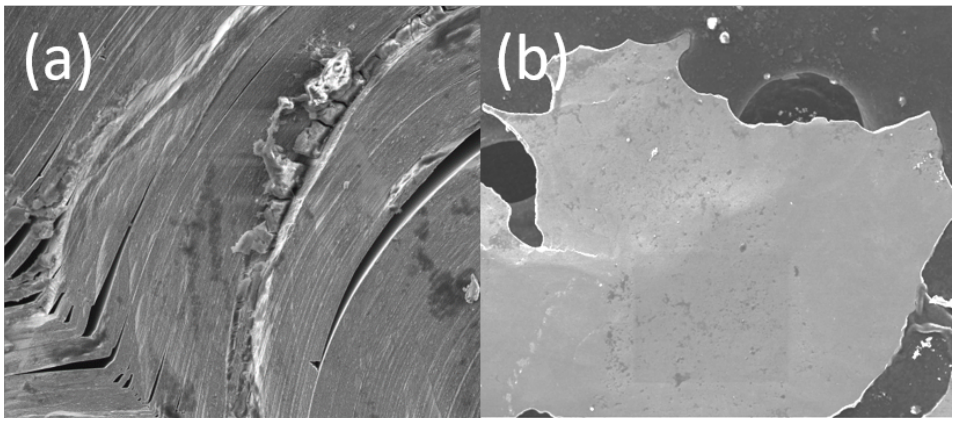

Figure 1.6. (a) Cr_2AlC bent single crystal cross-section (b) Cr_2AlC single crystal surface

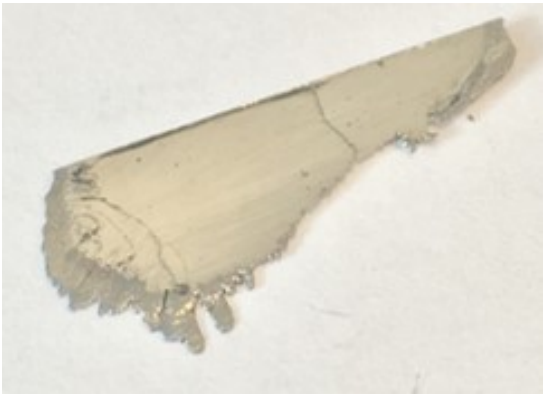

Figure 1.7. Cleaved surface of Cr_2AlC single crystal

1.3.2 Vibration modes detected by Raman spectroscopy

The MAX phases are members of space group D^4_{6h} (P^6_3/mmc). According to the experimental measurements and structure, for 211 phases, there are 24 modes in total, including four Raman active optical modes ($A_g+2E_{2g}+E_g$) [55]. Representative schematics of atomic displacements corresponding to the Raman active optical modes are shown in Fig.1.8. These optical modes could be observed in the Raman spectrum of Cr_2AlC (Fig.1.9). Although it has four peaks, the E_g and one of the E_{2g} modes overlap. Therefore, only three distinct sharp peaks could be observed at approximately 150.9, 246.3 and 339.2 cm^{-1}. Except Cr_2AlC, most other211 phases, such as V_2AlC and Ti_2AlC, exhibit four distinct peaks in their Raman spectrum [55].

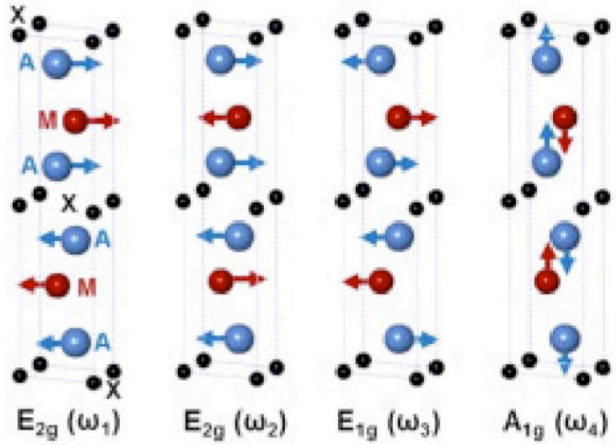

Figure 1.8. Vibration modes of the V-Al bonds corresponding to the four peaks of the Raman spectrum of V_2AlC, as obtained by Spanier et al.[55]

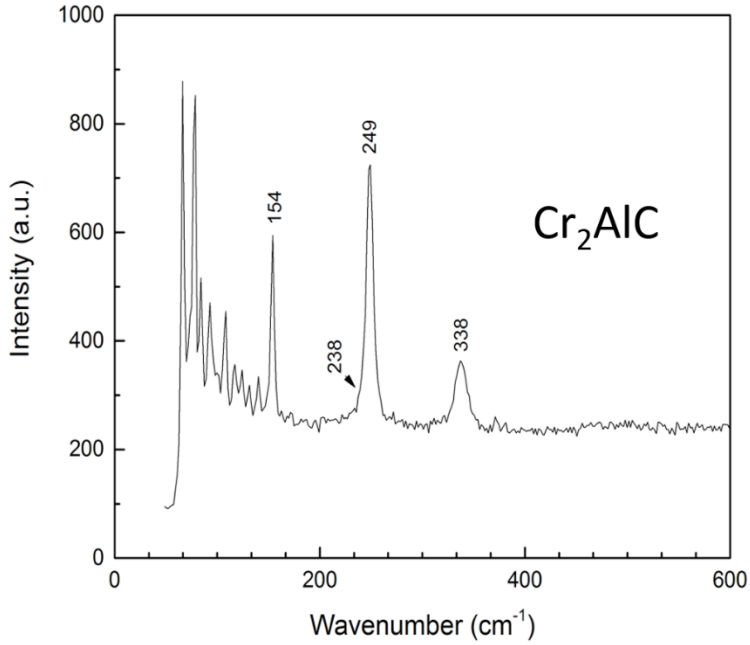

Figure 1.9. Raman spectrum of Cr_2AlC single crystal with the laser beam parallel to the c axis (wavelength$\lambda = 514.532\ nm$)

For the 312 phases, there are seven Raman-active optical modes ($2A_g+2E_g+3E_{2g}$) and 33 total optical modes. However, in experimental measurements, only six active modes could be evidenced [56-58](Fig.1.10). Furthermore, the 413 structure shows 10 Raman-active optical modes ($3A_g+3E_g+4E_{2g}$). Similarly, to the previous phases, there are two overlapping vibration modes [55].

1.4 Physical properties

The study of the main physical properties of the MAX phases has been extensively developed since Barsoum discovered the pure MAX phase compounds in 1996. Here, we focus on particular features that could reveal to be significant parameters for potential applications.

1.4.1 Hardness

Different with the nitrides and carbides with MX stoichiometry, the MAX phase compounds are relatively soft and elastic. They exhibit a better tolerance to damage. As the MAX phase compounds combine the properties of metals and ceramics, they are softer than most structural ceramics and harder than the majority of metals.

The first investigation of MAX phase hardness was performed in 1972 [8]. Some isolated, small single crystalline platelets of Ti_3SiC_2 synthesized by chemical vapor deposition with sizes around 10μm, allowed the first analysis of mechanical anisotropy. The hardness along the c axis was found to be much higher than other orientations. Then subsequent work confirmed this result, and it was further proposed that the hardness is a function of indentation load. When the indenter load increases from 10 to 100 g, the Vickers hardness of Ti_3SiC_2 decreases from 1900 to 600 kg/mm^2. It finally reach a constant value of 600 kg/mm^2 in the range of 100 g to 1 kg load [9].

Based on all available hardness studies of MAX phase compounds, we can point out some conclusions:

1. The Vicher hardness Hv increases with decreasing load. It is not measurable below a certain lower limit value because of a lack of any trace of observable indentation [59,60].

2. Hv is dependent on grain size. The finer grain size results in a higher hardness.

3. The grain size also influences the coefficient between the hardness Hv and the load. The hardness of finer grained material will decrease more slowly than a coarser one with an increasing load.

1.4.2 Fatigue resistance

Fatigue test is one of the fundamental tests for mechanical applications. It determines the service life and whether the material is available and suitable for some particular use. Hence

the fatigue resistance largely limits the application range of the material. The investigation of MAX phase compounds on fatigue resistance is a main aspect as well. The estimation is generally divided into two aspects: observation of long cracks and short cracks, which determines the materials' behavior in different conditions.

The damage associated with cyclic loading in many ceramics is generally attributed to cycle -dependent frictional wear at grain bridging sites. As such, ceramic microstructures designed for high damage tolerance are generally more prone to cyclic fatigue degradation, a fact that has been well discussed for a lot of ceramic composites [61].

The testing of long cracks reveals that the threshold and the stress intensity range factor ΔK of MAX phases are comparatively higher than those of conventional structural ceramics and some metals [62,63]. ΔK is given by:

$$\Delta K = \xi(\sigma_{max}-\sigma_{min})\sqrt{\pi a}$$

and where σ_{max} and σ_{min} are the maximum and minimum stress applied. a is flow size

The crack growth rate is strong function ΔK[64]. For example, for Ti_3SiC_2 sample, the fatigue threshold and ΔK_{th} are some of the highest values ever-observed in monolithic, non-transformation ceramics.

In the investigation of short crack test in polycrystalline Ti_3SiC_2 [63], the result shows that the crack growth rates under cyclic fatigue are obviously faster than those under static one. This is valid for most other MAX phase compounds. Generally the crack growth rates are a stronger function of maximum stress intensity K_{max} than the stress intensity range factor ΔK_{th}. However, as the conclusion are based on a few studies, further work is required, especially if the MAX phase compounds are to be applied in the domain which requires strong fatigue resistance.

1.4.3 Damage tolerance

Damage tolerance is one of the key parameters for material applications, especially for the structural ceramics. It is usually assessed by pre-indenting the tensile surface of the bent bars with Vickers indentations made at increasing indentation loads.it is also intimately related to the ability of the MAX phases to contain and confine the extent of damage to small areas around the indentations by plastic deformation. Based on the available studies, the following conclusions can be given:

1. The post-indentation flexural strength are considerably less dependent on the indentation loads than typical structural ceramics [64].
2. Similar to other structural ceramics, the damage tolerance of coarse grain microstructures is superior to that of their finer-grained counterparts [65,66].

1.4.4 Machinability

In this last section related to mechanical properties, we will account for a parameter crucial for material applications: machinability. Here, most notable is the well known fact that ceramic materials are not machinable. In contrast, the MAX phase compounds are quite easily machinable with conventional tool steels or even manual hacksaws. It is very significant to mention that this ability doesn't occur by plastic deformation, as in the case of metals, but rather by the breaking off of small microscopic platelets [67]. In that respect, they are not similar to other machinable materials. The MAX phase compounds don't machine as one scope ice cream, but rather as in shaving ice [68]. Except for Be and Be-alloys, the MAX phases have some of the highest specific stiffness values for readily machinable solids.

Machinability of the MAX phases has not been sufficiently investigated. For example, Hwang et al. compared the cutting resistance of Ti_3SiC_2 to that of a middle-carbon steel, SM45C [69]. The values of the main forces measured during the machining of Ti_3SiC_2 were much lower than those of SM45C. After machining, the surface roughness of the Ti_3SiC_2 was lower than that of SM45C as well. However, the damage to the tool used for machining the middle carbon steel was less than the damage to those used for Ti_3SiC_2 [70].

1.5 Chemical properties

Chemical reactivity is at the heart of this thesis, including chemical resistance and potentially useful chemical transformations. In the following three chapters, we will present the performance of MAX phase compounds, focusing on Cr_2AlC, under conditions of corrosive solution and gas. Here we give an overview of the chemical stability of MAX phase compounds in common acids and bases.

In general, the MAX phase compounds inherit the merits of ceramic including corrosion resistance. The corrosion behaviors vary depending on the composition. In many cases, the starting step is the extraction of A atoms from the structure into the surrounding media, leaving behind MX binary compounds. Hence, how the A atoms diffuse out and what are the left structures are attractive issues, and this work focuses on some of them. If A elements are not soluble in the surrounding media, the MAX phase should be stable.

Aggressive molten salt with oxygen can oxidize the MAX phase and dissolve it in the solution. They can transform the nano-lamellar structure into a 3D rock salt structure [71-74]. If the oxides of A element are insoluble in the molten salt, the phase can stay stable. Most MAX phase compounds are rather stable in common acids and bases. Table 1.3 gives a summary of Ti_3SiC_2 behavior in common acids and NaOH. It is worth noting that Ti_3SiC_2 is not stable in HNO_3 and HF. The corrosion resistance crucially depends on the oxide layer formed on the surface. In chapter 4, the roles played by different A elements are summarized and compared, indicating appropriate conditions of applications for different phases. The mechanism of oxidation using HNO_3 is similar to the one with oxygen-containing molten salts [71-74], which can oxidize the MAX phase and dissolve it in the solution. Different MAX phases show different behaviors with respect to oxidation conditions, and we will see in chapter 2 that Cr_2AlC is quite stable in H_2O_2 after several days, whereas V_2AlC reacts when put in the same conditions.

Table 1.3. Corrosion rates measured by weight loss of Ti_3SiC_2 before and after etching [75-80]

Solution(vol%)	pH	Chemical corrosion rates(µm per year)			
		Ti_3SiC_2		Unalloyed Ti	
		Weight loss	SEM	Corrosion rate	Ref
70% HNO_3	<0	12,4	25±5	<5	[76-78]
11,6% HNO_3	<0	210	400±200	<5	[76-78]
6,4% HNO_3	≈ 0	162	243±200	<5	[76-78]
38% HCl	<0	≈ 0	-	2500	[76-78]
25% HCl	-	-	-	550	[79]
16% HCl	-	-	-	5045(37°C)	[76-78]
7,6% HCl	0,22	1,6	-	1270	[76-78]
95% H_2SO_4	-	≈ 0	-	1570	[76-78]
13,6% H_2SO_4	<0	0,8	-	1270	[78-80]
8,2% H_2SO_4	0,85	≈ 0	-	Soluble	
0% H_2SO_4	11,5	≈ 0	-	<3	

Sensitivity of the Al-based phases to HF exposure has attracted a lot of interest, as it can be put to good use to produce 2 dimensional binary compounds called MXenes. The latter are presented in the next section.

1.6 Mxenes

At elevated temperature, as the M-A bonds are weaker than M-X bonds, MAX phases selectively lose the A element in vacuum [81], in molten salts [71,72] and in some molten metals [73]. Besides, the high temperature induces de-twinning of the MX layers and turns them into a 3D MX rock salt structure [72,74]. Indeed, the M-A bonds are of a purely metallic nature while the M-X bonds are ionic, metallic and covalent. Unfortunately, in this high temperature decomposition, MX layers lose their layered structure to adopt that of gemstones, which makes them useless. As shown later in this work, MAX phase compounds can also lose both the M and A elements in the strong etchant H_2+Cl_2 gas at high temperature, and are transformed into MX binary compounds.

1.6.1 Synthesis

In 2011, Naguib et al. successfully transformed MAX phases into 2D dimensional layers which they named MXenes [82]. For the first time, this transformation avoided to turn the mother phase into a compound with 3D rock salt structure as in refs [71-74,81]. They reported the synthesis of MXene Ti_3C_2 from Ti_3AlC_2 through the use of HF at room temperature. The process and morphology of Ti_2C are shown in Fig.1. According to this study, the HF etching method is expected to be successful for several MAX phases except for MXenes phases that are not stable in the etchant solution. Until now, Ti_3C_2, Ti_2C, Nb_2C, V_2C, Ti_3CN, $(V_{0.5}Cr_{0.5})_3C_2$ [74,82-84] etc. have been successfully obtained. In 2015, Naguib et al. succeeded in exfoliating Ti_3AlC_2 to form Ti_3C_2 using a mixture of LiF, and HCl [82]. The obtained material was tested as a lithium ion battery electrode, and was shown to be more efficient than the same material obtained by HF etching. Presently this technic is only feasible with Ti_3SiC_2.

The samples are necessarily prepared in the form of powder. A very few microns are considered as the effective grain size for HF treatment. Synthesizing large size MXenes from MAX phase single crystals is therefore a challenge we started to attempt in this work. It will

be noted that the transformation kinetics of the MAX phases is an important factor to consider for the synthesis of MXenes from large crystals of MAX phases. Indeed, for very fine powders, the time spent in the solution ranges from 2h to 8h, whereas it can be imagined lasting several days for crystals of a size close to the centimeter [71].

The production of MXenes from the MAX phases is commonly carried out in HF hydrofluoric acid or NH_4HF_2. The associated reactions are respectively given below [74]:

$$\mathbf{M_{n+1}AlX_n + 3HF = AlF_3 + M_{n+1}X_n + 1.5H_2}$$

and

$$\mathbf{M_{n+1}AlX_n + 3NH_4HF_2 = (NH4)_3AlF_6 + M_{n+1}X_n + 1.5H_2}$$

The etching of MAX phases by HF is shown to be anisotropic: it preferentially occurs along the ab plane [83]. According to the reaction above, the etching preferentially breaks the M-A bonds and extracts A atoms from the structure, leaving MX layers. The 2D MXenes is significantly more important than the 3D rock salt. Hence, the idea of etching is to eliminate element A without destroying the M-X bonds. The choice of the concentration, time and temperature of the acid solution is therefore essential. In the reaction, stirring may be not necessary, but it can accelerate the kinetics. A higher temperature substantially accelerates the reaction rate. In chapter 2, we will study the concentration limit of the reacting agent. For a fast etching, the concentration of HF cannot be less than 48%, while a low concentration could lead to a exponential growth of etching time. During the selective etching, the element A is replaced in the structure by the elements F, O or OH. Consequently, the MX layers are no longer interconnected by metallic bonds but by Van der Waals interactions between the new side groups, which induces their delamination [84,85]. Blocks of MX layers can therefore be easily separated from one another after ultra-sonication, as shown in Fig. 1.12.

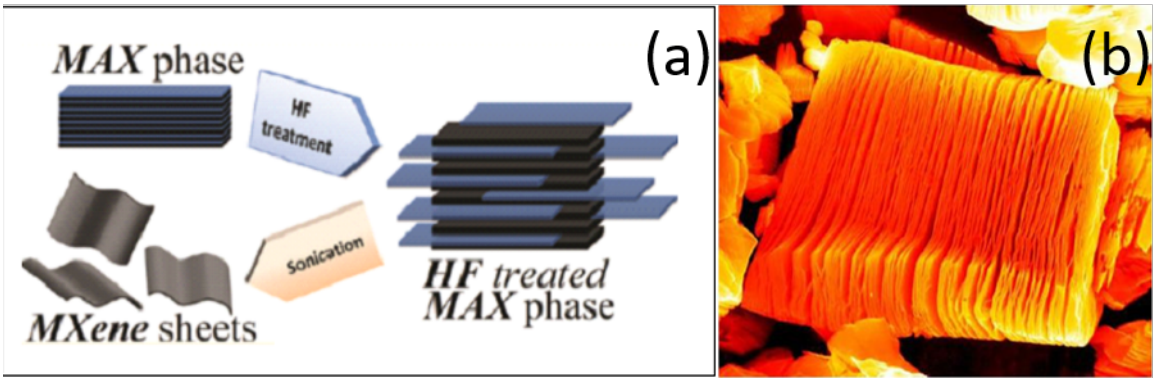

Figure 1.12. (a) Process of synthesis MXene of by attacking a MAX phase in HF and then using ultrasound [71] (b) SEM image of obtained Ti2C by HF etching [83]

The reactions associated with the new terminations are given below [74]:

$$M_{n+1}X_n + 2H_2O = M_{n+1}X_n(OH)_2 + H_2$$

and

$$M_{n+1}X_n + 2HF = M_{n+1}X_nF_2 + H_2$$

A representation of one of the configurations is shown in Figure 1.13:

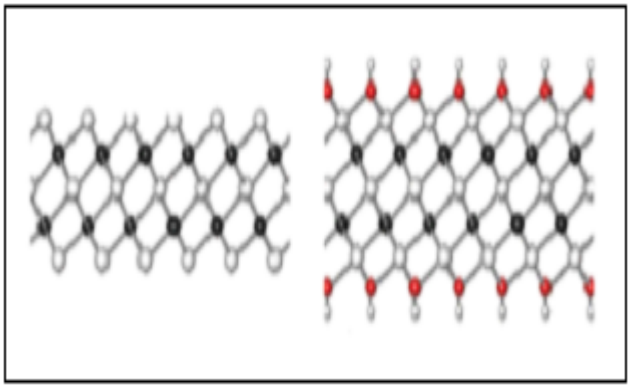

Figure 1.13. Arrangement of MXenes (left) and MXenes terminated by OH (right) [86]

However, the synthesis process in NH_4HF_2 often involves the intercalation of N_2H_4 between the layers of MXenes in the form of an independent monolayer structures. In addition, undesired phases may be formed during this synthesis method. For example, $TiOF_2$ phase was detected by X-rays when Ti_3C_2 was extracted from Ti_3AlC_2 by HF [81].

The MX sheets in MXene are interleaved with Van der Waals bonds or hydrogen bonds instead of M-A bonds in MAX phases [85] (Figure 1.14). After etching, the structure becomes loosely bonded, resulting in an accordion-like structure as for exfoliated graphene (Fig.1.12). The usually obtained MXene is formed of a few layers, which we called few-layer MXene (FL-MXene). Furthermore, the A element is probably replaced by various surface terminations. Hence, the MXene chemistry is rather $M_{n+1}X_nT_x$, where T denotes O, OH or F atoms.

The MAX phase transformation into MXene could lead to the attenuation or disappearance of all but (000l) peaks in the X-ray diffraction patterns. In the result for Nb_2AlC shown in Fig.1.15, the (000l) is the only peak observed. The peak intensity is enhanced because the sample in the literature is cold pressed [84]. Besides, as **ab** plane is unchanged, corresponding peaks are not broadened. However, XRD cannot quantify the unreacted MAX phase fraction. Therefore, we use EDS to analyze the element to access the actual percentage.

It is noted that this method will overestimate the fraction of conversion because the Al-containing salt, product of the exfoliation reaction, can still be present in the structure and be considered as unreacted part if the MXene is not completely washed and purified.

Table 1.4 is the summary of reported HF etching conditions for different MAX phase compounds with the correspondent c lattice parameter. The required etching time is dependent on the sample size, temperature, HF concentration and stirring condition. Therefore, reducing the particle size could help the reaction time decreasing from 90h to 8h [84]. It demonstrates from another aspect that for a large single crystal, it should be much longer than 90h. According to Naguib et al. [74], long etching times could result in the formation of defects such as deep holes that could accelerate the reaction rate while it could break the sample into pieces.

The loss of A element can be roughly assessed by measuring the weight before and after etching, rinsing, and drying of the samples. The result can be overestimated by the extraction of M atoms. Furthermore, it may be flawed by intercalation phenomena or if the drying of the samples is not complete.

In terms of the chemical resistance, the value n plays an important role. In general, a high n could result in a higher resistance and more stable MAX phases and MXenes [86], which could influence the reaction rate. Accordingly, the reaction design should take this factor into account.

Until now, most MXenes have been obtained from carbides, not from nitrides. It is noted that the calculated cohesive energies of $Ti_{n+1}N_n$ from $Ti_{n+1}AlN_n$ are less than those of $Ti_{n+1}C_n$ from $Ti_{n+1}AlC_n$ [88]. The former has a higher formation energy and the latter results in a lower chemical stability. Hence the bonds between Al and C are weaker than that of Al and N, which require more energy for extraction for Al-N bonds[88]. Another possibility is that the nitride MXene is not stable in HF and soluble in the solution.

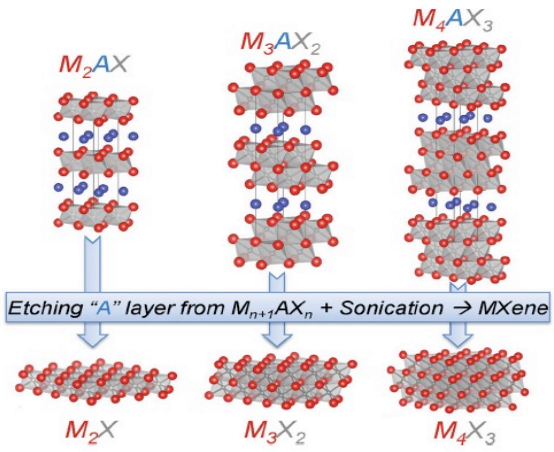

Figure 1.14. Structure of MAX phase (211,312 and 413) and the corresponding MXenes[84]

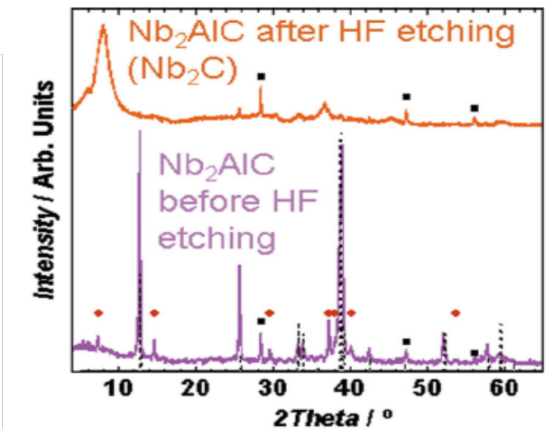

Figure 1.15. XRD pattern of Nb_2AlC before and after HF etching [89]

Table 1.4. Etching condition and c-lattice parameters for Mxene synthesis from MAX phases with the mother MAX phase c values

MAX	**MAX**	**MXene**	**RT etching condition**		**C lattice parameter/Å**		**Ref.**
Structure			HF conc%	Time/h	MAX	MXene	
211	Ti_2AlC	Ti_2CTx	10	10	13,6	15,04	[74]
	V_2AlC(attrition-milled powders)	V_2CTx	50	8	13,13	23,96	[84]
				90		19,73	
	Nb_2AlC	Nb_2CTx	50	90	13,88	22,34	[84]
	$(Ti_{0.5},Nb_{0.5})_2AlC$	$(Ti_{0.5},Nb_{0.5})_2CT_x$	50	23	13,79	14,88	[74]
312	Ti_3AlC_2	Ti_3CTx	50	2	18,42	20,51	[74,83]
			40	20	18,62	20,89	[87]
	$(V_{0.5},Cr_{0.5})_3AlC_2$	$(V_{0.5},Cr_{0.5})_3C_2T_x$	50	69	17,73	24,26	[74]
	Ti_3AlCN	Ti_3CNT_x	30	18	18,41	22,28	[74]
413	Ta_4AlC_3	$Ta_4C_3T_x$	50	72	24,08	30,34	[74]
	Nb_4AlC_3(secondary phase in Nb_2AlC	$Nb_4C_3T_x$	50	90	24,19	30,47	[84]

1.6.2 Structure

MX sheets of a few nanometers in thickness (two-dimensional character), with hexagonal structure, are thus recovered with the X atoms situated on the octahedral sites of the mesh formed by the element M. It is important to note that once the MX sheets are separated, they have T-termination elements at their surface that occupy the empty sites left by the element A [81] (Fig.1.16).

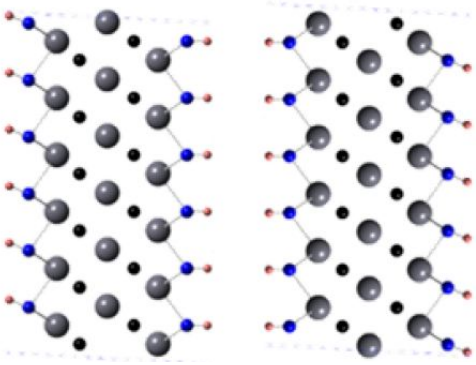

Figure 1.16. Schematic of the exfoliated Ti_3AlC_2 forming two OH-terminated MXene layers Model [74]

Thus, the MXene sheets are commonly referred to as $M_{n+1}X_nT_x$, with the T ending group possibly being OH, F, O and H. There are various possible arrangements of the T group on the MX structure conferring different dielectric and chemical properties to the material. The nature of the T group and their surface arrangement are not controllable at present.

The first MXene structure model calculated by DFT method, was Ti_3C_2 layers terminaed with OH groups. The real structure could be more complicated than the simple simulation model because of mixed termination and incompletely converted structure. Besides, water molecules could interleave in the structure, leading to a larger c lattice parameter [84]. Then DFT predicts two energetically favorable orientations of T groups in $Ti_3C_2T_2$ [90, 91], shown as configurations I and II in Fig. 1.17. In type I, the T groups are located above the hollow sites among three neighboring C atoms and the T groups point directly toward the Ti(2) atoms on both sides of the M_3X_2 layers. In type II, the T terminations are located above the C atoms on both sides of the M_3X_2 layers. The mixed structure of I and II is commonly considered as configuration III, where one side is I and the other side is II.

The relative stability of structure of different $Ti_3C_2F_2$ and $Ti_3C_2(OH)_2$ configurations was estimated by DFT energy calculations. Briefly, the stability order is I >III>II. It demonstrates that both termination F and OH are more likely to adopt configuration I. hence, the low structural stability is ascribed to steric repulsion between T groups and the underlying C atoms [92]. Another configuration where terminations are linked to and located above Ti(1) atoms of MX layer is demonstrated to be unstable and easily transformed into the other two configurations.

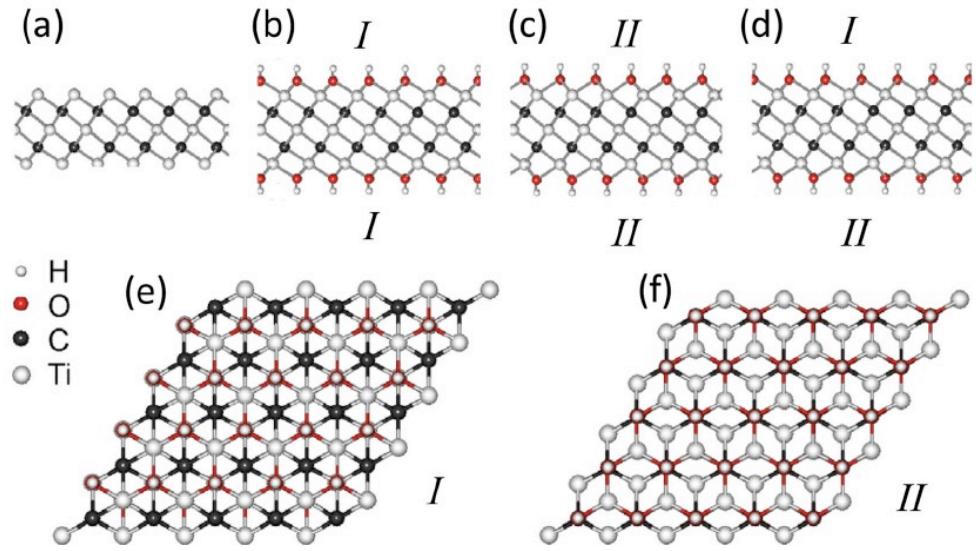

Figure 1.17. Configurations of functionalized MXenes with different arrangements of the surface atoms: side views of a) bare Ti_3C_2, b) I-$Ti_3C_2(OH)_2$, c) II-$Ti_2C(OH)_2$, and d) III-$Ti_3C_2(OH)_2$; e,f) top views of I-$Ti_3C_2(OH)_2$ and II-$Ti_3C_2(OH)_2$. As configuration III is a mixture of I and II, its top view is not shown. [90]

1.6.3 Properties

2D MX layers present excellent characteristics in terms of electrical and thermal conductivity and sometimes show better properties than their mother phases. Besides, the MXenes have a hydrophilic character.

MXenes can be considered as 2D dimensional "separated" MAX phase monolayers. So, they inherit corrosion resistance from the mother phases. The terminations could influence the electronic structure, which corresponds to a metallic monolayer with a high electron density at the Fermi level (E_f) [91-94]. In the mother phase, MAX phase, $N(E_f)$ is dominated by M3d orbitals and the valence states below Ef group are composed of two sub bands. Sub band A near Ef is made of hybridized Ti 3d-Al 3p orbitals and sub band B below Ef between -10ev and -3ev which is made of hybridized Ti 3d-C 2p and Ti 3d-Al 3s orbitals. In other words, sub-band A is due to Ti-Al bonds, and sub band B is the source of Ti-C bonds. The exfoliation of A layer could lead to the redistribution of Ti 3d states from missing Ti-Al bonds into delocalized Ti-Ti metallic bond states around the Fermi energy in Ti_2C. Therefore, $N(E_f)$ in MXene is much higher than in the mother MAX phase compound [83].

The high E_f value could lead to a magnetic instability. If the Stoner criterion is satisfied, the MXenes should be magnetic [91-95]. However, the bare surface is a theoretical state. The real MXenes with terminations could eliminate the magnetism due to p-d bonds between T groups and M atoms, resulting in a partial depopulation of the states around the Fermi energy.

Surface termination also influences the possible existence of a bandgap. Although most MXenes should be metallic conductors, a semiconducting behavior is predicted for $Ti_3C_2F_2$ and $Ti_3C_2(OH)_2$, with bandgaps of 0.1eV and 0.05eV respectively [96]. This could be ascribed to the tuning of the electronic structure by varying the T groups. Then this would confirm that the electronic structure is not only dominated by the surface termination type but also by the orientation relative to the MX layer. Sometimes, this could result in a semi-conducting state [96].

The expected mechanical properties of MXene are rather interesting since the M-X bonds are very strong bonds. In addition, these good properties are expected to be preserved at very high temperatures. DFT simulations allowed to estimate an elastic constant of the order of 300GPa for z-axis stress and $Ti_3C_2(OH)_2$[83].

MXenes are also expected to be more rigid than their mother MAX phase since the M-A bonds energies are much lower than that of the M-X bonds (Table 1.5)[97]. The expected elastic constants for MXenes are lower than for graphene. However, the flexural rigidity of MXenes seems better than that of graphene. This is explained by the fact that this stiffness behaves at t^3 , with t the of thickness of the layer, and that the Mxenes are constituted by at least three atomic layers against one fore graphene. Moreover, this thickness and therefore the flexural rigidity can be improved by playing on n in $M_{n+1}X_n$.

Table 1.5. In-plane elastic constant (c_{11}) of different MXenes with the corresponding a lattice parameter and DOS at E_f by first principles calculation [97]. The values in brackets in column 3 are c_{11} of corresponding MAX phases

Layer	a/Å	C_{11}/GPa Mxene(MAX)	DOS at E_f eV^{-1} $atom^{-1}$
M_2C			
Ti_2C	3,007	636(312)	2,63
V_2C	2,869	718(338)	1,45
Cr_2C	2,787	690(340)	2,55
Zr_2C	3,238	594(261)	1,77
Hf_2C	3,239	658(291)	2,25
Ta_2C	3,138	788(334)	0,89
M_3C_2			
Ti_3C_2	3,071	523(368)	2,19
Ta_3C_2	3,196	575(368)	1,44
M_4C_3			
Ti_4C_3	3,066	512(403)	1,83
Ta_4C_3	3,172	633(437)	0,56

1.6.4 Potential applications

Since the appearance of graphene in 2000, two-dimensional materials are the subject of particular attention. The MXene family is of great interest for two-dimensional materials because of its versatility and the diversity of its members.

Indeed, because graphene is composed solely of carbon, by playing on the elements M and X of the 2D sheets of metal carbide, or by choosing the number of layers n, a vast variety of properties can potentially be obtained.

Due to their expected electrical, optical and mechanical properties, these materials can potentially be used for many applications such as supercapacitors, sensors, electronic devices, catalysts [98-100] for the chemical industry, conductive polymer reinforcements or electrochemical energy. More and more research has been done on these applications. Here we give an overview of these fields of application, based on a recent review by Barsoum et al. [81].

Energy storage

DFT simulations have made possible to predict the intercalation process of Li in Ti_3C_2 sheets in order to use it as the LiB anode [101,102]. By plunging these 2D sheets into a Li-rich

environment, the formation of $Ti_3C_2Li_2$ makes possible to store Li-ions. For Ti_3C_2, similarly as for $Ti_3C_2F_2$ and $Ti_3C_2 (OH)_2$, the Li atom is placed above the carbon atom. A charge transfer takes place between $Ti_3C_2T_2$ and Li via a Coulomb interaction. The theoretical capacity of the sheets of Ti_3C_2, $Ti_3C_2F_2$ and $Ti_3C_2(OH)_2$ would be respectively 320, 130 and 67 mAh/g [91]. Moreover, these calculations predict that the Ti_3C_2 sheets are better anodes than the current phase TiO_2. Indeed, they are better conductors (metallic character), have a lower open circuit voltage, better Li storage capacity, and a high cycle rate. Moreover, the diffusion barrier of Li in Ti_3C_2 amounts to 0.07 eV against more than 0.3 eV for TiO_2. This means that Ti_3C_2 could take on higher charging and discharge rates, making them promising for high-power batteries. It has been estimated that the larger n is, the more atomic layers will be in per sheet, the better the storage of Li ions will be.

In addition, the ability of Ti_3C_2 to withstand high cycle rates makes them suitable candidates for hybrid cells, asymmetric and non-aqueous energy storage devices, which combine high-density LiB energy and high-power density EDLC (Electrical Double Layer Capacitors) [103].

Such supercapacitors have been tested with an activated carbon cathode and an anode of Ti_3CT_2 with KOH as the electrolyte. With a current of 1A/g, the reversible capacity of the supercapacitor was 51 F / g, which is greater than that of the best EDLCs[104].

Finally, many other applications may be provided for these multilayer materials. Among them are the multivalent ion batteries (Mg^{2+} or Al^{3+} intercalation). Very recently, Xie et al. [105] have used Ti_3C_2Tx as a support material for Platinum Nano-particles in order to manufacture a fuel cell. They have thus demonstrated that the Pt / Ti_3C_2Tx combination is more durable and more stable than the conventionally used Pt / C pair. After 10,000 cycles, the Pt / Ti_3C_2Tx catalyst lost 15.7% of its active electrochemical surface of Platinum, while the Pt / C electrode lost 40%.

Electrical devices

The two-dimensional morphology of MXenes and their excellent electrical conductivity make them attractive for electronic applications, especially when combined with other 2D semiconducting materials such as MoS_2 [106]. In these hybrid systems, the MXene sheets can be utilized as a conductive interface. They can also be used to modify the electrical properties of the other 2D materials with which they are in contact. At present, no experimental studies have confirmed these hypotheses; only a few DFT simulations are able to predict the

prospective behavior of such hybrid devices. For example, a layer of Ti_2C deposited on MoS_2 would give the latter a metallic character because of covalent bonds introduced at the Ti_2C/MoS_2 interface. On the other hand, for hybrid systems such as Ti_2CF_2 / MoS_2 or $Ti_2C(OH)_2$ / MoS_2, the bonds formed are not covalent, which preserves the semiconducting character of MoS_2. Such hybrid MoS_2 / M_2XT_2 systems provide n-type doping to MoS_2 and operate on the principle of Schottky diodes. For Ti_2CF_2, the barrier is 0.85 eV, for $Ti_2C(OH)_2$, it is 0.26 eV.

In addition, MXenes are efficient heat conductors, which is important for electrical devices. Indeed, DFT simulations made possible to envision high Seebeck coefficients for MXenes, of the order of 1000 μV/K.

1.7 Applications of MAX phases

Since they combine good properties of ceramics and metals, the MAX phases have been promised to a broad range of applications, some of which are already used in the industry. The previous section gave us a basic understanding of the physical properties. In this section, we concretely describe some examples of the rich potential applications that the MAX phases could be put to good use for.

1.7.1 Replacement of Graphite in high Temperature applications

Graphite is a crucial high-temperature resistant material used extensively in many industries. In practice, graphite can be used as rigid insulation, connectors, fasteners, shields, furnace linings, curved heating elements, and heaters in vacuum furnaces. Graphite is also a good candidate material for the hot pressing of diamond-cutting tools and other materials, for the construction industry. With the discovery of MAX phase compounds, some of these requirements can be well fulfilled by the MAX phases, such as Ti_2AlC and Ti_3SiC_2, which have several advantages over graphite such as better wear and corrosion resistances as well as high tolerance resistance. The good mechanical properties and high thermal conductivity of the MAX phases are also attractive. Fig. 1.18 shows that MAX phase insets are tested in industrial dies and perform quite well [42].

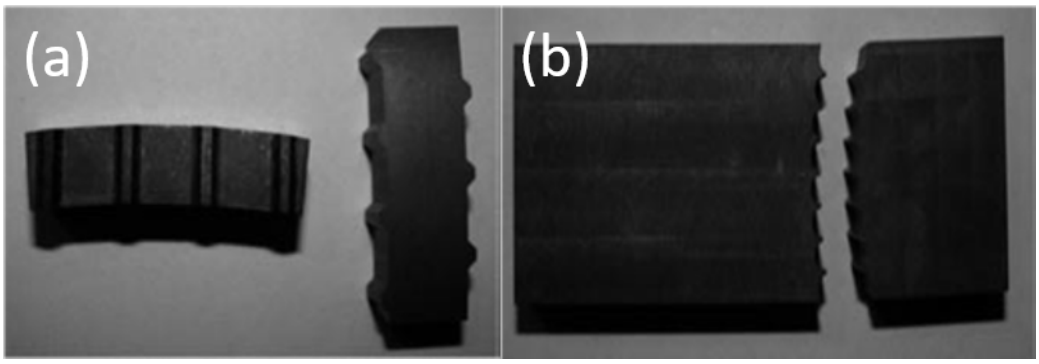

Figure 1.18. (a, b) MAX phase-based insets tested in industrial dies at high temperatures. (Products of 3-ONE-2 Inc.).[42]REF is insufficiently described.

1.7.2 Heating Elements

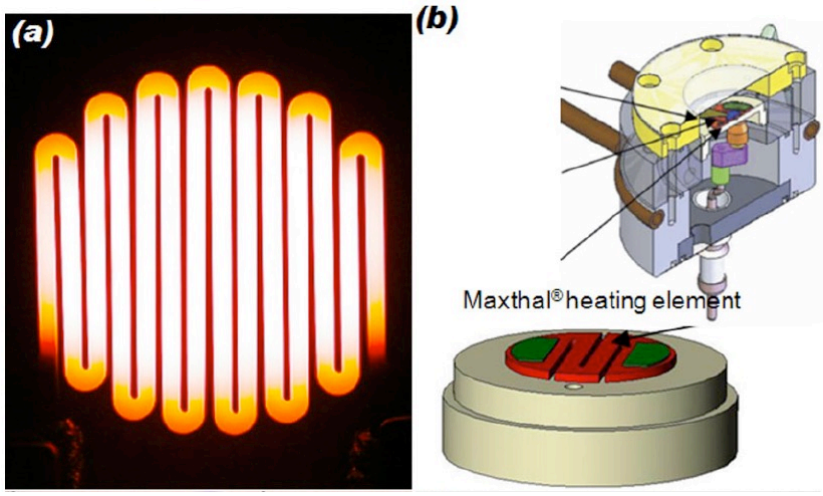

Figure 1.19. (a)An example of Ti_2AlC-based heating element resistively heated to 1450°C in the air (Products of 3-ONE-2 Inc.). (b) Maxthal 211 heating elements in reactor cell for three-way catalyst

In the late 1990s, Kanthal Corp. transferred the MAX phase technology from Drexel University in the USA. As one of Kanthal's core business domains is heating elements, MAX phase heating elements are certainly one of the first practical application developed by the Swedish company. The heating element shown in Fig. 1.19 a is heated up to 1350 °C and cooled down to room temperature for around 10 000 cycles [107,108]. The resistance of the element demonstrates to be very stable, and the formed protective oxide was quite adherent and highly oxidation resistant. Its utilization condition is quite versatile and can be used up to 1400 °C in air, argon, hydrogen, or vacuum. The performance is quite close to that of SiC, which is mechanically, thermally, and chemically resistant up to 1500 °C [109]. Furthermore,

MAX phase heating elements possess a combination of properties such as electrical conductivity and shock resistance, which could remedy the application disadvantage of SiC.

1.7.3 High-Temperature Foil Bearings and Other Tribological Applications

Based on the super mechanical properties, the office of Navy research funded a project aiming at developing MAX phases for new foil bearing elements [110]. Results were successful and showed that the MAX phase material possess low friction and wear resistance in a temperature range from ambient temperature to 650°C. Fig.1.20 illustrates the comparison between a Ta_2AlC/Ag shaft and a super alloy foil bearing after 10 000 cycles in a rig at 50 000 rev min^{-1}. [110]

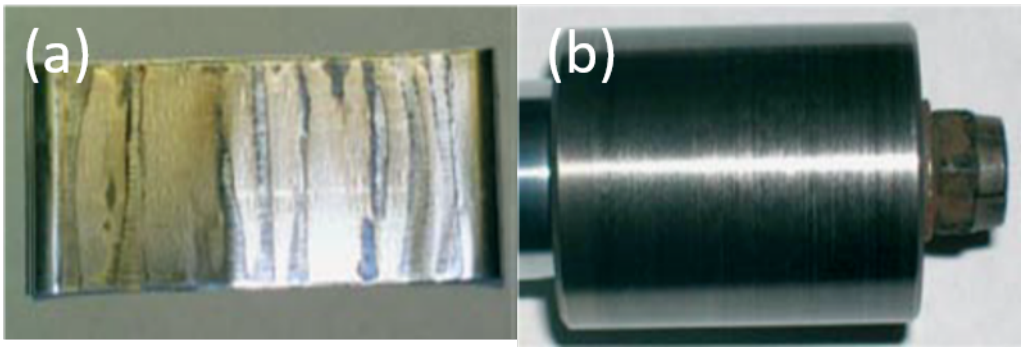

Figure 1.20. (a) Ta_2AlC-based cylinder and (b) Superalloy foil both after rig test on a shaft after 10000 stop–start cycles [110].

1.7.4 Gas Burner Nozzles

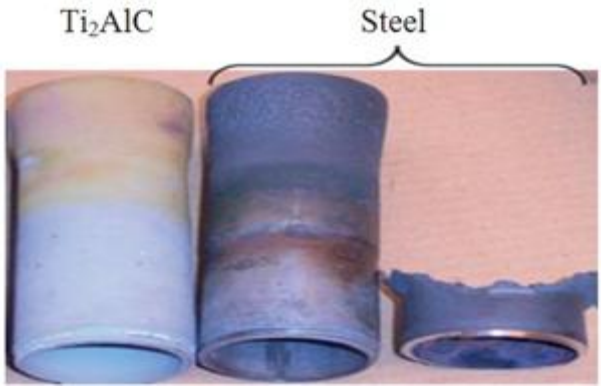

Figure 1.21. Ti_2AlC and steel nozzles used in gas burners. MAX-based nozzles are much more resistant than the steel one in the same corrosive condition. (Courtesy of Kanthal)

The super high-temperature resistance, due to high activation energy and protective oxide films, allows the MAX phase to be applied in many domains extensively. Burning devices are a good example. Ti_2AlC is expected to replace traditional alloys in gas burning applications with fewer limitations and longer service life(Fig.1.21) [42]. Furthermore, the properties fulfill the requirements in the more elevated temperature and harsher environment. In the future, the restriction to the utilization of burning devices can be mostly overcome by MAX phase based materials for long service life and low cost [42].

1.7.5 Tooling for Dry Drilling of Concrete

In the early 2000s, the company 3-ONE-2 founded by one of the MAX phase researchers, Dr. T. El-Raghy, brought out a tool on the front for dry drilling of concrete. This novel element contains diamonds embedded in 312 Ti_3SiC_2 MAX phase segments. The feedback of the material is much better than the traditional elements formed by diamond/Co segments (Fig. 1.22 a,b). With further developments in design to overcome the limits of smearing of concrete powders due to high temperatures and the low toughness of the segments, this material could come to the market.

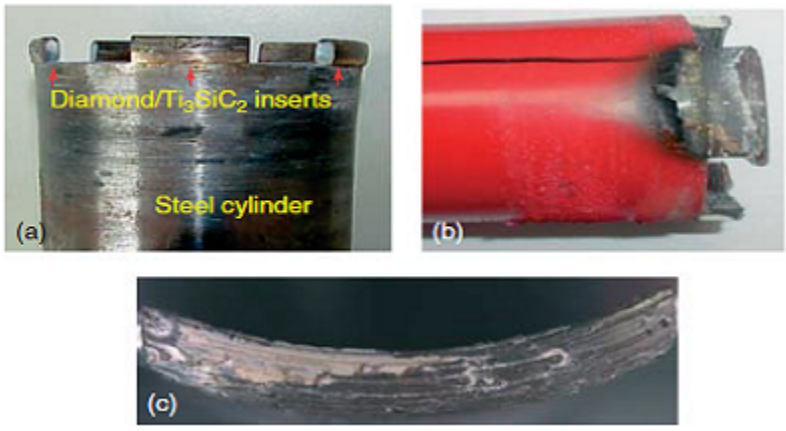

Figure 1.22. (a) Diamond/Ti_3SiC_2 insert (b) Diamond/Co inset, both brazed on steel hollow cylinder after dry drilling of concrete, (c) insert detail of MAX based inset after dry drilling. (Products of 3-ONE-2.). [42]

1.7.6 Glove and Condom Formers and Nonstick Cookware

Ansell Healthcare and Drexel University started to improve gloves and condom formers to manufacture latex products. The plan resulted in the improvement of the slip casting technology for manufacturing large, thin-walled complex parts (Fig. 1.23 a–c) and in a patent. In 2007, another patent was issued by Dr. T. El-Raghy for the application of the MAX phases used as durable, stick and stain and thermal shock resistant coatings, such as dishwasher safe, cookware, cutlery, and other cooking utensils[111].

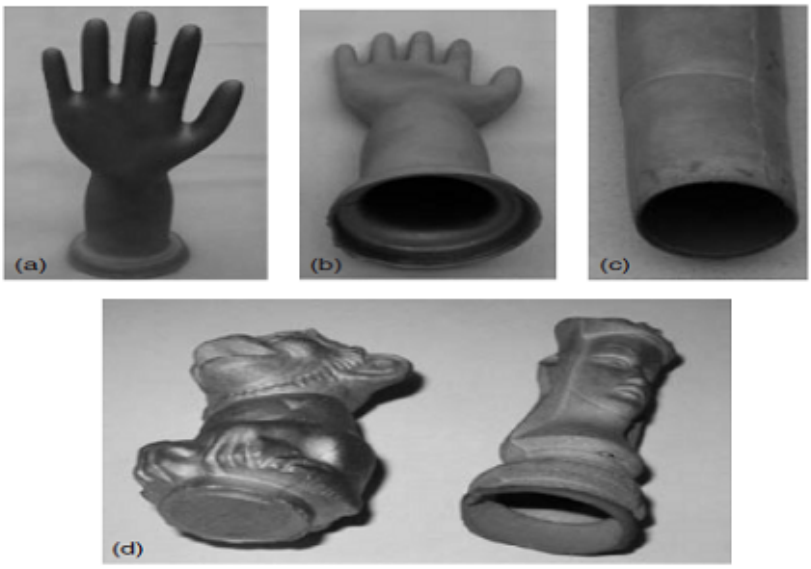

Figure 1.23. (a)-(c) hollow, slip cast Ti_3SiC_2 glove former photographed from different views; and (d) complex solid and slip casting elements made of MAX powders. (Product of 3-ONE-2 Inc.).

1.7.7 Applications in the Nuclear Industry

Availability of electrical energy worldwide is a critical prospect issue. After the leakage of the nuclear raw material of Fukushima in Japan, people worried about the utilization of nuclear power plants. In order to prevent the catastrophe happening again, new technology developments are required to enhance the safety. Among them, the selection of more suitable materials becomes an indispensable factor. Due to the radiation damage tolerance, some MAX phase compounds are considered as promising to be substituted to the traditional ones [112-115]. Hence, they are designed to fulfill some accident prevention requirements. In the perspective of cost, one of the simplest ways is to spray a film of a suitable MAX phase as the coating onto the Zircaloy tubes [116]. A thin film, keeping the

property of protective film forming in the presence of oxygen, is crucial for preventing the accident due to the loss of coolant. For Al containing MAX phases, in the nuclear reactor, they usually form titania rather than alumina, which doesn't have the similar protective ability [114-115]. However, the Si containing MAX phases reveal excellent stability since it does not react with molten Pb and or Pb–Bi alloys [116-118] and are suitably used for containing molten Pb or Pb–Bi alloys in nuclear reactors. Recently, Ti_3SiC_2 was proposed, as a promising candidate, in a developed natural circulation Pb-cooled modular fast reactor [119].

1.7.8 Ignition device and Electrical Contacts

MAX phase compounds have been proposed for new applications like spark plugs and other such ignition devices [122]. One is Ti_3SiC_2 applied by a Swedish company, Impact Coatings, as sputtering targets for the deposition of electrical contacts. This could be used for replacing more expensive gold-coated, non-oxidizing contacts. Currently, other phases are deposited by sputtering, which result, for example, in the formation of Cr_2AlC thin films on steels and turbine blades [123]. In the circumstance of the booming worldwide interest in the MAX phases, it is reasonable to assume that a strong interest could be developed for MAX phases for sputter targets soon. Owing to their excellent electrical conductivity and tribological properties, in addition to the acceptable mechanical properties, MAX phase compounds such as Ti_3SiC_2 and Ti_3AlC_2 are satisfying candidates that could behave better than carbon based pantographs for electric trains. At present, a few leading projects are running in China, aiming for application on the high-speed railway under construction.

1.7.9 Electrical Contact for SiC-based Devices

Currently, SiC-based devices are developed in electronic devices for high resistance in the harsh environment such as high temperatures and corrosive environments. Silicon carbide materials possess far superior properties (high-thermal conductivity, extremely high-melting and decomposition temperatures, large band-gap, excellent mechanical properties, high breakdown field and exceptional chemical stability) to those of Si, rendering them

suitable for installation in harsh circumstance [124-126]. Since its band gap is nearly three times larger than that of Si, SiC possesses properties as a semiconductor. For example, at temperatures as high as 1000 °C, its still acceptably low intrinsic carrier concentration allows operation within the dopant-controlled saturation regime, as required for semiconducting devices. One of the challenges of this technology is to select a suitable material keeping electrical contact with SiC without phase transformation at elevated temperatures and holding low contact resistances. In 2003, a patent was issued [127] for Ti_3SiC_2 as an electrical contact with SiC electronic components. The principle advantage of Ti_3SiC_2 is that it can be kept in thermodynamic equilibrium with SiC. It would, in turn, render the SiC devices feasible for the operation in high-temperature environments without contact reaction with the SiC and deterioration of the device performance. Based on SiC field effect transistors, some sensor application exploit the wide band gap of SiC and its chemical inertness. In such conditions, compatible inert electrode materials, such as Ti_3SiC_2, are also needed.

1.7.10 Forming Processes and Sintering

One of the important properties of the MAX phases is that they can be sintered at low pressure to full density by heating in inert atmospheres such as argon. The first study reporting pressureless sintering of some MAX phases to full density was issued in 2002 [128]. Then another paper published in 2004 [129] did not only focus on the pressureless sintering of Ti_3SiC_2 but also on its tape casting through a process that, reasonably, result in orienting the flaky pre-reacted hexagonal grains. In this paper, it was shown that the simplest method to produce highly oriented microstructures is slightly shaking or taping the dies containing the pre-reacted Kanthal powders before sintering. Hence, this discovery greatly enhances the possibility of commercialization, since the MAX phases could be synthesized to full density without pressure control. The methods of forming the green bodies are quite diverse. They include slip casting, to produce complex, thin wall shapes (e.g., Figure 1.22) [42], extrusion to form tubes (Figure 1.20) [42], cold pressing to form simple shapes (Figure 1.18) [107], cold isostatic pressing [130] and metal injection molding [131]. It is important to note that the inherent ductility of the MAX phases helps to form green bodies without any binder [129]. Spark plasma sintering (SPS) is also considered as a viable method to fabricate and densify the MAX phases [132-134]. At present, further investigations are required to

compare the high-temperature properties of samples made by SPS with those made by reactive hot pressing or pressureless sintered commercial powders.

In addition to the applications mentioned above, MAX phases exhibit a strong potential in a number of other applications which are currently being explored, including electrodes [135], exhaust gas filters for automobiles [136], free-cutting elements [137], etc.

1.8 synthesis

In this section, we will concisely describe typical synthesis methods of MAX phases. These methods will be presented in two groups, according to the quality of the crystal structure which can be obtained, from a polycrystalline form to single crystals. As this thesis focuses on MAX phase single crystals, details about the high temperature solution growth method are more thoroughly expounded.

1.8.1 Polycrystalline materials

1.8.1.1 Hot isostatic pressing

Since 1996, this method has been extensively used in the fabrication of MAX phase compounds [11]. It usually mixes M element substance, X element substance and AX compounds with a precise stoichiometry. Then the mixture powder passes the following steps in order: cold-pressing under high pressure (ex. 180MPa) and hot pressing at high temperature (ex. 1600C) for several hours at high pressure (ex. 40MPa) with the heating rate of 10°C/min. In most cases, this method ensures that the purity of the sample is greater than 98%.

1.8.1.2 The solid-state reaction

MAX phase pure compounds have been prepared by solid state reaction for the first time in 1994[138]. At that moment, it was proposed to advantageously replace other difficult prepared approaches, such as ref[5]. Different with the one-step synthesis [5], this approach consists three steps. The first step is the preparation of the mixture of titanium powder, silicon powder and graphite powder with the molar ratio 0.42,0.29 and 0.29 respectively. Then the mixture is compacted to a pellet and put in an evacuated silica tube. Through 1000°C thermal treatment, a mixture of Ti_3SiC_2, $TiSi_2$ and TiC is obtained. The second step is to remove the

$TiSi_2$ and TiC. At first, HF solution could well dissolve $TiSi_2$ in solution. Then through oxidation in air at 450°C for 10h, TiC could be completely transformed to TiO_2 in order to be dissolved in $(NH_4)\ SO_4$ and H_2SO_4 at 100°C. Here, a pure phase Ti_3SiC_2 is obtained.

1.8.1.3 Pulse Discharge Sintering (PDS)

This method was initially referred to as Spark Plasma Sintering (SPS). It is based on an electrical discharge device used for facilitating the material sintering [132-134][139]. As recent studies indicated that there is neither spark nor plasma in the sintering process, hence this method is correctly named pulse discharge sintering PDS [140] instead of SPS. This approach bears several characteristics: (1) effect of electrical field (2) electrical current impact in conductors or that of skin currents in semiconductors or insulators (3) fast heating and cooling. This induces major differences with the convention methods like hot pressing. The samples in this approach can be sintered in few minutes and need much lower sintering temperature. It can also deal with some difficult-to sinter material. The configuration of PDS device is as Fig.1.24. The mechanical press and electrical current are applied simultaneously to synthesize and densify the powders. The particles are commonly placed in dies made of graphite or metallic materials. In the case of conductive powders, the electrical current will pass through the sample and cause Joule heating for sintering. As to insulating material, the dies should guarantee the electrical conductivity serving as a furnace. Unfortunately, the possibility to produce mechanical parts with a very large volume are hindered by the requirement of using too strong an electrical current.

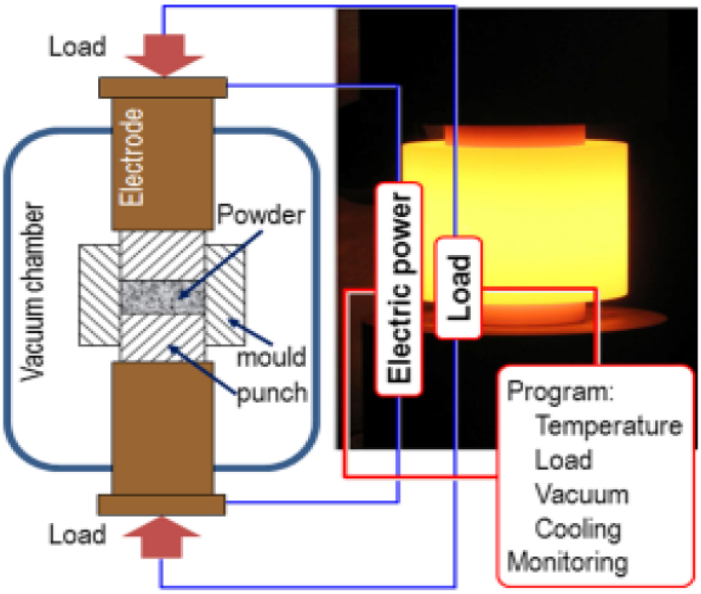

Figure 1.24. Configuration of a pulse discharge sintering machine. The inset is a die setting heating during sintering. [140]

1.8.1.4 Chemical Vapor Deposition (CVD)

This method is only available for the thin MAX phase film. Until now, this method was only applied to a few compounds, mainly the Ti_3SiC_2 compound [9]. We therefore focus on this phase as an example. Starting from the gaseous reactants $SiCl_4$, $TiCl_4$, CCl_4, and H_2, the MAX phase grows on the substrate wafer under extremely low pressure at high temperature [9]. The obtained sample normally has a homogeneous thickness and morphology. However, this method produces a highly polycrystalline film. In general, the gas rate, temperature, pressure play a crucial role in the synthesis of different phases.

1.8.2 Single crystalline materials

1.8.2.1 High Temperature Solution growth method

High-temperature solution growth is one of the most powerful techniques for single crystal synthesis, which allows intrinsic material property measurements [141]. Herein, MAX phase single crystals at LMGP are all synthesized by high-temperature solution growth following a process described in detail in previous articles (see ref. [142] for Ti_3SiC_2, ref. [143] for V_2AlC and ref. [14] for Cr_2AlC). In this section, we take the example of the synthesis of Cr_2AlC, which is the mainly investigated compound in this thesis [144].

According to the Cr -Al-C phase diagram [145], it is feasible to grow Cr_2AlC from a binary Al-Cr beginning melt with $x_{Cr} \approx 0.4$. Beyond 1400℃, further dissolution of an appropriate (small) amount of carbon can lead to the growth of the expected crystals (Fig.1.25).

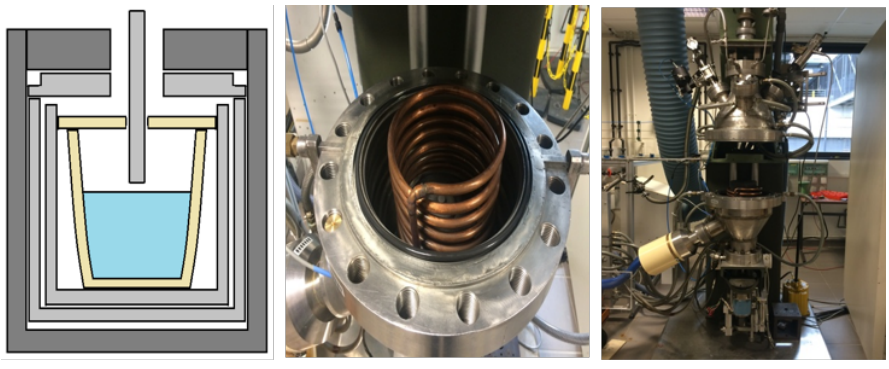

Figure 1.25. Experimental apparatus: a) Schematic of crucible set up, b) heating coil, c) reaction furnace entire view.

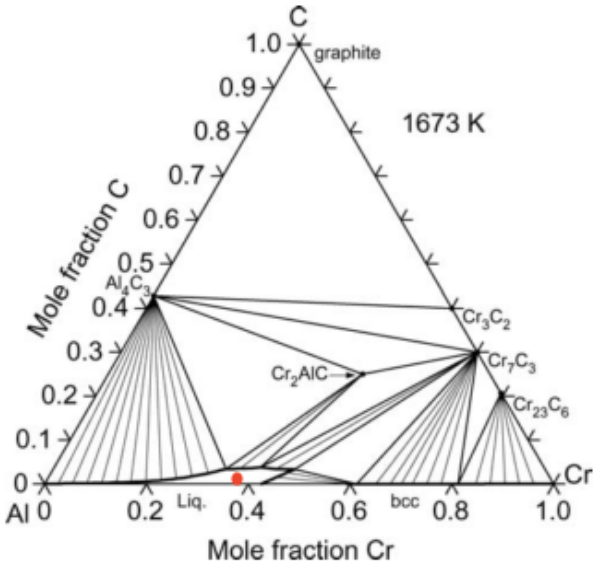

Figure 1.26. Isothermal section at 1673 K of the Cr-Al-C phase diagram [145]

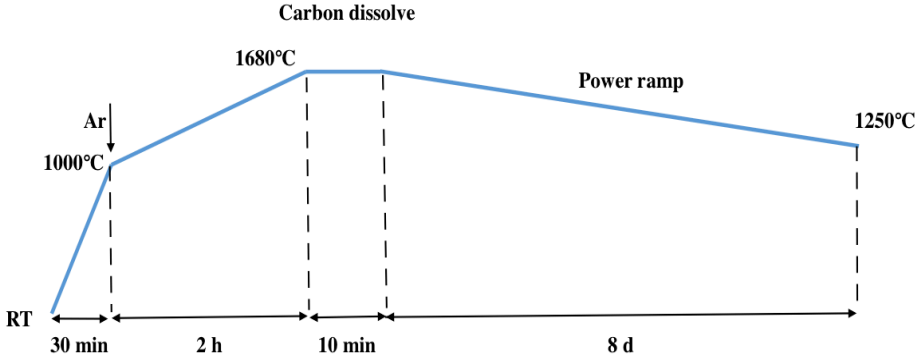

Figure 1.27. Whole process of the high temperature solution growth

Cr and Al powders are at first melted in an alumina crucible which is positioned inside double graphite crucibles, to form the growth solution, with an atomic ratio x_{Al}/x_{Cr} around 8/13. A protective insulating graphite layer is set to reduce heat radiation (Fig.1.25 a). The crucible is heated through induction current furnished by a copper coil (Fig.1.25 b). And all of the steps take place in the furnace shown in Fig.1.25 c). Then, the binary mixture is heated fast to 1000°C under vacuum. Depending on the heating rate, this step is maintained for about 30 minutes. At 1000°C, protective gas Argon is introduced to prevent evaporation.

Then, the crucible is heated to 1600°C slowly during 2 hours. The growth starts from the binary mixtures of Cr and Al granules with the composition close to Al_8Cr_5 as the red mark shown in Fig.1.26. Beyond the melting point of Al, in the ternary Cr-Al-C diagram, a liquid surface forms along the Cr-Al line in the isothermal section [145]. In the temperature range around 1400°C, from a fraction ratio x_{Cr}=0.4 in the binary of Cr-Al, a little quantity of C could result in an equilibrium liquid phase with Al_4C_3 alone, Al_4C_3 and Cr_2AlC, Cr_2AlC alone, or Cr_2AlC and Cr_7C_3 [145]. It provides the possibility to obtain Cr_2AlC from liquid phase. Here, the carbon source is a graphite rod. At a temperature higher than 1600°C which favors carbon dissolution into the solution, the motor-controlled rotating graphite rod is dipped into the solution to diffuse carbon into the system, until a final atomic fraction x_C slightly below 0.1 is obtained. Afterwards, the temperature decreases slowly to avoid the nucleation of numerous Cr_2AlC crystals by favoring Ostwald ripening phenomena [14]. The whole growth process is shown in Fig.1.27. Usual cooling rate is 2-3°C per hour. The slow cooling process is stopped at 1250°C and then the sample goes back to room temperature with natural cooling.

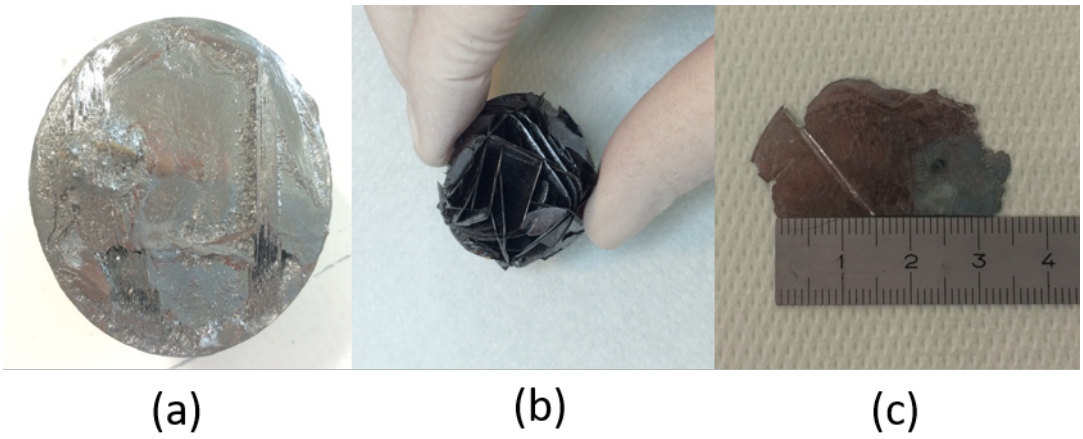

Figure 1.28. Different steps after cooling (Cr_2AlC): a) bulk b) after HCl etching c) a typical sample after sonication

Fig.1.28 a shows the Cr_2AlC bulk taken out of the Alumina crucible after cooling. A big block is formed by the solidified flux, with crystals trapped inside. Due to spontaneous nucleation and crystal growth, after etching in diluted HCl, the crystals are regularly interlocked (Fig.1.28 b) and they can then be extracted from the dissolved solidified flux. Limited by the space of the crucible and complex conditions, the crystals are closely aligned and interlocked with each other. At last, crystals are sonicated in distilled water and ethanol. A typical single crystal of Cr_2AlC is shown in Fig.1.28 c. The platelet area is a few cm^2.The thicknesses of the crystals vary mainly from 100μm to 1000μm.

The power ramp duration is the key point that dominates the platelet size. The longer the ramp time is, the bigger are the crystal sizes. If the ramp time is of order of one hour, the

crystal sizes are smaller than 3 mm^2 as shown in Fig.1.29. And if it lasts 7-8 hours, the biggest platelets can reach several cm^2. Extending the power ramp to 7-8 days can result in crystals with areas bigger than 10 cm^2.

Figure 1.29. Cr_2AlC platelet by one hour power ramp

The carbon proportion is another significant factor that influences the crystallization process. Cr-Al binary compounds could be formed instead of Cr_2AlC under the condition of carbon ratio lower than 4%. The optimized carbon ratio is around 9%.
By this method, the group at LMGP has successfully synthesized relatively large-scale MAX phase single crystals such as Cr_2AlC, V_2AlC, Ti_3SiC_2, etc. Furthermore, new complex MAX compounds are currently developed.

1.8.2.2 Physical vapor deposition by sputtering

This is another important method for synthesizing thin layers of MAX phase single crystals [146-147]. Just as the name implies, it is different from the chemical vapor deposition of polycrystals, because there is no chemical dissociation and reaction of gaseous compounds. According to the reagent sources, we can dissociate to variants: use of a stoichiometric MAX phase compound target or unbalanced dc magnetron sputtering of elemental substances. In the first method, MAX phase target is prepared in polycrystalline form by the conventional method of hot pressing [11]. A magnetron current with a discharge voltage is applied to the compound target. Then the single phase is deposed on the substrate. In the second method, the films are synthesized by unbalanced (type II) magnetron sputtering in an ultra-high vacuum [146]. Before insertion, substrates, which are single crystals of Al_2O_3 or MgO, are ultrasonically degreased in a three-step process by trichloroethylene, acetone, and isopropanol [146]. Similarly with the

first method, all depositions proceed at a constant low pressure with pure argon as the discharge gas and high purity targets of M, X, and A elemental substances. The usual carbon source is co-evaporated C_{60}. As each element target has its own magnetron, different currents, voltages and magnetron positions should be adjusted. The evaporated elements normally arrive onto the substrate table from underneath. Then the substrates are annealed by an in situ heating at high temperature before the growth of a thin epitaxial MX layer seed on the substrates at the same temperature as the subsequently deposited MAX-phase. This growth method is limited to thin layers, and in the available literature, crystal quality has not yet been demonstrated to be excellent and most of all homogeneous over large areas.

1.9 Objectives of this work

Thanks to the improvements brought in Grenoble to the MAX phase crystal growth techniques, studying the chemical reactivity of large size single crystals has become quite feasible. MAX phase chemical reactivity forms indeed the main subject of the present thesis. In the following three experimental chapters, we will present the work achieved for addressing issues all related to reactivity aspects: How do Cr_2AlC single crystals behave in common acids and bases? How do the same crystals behave in high-temperature aggressive environments, such as high T chlorination? What is the role played by the nano-lamellar structure of the MAX phases in each of the chemical reactions involved in such conditions?

In order to answer to the first question, we carried out experiments under different chemical conditions. In chapter 2 and chapter 3, series of experiments in common acids and bases, and high-temperature chlorination are performed. Before our study, researchers have already tested the MAX phase powder in similar conditions. HF has been confirmed as the appropriate method for exfoliating MXenes from MAX phase compounds. Here, we wish to extend the previous results to the case of single crystals, which for some applications possess significant advantages over powders. For instance, owing to the large crystal size, we were able to use the X-ray diffraction Laue method for the first time in order to to characterize the structural evolution of a MAX phase during a chemical reaction.

As already known, MAX phase chemical properties are strongly dependent on the more reactive A elements. Our first question could therefore be substituted by a more restrictive one: how does the A element behave in these chemical reactions? And this question itself could even

be divided into two new ones: What are the appropriate conditions for which the A element can be extracted and what is the structure left behind, depending on those conditions?

Chapters 2 and 3 reveal that A elements can be oxidized by active reagents such as HF and chlorine at high temperature, or at a high polarization potential in electrochemical etching conditions. Concerning chemical reagents used at room temperature, HF and strong oxidants in acid solutions can oxidize the MAX phase single crystals, the yield being as a function of the concentration, time and phases involved. HF and HF-based reagents show an efficient exfoliation power on MAX phases. The acid and proper complexing elements as H^+ and F^-, therefore, are considered to be responsible for selective exfoliation, which could give us the answer for the choice of a suitable exfoliating reagent.

Let us now focus on our second question: what is left behind after the A element removal? The most interesting products of A element extraction are MXenes. These 2D dimensional compounds inherit the nano-lamellar structure of the mother MAX phase, thus making them to benefit from a vast number of interesting properties. Besides, they present similarities with graphene, but might also offer several advantages over the latter [148]. In general, the extraction is performed in HF and HF-based solutions. As explained above, the A element is the most reactive in the ternary system. Hence, it dominates the chemical stability of the whole structure.

The XRD Laue analysis shows the structural evolution from MAX to MXene in HF. With the immersion time increasing, the crystalline order is modified. The less strongly bonded M-A bonds are generally broken and substituted with other side groups. Hence, the c lattice has been modified but it still keeps an order. The ab-plane is shown to become disordered after long etching times and it is proposed that the bonds breaking and terminated group insertion lead to corrosion-induced, stress-induced cracks, which break the structure into pieces. It could explain why the 2D left structure could not reach large-scale through simple HF etching. For future research, a new exfoliation method is needed for obtaining large area MXenes.

In addition to forming 2D structures, in some other conditions, the extraction of the A elements can convert the nano-lamellar structure into a 3D rock salt structure. Previous studies show that in high-temperature chlorination, the MAX phase could be completely converted into graphite. Here owing to the addition of H_2 in the chlorination process, we could focus on the formation of intermediate products. According to the Cr-Al-C phase diagram, Al extraction results in MX binaries with unique features, which could reveal to be interesting for application requirements in the area of gas storage and catalyst carrier.

The anisotropic nano-lamellar structure is a crucial feature of MAX phase compounds. This anisotropy can have a strong impact on the reactivity. In chapter 4, we present the first direct results about the anisotropy influence on electrochemical corrosion resistance, using Cr_2AlC single crystals. A significant anisotropy is demonstrated for the corrosion current and electrochemical impedance analysis proves that the resistance clearly depends on the crystalline orientation. ab-plane presents a higher resistance than c-plane, with complex microscopic mechanism at play. Unveiling those mechanisms could help us to better understand the anisotropy. Furthermore, the characteristic etching patterns which appear during the polarization could be the signature of defects specific to lamellar materials, named ripplocations. The polishing process used before the electrochemical experiment would create these ripplocations, which would transform into deep trenches under polarization.

We hope that even if we did not fully answer to all questions detailed in this introduction, our results will nevertheless bring a useful contribution to a field of research which is driven both by strong academic interests and useful potential applications.

References

[1]. W. Jeitschko, H. Nowotny, F. Benesovsky, Carbides of formula T_2MC, J. Less Common Met. 7 (1964) 133-138.

[2]. J.C. Schuster, H. Nowotny, C. Vaccaro, The ternary systems: Cr-Al-C, V-Al-C, and Ti-Al-C and the behavior of H-phases (M_2AlC), J. Solid State Chem. 32 (1980) 213–219.

[3]. W. Jeitschko, H. Nowotny, F. Benesovsky, Ti_2AlN, eine stickstoffhaltige H-phase, Mon. Chem. 94 (6) (1963) 1198–1200.

[4]. Jeitschko W, Nowotny H, Benesovsky F. Die h-phasen: Ti_2CdC, Ti_2GaC, Ti_2GaN, Ti_2InN, Zr_2InN und Nb_2GaC. Monatshefte für Chemie und verwandte Teile anderer Wissenschaften, 95(1) (1964)178–179.

[5]. W. Jeitschko, H. Nowotny, Die Kristallstructur von Ti_3SiC_2-Ein Neuer Komplexcarbid-Typ, Monatsh Chem. 98 (1967) 329-337.

[6]. H. Wolfsgruber, H. Nowotny, and F. Benesovsky, Die Kristallstruktur von Ti_3GeC_2, Monatsh. Chem. 98 (1967) 2403.

[7]. M.W. Barsoum, B. Houng, Transient plastic phase processing of titanium–boron–carbon composites, J. Am. Ceram. Soc. 76 (6) (1993) 1445–1451.

[8]. Nickl JJ, Schweitzer KK, Luxenberg P. Gasphasenabscheidung im Systeme Ti-C-Si. J Less-Common Met, 26(3) (1972)335–53.

[9]. Goto T, Hirai T. Chemically vapor deposited Ti_3SiC_2 [J]. Material Research Bulletin, 22 (1987) 1195−1201.

[10]. J. Lis, R. Pampuch, J. Piekarczyk, La Stobierski, New ceramics based on Ti_3SiC_2, Ceram. Int. 19 (4) (1993) 219–222.

[11]. M.W. Barsoum, T. El-Raghy, Synthesis and characterization of a remarkable ceramic: Ti_3SiC_2, J. Am. Ceram. Soc. 79 (1996) 1953.

[12]. M.W. Barsoum, D. Brodkin, T. El-Raghy, Layered machinable ceramics for high temperature applications, Scr. Mater. 36 (1997) 535–541.

[13]. A. T. Procopio, T. El-Raghy, and M. W. Barsoum, “Synthesis of Ti_4AlN_3 and Phase Equilibria in the Ti-Al-N System,” Metall. Mater. Trans., 31(2000)373–378.

[14]. T. Ouisse, E. Sarigiannidou, O. Chaix-Pluchery, H. Roussel, B. Doisneau, D. Chaussende, High temperature solution growth and characterization of Cr_2AlC single crystals, J. Cryst. Growth 384 (2013) 88–95.

[15]. D.A.H. Hanaor, L. Hu, W.H. Kan, G. Proust, M. Foley, I. Karaman, M. Radovic, Compressive performance and crack propagation in Al alloy/Ti_2AlC composites, Mater. Sci. Eng. A 672 (2016) 247–256.

[16]. H. Yang, B. Manoun, R.T. Downs, A. Ganguly, M.W. Barsoum, Crystal chemistry of the ternary layered carbide, $Ti_3(Si_{0.43},Ge_{0.57})C_2$, Journal of Physics and Chemistry of Solids 67 (2006) 2512–2516.

[17]. M.W. Barsoum, The $M_{N+1}AX_N$ phases: a new class of solids: thermodynamically stable nanolaminates, Prog. Solid State Chem. 28 (2000) 201-281.

[18]. C. Fang, R. Ahuja, O. Eriksson, Prediction of MAX phases, $V_{n+1}SiC_n$ (n = 1, 2), from first-principles theory, J. Appl. Phys. 101 (2007) 013511.

[19]. G. Hug, Electronic structures of and composition gaps among the ternary carbides Ti_2MC, Phys. Rev. B 74 (2006) 184113.

[20]. D. Music, D.P. Riley, J.M. Schneider, Energetics of point defects in TiC, J. Eur. Ceram. Soc. 29 (2009) 773–777.

[21]. S. Dubois, T. Cabioc'h, P. Chartier, V. Gauthier, M. Jaouen, A new ternary nanolaminate carbide: Ti_3SnC_2, J. Am. Ceram. Soc. 90 (2007) 2642-2644.

[22]. M. B. Kanoun and M. Jaouen, Structure of the ternary carbide Ti_3SnC_2 from ab initiocalculations, J. Phys.-Cond. Matter, 20 (2008)085211.

[23]. J. Etzkorn, M. Ade, H. Hillebrecht, Ta_3AlC_2 and Ta_4AlC_3 – single-crystal investigations of two new ternary carbides of tantalum synthesized by the molten metal technique, Inorg. Chem. 46 (2007) 1410–1418.

[24]. Y. Zhou, F. Meng, J. Zhang, New MAX-phase compounds in the V–Cr–Al–C system, J. Am. Ceram. Soc. 91 (2008) 1357–1360.

[25]. A. Grechnev, S. Li, R. Ahuja, O. Eriksson, U. Jansson, O. Wilhelmsson, Layered compound Nb_3SiC_2 predicted from first-principles theory, Appl. Phys. Lett. 85 (2004) 3071.

[26]. H. Hogberg, P. Eklund, J. Emmerlich, J. Birch, L. Hultman, Epitaxial Ti_2GeC, Ti_3GeC_2, and Ti_4GeC_3 MAX-phase thin films grown by magnetron sputtering, J. Mater. Res. 20 (2005) 779-782.

[27]. Hu CF, Lin ZJ, He LF, Bao YW, Wang JY, Li MS, et al. Physical and mechanical properties of bulk Ta_4AlC_3 ceramic prepared by an in situ reaction synthesis/hot-pressing method. J Am Ceram Soc, 90 (2007)2542–8.

[28]. C.F. Hu, F.Z. Li, L.F. He, M.Y. Liu, J. Zhang, J.M. Wang, Y.W. Bao, J.Y. Wang, Y.C. Zhou, In situ reaction synthesis, electrical and thermal, and mechanical properties of Nb_4AlC_3, J. Am. Ceram. Soc. 91 (2008) 2258–2263.

[29]. Barsoum, M., Golczewski, J., Seifert, H. & Aldinger, F. *Fabrication and electrical and thermal properties of Ti_2InC, Hf_2InC and $(Ti,Hf)_2InC$*. J. Alloys Compd. 340 (2002)173–179.

[30]. T. El-Raghy, S. Chakraborty, M.W. Barsoum, Synthesis and characterization of Hf_2PbC, Zr_2PbC and M_2SnC (M=Ti, Hf, Nb or Zr), J. Eur. Ceram. Soc. 20 (2000) 2619–2625.

[31]. W. Tian, P. Wang, G. Zhang, Y. Kan, Y. Li, D. Yan, Synthesis and thermal and electrical properties of bulk Cr_2AlC, Scr. Mater. 54 (2006) 841–846.

[32]. Palmquist JP, Li S, Persson POA, et al. $M_{n+1}AXn$ phases in the Ti-Si-C system studied by thin-film synthesis and ab initio calculations. Phys Rev B, 70(2004) 165401.

[33]. Rahman, A. & Rahaman, Z. Study on Structural , Electronic , Optical and Mechanical Properties of MAX Phase Compounds and Applications, American Journal of Modern Physics. 4 (2015)75–91.

[34]. X.D. He, Y.L. Bai, C.C. Zhu, Y. Sun, M.W. Li, M.W. Barsoum, General trends in the structural, electronic and elastic properties of the M_3AlC_2 phases (M= transition metal): a first-principle study, Comput. Mater. Sci. 49 (3) (2010) 691-698.

[35]. Hug G, Jaouen M, Barsoum MW. XAS, EELS and full-potential augmented plane wave study of the electronic structures of Ti_2AlC, Ti_2AlN, Nb_2AlC and $(Ti_{0.5},Nb_{0.5})_2AlC$. Phys. Rev. B 71 (2005)24105.

[36]. H. Wolfsgruber, H. Nowotny and F. Benesovsky, “Die Kristallstuktur von Ti,GeC,“, Monatsh. Chem., 98 (1967)240l.

[37]. M.W. Barsoum, T. El-Raghy, C.J. Rawn, W.D. Porter, H. Wang, E.A. Payzant, C.R. Hubbard, Thermal properties of Ti_3SiC_2, J. Phys. Chem. Solids 60 (4) (1999) 429–439.

[38]. Kisi, E. H., Crossley, J. A. A., Myhra, S. & Barsoum, M. W. Structure and crystal chemistry of Ti_3SiC_2. 59 (1998)1437–1443.

[39]. Barsoum, M. W., Yoo, H., Polushina, I. K., Rud, V. Y. & Rud, Y. V. The phases with the general formula M. 62 (2000)194–198.

[40]. R. Lye, E. Logothetis, Optical Properties and Band Structure of Titanium Carbide, Phys. Rev. 147 (1966) 622–635.

[41]. M. Barsoum, MAX phases: Properties of Machinable Ternary Carbides and Nitrides, Wiley-VCH, Weinheim, 2013.

[42]. A.H. Cottrell, Chemical Bonding in Transition Metal Carbides, Institute of Materials, 1995

[43]. Medvedeva, N. I. Electronic properties of Ti_3SiC_2-based solid solutions. 58 (1998)42–50.

[44]. Wang, J., Zhou, Y., Liao, T. & Lin, Z. A first-principles investigation of the phase stability of Ti_2AlC with Al vacancies. 58 (2008)227–230.

[45]. Barsoum, M. W., Farber, L., Levin, I., Procopio, A. & El-raghy, T. High-Resolution Transmission Electron Microscopy of Ti_4AlN_3, or Ti_3AlN_2 Revisited. 47 (1999)2545–2547.

[46]. Musicrajeev, D. & Schneider, A. M. Theoretical study of nitrogen vacancies in Theoretical study of nitrogen vacancies in Ti4AlN3. 31911 (2005)1–4.

[47]. Du, Y. L., Sun, Z. M., Hashimoto, H. & Tian, W. B. First-Principles Study of Carbon Vacancy in Ta_4AlC_3. 49 (2008) 1934–1936.

[48]. Levin, I. Dislocations and Stacking Faults in Ti_3SiC_2. 81 (1998)1677–1681.

[49]. Kooi, B. J., Poppen, R. J., Carvalho, N. J. M. & Hosson, J. T. M. De. Ti_3SiC_2 : A damage tolerant ceramic studied with nano- indentations and transmission electron microscopy. 51 (2003)2859–2872.

[50]. J. Morgiel, J. Lis, R. Pampuch, Microstructure of Ti_3SiC_2-based ceramics, Mater. Lett. 27 (3) (1996) 85–89.

[51]. L. Farber, I. Levin, M.W. Barsoum, HRTEM study of a low-angle boundary in plastically deformed Ti_3SiC_2, Philos. Mag. Lett. 79 (1999) 163.

[52]. SUN, Z., MURUGAIAH, A., ZHEN, T., ZHOU, A. & BARSOUM, M. Microstructure and mechanical properties of porous TiSiC. *Acta Mater.* **53,** 4359–4366 (2005).

[53]. Barsoum, M. W., Farber, L. & El-Raghy, T. Dislocations, kink bands, and room-temperature plasticity of Ti3SiC2. *Metall. Mater. Trans. A* **30,** 1727–1738 (1999).

[54]. M.W. Barsoum, T. El-Raghy, The MAX Phases: unique new carbide and nitride materials, Am. Sci. 89 (2001) 334.

[55]. J.E. Spanier, S. Gupta, M. Amer, M.W. Barsoum, Vibrational behavior of the M n+1AX n phases from first-order Raman scattering (M=Ti, V, Cr, A=Si, X=C, N), Phys. Rev. B - Condens. Matter Mater. Phys. 71 (2005) 2–5.

[56]. O.D. Leaffer, S. Gupta, M.W. Barsoum, J.E. Spanier, On Raman scattering from selected M_2AC compounds, J. Mater. Res. Soc. 22 (2007) 2651–2654.

[57]. J.E. Spanier, S. Gupta, M. Amer, M.W. Barsoum, Vibrational behavior of the M n+1AX n phases from first-order Raman scattering (M=Ti, V, Cr, A=Si, X=C, N), Phys. Rev. B - Condens. Matter Mater. Phys. 71 (2005) 2–5.

[58]. J.Y. Wang, Y.C. Zhou, Polymorphism of Ti_3SiC_2 ceramic: First-principles investigations, Phys. Rev. B - Condens. Matter Mater. Phys. 69 (2004) 1–13.

[59]. Murugaiah, A., Barsoum, M. W., Kalidindi, S. R. & Zhen, T. Spherical Nanoindentations and Kink Bands in Ti_3SiC_2. J. Mater. Res. 19 (2004)1139–1148.

[60]. El-raghy, T., Zavaliangos, A., Barsoum, M. W. & Kalidindi, S. R. Damage Mechanisms around Hardness Indentations in Ti_3SiC_2. 16 (1997) 513–516.

[61]. Ritchie R. O., Gilbert C. J. & McNaney J. M. Mechanics and mechanisms of fatigue damage and crack growth in advanced materials. Int. J. Solids Struc. 37 (2000) 311–329.

[62]. H. Zhang, Z. Wang, Q. Zang, Z. Zhang, Z. Sun, Cyclic fatigue crack propagation behavior of Ti_3SiC_2 synthesized by pulse discharge sintering (PDS) technique, Scr. Mater. 49 (2003) 87–92.

[63]. Gilbert, C. J. *et al.* Fatigue-crack growth and fracture properties of coarse and fine-grained Ti_3SiC_2. *Scr. Mater.* **42,** 761–767 (2000).

[64]. El-Raghy T, Barsoum MW, Zavaliangos A, et al. Processing and mechanical properties of Ti_3SiC_2: II, Effect of grain size and deformation temperature. J Am Ceram Soc, 82(1999)2855–60.

[65]. Wang, X. . & Zhou, Y. . Microstructure and properties of Ti_3AlC_2 prepared by the solid–liquid reaction synthesis and simultaneous in-situ hot pressing process. *Acta Mater.* **50,** 3143–3151 (2002).

[66]. Zhang, W., Travitzky, N., Hu, C., Zhou, Y. & Greil, P. Reactive hot pressing and properties of Nb_2AlC. *J. Am. Ceram. Soc.* **92,** 2396–2399 (2009).

[67]. Barsoum MW, El-Raghy T, Radovic M. Ti_3SiC_2: a layeredmachinable ductile ceramic. Interceram Int Ceram Rev .2000; 49:226-233.

[68]. Barsoum, M. W., Radovic, M., Finkel, P. & El-Raghy, T. Ti_3SiC_2 and ice. *Appl. Phys. Lett.* **79,** 479–481 (2001).

[69]. Hwang, S., Chul, S., Han, J., Lee, D. & Park, S. Machinability of Ti_3SiC_2 with layered structure synthesized by hot pressing mixture of TiC_x and Si powder. 32 (2012)3493–3500.

[70]. Naguib, M.; Halim, J.; Lu, J.; Cook, K. M.; Hultman, L.; Gogotsi, Y.; Barsoum, M. W. New Two-Dimensional Niobium and Vanadium Carbides as Promising Materials for Li-Ion Batteries. J. Am. Chem. Soc. 135 (2013) 15966−15969.

[71]. Naguib, M. et al. On the topotactic transformation of Ti_2AlC into a Ti–C–O–F cubic phase by heating in molten lithium fluoride in air. J. Am. Ceram. Soc. 94 (2011). 4556–4561

[72]. Barsoum, M. et al. The topotactic transformation of Ti3SiC2 into a partially ordered cubic $Ti(C_{0.67}Si_{0.06})$ phase by the diffusion of Si into molten cryolite. J. Electrochem. Soc. 146 (1999) 3919–3923

[73]. El-Raghy, T., Barsoum, M. & Sika, M. Reaction of Al with Ti_3SiC_2 in the 800–1000ºC temperature range. Mater. Sci. Eng. A 298, 174–178 (2001).

[74]. Naguib M, Mashtalir O, Carle J, PresserV, Lu J, Hultman L, Gogotsi Y and Barsoum MW, Two-dimensional transition metal carbides ACS Nano, 6 (2012) 1322–31

[75]. J. Travaglini, M.W. Barsoum, V. Jovic, T. El-Raghy, The corrosion behavior of Ti_3SiC_2 in common acids and dilute NaOH, Corros. Sci. 45 (2003) 1313–1327.

[76]. R. Schutz, D.E. Thomas, in: Metals Handbook: Corrosion, ninth ed., vol. 13, ASM International, 1987, pp. 680–681, 684, 702–704.

[77]. A.D. McQuillan, M.K. McQuillan, Titanium, Butterworths, 1956, pp. 430, 439, 444

[78]. E.J. Kelly, Electrochemical behavior of titanium, in: J.O.M. Bockris, B.E. Conway, R.E. White (Eds.), Modern aspects of electrochemistry No. 14, Springer, 1982, pp. 319–424

[79]. S.Y. Yu, Effects of Nb and Zr Alloying Additions on the Activation Behavior of Ti in Hydrochloric Acid, J. Electrochem. Soc. 146 (1999) 4429.

[80]. C.Y. Yang, Ph.D. Thesis, Department of Materials Engineering, Drexel University, September 2000.

[81]. Barsoum, M., Golczewski, J., Seifert, H. & Aldinger, F. Fabrication and electrical and thermal properties of Ti_2InC, Hf_2InC and $(Ti, Hf)_2InC$. J. Alloys Compd. 340(2002) 173–179.

[82]. Ghidiu, M., Lukatskaya, M. R., Zhao, M.-Q., Gogotsi, Y. & Barsoum, M. W. Conductive two-dimensional titanium carbide `clay' with high volumetric capacitance. Nature 516 (2014) 78–81.

[83]. Naguib, M.; Kurtoglu, M.; Presser, V.; Lu, J.; Niu, J.; Heon, M.; Hultman, L.; Gogotsi, Y.; Barsoum, M. W. Two-Dimensional Nanocrystals Produced by Exfoliation of Ti_3AlC_2. Adv. Mater., 23 (2011)4248−4253.

[84]. Mashtalir, O., Naguib, M., Mochalin, V. N., Dall'Agnese, Y., Heon, M., Barsoum, M. W., & Gogotsi, Y. (2013). Intercalation and delamination of layered carbides and carbonitrides. *Nature Communications*, *4*, 1–7. https://doi.org/10.1038/ncomms2664

[85]. M. W. Barsoum , The $M_{N+1}AX_N$ phases: A new class of solids: Thermodynamically stable nanolaminates, Prog. Solid State Chem., 28 (2000) 201.

[86]. M.Naguilb, V. N. Mochalin, M. W. Barsoum, and Y, Gogotsi, 25th Anniversary Article: MXenes: A New Family of Two-Dimensional Materials, Adv. Mater. 26(2013)992,

[87]. F. Chang, C. Li, J. Yang, H. Tang, M. Xue, Synthesis of a new graphene-like transition metal carbide by de-intercalating Ti_3AlC_2, Mater. Lett. 109 (2013) 295–298.

[88]. Xie, J., Wang, X., Li, A., Li, F. & Zhou, Y. Corrosion behavior of selected $M_{n+1}AXn$ phases in hot concentrated HCl solution : Effect of A element and MX layer. Corros. Sci. 60 (2012) 129–135.

[89]. I.R. Shein, A.L. Ivanovskii, Graphene-like titanium carbides and nitrides $Ti_{n+1}C_n$, $Ti_{n+1}N_n$ (n = 1, 2, and 3) from de-intercalated MAX phases: First-principles probing of their structural, electronic properties and relative stability, Comput. Mater. Sci. 65 (2012) 104–114.

[90]. A.N. Enyashin, A.L. Ivanovskii, Atomic structure, comparative stability and electronic properties of hydroxylated Ti_2C and Ti_3C_2 nanotubes, Comput. Theor. Chem. 989 (2012) 27–32.

[91]. Tang Q, Zhou Z, Shen P, Are MXenes promising anode materials for Li ion batteries? Computational studies on electronic properties and Li storage capability of Ti_3C_2 and $Ti_3C_2X_2$ (X = F, OH) monolayer.". J. Am. Chem. Soc. 134 (2012) 16909–16916

[92]. Enyashin, A.N.; Ivanovskii, A.L. "Structural and Electronic Properties and Stability of MXenes Ti_2C and Ti_3C_2 Functionalized by Methoxy Groups". J Phys. Chem. C. 117 (26): 13637–13643

[93]. Khazaei, M.; Arai, M.; Sasaki, T.; Chung, C.-Y.; Venkataramanan, N.S.; Estili, M.; Sakka, Y. W.; Kawazoe, Y. "Novel Electronic and Magnetic Properties of Two-Dimensional Transition Metal Carbides and Nitrides". Adv. Funct. Mater. 23(2013): 2185–2192.

[94]. Xie, Y.; Kent, P.R.C. "Hybrid density functional study of structural and electronic properties of functionalized $Ti_{n+1}X_n$ (X=C, N) monolayers". Phys. Rev. B. 87 (2013): 235441.

[95]. K. Rasool, M. Helal, A. Ali, C.E. Ren, Y. Gogotsi, K.A. Mahmoud, Antibacterial Activity of $Ti_3C_2T_x$ MXene, ACS Nano. 10 (2016) 3674–3684.

[96]. N.J.Lane, M. W. Barsoum , J. M. Rondinelli , Correlation effects and spin-orbit interactions in two-dimensional hexagonal 5d transition metal carbides, $Ta_{n+1}C_n$ (n = 1,2,3) EPL, 101 (2013) 57004 .

[97]. M. Kurtoglu , M. Naguib , Y. Gogotsi , M. W. Barsoum , First principles study of two-dimensional early transition metal carbides. *MRS Commun. 2 (***2012)** 133 .

[98]. X. Xie, S. Chen, W. Ding, Y. Nie, and Z. Wei, An extraordinarily stable catalyst: Pt NPs supported on two-dimensional $Ti_3C_2X_2$ (X = OH, F) nanosheets for oxygen reduction reaction, Chem. Commun. 49 (2013)10112

[99]. X. Li, G. Fan, and C. Zeng, Synthesis of ruthenium nanoparticles deposited on graphene-like transition metal carbide as an effective catalyst for the hydrolysis of sodium borohydride, Int. J. Hydrogen Energy 39 (2014) 14927

[100]. Y. P. Gao, L. B. Wang, Z. Y. Li, A. G. Zhou, Q. K. Hu, and X. X. Cao, Preparation of MXene-Cu_2O nanocomposite and effect on thermal decomposition of ammonium perchlorate, Solid State Sci. 35 (2014) 62

[101]. Lukatskaya, M.R. ; Halim, J. ; Dyatkin, B. ; Naguib, M. ; Buranova, Y.S. ; Barsoum, M.W. ; Gogotsi, Y.; Room-Temperature Carbide-Derived Carbon Synthesis by Electrochemical Etching of MAX Phases. Angewandte Chemie, Ed.53(2014) 4877-4880

[102]. Naguib M, Come J, Dyatkin B, Presser V, Taberna PL, Simon P, et al. MXene: a promising transition metal carbide anode for lithium-ion batteries. Electrochem Commun, 16(2012)61–4.

[103]. D. Er, J. Li, M. Naguib, Y. Gogotsi, V.B. Shenoy, Ti_3C_2 MXene as a high capacity electrode material for metal (Li, Na, K, Ca) ion batteries, ACS Appl. Mater. Interfaces 6 (2014) 11173–11179.

[104]. Rakhi, R. B., Ahmed, B., Hedhili, M. N., Anjum, D. H., & Alshareef, H. N. (2015). Effect of Postetch Annealing Gas Composition on the Structural and Electrochemical Properties of Ti_2CT_x MXene Electrodes for Supercapacitor Applications. *Chemistry of Materials*, *27*(15), 5314–5323. https://doi.org/10.1021/acs.chemmater.5b01623

[105]. M. Hu, Z. Li, H. Zhang, T. Hu, C. Zhang, Z. Wu, X. Wang, Self-assembled $Ti_3C_2T_x$ MXene film with high gravimetric capacitance, Chem. Commun. 51 (2015) 13531–13533.

[106]. Xie Y, Dall'Agnese Y, Naguib M, Gogotsi Y, Barsoum MW, Zhuang HLL, et al. Prediction and characterization of MXene nanosheet anodes for nonlithium-ion batteries. ACS Nano, 8 (2014)9606–15.

[107]. Sundberg M, Malmqvist G, Magnusson A, et al. Alumina forming high temperature silicides and carbides. Ceram Int., 30(7)(2004) 1899–1904.

[108]. Guilera, G. *et al.* Novel high-temperature reactors for in situ studies of three-way catalysts using turbo-XAS. *J. Synchrotron Radiat.* 16, 628–634 (2009).

[109]. Kremsner, J. M. & Kappe, C. O. Silicon carbide passive heating elements in microwave-assisted organic synthesis. *J. Org. Chem.* 71, 4651–4658 (2006).

[110]. S. Gupta, D. Filimonov, T. Palanisamy, T. El-Raghy, M.W. Barsoum, Ta_2AlC and Cr_2AlC Ag-based composites—new solid lubricant materials for use over a wide temperature range against Ni-based superalloys and alumina, Wear 262 (2007) 1479–1489.

[111]. Gromelski, S.j., Caciolo, P., and Cox, R.L.(2007) Carbide and nitride ternary ceramic glove and condom formers. US Patent 7, 235, 505, P.Office,ed(US).

[112]. M. Le Flem, X. Liu, S. Doriot, T. Cozzika, I. Monnet, Irradiation Damage in $Ti_3(Si,Al)C_2$: a TEM Investigation, Int. J. Appl. Ceram. Technol. 7 (2010) 766–775.

[113]. X.M. Liu, et al., XRD investigation of ion irradiated $Ti_3Si_{0.90}Al_{0.10}C_2$, Nucl. Instrum. Methods Phys. Res. Sect. B-Beam Interact. Mater. Atoms 268 (2010) 506-512.

[114]. J.C. Nappe, I. Monnet, F. Audubert, P. Grosseau, M. Beauvy, M. Benabdesselam, Formation of nanosized hills on Ti_3SiC_2 oxide layer irradiated with swift heavy ions, Nucl. Instrum. Methods Phys. Res. Sect. B 270 (2012) 36-43.

[115]. K.R. Whittle, M.G. Blackford, R.D. Aughterson, et al., Radiation tolerance of $M_{n+1}AX_n$ phases, Ti_3AlC_2 and Ti_3SiC_2, Acta Mater. 58 (13) (2010) 4362-4368.

[116]. J. Frodelius, M. Sonestedt, S. Björklund, J.P. Palmquist, K. Stiller, H. Högberg, et al., Ti_2AlC coatings deposited by high velocity oxy-fuel spraying, Surf. Coat. Technol. 202 (2008) 5976–5981.

[117]. M. Sonestedt, J. Frodelius, J.P. Palmquist, H. Högberg, L. Hultman, and K. Stiller, Microstructure of High Velocity OxyFuel Sprayed Ti_2AlC Coatings, J. Mater. Sci., 2010, 45(10), p 2760-2769.

[118]. L.A. Barnes, N.L.D. Rago, L. Leibowitz, Corrosion of ternary carbides by molten lead, J. Nucl. Mater. 373 (2008) 424–428.

[119]. Heinzel, A., Müller, G. & Weisenburger, A. Compatibility of Ti_3SiC_2 with liquid Pb and PbBi containing oxygen. J. Nucl. Mater. 392 (2009)255–258.

[120]. Utili, M., Agostini, M., Coccoluto, G. & Lorenzini, E. Ti_3SiC_2 as a candidate material for lead cooled fast reactor. Nucl. Eng. Des. 241 (2011) 1295–1300.

[121]. Cinotti, L., et al., 2011. Lead-cooled system design and challenges in the frame of Generation IV International Forum. J. Nucl. Mater. 415 (3), 245-253.

[122]. Markus Diebel. Portable electronic device case, (2010) USD623180 S1.

[123]. D. E. Hajas, M. Baben, B. Hallstedt, R. Iskandar, J. Mayer, and J. M. Schneider, Oxidation of Cr_2AlC coatings in the temperature range of 1230 to 1410◦C. Surface and Coatings Technology, 206(4) (2011) 591

[124]. G. L. Harris, *Properties of Silicon Carbide*, EMIS Datareviews Series, no. 13, INSPEC, IEE, UK, 1995.

[125]. G. Pensl, H. Morkoc, B. Monemar, and E. Janzen, MSF 264-268, pp.3, 1998.

[126]. H. Abderrazak and E. S. Bel Hadj Hmida, *Properties and Applications of Silicon Carbide*, Eds Rosario Gerhardt, ISBN, pp.361-388, 2011.

[127]. J.T. Fraval, M.T. Godfrey, (12) UnIted States Patent, 1 (2013) 5. doi: 10.1126/science.Liquids.

[128]. Michel W. Barsoum, Mats Sundberg, Hans Pettersson, Process for forming 312 phase materials and process for sintering the same,(2002), US6461989 B1.

[129]. A. Murugaiah, A. Souchet, T. El-Raghy, M. Radovic, M. Sundberg, M.W. Barsoum, Tape Casting, Pressureless Sintering, and Grain Growth in Ti_3SiC_2 Compacts, J. Am. Ceram. Soc. 87 (4) (2004) 550-556.

[130]. Salama, I. & Barsoum, M. W. S ynthesis and mechanical properties of Nb_2AlC and (Ti, $Nb)_2AlC$. **347,** 271–278 (2002).

[131]. http://www.fz-juelich.de/iek/iek1/EN/Expertise/Partikelbasierte_Herstellungsverfahren_Sintern/NasschmischeFormgebungsverfahren_Teaser.html? nn=1834806[dataset] 2017

[132]. Cui, B. et al. Microstructural evolution during high-temperature oxidation of spark plasma sintered Ti_2AlN ceramics. Acta Mater. 60 (2012)1079–1092.

[133]. C.F. Hu, Y. Sakka, H. Tanaka, T. Nishimura, S. Grasso, Low temperature thermal expansion, high temperature electrical conductivity, and mechanical properties of Nb_4AlC_3 ceramic synthesized by spark plasma sintering, J. Alloys Comp. 487 (2009) 675–681.

[134]. C. Hu , Y. Sakka , H. Tanaka , T. Nishimura , and S. Grasso : Fabrication of textured Nb_4AlC_3 ceramic by slip casting in a strong magnetic field and spark plasma sintering. J. Am. Ceram. Soc. 94 (2011)410.

[135]. Stolin, A. M. *et al.* Electrode materials based on a Ti–Al–C MAX phase. *Inorg. Mater.* **52,** 998–1001 (2016).

[136]. Sun, Z., Liang, Y., Li, M. & Zhou, Y. Preparation of reticulated MAX-phase support with morphology-controllable nanostructured ceria coating for gas exhaust catalyst devices. *J. Am. Ceram. Soc.* **93,** 2591–2597 (2010).

[137]. F. Parvin, M. M. Hossain and A. K. M. A. Islam ,Phase stability and physical properties of hypothetical V_4SiC_3. arXiv:1110.4452(2011)

[138]. C. Racault, F. Langlais, R. Naslain, Solid-state synthesis and characterization of the ternary phase Ti_3SiC_2, J. Mater. Sci. 29 (1994) 3384–3392.

[139]. Omori, M. Sintering, consolidation, reaction and crystal growth by the spark plasma system (SPS). 287 (2000)183–188.

[140]. Sun, Z., Hashimoto, H. & Tian, W. Synthesis of the MAX Phases by Pulse Discharge Sintering. 718 (2010) 704–718.

[141]. P. C. Canfield and I. R. Fisher, 'High temperature solution growth of intermetallic single crystals and quasicrystals', *J. Cryst. Grow.*, **225**, 155-61 (2001).

[142]. F. Mercier, T. Ouisse, D. Chaussende, Morphological instabilities induced by foreign particles and Ehrlich-Schwoebel effect during the two-dimensional growth of crystalline Ti_3SiC_2, Phys. Rev. B. 83 (2011) 075411.

[143]. L. Shi, T. Ouisse, E. Sarigiannidou, O. Chaix-Pluchery, H. Roussel, D. Chaussende, B. Hackens, Synthesis of single crystals of V_2AlC phase by high-temperature solution growth and slow cooling technique, Acta Mater. 83 (2015) 304–309.

[144]. S. Zhang, L. Shi, F. Mercier, O. Chaix-Pluchery, D. Chaussende, I. Gélard , B. Hackens , T. Ouisse, Conversion of MAX phase single crystals in highly porous carbides by high temperature chlorination. Ceramics International 43 (2017) 8246–8254.

[145]. B. Hallstedt, D. Music and Z. M. Sun, Thermodynamic evaluation of the Al-Cr-C system, *Int. J. Mat. Res*., **97**, 539-42 (2006).

[146]. J.P. Palmquist, U. Jansson, T. Seppänen, P.O.Å. Persson, J. Birch, L. Hultman, et al., Magnetron sputtered epitaxial single-phase Ti_3SiC_2 thin films, Appl. Phys. Lett. 81 (2002) 835–837.

[147]. J. Emmerlich, H. Hogberg, S. Sasvari, P.O.A. Persson, L. Hultman, J.P. Palmquist, U. Jansson, J.M. Molina-Aldareguia, Z. Czigany, Growth of Ti_3SiC_2 thin films by elemental target magnetron sputtering, J. Appl. Phys. 96 (2004) 4817–4826.

[148]. D.N. Bunck, W.R. Dichtel, Bulk synthesis of exfoliated two-dimensional polymers using hydrazone-linked covalent organic frameworks, J. Am. Chem. Soc. 135 (2013) 14952–14955.

Chapter 2

Exfoliation of MAX phase to Mxene

At present, the extraction of MXenes from MAX phases has been carried out and studied only on compacted powders and not directly on large single crystals. The goal of our study is, therefore, to transpose these extraction methods onto large crystals and attempt to discover other effective approaches. In the following paragraphs, we mainly present the diverse trials of extraction of these sheets from the MAX phases and discuss the results.

2.1 Introduction

At elevated temperature, as the M-A bonds are weaker than M-X bonds, MAX phases selectively loss the A element under vacuum [1], in molten salts [2, 3] and some molten metals [4]. Besides, the high temperature makes the de-twining of MX layer into 3D MX rock salt structure [3,5]. Indeed, in MAX phases, the bonds are a mixture of ionic, metallic and covalent. In this high temperature decomposition, MX layers lose their layered structure to adopt that of gemstones, which makes them useless. We will talk about in the next chapter that the MAX phase compounds could lose both M and A elements in the strong etchant H_2+Cl_2 gas at high temperature and are transformed into MX binary compounds. The task of this section is to synthesize large size layers of MXenes and attempt to understand the mechanism and process.

2.2. Experiments and results

The presentation of MXenes is given in the first chapter introduction. In this section, we present all the approaches that we attempt to exfoliate the MAX phases Cr_2AlC and V_2AlC. Although we don't reach the ultimate goal of synthesis of large scale MXenes from MAX phase single crystals, we have a deeper understanding of their chemical reactivity in different conditions and the corresponding mechanisms.

The trials are performed through chemical method and electrochemical polarization method(Fig.2.1). The treated samples are analyzed by XRD Laue method (Bruker D8 Advance diffractometer with Cu Kα1 radiation (λ =1.540598 nm) in the Bragg-Brentano configuration), Raman (Jobin Yvon/Horiba Labram spectrometer), ICP (ICP-MS), and SEM (FEG-SEM, ZEISS ULTRA 55) in order to investigate the reaction process (Fig.2.1) and its etching selectivity toward the A-element.

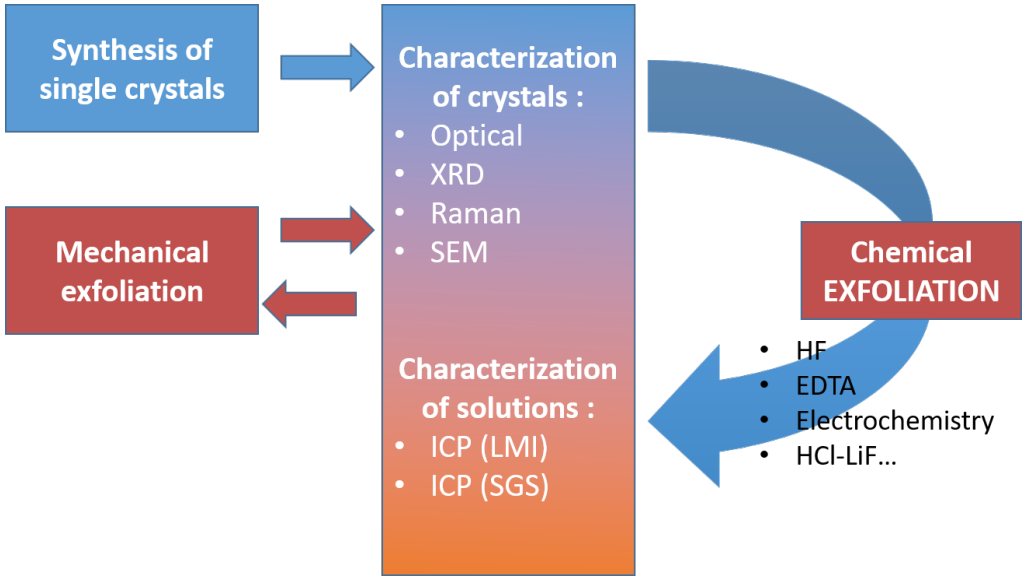

Figure 2.1. Schema of investigation of methods and characterization

2.2.1 Chemical method

According to the previous investigations, HF etching is a conventional method to exfoliate MAX phase into MXene. V_2C have already been synthesized from powder [8]. Therefore, we attempt to convert V_2AlC single crystal into large-scale MXene through different chemical reagents. The V_2AlC has been treated through HF, several HF-based solutions and other chemical solutions. As in the conclusion (Fig. 2.2), conventional inorganic acid HCl and H_2SO_4 seem to not react with MAX phase compounds. Moreover, oxidant reagents in acid could completely dissolve V_2AlC, but not Cr_2AlC. Hence the representative combination H_2O_2+HF is also discussed in this section. Here we primarily present the results in HF, HF base reagent and EDTA, which are typical reagents for the etching and show some positive results. In the end, we present the results of electrochemical polarization that could give us some critical indication for the further investigation.

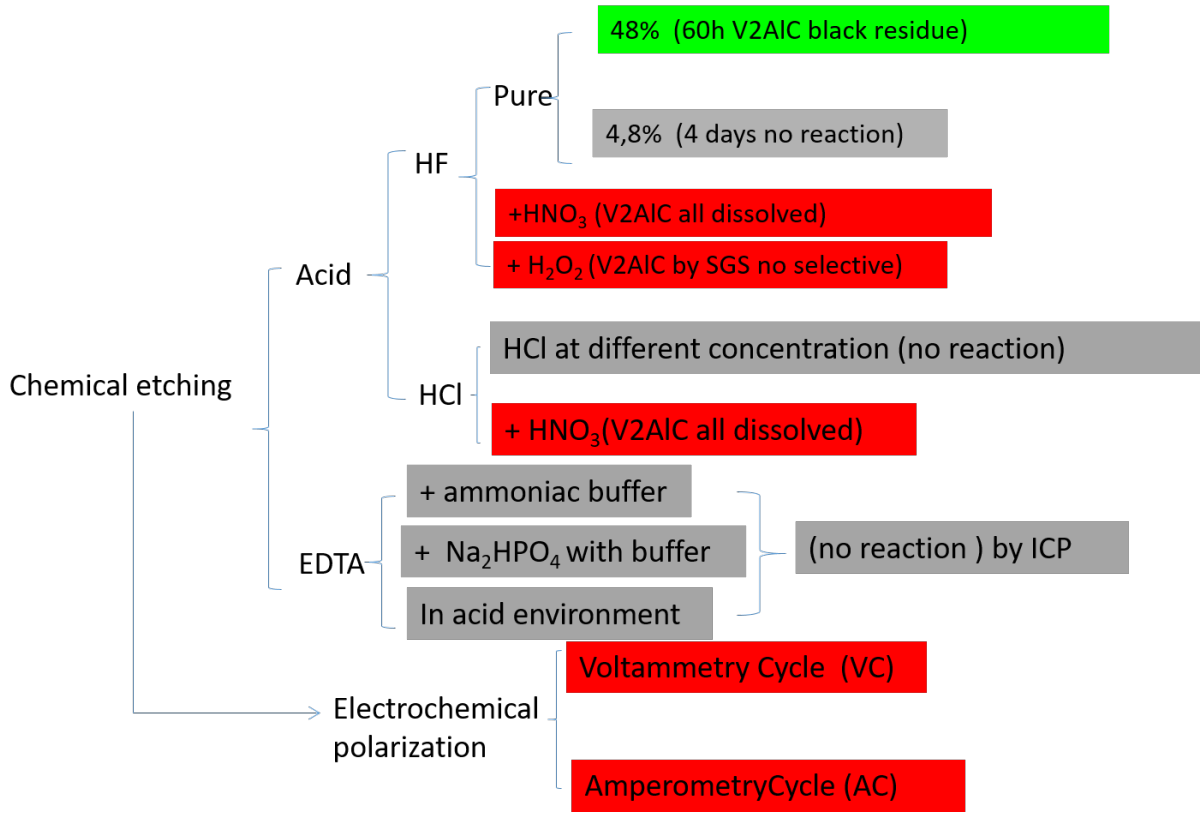

Figure 2.2. Schematic view of the different chemical methods used for etching of V_2AlC and the associated results

2.2.1.1 HF solution and HF based solution

Without doubt, exfoliation for MXene is usually started with HF, as it is the first efficient method. In order to observe the influence of etching time and acid concentration on the extraction of the MXene sheets from the MAX phases, series of experiments were carried out. Crystals of V_2AlC and Cr_2AlC were immersed in different baths at different concentrations and for different etching times. They are summarized in Table 2.1:

Table 2.1. Parameters of partial experiments

Sample Number	Sample	Etchant and concentration	Time
1.1	V_2AlC	HF 48%	16h
1.2	V_2AlC	HF 48%	24h
1.3	V_2AlC	HF 48%	60h
1.4	V_2AlC	HF 24%	7d
1.5	V_2AlC	HF4.8%	7d
1.6	V_2AlC	$HF+HNO_3$	16h
1.7	V_2AlC	$HF+H_2O_2$	16h
1.8	V_2AlC	HF+HCl	16h
2.1	V_2AlC	$HCl+HNO_3$	16h
3.1	Cr_2AlC	HF 48%	16h
3.2	Cr_2AlC	HF 48%	24h
3.3	Cr_2AlC	HF 48%	48h
3.4	Cr_2AlC	$HF+HNO_3$	16h
3.5	Cr_2AlC	$HF+ H_2O_2$	16h
3.6	Cr_2AlC	$HCl+ H_2O_2$	16h

Handling of hydrofluoric acid requires suitable equipment because Fluor elements have a strong chemical activity. All manipulation of hydrofluoric acid proceeds under a fume hood. Wearing the protective suit and safety glasses is compulsory. In addition, we must wear protective boots, a covering apron, and special gloves in order to avoid any contact of the acid with the skin. Much attention should also be paid during the various operations to pour the acid into the water and not vice versa to avoid any acid splashing. The acidic solutions will be drained into the tank provided for this purpose. The dishes contaminated with the acid will be rinsed thoroughly before being cleaned. All the equipment used that could be in contact with hydrofluoric acid should be made of PTFE or PFA so that it does not react in our experiments.

For the mixed solution, the volume ratio is normally 1. The corresponding volume of solution is placed in a Teflon beaker, and the volume of acid (ex. HF 48%) is added to achieve the desired percentage. Using small metal clamps and taking care not to damage them, the crystals of Cr_2AlC or V_2AlC are placed in the Teflon beaker containing dilute hydrofluoric acid.

A parafilm is placed on the beaker in order to protect the solution from the oxygen in air. The beakers are thus left under a fume hood during all the chemical attack. Once the reaction is stopped, we try to rinse our samples thoroughly to ensure that no reagent is left. For this purpose, the acidic solution containing the crystals is passed through a PTFE filter, the crystals and any suspensions are retained by the filter while the acid solution is evacuated. This filter is then rinsed in order to recover the crystals in a highly diluted solution. The operation is repeated until the solution in which the attacked crystals rest are neutral. A pH paper test can simply verify the neutrality of the solution.

Once the crystals are attacked and rinsed, they are placed in a solution of ethanol in order to pass them to the ultrasound. This operation will break up the Van Der Waals bonds established between the sheets after extraction of the Aluminum and thus obtain MXene sheets.

HF 48%

Cr_2AlC and V_2AlC show significantly different chemical resistance. Cr_2AlC single crystal is really vulnerable that it could not resist more than one day in HF at 48% concentration. After 24h, the crystals completely lose their luster and could be crumbled easily. Suspensions are observed which float in the bath from the first hours of the attack. These suspensions are probably detached MAX leaflets. Through special ICP element analysis, suitable to HF condition, the ratio between chrome and aluminum elements in the solution after etching is 2:1, which shows that longtime etching, such as 24h, could turn the selective etching in several hours of the beginning to non-selective. However, in short time, the samples are broken into small pieces and show no difference with the product from MAX powder.

V_2AlC single crystal could keep the metallic luster for several days. This give us more possibility to obtain the large scale MXene and investigate the mechanism. Fig.2.3 shows the morphology of V_2AlC single crystal after 16h HF 48% treatment. The samples still keep the initial shape. However, the edge of crystal loses luster and the center stays metalescent. The surface could be exfoliated by scotch more easily than raw crystal because the M-A bonds on the surface are partially removed and transformed (Fig.2.3a). We could easily perform exfoliation several times on the same sample by scotch tape and obtain a few layers each time. Accordingly, in the following paragraphs (Fig.2.12), we carry on the Raman spectroscopy to measure each exfoliated layer to investigate the conversion process. Obtaining a mole ratio M/C about 2, EDS analysis confirms the chemical composition of the exfoliated compound is MXene

(Table 2.2). Through observation of exfoliated section and no exfoliated section, defects are created through etching as inferred in the literature [5].

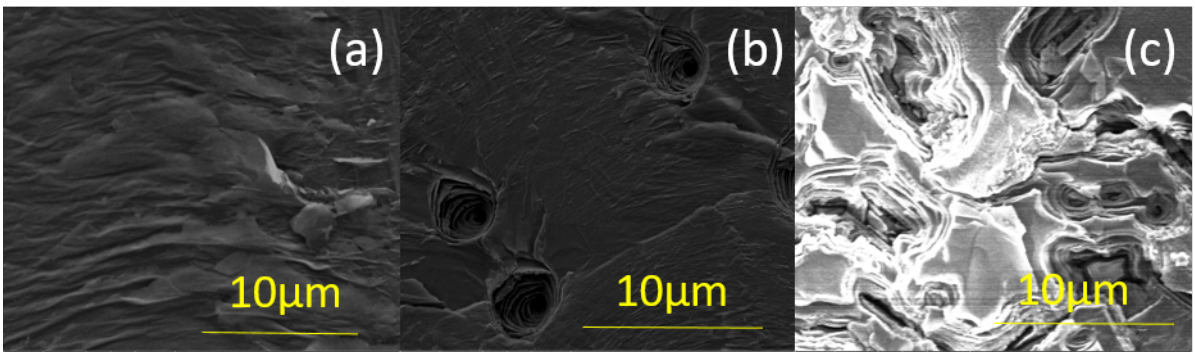

Figure 2.3. SEM observation of V_2AlC single crystal after 16h HF 48% treatment(a) layer exfoliation(b) defect holes(c) defect by HF etching

Table 2.2. EDS elemental analysis of exfoliated V_2AlC single crystal after 16h HF treatment

	El	AN	Series	unn	C norm.	C Atom.	C Error (1 Sigma)
Measure 1				[wt.%]	[wt.%]	[at.%]	[wt.%]
	C	6	K-series	8.33	8.93	24.33	1.50
	O	8	K-series	6.16	6.61	13.51	1.39
	F	9	K-series	6.67	7.15	12.31	1.41
	Al	13	K-series	0.26	0.28	0.33	0.05
	V	23	K-series	71.72	76.91	49.40	2.71
Total				93.25	100.00	100.00	
Measure 2	C	6	K-series	22.61	22.61	46.31	2.76
	O	8	K-series	5.16	7.61	12.45	1.39
	F	9	K-series	14.53	12.08	13.05	2.51
	Al	13	K-series	0.75	0.75	0.68	0.07
	V	23	K-series	56.95	56.95	27.51	6.95
Total				100.00	100.00	100.00	

It is thus found that the longer the etching time, the more the crystals lose their luster and the more they become brittle. As the etching process is gradual, the etched sample is a combination of MAX phase, MXene, and graphene at the same time. Moreover, after long time in the baths samples tend to fragment. This creates difficulties for the synthesis of large-scale MXene.

The coloring of the solution is also a good indicator of the selectivity of the etching. The colorful solution indicates the extraction of M elements and that a part of MAX phase is transformed to graphene. However, assessment of this staining may be difficult, if the MAX / acid ratio is too low (dilute solution).

Finally, in the same series, it is found that some crystals seem to remain unchanged while others are more fragmented and less brilliant. One can think that the quality of crystals plays a role on their ability to be attacked. It is therefore possible to draw conclusions without any doubt that the reactivity of the crystals is not only related to the experimental conditions but also to the quality of the crystals.

After 60h etching in HF, the crystal entirely loses the luster. The mechanical exfoliation is easily done. The Raman and EDS analysis confirm that it is totally converted into graphene (Fig.2.4). An attenuation of the characteristic peaks of the V_2AlC network is first observed in Fig.2.4a. This attenuation confirms the hypothesis according to which chemical etching has been carried out (reduction in the importance of the V_2AlC network). Next, we can notice the appearance of two peaks for high Raman shifts (1372 and 1590 cm^{-1}). These new peaks (Fig.2.4a red curve) resemble the D and G bands observed in Raman microscopy on graphene samples (Fig.2.5)[33]. By EDS, the only detected element is carbon, indicating extraction of both M and A elements (Fig.10 b).

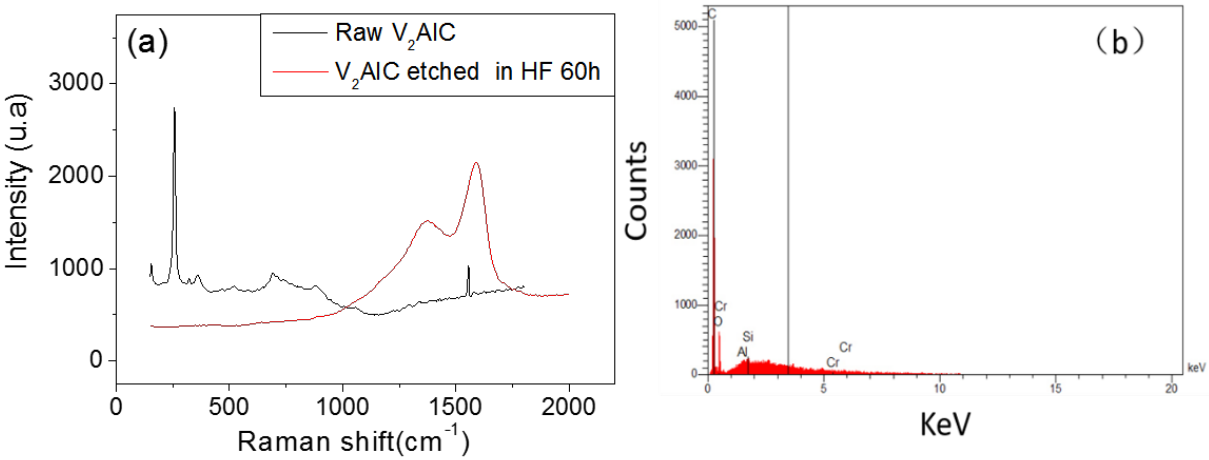

Figure 2.4. (a) Raman spectra of raw crystal V_2AlC and V_2AlC etched in HF 60hours. Wavelength: 473 nm. Hole: 200 µm. Network: 1800. Exposure time: 10s and 8 cycles (b) EDS analysis of V_2AlC etched in HF 60 hours.

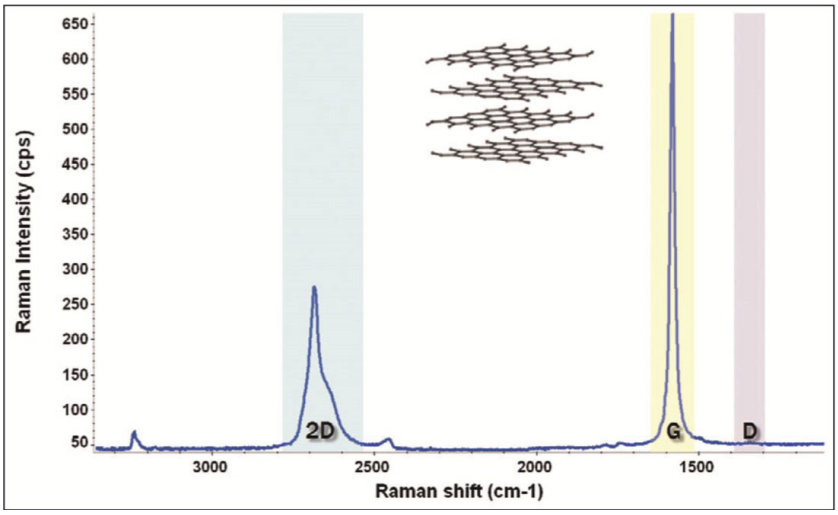

Figure 2.5. Raman spectrum of very orderly pyrolytic carbon. The wavelength used is 633 nm [33]

Fig.2.5 shows a typical Raman spectrum of graphite or graphene. The band G corresponds to vibrations of the sp^2 domains of the graphene. In Fig.2.6, a shift of the band G towards the high wavelengths is observed when the thickness of the graphene decreases. The D band is related to defects and disorder in the structure. It corresponds to a respiration movement of the sp2 domains of the Carbon rings (Fig.2.5). This mode of vibration is only possible if the ring is adjacent to a defect. The D band is therefore directly proportional to the defect amount in the structure [33]. The characteristics of the D and G bands, such as their positions, their intensities or their widths at height, are related to the structure of the studied carbon.

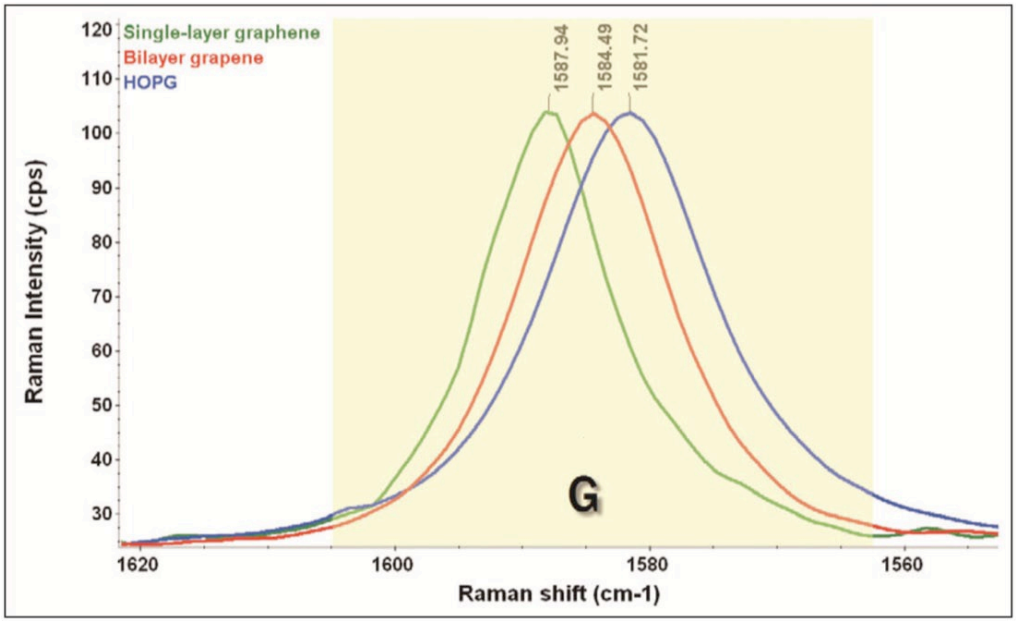

Figure 2.6. Raman spectrum where a shift of the G-band is observed when the thickness of the graphene layer varies. The wavelength used is 633 nm [29].

In the publication [34], the study of the influence of the thickness of chromium layer and of carbon deposited on a chromed amorphous carbon base is carried out. The Raman spectrum in the following Fig. 2.7 is obtained for different individual thicknesses of the Chromium and Carbon layers:

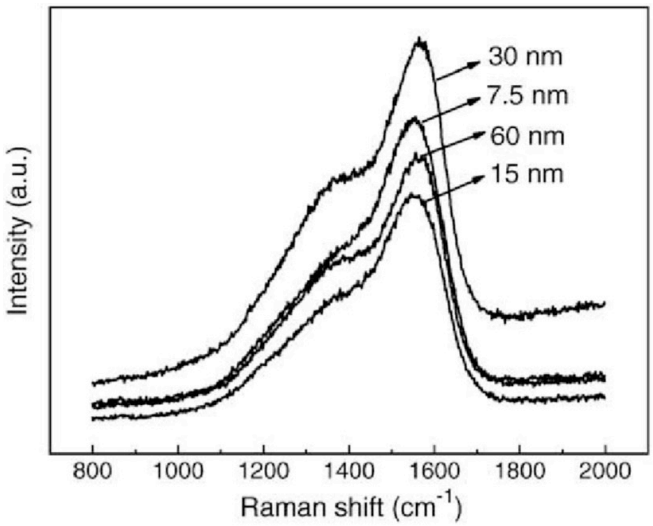

Figure 2.7. Raman spectrum of a Cr-C / a-C: Cr structure with different individual thicknesses of chromium and carbon layers [34].

When the fraction of the sp3 domains of the carbon decreases, the G band is shifted to the high wavelengths and the ID / IG intensity ration decreases [34]. By increasing the thickness of the Cr-C layers, the band G is shifted towards the high wavelengths and the ID / IG ratio is increased, which means an increase in the sp2 domains. The more chromium atoms are introduced, the more the formation of the sp2 domains and the chromium carbide is observed.

The fact that the insertion of metallic atoms, such as Chromium or Vanadium, into an amorphous carbon matrix catalyzed the formation of sp2 structures has already been mentioned in the literature and is also highlighted in this publication [34]. In our case, the peaks of G band are slightly shifted to the right: it is 1600 cm^{-1} for V_2AlC for monolayer graphene [33]. It is this structure that should most closely relate to the crystals, since we also have only one layer of carbon between two layers of element M. This could be due to the presence of a layer of vanadium, which catalyzes the formation of sp2 domains. It is, however, difficult to say in this case whether we have carbides, or residual metal, and graphene. The peak D observed corresponding to the disorder would not be surprising after an attack with hydrofluoric acid.

Another explanation is possible for the appearance of these two new peaks after attack. The Raman spectra of graphene and of oxidized graphene are found in the publication [35](Fig.2.8):

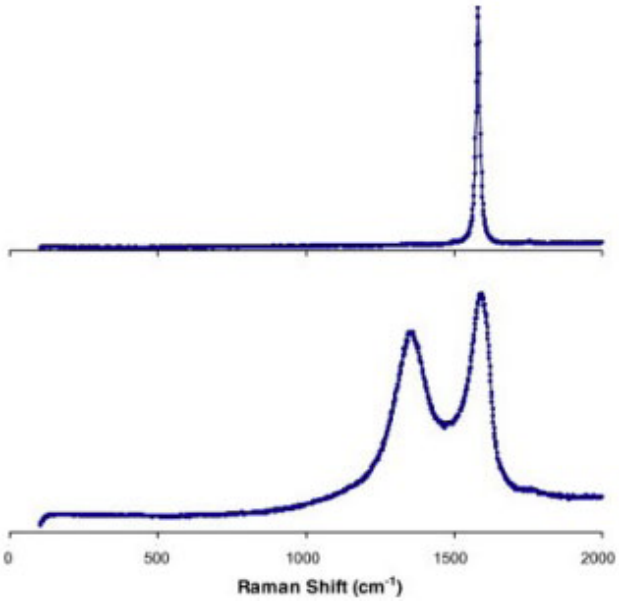

Figure 2.8: Raman spectra of graphene (top) and graphene oxide (below) [36].

It is noted that the two peaks visible for the oxidized graphene may correspond to those observed on the crystals after attack. Indeed, one publication lists these peaks for 1352 and 1605 cm^{-1} oxidized graphene [36], compared to 1380 and 1600 cm^{-1} for V_2AlC sheets after 60h etching in HF (see Figure 2.4a).

For the oxidized graphene, these peaks at 1352 and 1605 cm^{-1} correspond respectively to the bands D and G (Fig. 2.8). The band G is linked to a vibrational mode of the carbon sp2 bonds, and the D band is associated with structural defects and a partial disorder of sp2 domains due to the presence of surface OH groups [37]. The peaks observed at 1380 and 1600 cm^{-1} could therefore correspond to the presence of these groups on the surface of our phases after acid attack.

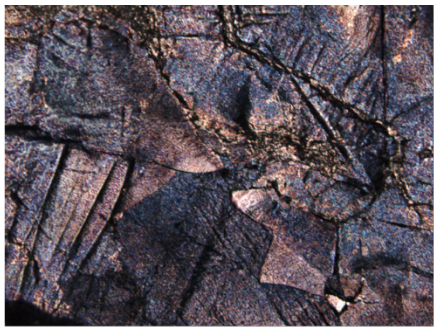

Figure 2.9. Optical microcopy of V_2AlC immersed in HF 48% for 60 hours.

Fig.2.9 shows the V_2AlC etched surface. After 60h etching the V_2AlC are found to be broken into smaller fragments. The obtained pieces are about several millimeters. This fragmentation is a beneficial step for our manipulation since it allows easier delamination

during their passage to ultra-sound. However, it also hinders the formation of large-scale MXenes sheets. The fragmentation could be ascribed to the limitation of the HF diffusion and possibly to the stress corrosion crack [38]. Insertion of T-groups inside the structure during etching, these groups occupying the empty sites could create stress such as torsion between the etched structure and non-etched one, and accelerate the crack formations. Meanwhile, the c lattice increases as well. The results below confirm our assumption and provide a better understanding of the etching mechanism.

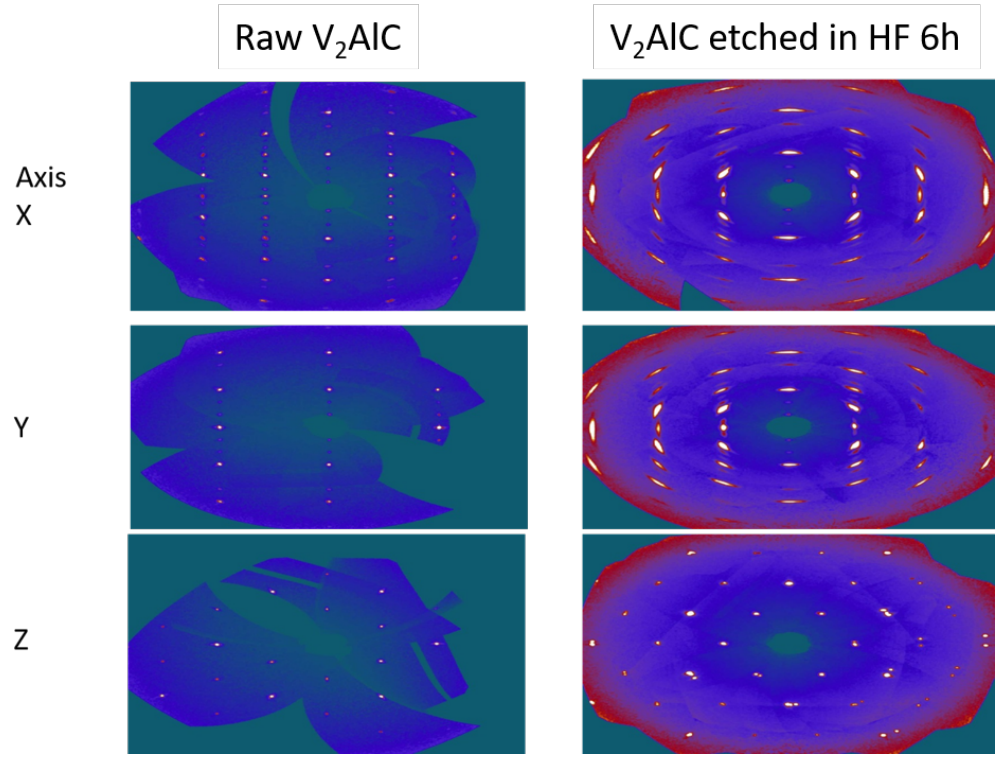

Fig.2.10. XRD diagram of raw single crystal V_2AlC (left) and V_2AlC etched in HF for 6h (right)

Figure 2.10 shows the comparison of XRD diagram between raw V_2AlC and V_2AlC etched in HF for 6 hours. The XRD diagram on the left reveals a perfect structure of single crystal V_2AlC, where diffraction spots are perfectly round shape and symmetrical. In the diagram on the right, the crystal after 6 hours HF treatment demonstrates a different result. The structure along x and y-axis obviously become disordered. The diffraction spots are clearly asymmetrically broadened and tend to form banana shape spot, which shows the variety of the structural lattice parameters. Hence it is reasonable to assess that the original crystalline orientation of **a** and **b** (x and y) rotate and produce more new orientations. In other words, the single crystal turns to polycrystal. It is noted that the diffraction along the z axis (**c** direction) keep the initial state. We assume that the order along c axis remains constant. As these first

results are obtained on different crystals, in order to further investigate the process, we perform a series of experiment on the same single crystal V_2AlC, observed by XRD after each etching step with the same time (Fig.2.11). The selected sample is etched in HF 48% for 8h, and it is repeated two times later. After each acid attack, the sample is passed through XRD analysis. Until to 16h etching, the XRD diagram presents a perfect structure of the single crystal. Then after 24h, the basal plane (along direction x and y) become to disorder, and on the contrary, the **c** axis remains unchanged. The variety of the **a (0kl)** and **b (h0l)** direction demonstrate that in the basal plane, the crystal is no more single crystal. During the etching process, the opening of the structure and addition of terminated groups could create stress of torsion and bending. Therefore, the etching will crack the crystal and into smalls pieces.

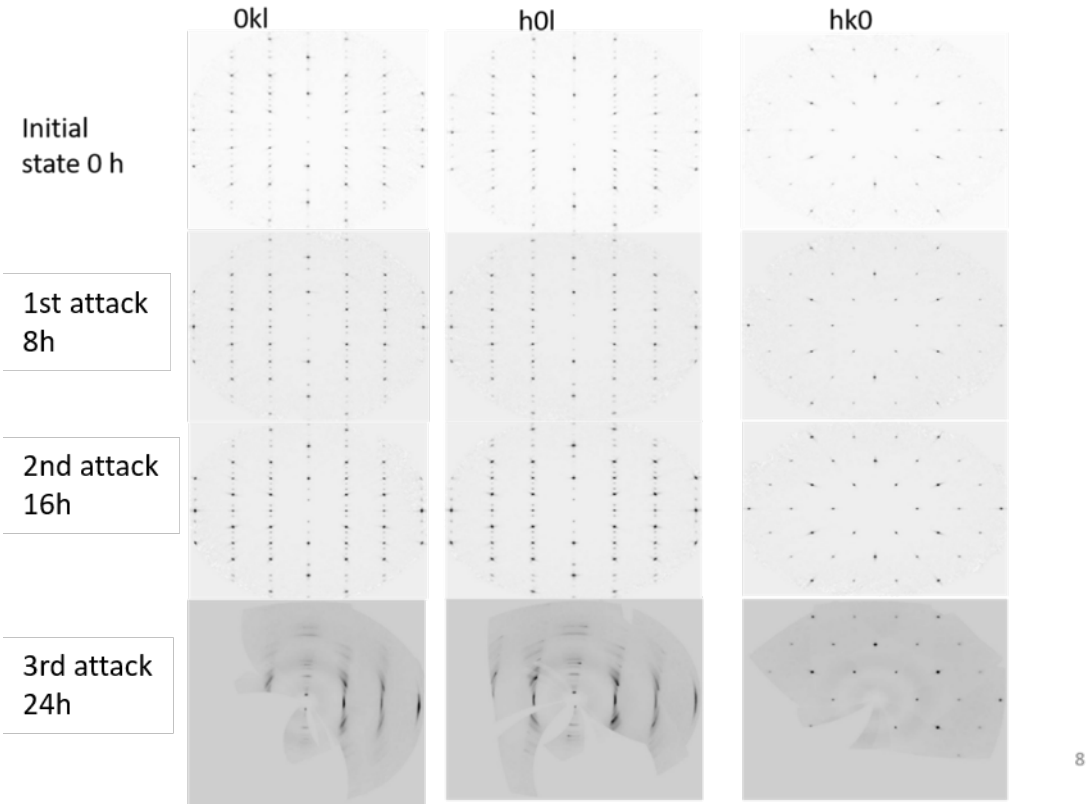

Figure 2.11. XRD diagram of V_2AlC from initial state, 8h etching, 16h etching and 24 etching.

As explained above, the chemical etching could produce stresses breaking the structure and also create defects in the structure. However, this provides us another point of view on the etching mechanism in order to understand the process. We immerse V_2AlC single crystal in HF for 60h. Then the crystal is mechanically exfoliated by scotch tape. As the sample surface has been partially etched, we could perform multi-exfoliations on the sample. The first exfoliation is denoted as 1st layer. In this way, all the exfoliated layers are named and analyzed by Raman

spectroscopy. Raman spectra of the exfoliated layers of V_2AlC after 60h etching are summarized in Fig. 2.12. The first layer (Fig.2.12 khiki curve) could be considered as the surface. Hence the chemical composition is close to the graphene as shown in Figure 2.4a. With the layer number increasing, the transformation portion of MAX phase decreases. Those between the first layer and no exfoliable section are the intermedia states with both graphene and MAX phase/MXene. The first layer has a high intensity of graphene and extremely weak MXene signals. When the measure goes deeper from the surface, the intensity ratio between graphene and MXene decreases. For the moderate number sample, MXene and graphene possess the same intensity, although we cannot give a conclusion that the quantity of MAX/MXene is equal to graphene, the percentage of each composition is probably close. The pic of graphene vanishes until to the no-exfoliable section of the sample. This could explain why the obtained MXene is always few layers because thick etched MAX crystal would finally be composed of MAX phase, MXene and graphene at the same time. According to the kinetics, the diffusion of the etchant limits the homogeneity of the product to several hundred microns.

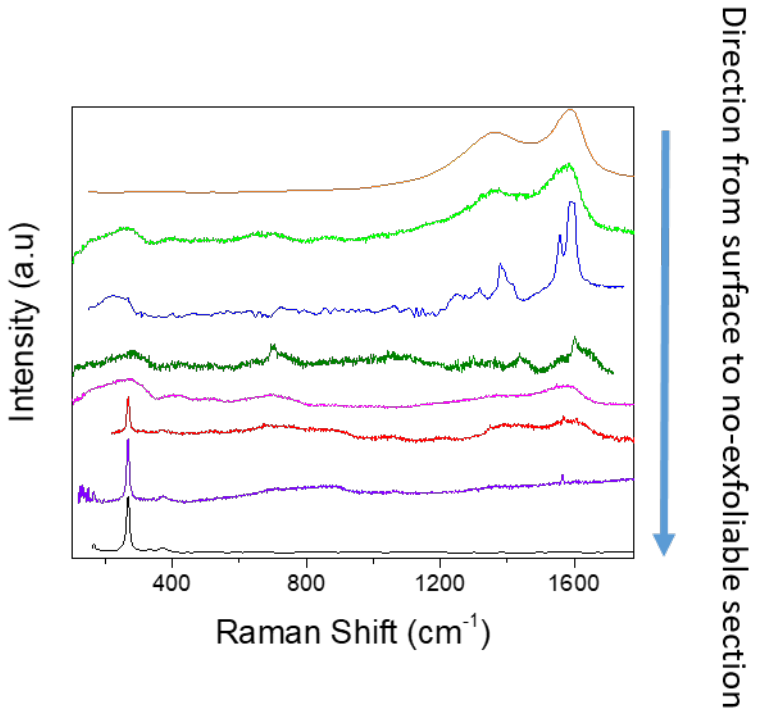

Figure 2.12. Summary of Raman spectra of different exfoliated layer of V_2AlC after 60h etching with raw V_2AlC. The order is from the first exfoliated layer (khaki at the top) to the no-exfoliable section (black at the bottom).

V_2AlC in HF (48%) +H_2O_2(5%)

V_2AlC MAX phase single crystal is put in HF(48%)+ H_2O_2 (Höfer Chemie GmbH 11,9 %) 1:1 at room temperature. We can assume that the oxidant such as H_2O_2 could increase the protective ability of the oxide on the surface. The oxidant largely oxidizes the M and A element to form oxide on the surface, which is an important role in the corrosion resistance for many potential applications. However, V_2AlC performs much less resistant and loses the metallic luster from the first hour. Here we discuss the V_2AlC etched in HF/H_2O_2 for 60h. The crystal completely lost the luster and the complete structure. Hence it is rather soft and easily broken into leaflets. Apparently, H_2O_2 could accelerate the etching process through the oxidation ability. It can be explained that the addition of oxidant could accelerate breaking of M-A bonds. Hence V_2AlC single crystal in HF solution could resist up to 8 days and keep its initial shape while in H_2O_2/HF the crystal is much less resistant. Exfoliated V_2AlC leaflet after 60h in HF/ H_2O_2 is shown in Fig.2.13. After 60 hours, there is no more bulk solid crystal in the solution, and only a black suspension at surface of the solution. Without any doubt, the Raman EDX show that the composition is pure carbon. Therefore the utilization of H_2O_2 in the HF etching could largely accelerate the decomposition process. However, the crystal is broken into smaller pieces than in HF solutions, and the process seems to be less controllable (no selectivity in the etching process) and also introduces higher valence states and secondary phases such as $Cr_2O_4^{2-}$. As a consequence this etching route will not be considered in the following.

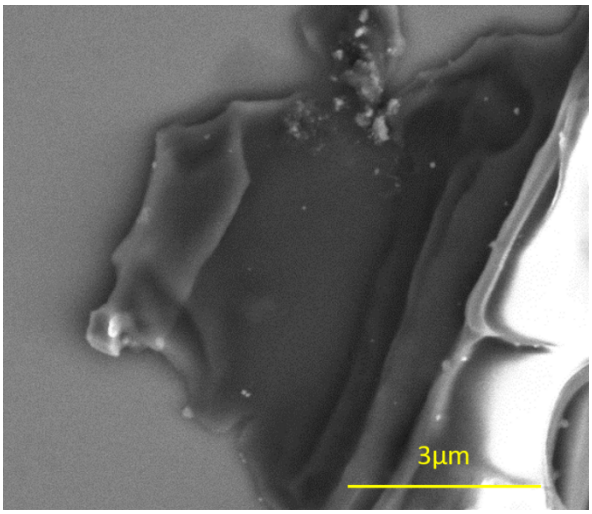

Figure 2.13. Exfoliated sheet after V_2AlC etching in HF 48% + H_2O_2 60 hours

LiF et HCl

In order to better understand and control the process of extraction of aluminum from hydrofluoric acid, the role of the Hydrogen and Fluoride elements in the acid attack of the MAX phases must be identified.

In 2014, a new publication proposed another efficient reagent composition LiF and HCl [6] for MXene formation. According to the chemical composition, the base of the reagent is still on H^+ and F^-. However, the handling of this method is much safer than the conventional way, which avoids the use of HF. Furthermore, as HF is a weak acid that H^+ and F^- are finitely soluble in the solution, LiF and HCl could break the correlation and largely increase the concentration of both two ions. In this way, the roles of both two ions could be enhanced. This method shows the better efficiency and higher purity product. Accordingly, H^+ and F^- could be considered as the essential chemical species in etching solution. Therefore, a series of experiments of different H^+ and F^- concentration solution is performed to investigate the role of H^+ and F^-. HCl is diluted to make the solution from 6mol/L to 0mol/L. Then LiF is dissolved in these acid solutions. Concentrations of H^+ and F^- and the correspondent pH and pF for different solutions are given in Table 2.3 and Fig.2.14 a. HF in different concentrations is listed in Table 2.4. The calculation is listed in the Annex. In comparison, the solubility of LiF in HCl limits the concentration of F^- which remains lower than that in HF. This could largely reduce the ability of exfoliation. According to the results, the low concentrations of F^- plot a red zone where the MAX phase couldn't be exfoliated. For example, in HF 24%, V_2AlC holds the metallic luster for more than two weeks. If the concentration of F^- increases up to the green zone, effective exfoliation is observed. Hence, according to the solubility of LiF, the HCl + LiF mixture cannot fulfill the active exfoliation requirement for V_2AlC.

According to the trials of the acid reagent in our investigation, we can conclude that, to exfoliate MAX phases, there are two fundamental factors. One is the pH value. Another is the amount of complexing agent, like F^-. Shown in Fig.2.14 b, H^+ can be responsible for attack of the M-A bonds and allows the complexing agent to penetrate in the structure (Fig.2.14 b). The F^- can be imagined to follow the way opened by H^+ to remove the A element. The size of complex agent should be critical for the chemical effectiveness. With a smaller diameter, comparing the complexing ability, the F^- is much better than other complexing agent such as Cl^- or EDTA molecule that we also tested. Therefore, an active complexing agent in strong acid is the precondition for the choice of the reagent of exfoliation.

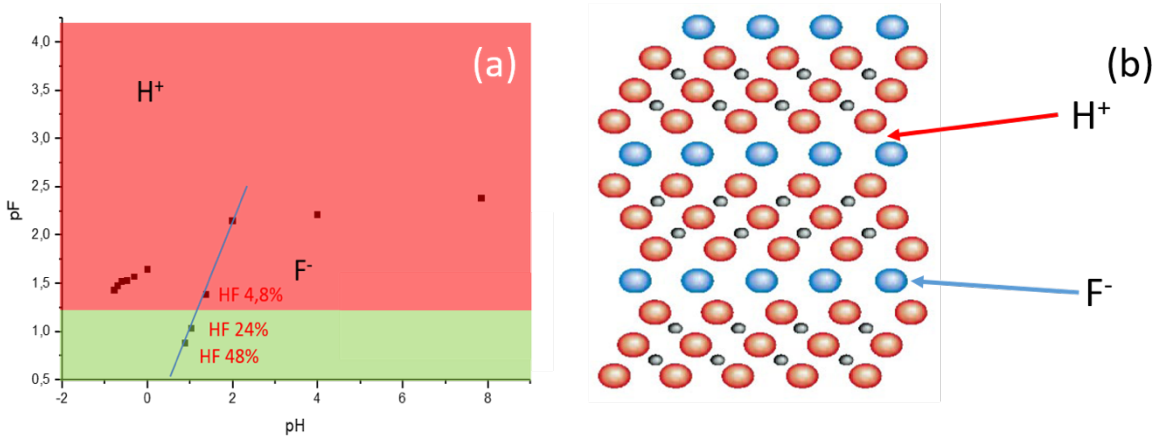

Figure 2.14. (a) pH and pF values of different LiF and HCl solutions (b) chemical exfoliation mechanism of a 312 MAX phase

Table 2.3. Concentrations of H^+ and F^- and the correspondent pH and pF for different solutions

Solution	C HCl(mol/l)	C H^+(mol/L)	pH	pF
1	6	6	-0,778	3,221
2	5	5	-0,69897	3,47315
3	4	4	-0,602	3,777
4	3	3	-0,47712	1,52915
5	2	2	-0,30103	1,56832
6	1	1	0	1,64261
7	0,01	0,01	2	2,14583
8	10^{-4}	10^{-4}	4	2,20751
9	0	$1,43*10^{-8}$	7,84466	2,38007

Table 2.4. pH and pF value of HF in different concentrations

HF%	pH	pF
4,8	1,382	1,382
24	1,032	1,032
48	0,882	0,882

2.2.1.2 Exfoliation in EDTA

Principle and objectives

In the last section, we talk about the roles of H^+ and F^- in the exfoliation of MAX phase. It is therefore interesting to explore other effective complexing agents without the presence of the H^+ ions. For this idea, we try to dissolve the Aluminum of the phases MAX in EDTA aqueous solution with a buffer of Ammonia (basic pH). The complete formulation of the EDTA dihydrate used is $C_{10}H_{14}N_2O_8Na_2{*}2H_2O$, which is usually used to extract metallic atoms [39]. Compared with F^- complexation constant of 6.69[40], EDTA possesses a higher complexation ability of 16.13with Al^{3+}[41]. It is devised to increase the efficiency of extraction. Besides, the presence of the buffer makes it possible to counterbalance the acidification generated by the release of H^+ when the EDTA is solubilized and maintain pH as a constant. The extraction kinetics associated with this complexation is very slow, especially since the etching is anisotropic and is made between thin layers. To overcome this problem, the extraction takes place at 100 ° C, bringing the reaction medium to a boiling point. Water cooling system will recover the vapors from the environment in order not to lose some species during extraction (reflux heating).

A diagram of the setup used is presented in Fig. 2.15:

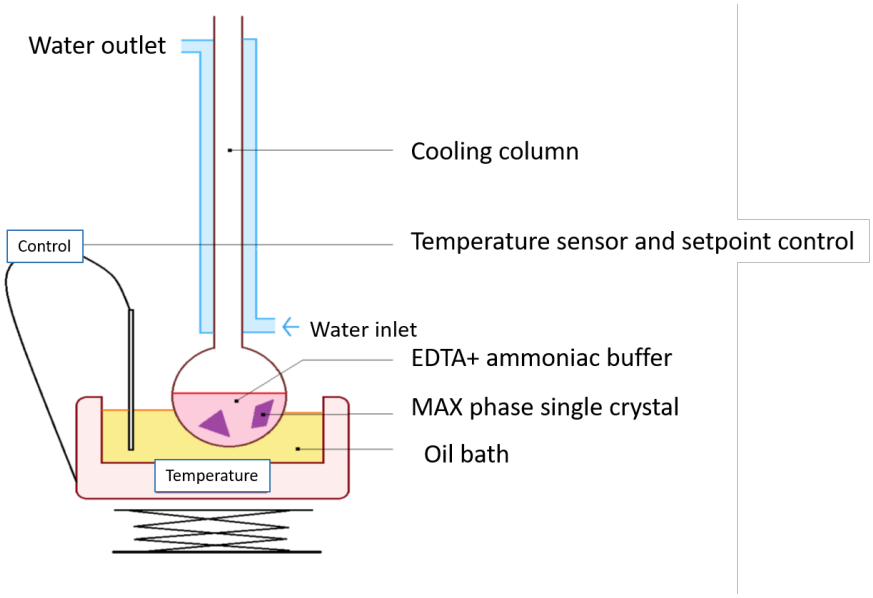

Figure 2.15. Schematic of the experimental device for the extraction of Aluminum by complexation with EDTA at 100 ° C.

A back-assay of EDTA can provide quantity of the metallic ions rest in the solution. In order to be able to perform titration of the quantity of remaining EDTA, the latter is introduced in excess concerning the species that it can complex. One mole of Aluminum reacts with one mole of EDTA. Besides, Chromium or Vanadium could react with EDTA at the same time. Hence, to make our titration back under suitable conditions, we introduce two or three times more EDTA than Aluminum. In order to carry on the attack, it will be sought to have a solution of EDTA as concentrated as possible, within the limit of the maximum solubility of EDTA in water. It is essential to keep in mind that Chromium or Vanadium potentially present in solution in the form of oxides that could also complex with EDTA, which would distort our titration operations. ICP analysis could also allow us to know the elements that are present in the solution and their quantities to determine whether the attack took place and whether it was selective or not. For this characterization method, the detection thresholds are rather low although a sufficiently high concentration of detected species is needed to quantify it reliably. This is why we carry out our attack in small balloons with small quantities of liquid so as not to dilute too much the solution.

Experiment

For this handling, it is necessary to have a flask of a capacity close to 100 mL, a refrigerating column fed with water, a thermostated oil bath, a temperature sensor and finally a

magnetic stirrer ensuring the homogeneity of the solution. The glassware used will be washed, rinsed with acetone and then placed in an oven for drying before use.

In order to carry out the attack of our samples in EDTA, the EDTA solution must be prepared in the desired concentration as well as the ammonia buffer solution which could ensure a pH close to 9. We should, therefore, prepare stock solutions which we keep with a parafilm on a glass beaker.

The aqueous solution of EDTA is prepared with 177 mg of EDTA in powder, diluted in 50 ml of distilled water, in order to obtain a concentrated solution at 8.4×10^{-3} mol /L.

The ammonia buffer solution is prepared by reacting 37% concentrated chloridic acid with 25% ammonia. This reaction is exothermic and is accompanied by harmful gaseous releases. It is therefore important to manipulate under a fume hood. A buffer solution of theoretical and experimental pH of the order of 9 is thus obtained. Such pH will make it possible to verify whether the acidity of the medium is necessary for extraction. It could also allow the back-assay of EDTA. To carry out the etching, 5 to 10% of ammoniacal buffer is added to the volume of diluted EDTA.

This mixture solution and the crystals Cr_2AlC or V_2AlC are placed in a 100 mL flask. The magnetic stirrer is placed in order to homogenize the solution throughout the extraction. Creating a vortex within the medium using this stirrer could also make sure the complete immersion of the crystals in the solution so that they could react better. Grease is applied to the tip of the balloon so that it and the refrigerating column placed above are tight.

The column is refrigerated with water at room temperature. The balloon is half immersed in an oil bath, the temperature of which is recorded by a device connected to a sensor immersed in the bath.

Picture of the whole setup is given below (Fig.2.16):

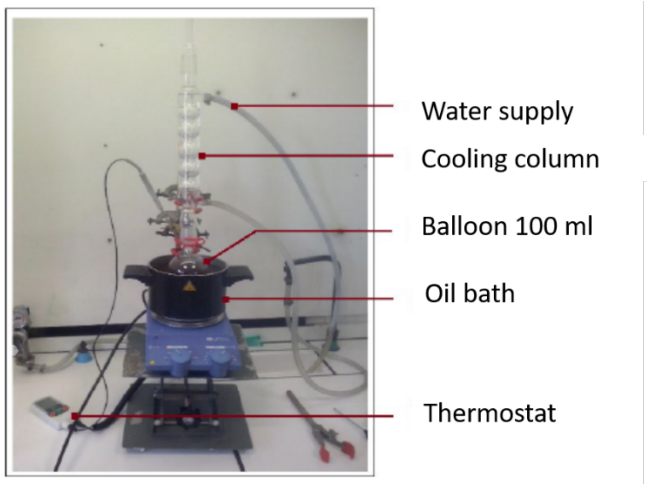

Figure 2.16. Photograph of the experimental setup for the extraction of Aluminum by complexation with EDTA at 100 ° C.

It should be checked that no smoke escapes from the column until the desired temperature is reached during the reaction. This makes it possible not to lose EDTA, which could modify the concentrations of the EDTA solution.

The mother solutions of EDTA, as well as that passed on the crystals are titrated by a complexometric technic using a solution containing Zn^{+} ions. The addition of ammonia buffer and NET colored indicator will make it possible to identify the equivalence for this titration. A turn from violet to blue is easier to spot than a turn from blue to violet. Consequently, the EDTA solution will preferably be placed in the burette for titration. Large amounts of 10^{-2} mol/L Zinc solution were prepared from 99.999% pure zinc bars dissolved in 37% hydrochloric acid. Another EDTA stock solution is also prepared which will serve as a reference for future manipulations.

For calculations related to the titration, it is important to remember that one mole of zinc reacts with one mole of EDTA

Observation: the crystals Cr_2AlC or V_2AlC do not crumble. They keep the metallic luster and have no difference with the initial state.

The first trials are Cr_2AlC, and V_2AlC reacted respectively with EDTA solution for 24h. The titration of the EDTA solution at the end of attack is realized with the 10^{-2} mol/L Zinc solution that is prepared with 99.99% pure zinc. Both equivalent volumes of around 9.85 mL of EDTA are found for 10 mL of Zinc. It shows that no reaction took place with the MAX phases.

Following these tests, the crystals are slightly fragmented because of the magnetic stirrer but retain their metallic luster. The use of a complexing agent such as EDTA alone does not seem to be sufficient to attack the crystals.

Then we ascribe the failure to the solution pH that impair the complexation ability of EDTA. Hence a combination of the complexing agent and an acidic or basic buffer was performed. The concentration of EDTA changed after the addition of the ammonia buffer. A new concentration of 0.88×10^{-2} mol/L is found. Hence, the equivalent volume of EDTA is about 12.1 ml, different with the no-reaction one of 11.4 ml. According to the difference, we could obtain that 6.2×10^{-6} mole of EDTA has complexed with Al^{3+}. Compared with MAX phase quantity of 1.2×10^{-4} mole, 5% of the Aluminum has been confirmed for extraction.

The reaction seems to have successfully taken place. However, it is not convincing. ICP analysis of elements in the solution reveals that the quantity ratio between M and A is about 2.

Hence the EDTA could slightly etch the MAX phase compounds but could not only extract A element.

2.2.1.3 Electrochemical etching

Electrochemical methods can be envisaged for the synthesis of MXene from MAX phases by selective oxidation of element A. Besides, until now, MXenes of Cr-containing phase haven't been successfully obtained by HF. Hence the electrochemical polarization is tried here in different electrolytes.

In 2014, the team of M. Naguib and M. W. Barsoum extracted Aluminum and Titanium from Ti_3AlC_2 by electrochemical anodization, in order to obtain CDC material (carbide-derived carbon)[23]. However, they concluded that this method is not effective for Mxene synthesis of Ti_3AlC_2. Hence, we explore more on the choice of electrolyte and phase. The polarization curve below is Cr_2AlC polarization curve (black) in H_2SO_4 1mol/L with sweep rate of 1mv/s (Fig.2.17)[42]:

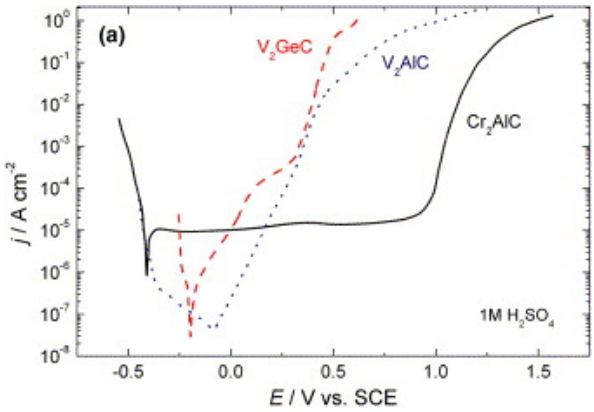

Figure 2.17. Cr_2AlC polarization curve (black) in H_2SO_4 1mol/L with sweep rate of 1mv/s [42].

Two distinct current density increasing slopes are observed at -0.4V and 1V vs. SCE respectively (Fig.23). Each increasing is ascribed to the oxidation of new elements. Since the M-A bonds are less energetic than the M-X bonds, the first increasing is reasonably thought to be ascribed to the corrosion of Aluminum and the second to Titanium or both two elements. Furthermore, between the two density increasing potentials, there is a large gap that could ease the anodization potential choice. For the MAX phase V_2AlC and Cr_2AlC phases, redox standard potentials corresponding to the elements are listed below [43]:

- **Aluminum: -1.66 V relative to hydrogen for the reaction $Al^{3+}+ 3e^- <=> Al$**
- **Chromium: -0.74 V relative to hydrogen for the reaction $Cr^{3+}+ 3e^- <=> Cr$**
- **Vanadium: -1.20 relative to hydrogen for the reaction $V^{2+}+ 2e^- <=> V$**

Aluminum element has the lowest oxidation potential among the three elements. Hence it should be theoretically (thermodynamically) oxidized before Vanadium or Chromium. The synthesis of MXenes could then probably be realized by an electrochemical method. The first step is to realize the polarization curve of the MAX phase. If it shows two distinct peaks, selective etching is maybe possible. We can focus on the potential where the aluminum corrodes according to the polarization curves, and characterize after a few hours the phases obtained. Then with the help of Dr. Malicet, ICP method could determine the elemental quantity in the electrolyte so as to investigate the selectivity.

Experiments

The first goal to reach in order to progress on the extraction of Aluminum by electrochemistry is to obtain the polarization curves of MAX phase single crystals. These curves will allow us to determine whether extraction can be selective for Cr_2AlC and V_2AlC or not and define a possible range for the potential.

To make these curves, we use the following setup (Fig.2.18):

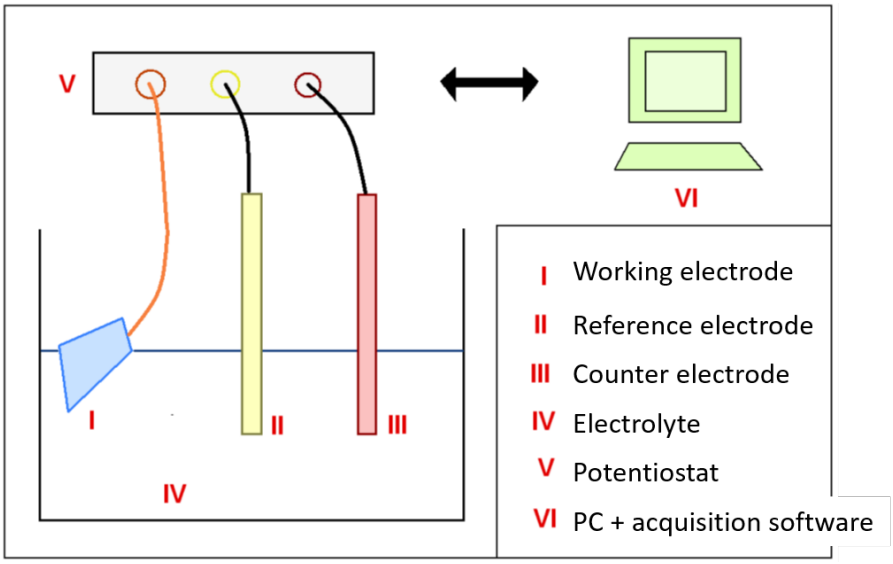

Figure 2.18. Diagram of the setup used for the electrochemical extraction

I - Working electrode: since small sample causes the problem for implementation and the single crystal MAX must be partially immersed in the electrolyte, large crystals are, therefore, selected in order to make good electrical connection and super sealing. In terms of this connection, the Naguib and Barsoum team had welded a copper wire to the crystal and then coated the crystal in a polyester resin, in order to avoid any contact between the copper wire and the electrolyte. This method is not possible in our case because tin does not stably adhere to MAX phase single crystals.

For simplicity, we have chosen to use a Teflon device immersed in the electrolyte. The device ensures the electrical contact between crystal and copper wire and permits to expose a fixed surface of the crystals in order to be able to compare the results obtained from one serie to the other. A description of this device is given in Fig. 2.19.

II - Reference electrode: saturated Calomel Chloride electrode with KCl.

III - Counter-electrode: A graphite counter electrode which does not react with the electrolyte.

IV - Electrolyte: We want to carry out the corrosion of the Aluminum of our MAX phases, so we must choose a suitable solution. Among the media contemplated corroding Aluminum, the usual solution is NaCl, HCl and HF. In the solution of NaCl, the aluminum is corroded by pitting, it means that the reaction is much localized at the level of a local rupture of the passive film as well as HCl. We wish to have uniform corrosion in order to control the corrosion kinetics and to completely remove the Aluminum. Therefore, Aluminum complexing media with non-neutral pH are contemplated, such as EDTA with an ammonia buffer, is our primary choice. H_2SO_4 is also performed for comparison.

V - Potentiostat: A potentiometer / galvanostat of type EG & G273 is used to carry out a potential rise as well as to fix a potential.

VI - PC and acquisition software: The acquisition of potentials must be retrieved on a computer, with appropriate software, in order to draw the polarization curves.

The device used for holding the working electrode consists of a threaded Teflon tube and a Teflon tip which could internally insert inside the tube for impermeability. A metal frame in the core of the nozzle makes it possible to take electrical contact. Once the two parts are assembled, the device is supposed to be sealed. We add washers and Viton seals at the end of the device to improve the seal. A gasket of small internal diameter will also ensure a constant contact surface between crystal and electrolyte. A small metal part will allow to prolong the electrical contact between the tip and our samples because the latter are very thin. A photo of the parts used is shown below (Fig.2.19):

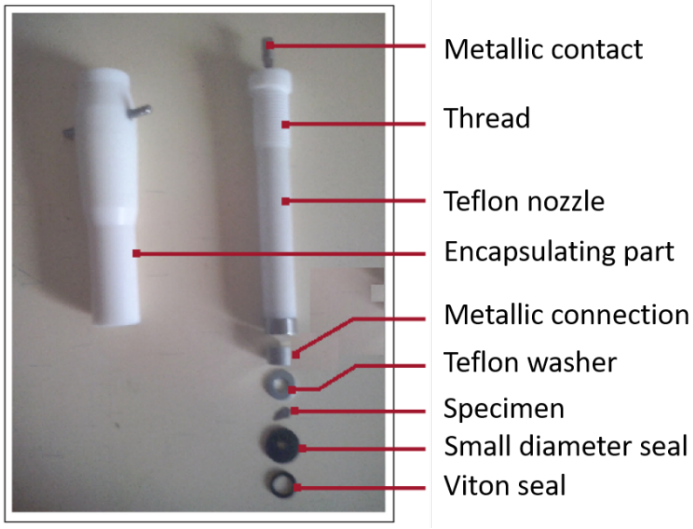

Figure 2.19. Photograph of the device used for the working electrode, shown in exploded view

For simplicity of apparatus, it may be thought to re-machine the encapsulating part of the device so that it is well sealed even without the washers and joints used for the moment. The working electrode, the graphite counter-electrode and the reference electrode are introduced into a glass device, the picture of which is shown in Fig. 2.20.

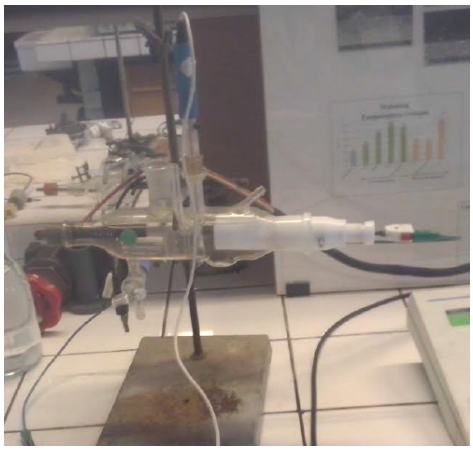

Figure 2.10. Assembly of apparatus for electrochemical experiments.

The potentiometer connected to the computer makes it possible to plot the polarization curves of our samples and treat the data as required. For this manipulation, several experimental parameters can be adjusted, namely:

- The maximum current not to be exceeded (1.5A)
- The sweep range of the imposed potential
- The scanning speed (2.5 mV / s or 5 mV / s)

The last two parameters together determine the electrolysis time.

Before starting data acquisition, it is important to ensure the stability of the corrosion potential of the crystal immersed in the electrolyte. An automatic mode of the potentiostat allows to carry out this check at OCP(open circuit potential) and then automatically starts the voltage scan. In electrolyte EDTA without ammoniac buffer, the obtained curve shows only one sharp current density increasing slope, which could indicate the oxidation of one or both two elements. In comparison, electrolyte of concentrated EDTA solution, to which ammoniacal buffer is added, could demonstrate two distinct increasing slopes of current density. Hence, several voltage scans are perform on Cr_2AlC and V_2AlC single crystal at different sweep rate and with different anodization times. The polarization curves obtained are presented in Fig.2.21 and 2.22. For the scanning carried out on V_2AlC, a bad coupling between the Aluminum stud and the crystals appeared due to a lack of sealing of the assembly (crystals too small, too thin or too irregular, bad clamping). Polarization in Fig. 2.21 is, therefore, difficult to interpret. Hence the investigation is primarily focused on the Cr_2AlC samples. Moreover, we have observed oscillations of intensity during the sweep, which could be possibly explained by a mode of corrosion by crevice as well as bad sealing. Other scans have separate plateaus (Fig. 2.22). It can be assumed that at each of these stages, there is at least one element extracted into solution, which encourages us to realize the selectivity. The orange color solution also appeared on the last stage for the Cr_2AlC phase corrosion. This staining is characteristic as CrO_4^{2-} stable ions in basic solution. This is encouraging, since the oxidation of chromium seems to start only from a high potential.

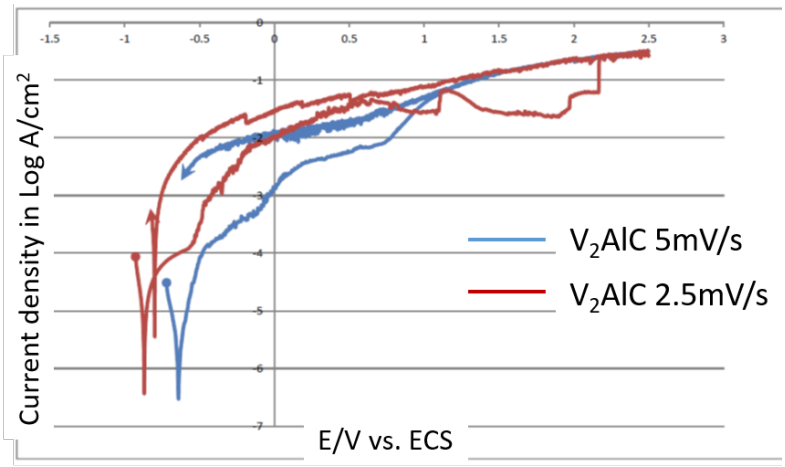

Figure 2.21. V_2AlC polarization curve for two different scan speeds 2.5mV/s and 5mV/s from OCP to 2.5V in EDTA with ammoniac buffer at 25C°

An addition of H^+ ions in the recovered green solution would make it possible to determine whether Chromium is responsible for this coloration (change of color towards orange).

It will be noted that the use of an aluminum stud to prolong the electrical contact is not necessarily welcome since it is not easy to see if there is coupling with the crystals. Moreover, we try to extract the Aluminum from the crystals, thus, coupling and extraction are not distinguishable on the polarization curve plotted with an Aluminum stud. Hence the sealing is a significant factor for the selectivity determination.

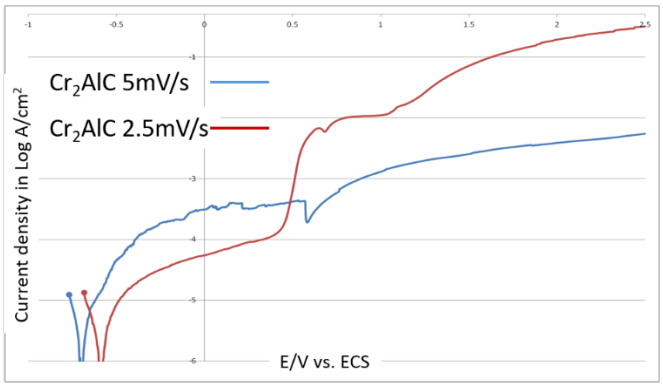

Figure 2.22. Cr_2AlC polarization curve for two different scan speeds 2.5mV/s and 5mV/s from OCP to 2.5V vs SCE in EDTA with ammoniac buffer at 25C°

After improvements of the setup, the polarization curves become stable. We perform the anodization on Cr_2AlC, Cr pure metal, and Al pure metal in EDTA with ammoniac buffer. In Fig. 2.23, apparently, the Cr_2AlC phase possess a better resistance than the two metals. In the polarization plot, for each compound, two distinct plateaus could be observed. Accordingly, we fix a potential on the first plateau to detect the first decomposition element. Then According to the potential in Fig.2.23, we perform the polarization at different potential 250mV, 300mV, 400mV and 500mV in EDTA with ammoniac buffer (pH=9) (Fig.2.24). The polarized crystal surface shows no significant difference with the initial state by optical microscopy. As the electrolyte is basic, there should be already oxide formed on the surface, which increases the corrosion resistance. Hence, in the beginning, the current density is low. With the reaction going on, the electrolysis dissolves the oxides and leading to increase of current and then go to saturation [38]. Beyond our expectation, the element ratio Cr/Al by ICP reveals no selectivity with a stoichiometric value by weight of 4:1. In consideration that Aluminum oxides are insoluble in the solution ($4<pH<12.4$), the real ratio may correspond to the chemical stoichiometry of MAX phase.

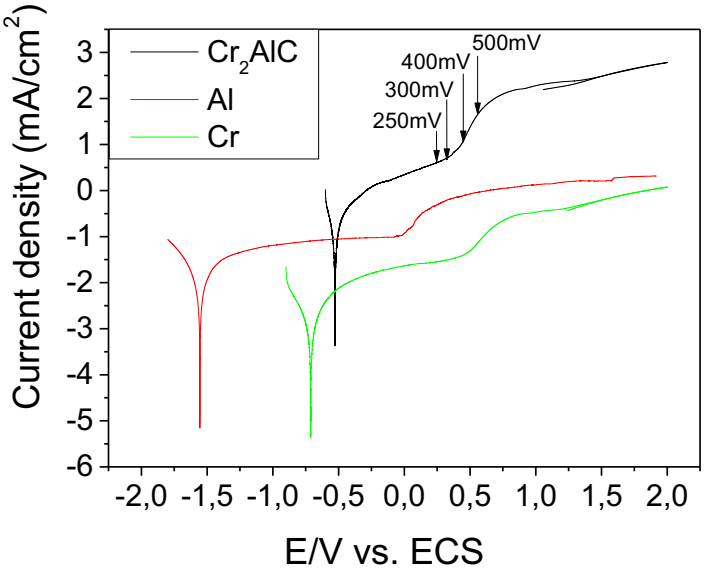

Figure 2.23. Polarization curve of Cr_2AlC, Chromium and aluminum metals with sweep rate 1mV/s from OCP to 2.5V in EDTA with ammoniac buffer at 25C°. The arrows indicate the anodization potential of chrono-amperometry.

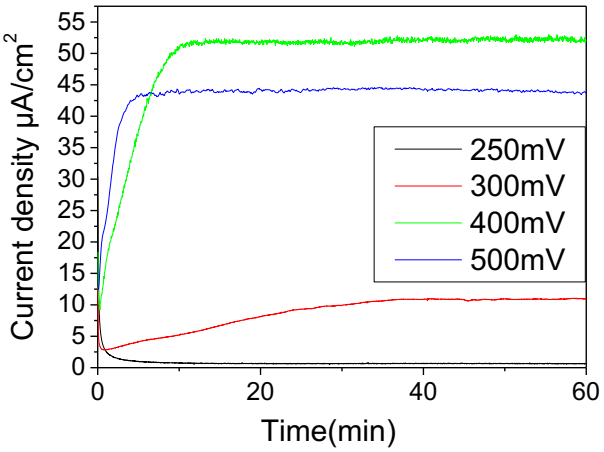

Figure 2.24. Chrono-amperometric curve of Cr_2AlC at 250mV (black line), 300mV (red line), 400mV (blue line) and 500mV (green line) in EDTA with ammoniac buffer (pH=9) at 25C°

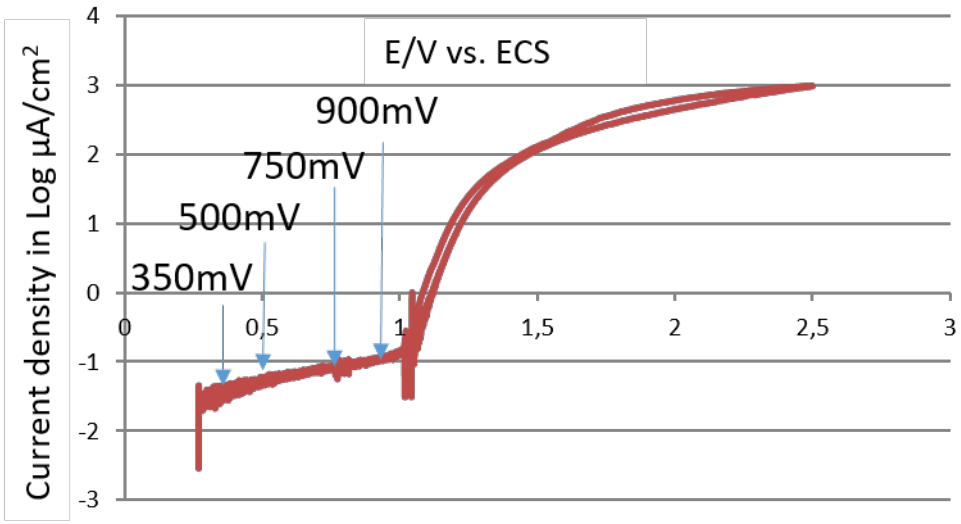

Fig. 2.25. Polarization cycle of Cr_2AlC with sweep rate 1mV/s from OCP to 2.5V in H_2SO_4 at 25C°. The arrows indicate the anodization potential of chrono-amperometry.

In comparison with polarization in EDTA, we perform a series of polarization in H_2SO_4. Fig.2.25 shows the polarization of Cr_2AlC from OCP (-700mV) to 2500mV in 1M H_2SO_4. It is clear that in solution EDTA, the Cr_2AlC has a better corrosion resistance than in H_2SO_4. The first plateau is from about 0.3V to 1.1V vs. SCE respectively. Then we try to polarize Cr_2AlC respectively in H_2SO_4 at constant potential 350mV, 500mV, 750mV and 900mV (Fig.2.26). The curve shows a different phenomenon. At the beginning of the polarization, the starting current density present the maximum value. Then it decreases slowly until to 20h to saturation. It could be ascribed to alkaline environment favoring formation of oxide and without peak corrosion. It can be explained that during the polarization, more oxide layer is formed on the surface which limit the corrosion and that is the reason of saturation in the end. Similarly, in the EDTA solution, Cr_2AlC shows no significant difference with the initial state. The current is possibly ascribed to the electron exchange in the formation of oxides.

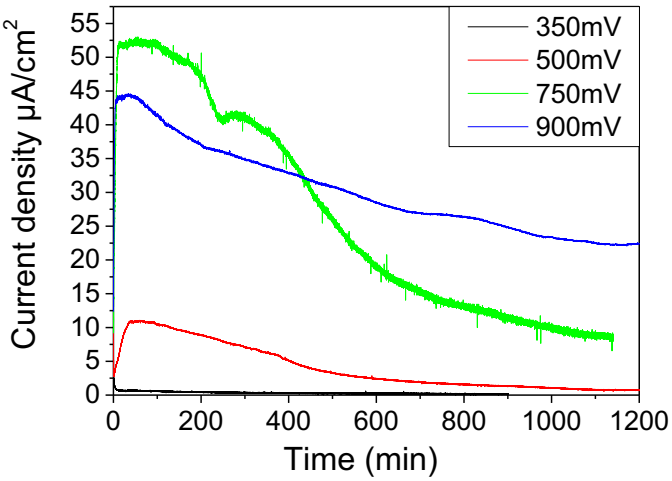

Figure 2.26. Chrono amperometric anodization curve of Cr_2AlC at 350mV (black line), 500mV (red line), 750mV (blue line) and 900mV (green line) in 1M H_2SO_4 buffer at 25C°

However, the anodization potential in the first plateau (Fig.2.23 black curve) could not effectively oxidize the crystals that none of the two elements is detected by ICP in the electrolyte. Therefore, a test of Chrono amperometric anodization at 900mv for Cr_2AlC in EDTA with ammoniac buffer is carried on, at a potential in the second plateau (Fig.2.23 black curve). Fig.2.27 shows image of the crystal after polarization at 900mV for 6h. Yellow deposits are observed on the surface meanwhile the anodization creates defects (Fig.2.27). The clean crystals are obtained by removing deposits in HCl (3mol/L) under ultra-sound (Fig.2.28). The dissolution of deposits in HCl contains high concentration of Chromium and Aluminum by ICP. In comparison with the initial value, the reduction of crystal length and width are significantly greater than that of thickness. It reveals that the corrosion preferentially take place at the edge of the sample. The mechanism and detail are discussed in the chapter 4.

According to the defects on the surface (Fig.2.28), however, the electrochemical anodization is not able to exfoliate the lamellar structure and it creates 3D defects rather than 2D exfoliation. Hence, it doesn't fulfill the requirements of synthesis of MXene that the element A is preferentially extracted and the reaction leaves a 2D compounds.Furthemore, extraction of chromium reveals the failure of selective oxidation of Al, that no MXene is expected.

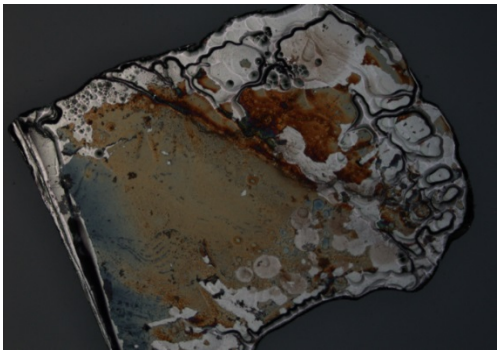

Figure 2.27. Cr_2AlC polarized at 900mV for 6h in EDTA with ammonic buffer by optical spectroscopy.

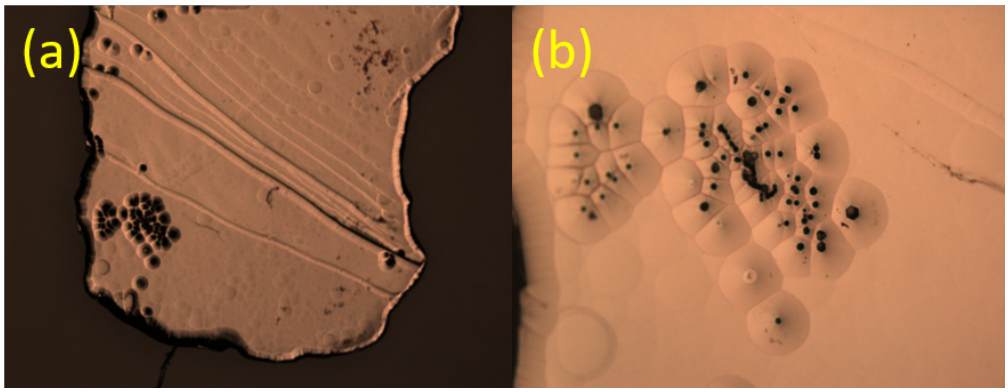

Figure 2.28. Cr_2AlC cyrstals surface after polarization t 900mV for 6h in EDTA with ammonic buffer and ultrasonic cleaning with 3M HCl

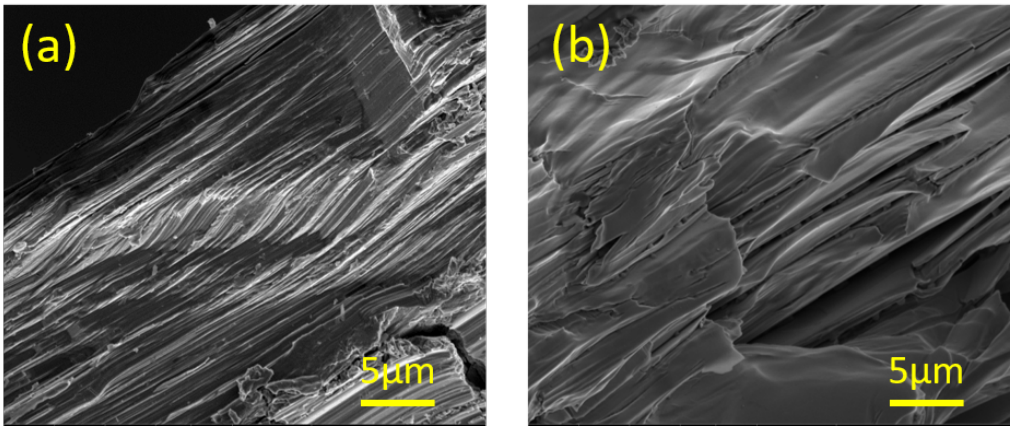

Figure 2.29. cross-section of broken crystal Cr_2AlC (a) raw (b) after chrono-amperometric anodization at 900mV for 6h in EDTA with ammoniac buffer.

A single crystal Cr_2AlC is snapped before polarization. Then a chrono-amperometric anodization is performed on. Fig.2.29 shows the cross-section of snapped Cr_2AlC before and after polarization in EDTA with ammoniac buffer at 900mV for 6h. Compared with raw structure, polarized cross-section exhibits some micro-fissures (Fig.2.29b). However, the ICP

result is quite disappointing. Table 2.5 reveals the ICP result for the electrolyte of polarization of Cr_2AlC and V_2AlC at 900mV. The weight ratios Cr/Al and V/Al is around 4, which correspond to the chemical stoichiometry ratio. This indicates that the polarization is not selective for any elements. These phenomena have already been described in the literature [10]. The result shows that electrochemical polarization is not an effective way for MXene synthesis in the electrolyte we used in the present study.

Table 2.5. ICP result of electrolyte of polarization for V_2AlC and Cr_2AlC

Sample	**type**	**Electrolyte**	**M ppm**	**A ppm**	**M/A**
Cr_2AlC (M/A =3,854 by weight)	CV OCP to 2000mv	EDTA with ammoniac buffer	148,1	37,4	3,95
	CA 900mv 1h		20,044	4,95	4,05
V_2AlC (M/A =3,776 by weight)	CV OCP to 2000mv	EDTA with ammoniac buffer	96,312	23,958	4,02
	CA 900mv 1h		27,104	6,62	4,09

2.3 Conclusion

In this chapter, we have proposed and evaluated some methods in order to extract MXene sheets from large scale MAX phase single crystals. At the meantime, the chemical stability is investigated as well.

In the first part we present the chemical solution methods. HF and other corrosive solution are tested for the feasibility of a selective chemical etching of the A element. MAX phase compounds are shown to be stable in HCl, H_2SO_4, and other conventional corrosive solutions. Oxidant reagent, such as HNO_3 and H_2O_2 can react with V_2AlC, but lead to uncontrolled process. Among different solutions, HF is revealed to be the most efficient approach. In particular, the effective etching depends on the essential elements, the agent which

breaks M-A bonds and the complexing agent. Accordingly, the representatives are H^+ and F^-, which is proved to be the only effective combination until now. Compared in different concentration of H^+ and F^-, the roles of the two elements are investigated. Low concentration of F^- could limit the result even lose the effectiveness. Therefore, the choice of the complexing agent and the concentration are the key points to ensure selective etching. Furthermore, the time, temperature and concentration, even the stirring could largely influence the etching process. Except for the reaction parameter, the basic reason for the failure of conversion to large-scale MXene, however, could be ascribed to the limitation of the reagent diffusion and also probably to the corrosion strength created during the etching. The addition of terminated group and cut bonds create the stress, such as rotation, to the structure and lead to the structural reorganization.

Moreover, based on the previous electrolysis study, we optimize the parameter to approach the selective etching for Cr_2AlC single crystal. Different electrolytes are attempted to distinguish the oxidation of M, and A. At low potential there are no much elements leaked in the electrolyte and oxide layer is formed on the surface to resist the corrosion. With the potential going on, the protective layer is broken and more M and A are oxidized at the same time. Consequently, electrochemical polarization couldn't fulfill our requirements. It is noted that different electrolyte, rather the pH, plays importantly on the formation of the oxide layer.

Reference:

[1]. Barsoum, M., Golczewski, J., Seifert, H. & Aldinger, F. Fabrication and electrical and thermal properties of Ti_2InC, Hf_2InC and $(Ti, Hf)_2InC$. J. Alloys Compd. 340(2002) 173–179.

[2]. Naguib, M. et al. On the topotactic transformation of Ti_2AlC into a Ti–C–O–F cubic phase by heating in molten lithium fluoride in air. J. Am. Ceram. Soc. 94 (2011). 4556–4561

[3]. Barsoum, M. et al. The topotactic transformation of Ti_3SiC_2 into a partially ordered cubic $Ti(C_{0.67}Si_{0.06})$ phase by the diffusion of Si into molten cryolite. J. Electrochem. Soc. 146 (1999) 3919–3923

[4]. El-Raghy, T., Barsoum, M. & Sika, M. Reaction of Al with Ti_3SiC_2 in the 800–1000ºC temperature range. Mater. Sci. Eng. A 298, 174–178 (2001).

[5]. Naguib M, Mashtalir O, Carle J, PresserV, Lu J, Hultman L, Gogotsi Y and Barsoum MW, Two-dimensional transition metal carbides ACS Nano, 6 (2012) 1322–31

[6]. Ghidiu, M., Lukatskaya, M. R., Zhao, M.-Q., Gogotsi, Y. & Barsoum, M. W. Conductive two-dimensional titanium carbide `clay' with high volumetric capacitance. Nature 516 (2014) 78–81.

[7]. Naguib, M.; Kurtoglu, M.; Presser, V.; Lu, J.; Niu, J.; Heon, M.; Hultman, L.; Gogotsi, Y.; Barsoum, M. W. Two-Dimensional Nanocrystals Produced by Exfoliation of Ti_3AlC_2. Adv. Mater., 23 (2011)4248−4253.

[8]. Naguib, M.; Halim, J.; Lu, J.; Cook, K. M.; Hultman, L.; Gogotsi, Y.; Barsoum, M. W. New Two-Dimensional Niobium and Vanadium Carbides as Promising Materials for Li-Ion Batteries. J. Am. Chem. Soc. 135 (2013) 15966−15969.

[9]. M. W. Barsoum , The $M_{N+1}AX_N$ phases: A new class of solids: Thermodynamically stable nanolaminates, Prog. Solid State Chem., 28 (2000) 201.

[10]. M.Naguilb, V. N. Mochalin, M. W. Barsoum, and Y, Gogotsi, 25th Anniversary Article: MXenes: A New Family of Two-Dimensional Materials, Adv. Mater. 26(2013)992,

[11]. Xie, J., Wang, X., Li, A., Li, F. & Zhou, Y. Corrosion behavior of selected $M_{n+1}AXn$ phases in hot concentrated HCl solution : Effect of A element and MX layer. Corros. Sci. 60 (2012) 129–135.

[12]. F. Chang, C. Li, J. Yang, H. Tang, M. Xue, Synthesis of a new graphene-like transition metal carbide by de-intercalating Ti_3AlC_2, Mater. Lett. 109 (2013) 295–298.

[13]. I.R. Shein, A.L. Ivanovskii, Graphene-like titanium carbides and nitrides $Ti_{n+1}C_n$, $Ti_{n+1}N_n$ (n = 1, 2, and 3) from de-intercalated MAX phases: First-principles probing of their structural, electronic properties and relative stability, Comput. Mater. Sci. 65 (2012) 104–114.

[14]. A.N. Enyashin, A.L. Ivanovskii, Atomic structure, comparative stability and electronic properties of hydroxylated Ti_2C and Ti_3C_2 nanotubes, Comput. Theor. Chem. 989 (2012) 27–32.

[15]. Tang Q, Zhou Z, Shen P, Are MXenes promising anode materials for Li ion batteries? Computational studies on electronic properties and Li storage capability of Ti_3C_2 and $Ti_3C_2X_2$ (X = F, OH) monolayer.". J. Am. Chem. Soc. 134 (2012) 16909–16916

[16]. Enyashin, A.N.; Ivanovskii, A.L. "Structural and Electronic Properties and Stability of MXenes Ti_2C and Ti_3C_2 Functionalized by Methoxy Groups". J Phys. Chem. C. 117 (26): 13637–13643

[17]. Khazaei, M.; Arai, M.; Sasaki, T.; Chung, C.-Y.; Venkataramanan, N.S.; Estili, M.; Sakka, Y. W.; Kawazoe, Y. "Novel Electronic and Magnetic Properties of Two-Dimensional Transition Metal Carbides and Nitrides". Adv. Funct. Mater. 23(2013): 2185–2192.

[18]. Xie, Y.; Kent, P.R.C. "Hybrid density functional study of structural and electronic properties of functionalized $Ti_{n+1}X_n$ (X=C, N) monolayers". Phys. Rev. B. 87 (2013): 235441.

[19]. M. Naguib, M. Kurtoglu, V. Presser, J. Lu, J. Niu, M. Heon, L. Hultman, Y. Gogotsi, M.W. Barsoum, Two-dimensional nanocrystals produced by exfoliation of Ti_3AlC_2, Adv. Mater. 23 (2011) 4248–4253.

[20]. N.J.Lane, M. W. Barsoum , J. M. Rondinelli, Correlation effects and spin-orbit interactions in two-dimensional hexagonal 5d transition metal carbides, $Ta_{n+1}C_n$ (n =1,2,3) EPL, 101 (2013) 57004 .

[21]. M. Kurtoglu , M. Naguib , Y. Gogotsi , M. W. Barsoum , First principles study of two-dimensional early transition metal carbides. *MRS Commun. 2 (***2012)** 133 .

[22]. X. Xie, S. Chen, W. Ding, Y. Nie, and Z. Wei, An extraordinarily stable catalyst: Pt NPs supported on two-dimensional $Ti_3C_2X_2$ (X = OH, F) nanosheets for oxygen reduction reaction, Chem. Commun. 49 (2013)10112

[23]. X. Li, G. Fan, and C. Zeng, Synthesis of ruthenium nanoparticles deposited on graphene-like transition metal carbide as an effective catalyst for the hydrolysis of sodium borohydride, Int. J. Hydrogen Energy 39 (2014) 14927

[24]. Y. P. Gao, L. B. Wang, Z. Y. Li, A. G. Zhou, Q. K. Hu, and X. X. Cao, Preparation of MXene-Cu_2O nanocomposite and effect on thermal decomposition of ammonium perchlorate, Solid State Sci. 35 (2014) 62

[25]. Lukatskaya, M.R. ; Halim, J. ; Dyatkin, B. ; Naguib, M. ; Buranova, Y.S. ; Barsoum, M.W.;Gogotsi,Y.; Room-Temperature Carbide-Derived Carbon Synthesis by Electrochemical Etching of MAX Phases. Angewandte Chemie, Ed.53(2014) 4877-4880

[26]. Naguib M, Come J, Dyatkin B, Presser V, Taberna PL, Simon P, et al. MXene: a promising transition metal carbide anode for lithium-ion batteries. Electrochem Commun, 16(2012)61–4.

[27]. D. Er, J. Li, M. Naguib, Y. Gogotsi, V.B. Shenoy, Ti_3C_2 MXene as a high capacity electrode material for metal (Li, Na, K, Ca) ion batteries, ACS Appl. Mater. Interfaces 6 (2014) 11173–11179.

[28]. O. Mashtalir, M. Naguib, V. N. Mochalin, Y. Dall'Agnese, M. Heon, M. W. Barsoum, and Y. Gogotsi, Intercalation and delamination of layered carbides and carbonitrides, Nat. Commun. 4, 1716 (2013)

[29]. M. Hu, Z. Li, H. Zhang, T. Hu, C. Zhang, Z. Wu, X. Wang, Self-assembled $Ti_3C_2T_x$ MXene film with high gravimetric capacitance, Chem. Commun. 51 (2015) 13531–13533.

[30]. Xie Y, Dall'Agnese Y, Naguib M, Gogotsi Y, Barsoum MW, Zhuang Hll, et al. Prediction and characterization of MXene nanosheet anodes for nonlithium-ion batteries. ACS Nano, 8 (2014)9606–15.

[31]. J. Yang, B. Chen, H. Song, H. Tang, and C. Li, Synthesis, characterization, and tribological properties of twodimensional Ti_3C_2, Cryst. Res. Technol. 49(11), 926 (2014) 71.

[32]. X. H. Zhang, M. Q. Xue, X. H. Yang, Z. P. Wang, G. S. Luo, Z. D. Huang, X. L. Sui, and C. S. Li, Preparation and tribological properties of $Ti_3C_2(OH)_2$ nanosheets as additives in base oil, RSC Adv. 5 (2015)2762

[33]. Hodkiewicz J. Characterizing Graphene with Raman Spectroscopy. Thermo Fisher Scientific. (2010).

[34]. Xinchun C., Zhijian P., Zhiqiang F., Wen Y., Xiang Y., Chengbiao W. ; Influence of individual Cr-C layer thickness on structural and tribological properties of multilayered Cr-C/a-C:Cr thin films. Surface& Coating Technology, vol 204, p. 3319-3325. (2010).

[35]. Childres I., Jaureguib L. A., Park W., Caoa H., Chena Y. P. ; Raman Spectroscopy of Graphene And Related Materials.

[36]. Surajit S., Youngmin K., Yeoheung Y., HeeJoun Y., Saemi L.,Younghun P., Hyoyoung L. ; High-Quality Reduced Graphene Oxide by a Dual-Function Chemical Reduction and Healing Process. (2013).

[37]. Loryuenyong V., Totepvimarn K., Eimburanapravat P., Boonchompoo W., Buasri A. ; Preparation and Characterization of Reduced Graphene Oxide Sheets via Water Based Exfoliation and Reduction Methods. (2013).

[38]. B.F. Brown, C.T. Fujii, E.P. Dahlberg, J. Electrochem. Soc. 116 (1969) 218

[39]. A.E. Martell, R.D. Hancock, Metal Complexes in Aqueous Solutions, Springer Science & Business Media, 2013.

[40]. R.P. Agarwal, E.C. Moreno, Stability constants of aluminium fluoride complexes, Talanta. 18 (1971) 873–880.

[41]. R.M. Smith and A.E. Martell, program developed by R.J. Motekaitis, Critical stability constants of metal complexes database, NIST standard reference database,2004.

[42]. Jovic, V. D., Jovic, B. M., Gupta, S. & El-raghy, T. Corrosion behavior of select MAX phases in NaOH , HCl and H_2SO_4, Corr.Sci. 48 (2006) 4274–4282

[43]. ELECTROCHEMICAL SERIES, Petr Vanýsek, Handbook of Chemistry and Physics, (1998)

Annex Calculation of pH and pF

LiF could break the correlation between F^- and H^+ in form of HF, which reaches a higher concentration of F^- in solution. F^- in this chapter is seen as an essential factor for the selective etching. Therefore, in order to check the correlation between the concentration of F^- in solution and complexation ability, we prepare the solutions with LiF in different concentrations.
The values of pF of LiF and HF are calculated below in order to discover the relation between F^- and complexation ability.

HF

As the HF is weak acid, the concentrations of both H^+ and F^- are calculated with acid dissociation constant.

	$HF <=> H^+ + F^-$		
E_I	n	0	0
E_F	$n-C_{H^+}$	C_{H^+}	C_{H^+}

Hence,

$(C_{H^+} * C_{F^-}) / C_{HF} = K_1 = 6.8*10^{-4}$

$C_{H^{+2}} = C_{HF} * K_1$

$C_{H^{+2}} = (n-C_{H^+}) * K_1$

EI and EF represent initial and final quantity in mole respectively. an is the quantity of HF in the solution in mol. C_{HF}, C_{H^+} and C_{F^-} are concentrations of correspondent components. As it is prepared with 48% HF(Sigma-Aldrich) and the density of 1.15g/ml, the quantity of HF could be obtained directly. K_1 is the decomposition constant of HF in water. According to the acid dissociation constant table of analytical chemistry 7th edition, the value is $6.8*10^{-4}$. The concentration of H+ could be obtained. As the $C_{H^+} = C_{F^-}$, pH=pF

For 48% HF, 24%HF and 4,8%HF, the values of pH and pF are listed below

HF%	pH	pF
4,8	1,382	1,382
24	1,032	1,032
48	0,882	0,882

LiF+HCl

As the HCl is strong acid and more soluble than Lif, pH of the solution is dominated by H^+ from HCl. The equations of dissociation of LiF solution are listed below:

$F^-+H^+<=>HF$ Ka

$H_2O<=>H^++OH^-$ Kc

Ka and Kc are constants of the two correspondents reactions.

Hence, the constant of reaction below could be defined as:

$Kb=Kc/Ka=10^{-14}/10^{-3.2}=1.25*10^{-11}$

$F^-+H_2O<=>HF+OH^-$

EI	C_0	0	0
EF	C_0-x	x	x

EI and EF are initial and final quantity respectively. From initial state to equilibrium state, there is x mole F^- combining to HF.

Therefore,

$Kb=[HF][OH^-]/[F^-]=x^2/(C_0-x)$

C_0 is the quantity of LiF soluble in the solution(known). In equilibrium state, x mole of F- has been formed into HF and produced OH^-. We can obtain the x to calculate the pF.

The obtained values are listed below:

Solution	C HCl(mol/l)	C H^+(mol/L)	pH	pF
1	6	6	-0,778	3,221
2	5	5	-0,69897	3,47315
3	4	4	-0,602	3,777
4	3	3	-0,47712	1,52915
5	2	2	-0,30103	1,56832
6	1	1	0	1,64261
7	0,01	0,01	2	2,14583
8	10^{-4}	10^{-4}	4	2,20751
9	0	$1,43*10^{-8}$	7,84466	2,38007

Chapter 3

High temperature chlorination

Chlorination of MAX phase compounds is not new. However, here we put for the first time chlorination to good use to convert the Cr_2AlC MAX phase into a highly porous chromium carbide. Following a brief introduction to the chromium carbide compounds and to high temperature chlorination, we will describe in detail the conducted experiments and their results, and we will present a systematic discussion of the relationship between the chlorination conditions and the physical properties of the resulting porous materials.

3.1 High Temperature Chlorination

Chlorination is an extensively used approach in the scientific research and industrial activity. It simply means the reaction of chlorine elements with the chosen materials. According to different conditions of chlorination reaction, one can make a distinction between “hot” chlorination[1], “light” chlorination[2] and “catalytic” chlorination [3], which, under different conditions, allow one to obtain various useful reaction products. In organic chemistry, there are two types of reactions: substitution chlorination and addition chlorination. Concerning substitution chlorination, for example, the hydrogen in the methane molecules can be replaced by chlorine so as to give chloromethane; In the presence of iron catalysts, hydrogen in benzene is substituted by chlorine to form chlorinated benzene (chlorobenzene) [4]. The addition of chlorination to benzene, with the combined action of light and chlorine, produces hexachlorocyclohexane [5]. In inorganic chemistry, elements or compounds react with chlorine in another form of chlorination. For instance, association of sulfur with chlorine form sulfur monochloride [6]. In the presence of carbon dioxide and chlorine, titanium dioxide and carbon tetrachloride are used to generate carbon dioxide and volatile titanium tetrachloride [7]. In metallurgical industry, utilization of chlorine or chloride to refine certain metals is also known as chlorination [8]. During the metallurgical treatment, it was found that non-ferritic compositions were too complex to be directly extracted from the metal. Hence, the chlorination method was introduced in order to transform these oxides, sulfides, carbonates and other compounds into more easily removable species [9]. This forms the main, primary use of the chlorinating reagent, such as gaseous chlorine, hydrochloric acid, etc. Furthermore, the use of chlorine or chlorine containing oxide in water is frequent to achieve oxidation and disinfection. Widely used chlorinated agents are liquid chlorine [10], gaseous chlorine [11], gaseous hydrogen chloride [12], various concentrations of hydrochloric acid [13], phosphoryl chloride [14], thionyl chloride [15], phosphorus trichloride[16], etc.

3.2 Previous work and purpose of our own study

In the scientific research, chlorination has a long history. In particular, this method has already been used before us in the domain of chemical carbide transformation, including MAX phases [17,18]. In general, but also in particular for the MAX phases, the main role of a

chlorination process in MAX phase is to remove some selected elements of the compounds, so as to convert the starting materials into a new compounds, possibly owning interesting physical properties or morphology. In 2001, Yury Gogotsi, and some colleagues demonstrated the transformation of SiC into diamond-structured carbon through high-temperature chlorination [19]. Ten years later, they were in a position to summarize a long-standing work, reviewing the production of the Carbide-Derived Carbons (CDC) through chlorination, with compounds extending from binary to ternary carbides [20]. This included CDCs with nanometer-sized pores obtained from polycrystalline Ti_2AlC [21] and Ti_3SiC_2 [22]. Obviously, gaseous chlorine has a preferential selectivity for the metallic elements and elements of groups 13 to 16, so that high T chlorination can easily form carbon or carbon mixed compounds. In particular, in this chapter, and in contrast with previous work, the chlorination conditions are chosen so as to avoid a total elimination of the transition metal from the MAX phase, and in order to form highly porous carbides rather than CDC's. Although we checked that our process also works for other MAX phases, here we focus on the case of Cr_2AlC, for which no chlorination study was previously available.

3.3 Chromium carbide

3.3.1 Introduction

Chromium carbides are a general name for several binary ceramic compounds Cr_xC_y. The compound preferentially used in the industry is Cr_3C_2. In standard conditions, it is a grey powder (Fig.3.1),which is not soluble in water and can resist acid and alkali [23]. The density is 6.65-6.68 g/cm^3, and Vickers hardness is 2700kg/mm^2 [24]. The melting point and boiling point are 1890 ℃and 3800 ℃respectively [25]. In high-temperature environments (1000-1100 ℃), it is an inorganic ceramic material with excellent wear resistance, corrosion/ oxidation resistance, which is widely used as metal surface protection under the form of a thermally sprayed covering layer. Furthemore, it is also used as the grain refining agent of cemented carbides and other wear resistant, corrosion-resistant components [26,27]. Cr_3C_2 based cermet has an excellent oxidation resistance at high temperature. For example, after 5 hours heating exposure at 982℃, the surface colour is only slightly darker [28]. Under the same conditions, 18-8 stainless steel has been significantly damaged, and WC - 6Co alloy is completely oxidized

[28]. The structure of Chromium carbide Cr_3C_2 is orthorhombic, and the lattice parameters a = 2.821Å, b = 5.52 Å and c = 11.46 Å (Fig.3.2).[23]

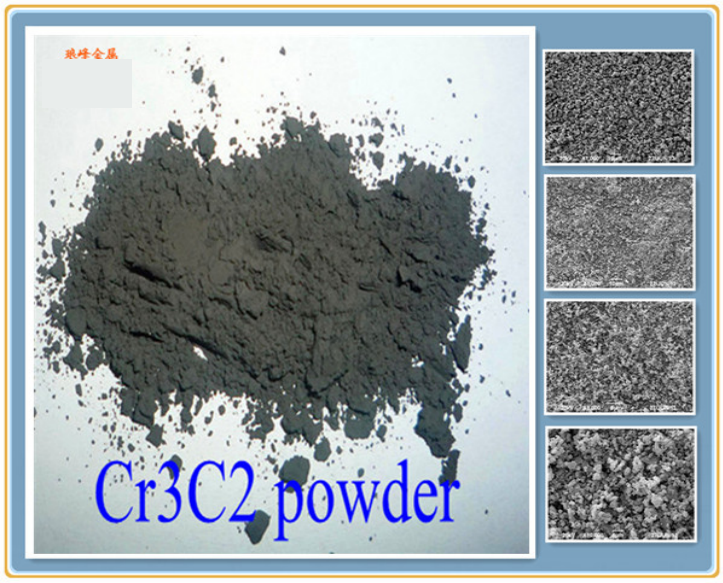

Figure 3.1. Cr_3C_2powder at standard condition(25℃) [29]

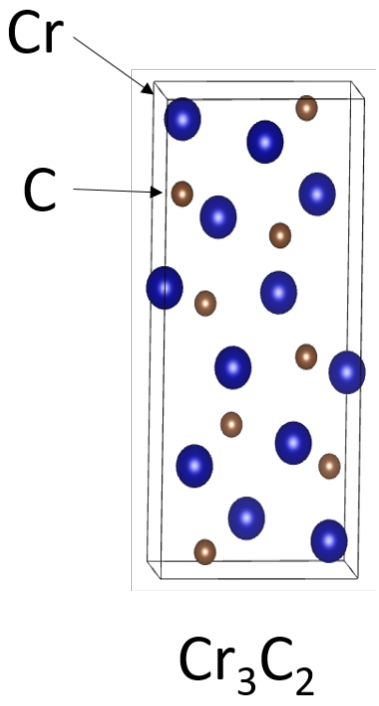

Fig. 3.2. orthorhombic structure of Cr_3C_2, as drawn with the VESTA visualization software.

3.3.2 Industry fabrication method

Metal chrome powder carbonization method:

In this method, 325 grid smashed chromium metal powder, obtained by electrolysis, and black carbon(purity>99%) are firstly mixed in weight ratio of around 13.5% and 86.5%. The carbon ratio is not strict but usually higher than 11.33% of the stoechiometric one. Then the mixture undergoes dry mixing and ball milling. After adding the carboxyl methyl cellulose, as the forming lubricant, in weight ratio of 3%, the treated powder is molded under pressure of 1 Ton/cm^2. The dried molded brick is put into graphite plates or crucible, in Taman or induction heating furnace. The reaction is divided into two steps in dynamic vaccum. The first is to heat the brick from room temperature to 1400℃ within 6 hours. Then after 3 hours heat perservation at 1400℃, it starts the second step from 1400℃ to 1800℃ within 8 hours. After another heat perservation of 5 hours, the furnace is quickly filled with Argon flow (purity>99.99%) to 0.1mbar and ended with a free cooling to 80℃. The obtained pulverized powder is detected with 86.2% of Cr and 13.3% of C [30]. The reaction could simplified as:

$$3Cr + 2C \Rightarrow Cr_3C_2$$

3.3.3 Application

(1) Chromium carbides are usually used in welding rods as hard-surfacing alloy with 31% chrome weight ratio, which has unmatched abrasive wear resistance. The special coating provides remarkable welding performance, which could allow a smooth surface. Despite high hardness, the coating retains well the toughness and wide weaving to the electrode in 3 times size that could be used without cracking [31].

(2) Chromium carbides could be used as contact materials for C-containing semiconductor thin film, which possess higher stability than the pure metal conductor and the solid-state reaction could be achieved by method of self-alignment [32]. The solid-state reaction between thin metal film (E.g., Cr) and C only takes place in the contact region, which could save the process for alignment and lithographic patterning [33].

(3) Hard chrome plating used to make wear-resistant coating with good surface at low costs, which is produced by submerging the matrix in the chemical solution containing chromium. However, increasing environmental concerns resulted from the disposal of the effluents have caused the process cost increasing as well [34]. Therefore, chromium carbides could be an excellent alternative to solve pollution. Chromium carbide-based coatings are

between two and a half and five times more wear resistant than hard chrome plating and do not produce pollutional effluent to the environment. Hence, it increasing alternates hard chrome plating, supporting a better wear resistance and significant harmony with the environment.

(4) Chromium carbide, combined with a metal matrix (E.g., Cr-Ni) is remarkable material for thermal spray applications [35]. The weight ratio between carbides and matrix is typically around 3:1. The coated substrate, to which carbides are bonded by metal matrix, provides an excellent corrosion resistance. The properties of corrosion and wear resistance make the thermally sprayed CrC-NiCr coating as a proper candidate for high temperature wear resistance. At present, it is extensively applied in the aerospace market as coatings for rod mandrels[36], hot forming dies[36], hydraulic valves[36], wear protection of aluminium parts[36] and other applications requiring excellent corrosion[37] and abrasion resistance at high temperature up to 700-800°C[36].

3.3.4 Fabrication of Chromium carbide reference sample

As detailed later on in this chapter, we detected two different phases of chromium carbide after high temperature chlorination of our Cr_2AlC single crystals. This made necessary to identify a proper way to differentiate both phases easily, and at a local level. To do so, we decided to produce both chromium carbides Cr_7C_3 and Cr_3C_2 in bulk form, so as to record the Raman spectra of the pure phases, which, to the best of our knowledge, were not available in the literature. The knowledge of such spectra was most useful for the analysis of the phases present in the porous materials after the chlorination-induced conversion of Cr_2AlC. Synthesis was achieved by introducing pure Cr in a graphite crucible and inductively heating it up to T=2000°C. Carbon was incorporated into the liquid by partial dissolution of the crucible graphite walls up to an atomic fraction $x_c \approx 0.4$, which corresponds to the composition of the liquid in equilibrium with graphite at 2000°C. By slow cooling, Cr_3C_2 primary crystals are first formed in the liquid, until the final solidification takes place around the eutectic temperature T=1747°C, leading to a solid phase with the two compounds Cr_7C_3 and Cr_3C_2. After cutting the solidified sample, one half was grinded for phase identification by X-ray diffraction (XRD). The other half was prepared for classical metallography, *i.e.* the as-cut surface has been polished to get a mirror-like finish, with no scratch detectable by optical microscopy. The different domains of Cr_7C_3 and Cr_3C_2 have been identified by Scanning Electron Microscopy (SEM) and EDX analysis. Measuring Raman spectra then indicated that each compound has a clear,

reproducible Raman signature, which we used as a reference for phase identification. These spectra are shown along with that of the chlorinated samples in a later section of this chapter.

3.3.5 Porous Cr_3C_2

Porous ceramic materials are potentially attractive for applications ranging from supports for catalysis agents to filters or thermal insulators in harsh environments due to their outstanding properties [17,38]. In particular, porous chromium carbide Cr_3C_2 has already been synthesized using a number of chemical routes [18,39-42] and then used to strengthen metal-ceramic composites [41,42]. Promising is the freeze casting technique [17], which was recently adapted to produce highly porous Cr_3C_2 [41]. In the latter case, it consists in wetting a chromium oxide powder with camphene, freezing the mixture so as to obtain a composite, sublimating camphene and finally sintering the resulting green powder at high T and in a carbonaceous gas mixture for a few tens of hours [41]. As revealed in this chapter, chemical conversion of MAX phase single crystals is not restricted to the synthesis of porous Cr_3C_2, but can also lead to the formation of porous VC or porous TiC, depending on whether the starting MAX phase is Cr_2AlC, V_2AlC or Ti_3SiC_2, respectively. Moreover, there is little doubt that other MAX phases should lead to the formation of other porous carbides. However, VC is not as chemically stable as Cr_3C_2 or TiC, and the typical volume of our Ti_3SiC_2 single crystals is much smaller than what can be achieved with the Cr_2AlC phase, for which crystal platelets with an area of 10 cm^2 and a thickness of a few mm are now easy to produce. Besides, Cr_3C_2 is electrically conducting and highly stable in corrosive and high T environments, and has been envisioned as a potentially interesting material for, *e.g.*, solid oxide fuel cell anodes [43], electroplates [44] or counter-electrodes in dye-sensitized solar cells [45]. These are the reasons why, in this section, we decided to focus on porous Cr_3C_2.

3.4 MAX phase high temperature chlorination

3.4.1 Experimental set-up

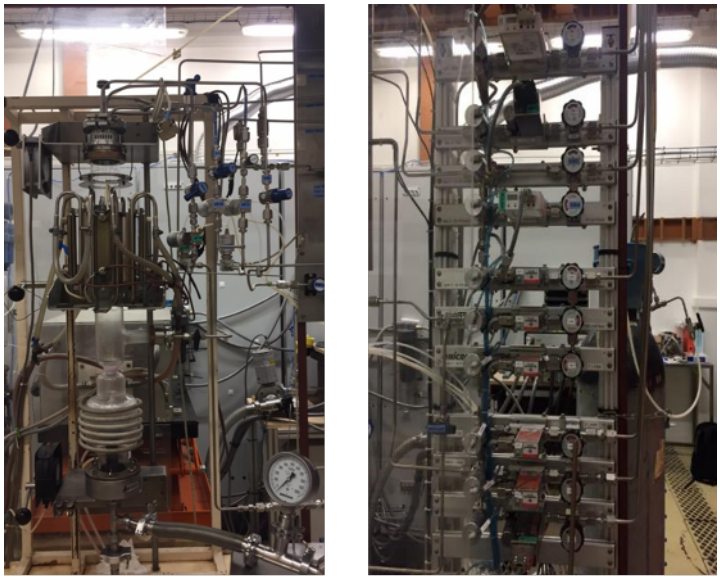

(a) (b)

Figure 3.3. (a) CVD reactor with induction heating system (b) gas control system

(a) (b) (c)

Figure 3.4. (a) Power generator and (b) exhaust treating and cooling jar(c) process control system

Chlorination is achieved in a reactor most often used for Chemical Vapor Deposition (CVD) and located in the SIMAP laboratory. It consists of several essential components:

1. Quartz reactor chamber, where the gas is brought to and where the reaction takes place (Figure 3.3a)
2. Gas delivery system- for precursor and inert gas carrier (Figure 3.3b)
3. Substrate – the position where deposition takes place.

4. Energy source- generates the heating power (Figure 3.4a).
5. Vacuum system- brings the reaction environment to low pressure or vacuum
6. Exhaust system- removes the volatile byproducts and non-reacted precursors.
7. Exhaust treatment system- cools down the exhausted gases and recycle them in order to protect the environment (Figure3.4b)
8. Process control equipment and gauges to monitor the in-situ parameters and control security alarms (Figure 3.4c)

3.4.2 Chlorination process

In our case, we use the CVD reactor in a way almost opposite to that of a conventional CVD process: Instead of using a gas for carrying reactive agents to a surface and ensure deposition of a layer by the surface decomposition and adsorption of some elements of the gas molecules, the gas is used to remove some of the chemical elements of the Cr_2AlC substrate, in order to form a new phase on top of the MAX phase, possibly up to a complete conversion of the starting Cr_2AlC crystals.

Before chlorination, all the crystals are weighted, and their dimensions are carefully recorded. Chlorination takes place in a CVD quartz reactor with chlorine and hydrogen flow gases. The MAX phase single crystals are put on an induction-heated graphite susceptor. In the preparation stage, after ensuring air impermeability and water cooling cycling, the samples are cleaned by repeating three times the vacuum and gasing process (with argon 1L/min) that the varying pressure and flow could remove the impurities on the surface, including absorbed oxygen. Then the atmosphere is replaced by hydrogen. The growth temperature is measured at the top edge of the susceptor with a dual wavelength pyrometer. Crystals are heated under hydrogen flow (0.1L/min) through a 5mn manual heating at 20% power and under a pressure of 13 mbar. Then, the heating power is automatically increased at a rate of 5%/min until the desired value is reached. At the end of the temperature plateau, the induction power is adjusted in order to get the desired chlorination temperature. After 2 minutes of temperature stabilization, chlorine gas is introduced with a flow rate of 10mL/min and maintained during the chosen process time. Following the high-temperature chlorination step, the reactor is filled with argon and cooled down (50°C/min) to room temperature. Before the samples are taken out, they are washed three times with argon using the same procedure as that used during the initial preparation stage.

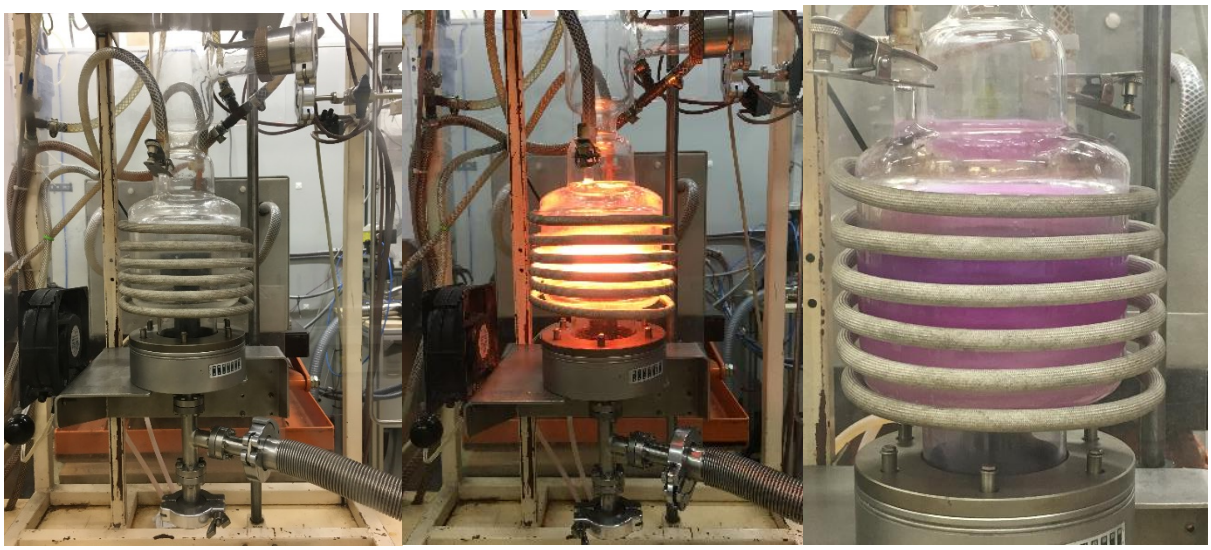

Figure 3.5. Reactor (a) before heating, (b) during heating and (c) after heating

Here we note that the chlorination leads to the side formation of deposits on the reactor wall. After around 15min of chlorination, the upper side and the down side of the reactor inner wall are covered by a white deposit. After about 10mn, the whole inner wall is covered by a purple composite. In figure 3.5c, we can still observe the white one at both two sides of the inner wall. According to XRD diffraction measurements, the purple deposit is chromium chloride, which corresponds to the mechanism inferred in the following section.

3.4.3 Products

Here we provide a thorough description of the structural and chemical composition of the porous chromium carbide layers obtained by high temperature chlorination, mainly based on X-ray diffraction and Raman spectroscopy. We also describe the kinetics of the transformation or the possibility of tuning the porous properties by varying some process parameters. In the last part, we focus on the electrical transport properties of porous Cr_3C_2, showing that in spite of a high porosity, the materials keep a resistivity of the same order of magnitude as that of bulk Cr_3C_2. We also discuss the magneto-resistive properties.

3.4.3.1 SEM morphology

Figure 3.6. Crystal platelets (a) before and (b) after chlorination

Comparing the crystal morphologies before and after chlorination (Figure 3.6), it can easily be seen that the samples lose their metallic luster. The main reasons are that the dense material is converted in a porous one, and turns from single crystalline into raw polycrystalline.

Typical SEM views of the top surface of converted materials are given in Figure 3.7, in the case of the three transformations $Ti_3SiC_2 \rightarrow$ porous TiC, $V_2AlC \rightarrow$ porous VC and $Cr_2AlC \rightarrow$ porous Cr_3C_2. For all investigated MAX phases, high T chlorination results in the formation of a porous carbide, the nature of which can be easily assessed by XRD and EDX analysis. From a systematic SEM observation of the sample cross-section after chlorination, when the conversion is not complete, there is a clear and distinct boundary separating a totally converted, porous region from a totally untransformed single crystal MAX phase region (see section 3.1.3). Transformation preferentially takes place at the upper layer, but a partial and much slower transformation of the bottom face in contact with the graphite susceptor also occurs. The edges are also transformed during the chlorination step, and there is a noticeable anisotropy between the progression of the reaction front perpendicular to the basal plane and that occurring at the sample edges, *i.e.* along the basal plane, the latter being faster. However, due to the initial very low aspect ratio of the platelets, the latter are mainly converted through the progress of the porous medium boundary from the top surface towards the core of the crystal. In all the remaining part of this section, we focus on the case of the Cr_2AlC transformation. As seen from Fig.3.6, the porous medium is clearly continuous. Typical pore diameters are of submicron size. Owing to our synthesis process, we observe just one typical scale, in contrast with the multi-size porous structure of ref. [46].

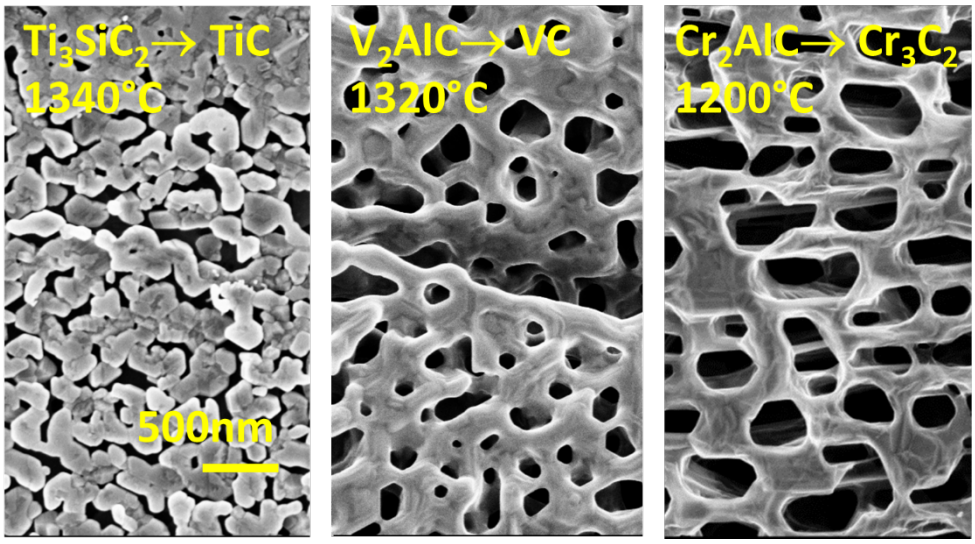

Figure 3.7. SEM view of the top surface of three porous layers obtained after high temperature chlorination of three different MAX phase single crystals (Ti_3SiC_2, V_2AlC and Cr_2AlC, respectively transformed into porous TiC, porous VC or porous Cr_3C_2). The nature of the converted layer was identified by X-ray diffraction analysis.

According to the chlorination working principle, the outside surface of the sample is firstly etched. A schematic of a partially converted crystal is shown in figure 3.8. As the top surface is submitted to homogeneous reaction parameters such as temperature and gas contact probability, the conversion depth is quite uniform over the whole surface. However, the surface of the sample edges and the bottom surface lying on the susceptor are submitted to appreciably different gas exposure conditions. A difference in vertical position as low as several hundred microns can lead to a temperature difference of several hundred degrees. As discussed later in much detail, temperature is a major parameter controlling the conversion thickness and pore size, which also limits the chlorination kinetics. A difference in T thus leads to an appreciable difference in converted layer thickness and morphology. Besides, the complex morphology of the samples edges also make it difficult to control the converted volume, because the fissures and defects will lead to a spatially inhomogeneous chlorine gas penetration. Although the bottom side is much less exposed to the chlorine gas, the roughness of both the sample and the substrate allow gas penetration and therefore conversion as well. As a consequence, samples may exhibit different conversion rates, depending on the investigated part of the surface, and in the following we restrict ourserlves to the analysis of the homogeneous top surface region to estimate the parameters of the reaction kinetics.

Figure 3.8. sketch of the incomplete transformed sample

3.4.3.2 Magneto-resistance

Totally converted, rectangular samples have been used to fabricate Hall bars and measure their electrical transport properties (chlorination temperature of 1200°C for 8 hours). The resistivity ρ_0 for zero magnetic field B and transverse magnetoresistance (MR) $\Delta\rho/\rho_0$ have been measured as a function of temperature from 300K to 4K. The dependence of ρ_0 on T is plotted in Fig.3.9, and Fig.3.10 shows the magnetoresistance dependence on B and T. It is worth noticing that in spite of a porosity in the range of 60%, the resistivity remains of the same order of magnitude as that published a long time ago by Grebenkina *et al.* in the case of bulk Cr_3C_2 [47] and is also similar to the resistivity of other chromium carbides [48].

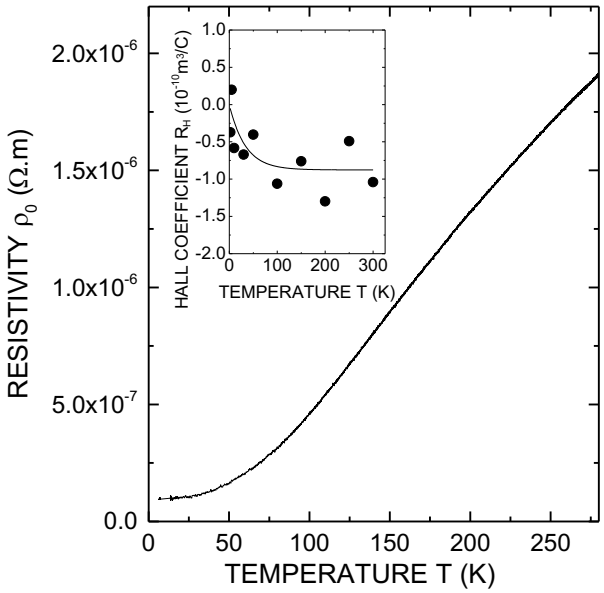

Figure 3.9. Electrical resistivity ρ_0 as a function of temperature of a totally converted sample. The insert shows the Hall coefficient R_H versus temperature T. In the insert the solid line is a guide to the eye.

Measuring the magnetoresistance as a function of magnetic field allows us to evidence some specific features. At temperatures below 5K and at low magnetic field, a negative MR component can clearly be observed (Fig.3.10a). This negative MR component is only observable for T roughly below 100K. It could be ascribed to weak localization (WL). According to the quantum mechanics, in a coherent disordered system, the probability for an electron to go from a given site to another one is given by the sum of the interfering, complex probability amplitudes of all possible paths that can be followed by the electron to go from one site to another (See Fig. 3.11). Since a path going back to the starting site can be followed in two opposite directions, in the absence of magnetic field, those two similar paths interfere constructively and enhance the probability for the electron to stay localized at a given site. This results in an increase of the resistivity and is known as the weak localization phenomenon. Since application of a magnetic field does not change the accumulated phase of those two opposite backward paths, this breaks the constructive interference between them and the resistance decreases with an increase in B. This is the signature of the WL effect. With the presence of a magnetic field and increasing temperature, the weak localization effect will decrease. Most remarkable is the particular behavior of the MR occurring at T below 100K and higher fields, for which a linear and positive contribution to the MR prevails (Fig.3.10a). By an appropriate fitting of the experimental curve in the high field regime, it is possible to extract the coefficient of the linear contribution. The negative component can then be extracted by withdrawing the linear component from the overall magnetoresistance values. As illustrated by Fig.3.10a, the negative MR seems to saturate at high field. When T increases, both the negative and positive linear contributions drop (Fig.3.10b). However, the linear positive component drops faster.

It is worth noticing that it is somewhat difficult to discriminate in the MR behavior between the contribution of Cr_3C_2 and that of the graphite, detected from Raman spectroscopy, if one stays at a qualitative level: Firstly, a linear MR and a negative MR components have already been observed in various kinds of graphite-like materials: A seemingly linear MR has already been observed in Kish graphite with a low value of the resistivity ratio at room temperature (300K) and at 4.2K (RRR), the latter value being equal to the minimum value obtained when defect or impurity scattering prevails [49,50]. Some tentative explanation was given, with no definitive proof of it [49]. In multi-layered graphene, a negative MR was first predicted [51] and subsequently observed [52] when measuring the inter-plane MR (*i.e.* along the **c**-axis) with **B** also aligned along **c**. A linear, positive MR was observed [52] for the MR measured along **c** but with B oriented in the basal plane, decreasing with T. The negative MR was ascribed to inter-layer tunneling between two-dimensional massless Dirac Fermions

[51,52]. In our case, assuming that regions of the Cr_3C_2 porous material are partially or entirely covered with graphite, it is reasonable to assume that for a given field orientation, some graphite-contributing regions are in the first regime, whereas others are in the second one, since all orientations are expected to be found. This might thus also qualitatively explain our experimental findings. Similar (though not identical) results were also recently found in 3D nanostructured carbon materials [53]. Eventually, Zhang et al. have shown that a linear, positive MR decreasing with T can be obtained in micro-sized graphite, whereas smaller particle size gives rise to a negative MR [54].

Secondly, it is also worth noticing that a linear dependence of the magnetoresistance has already been observed in the case of other inhomogeneous media, such as, *e.g.*, disordered MnAs-GaAs composite materials: Johnson *et al.* found that such materials exhibited a linear MR, with a slope equal to the sample mobility [55]. For a metal, this would imply that the linear MR is inversely proportional to the resistivity. In particular, for totally insulating inclusions (a case closer to ours), if the carrier mean free path remains much smaller than the typical linear dimension of the inclusions and if the volume fraction *f* of the inclusions remains small, it has been demonstrated that the MR is linear, proportional to *f* and to the mobility [56]. Similar conclusions can also be drawn from other theoretical approaches [57]. As a consequence, we cannot *a priori* exclude this second phenomenon, which could equally apply to the Cr_3C_2 porous medium. On one hand, we note that in our case, the linear MR does not scale with the mobility and therefore with the reciprocal resistivity as in [55], but rather with the fourth power of it (see Fig.3.10c). On the other hand, the Hall coefficient values we measured are negative and very small (of order $10^{-10}m^3/C$, see the insert of Fig.3.9), sometimes becoming positive at the lowest temperatures. In contrast, the negative Hall coefficients which were measured in the case of Kish graphite with low RRR and positive, linear MR were much higher (of order 10^7-$10^6 m^3/C$ [50]), as those measured by Zhang et al. [54], and in some samples they were even positive [50]. The only way to discriminate between both contributions would be to measure samples totally devoid of graphite. Unfortunately, this is difficult to achieve for relatively thick, handleable samples, which require long chlorination times to eliminate the Cr_2AlC layer totally. However, a quantitative analysis indicates that the linear MR most probably comes from the porous Cr_3C_2: Let us assume that the MR entirely comes from the graphite. By comparing the usual values of the resistivity of disordered graphite to that of Cr_3C_2, we note that we may also assume a large ratio between both ($\rho_{Cr3C2} << \rho_G$), still substantially enlarged by the volume ratio when comparing the resistances R_{Cr3C2} and R_G. A back-to-the-envelope calculation then shows that the overall MR can then be approximated as $\Delta R/R \cong (R_{Cr3C2}/R_G)(\Delta R_G/R_G)/(1+ \Delta R_G/R_G)$.

Therefore, both a large graphite MR and a small R_{Cr3C2}/R_G ratio should lead to a saturation of the MR with B at a very small value. The measured values are not very large, but if the graphite MR is linear, then the expression above is clearly not and saturates with B, whereas the measured MR is clearly linear at high B. Small values of the graphite MR could give a linear dependence with B, but then the overall MR should be extremely small. It is thus quite reasonable to attribute the linear MR to the porous Cr_3C_2 layer. This system constitutes an original illustration of an old theoretical problem [56].

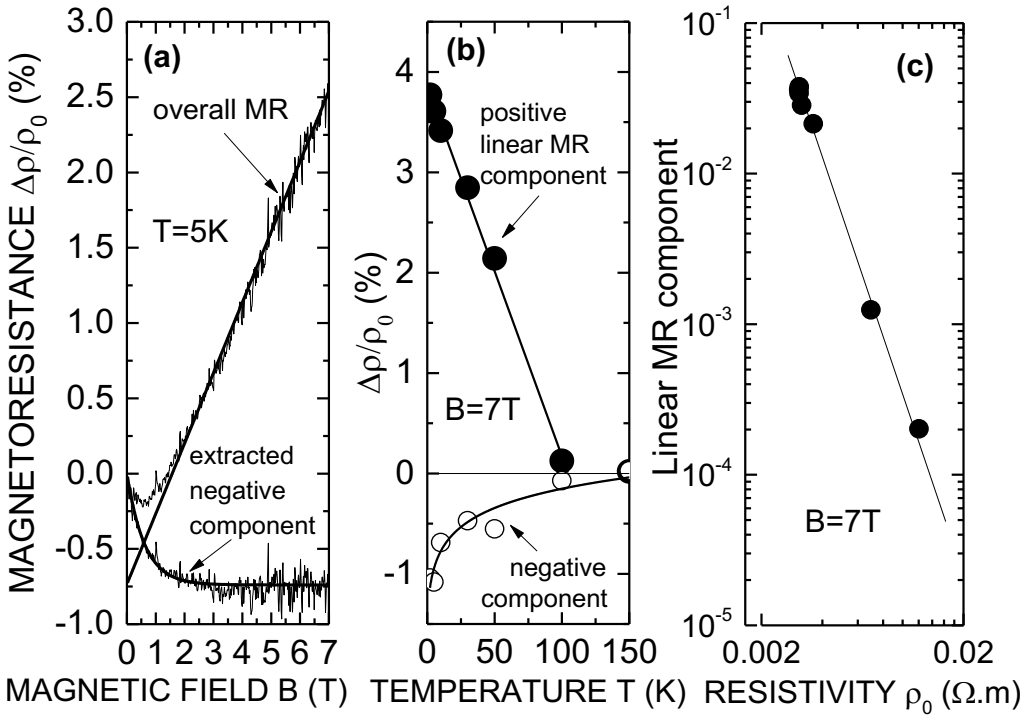

Figure 3.10. Magnetoresistance (MR) of the same sample as in Fig.9. (a) MR versus magnetic field at T=5K, (b) linear positive MR component at B=7T and saturated negative MR component at B=7T as a function of T and (c) variation of the linear positive MR component at B=7T as a function of the overall resistivity ρ_0 at B=0.

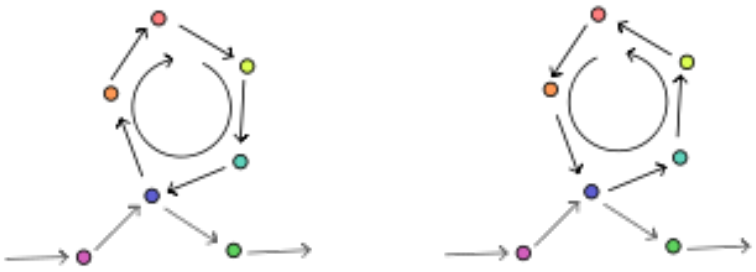

Figure 3.11. Self-crossing of interference terms in the weak localization effect: clockwise direction and counter clockwise direction.

3.4.3.3 Methods used for assessing the porosity

The relatively small volume and weight of the samples make difficult to use accurate methods such as the Brunauer–Emmett–Teller (BET) technique [58] or XRD tomography [59] in order to assess the porosity. This led us to rely on two alternative, different approaches. The first one requires to weigh the samples before and after chlorination and to achieve cross sectional SEM observations: systematic SEM observations demonstrate that the thickness of a partially or even totally converted sample does not change by more than 5%(Figure 3.12). This indicates that the sample volume is left roughly unchanged. Besides, even for partially transformed samples, there is a clear and sharp delimitation between the converted and untransformed sample parts (see Fig.3.13). Since the density of Cr_3C_2 is known, the knowledge of the thickness of the transformed layer and that of the initial and final sample masses allow us to assess the overall porosity p thanks to the expression below:

$$p = 1 - \frac{t}{t_{conv}} \frac{d_{Cr_2AlC}}{d_{Cr_3C_2}} \left(\frac{m_f}{m_i} + \frac{t_{conv}}{t} - 1 \right).$$

t is the overall sample thickness, t_{conv} is the thickness of the converted layer, d_{Cr3C2} and d_{Cr2AlC} are the Cr_3C_2 and Cr_2AlC densities, equal to 6.68g/cm^3 and 5.24g/cm^3, respectively. m_f is the final mass of the sample and m_i is the mass before chlorination. t_{conv} is assessed by averaging the values determined from five to six SEM cross section images acquired at different positions across the sample, after cutting it in its middle part. This method does not permit to estimate a variation of porosity as a function of the depth, but is nevertheless more precise than the second one we used, which is based on SEM image analysis: As illustrated by Fig.3.7, there is a significant contrast between the solid and pore sections. Therefore, after a proper adjustment of contrast, the image of the surface morphology can be converted into a binary color image in order to calculate the porosity (we used the ImageJ^{TM} software). The whole morphology of the sample cross section can be estimated through multi-image in order to access the porosity (Fig. 3.14). This method, although less accurate than the first one, allows us to estimate the porosity at a local level. However, it tends to underestimate the porosity, because some solid parts visible just below the surface also give rise to bright portions in the binary color image, whereas they

should lead to black regions. There is a clear correlation between both techniques, as shown in Fig.3.12, obtained by measuring the porosity of samples as a function of the chlorination time or the temperature. However, and also seen in Fig.3.13, experimental correlation turns out to be very noisy, mainly due to the uncertainty of the method based on image processing. As a consequence, we decided to assess the porosity from the first method whenever a global value was sought for, and we used the image treatment whenever a local measurement was required (*e.g.*, for evaluating a variation in porosity as a function of sample depth, or the porosity value at the top surface).

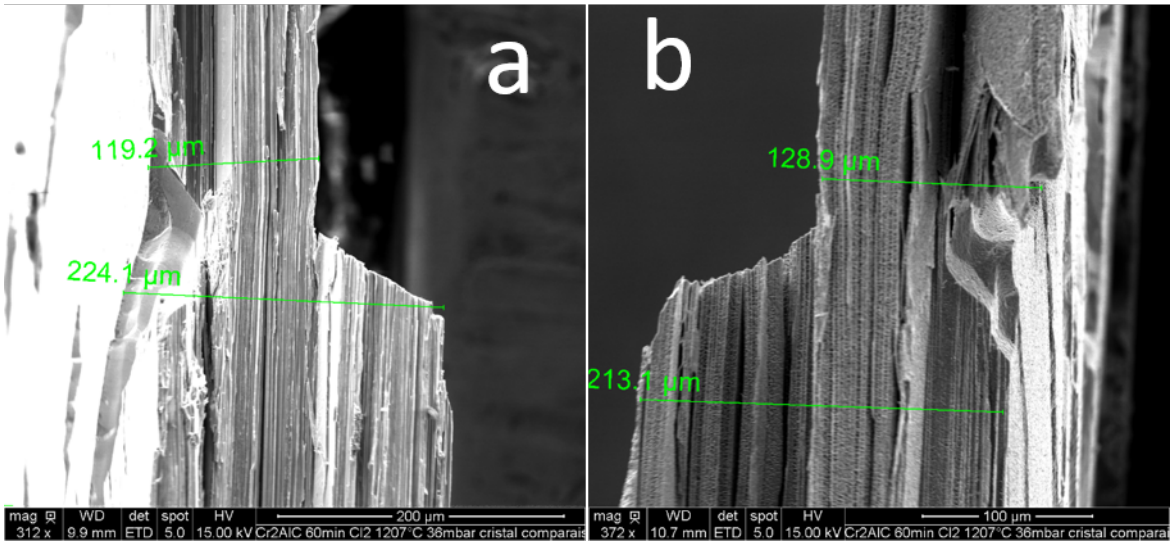

Fig. 3.12. Comparison of sample thickness (a) before chlorination and (b) after chlorination

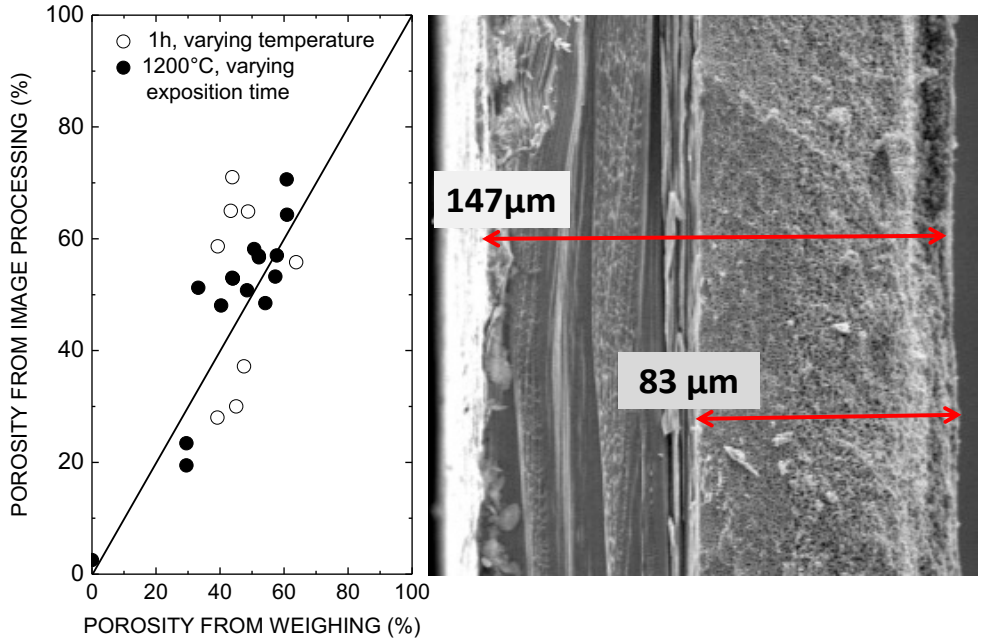

Figure 3.13. (a) Estimated porosity as computed from SEM image processing of the top surface *versus* estimated porosity as calculated from the mass variation of the sample after chlorination (see section 3.4.3.5 for details). One set of data was obtained at a constant T and varying exposition time Δt. A second one was obtained by varying T and maintaining Δt=1hour. (b) SEM image of the cross section of a partially converted Cr_2AlC crystal obtained after cutting it into two parts (chlorination at T=1200°C during Δt=3h).

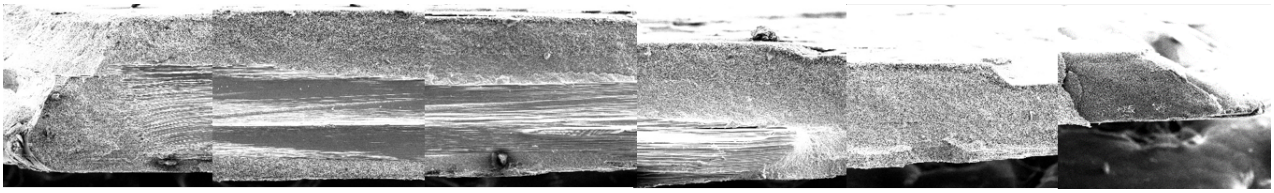

Figure 3.14. Multi-image of a cross section of chlorinated sample

3.4.3.4 Preferential orientation by XRD

XRD analysis has been performed on a Cr_2AlC sample chlorinated for 8h at 1200°C. As seen in Fig.3.15, the XRD pattern involves 29 peaks, 27 of them correspond to Cr_3C_2 and the two ones to carbon. Cr_7C_3 is not present in quantities sufficient for its characteristic diffraction peaks to be visible in the XRD pattern. It is worth noticing that the relative intensities of the Cr_3C_2 diffraction peaks do not correspond to the ones theoretically expected from a Cr_3C_2 ideal powder (some peaks are even lacking) (Figure 3.16). This indicates that one or several orientations are probably favored. We assessed this point further by carrying out a texture analysis following the method proposed by Harris [60,61]. It consists in the evaluation of a texture coefficient C_{hkl} for each crystallographic orientation, defined as $C_{hkl}=N(I_{hkl}/I_{0,hkl})/\Sigma(I_{hkl}/I_{0,hkl})$ [61,62], where N is the number of investigated peaks (here N=27), and I_{hkl} and $I_{0,hkl}$ are the intensities of the (hkl) reflections of the experimental sample and reference sample as given in the 00-035-0804 file from the International Center for Diffraction Data (ICDD), respectively. For a randomly oriented sample, the texture coefficient should be 1. For a sample with some preferred orientations, C_{hkl} falls below 1 for unfavoured orientations, and rises above 1 for a preferred orientation (hence a perfect crystalline orientation along a particular [hkl] direction would give $C_{hkl}=N$). According to Fig.3.17, the [140], [150], [060] and [350] directions are preferential, and among them the [060] one is prominent. This indicates that the orientation of the porous material is influenced by the original crystal orientation. The smallest dimension of the Cr_3C_2 orthorhombic unit cell tends to align parallel to the **c**-axis of

the MAX phase crystal. This result contrasts with those reported for the freeze casting technique [45].

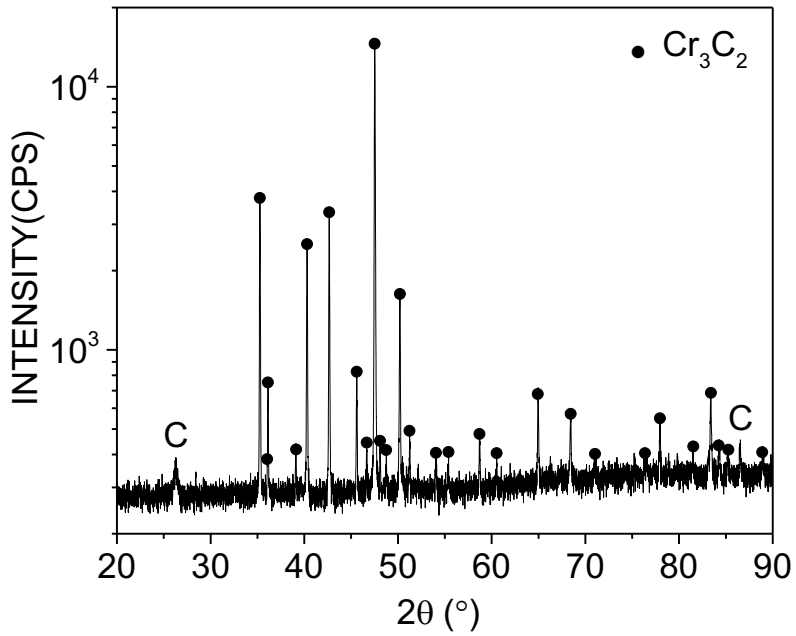

Figure 3.15. θ–2θ XRD reflections of a Cr_2AlC single crystal after high T chlorination.

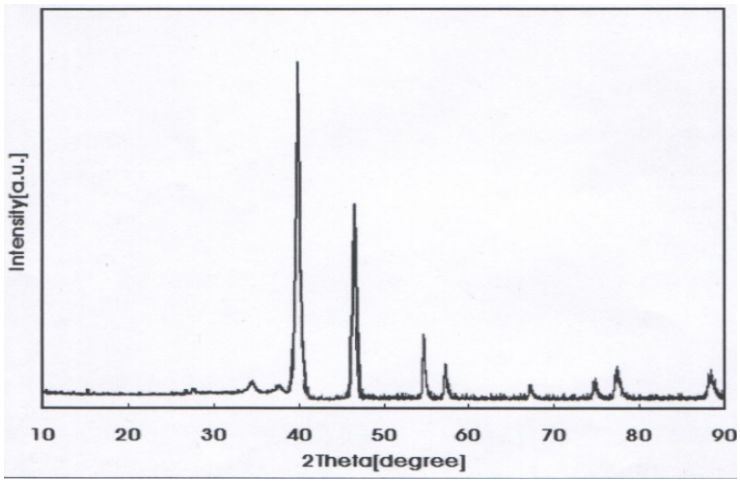

Figure 3.16. θ–2θ XRD reflections of a Cr_3C_2 ideal powder [25]

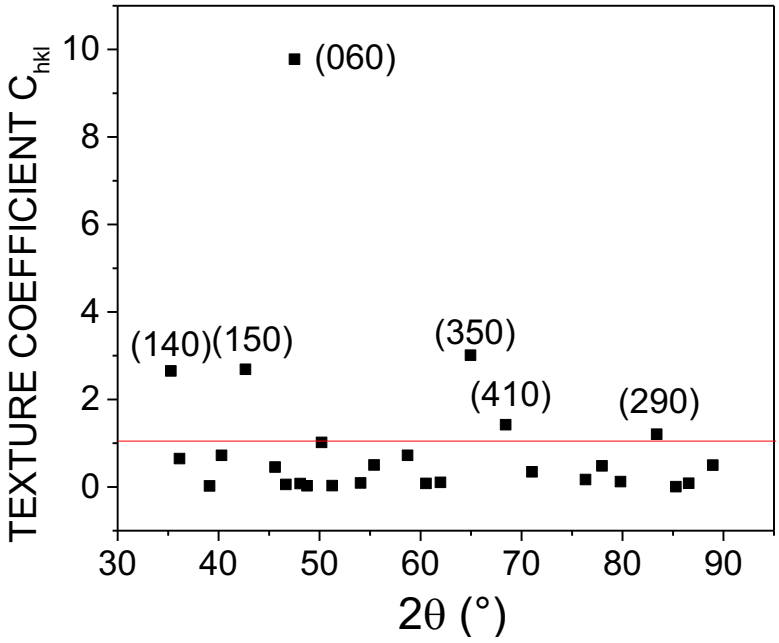

Figure 3.17. XRD Texture analysis of the same sample as in Fig.3.15.

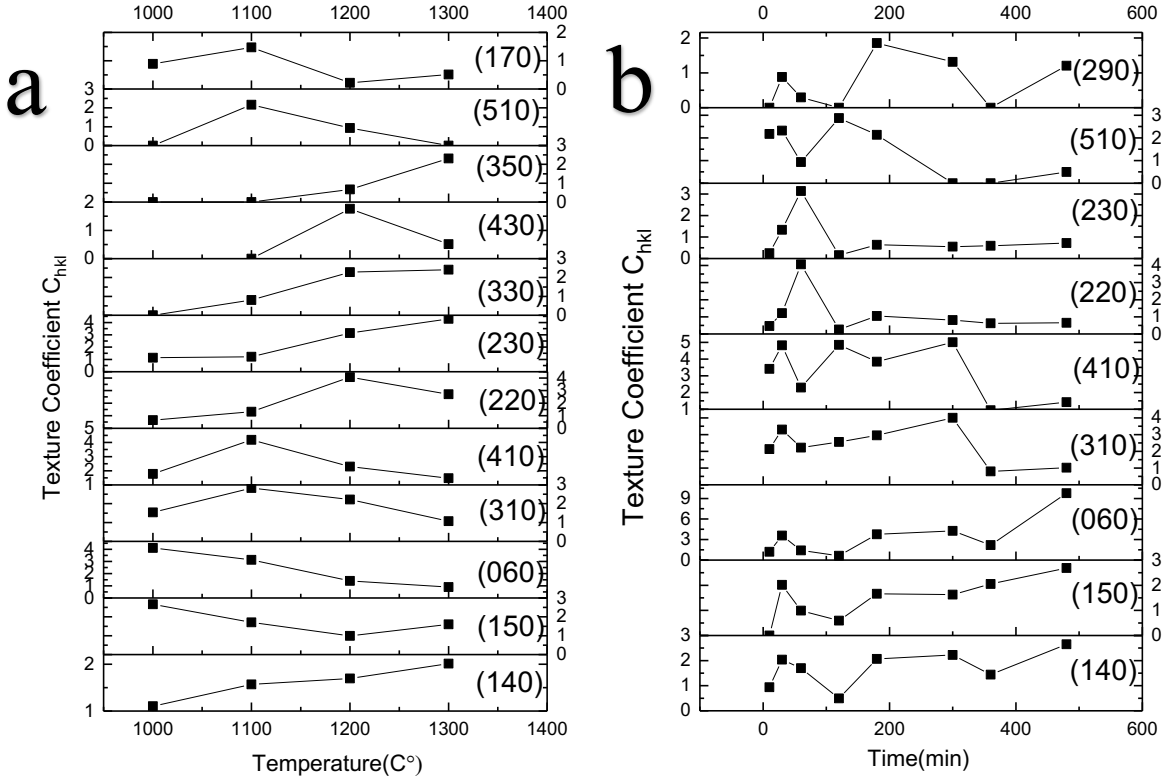

Figure 3.18. Summary of texture coefficient in experiments sets of (a)1h and (b)1200°C

Following the preferential orientation results of Cr_2AlC chlorinated at 1200°C for 8h, we summarize the texture coefficient analyses for both two sets of experiments. In Fig. 3.18 a,

the values of directions [060] and [150] show a decreasing trend while those of other orientations markedly increase. Certainly, the MAX phase is preferentially oriented. However, this effect is weakened by increasing temperature. Therefore, Chlorination at low temperature will make the sample less disordered. Besides, some trends can also be found in the 1200°C set. With increasing exposure time, it can be seen that the values of directions [140], [060] and [150] naturally increase (**Fig.3.18b**), and the initial crystalline orientation of Cr_2AlC probably plays an important role in imposing these directions.

3.4.3.5 Chlorination during 1 hour at variable temperature

Typical SEM images of the surface after chlorination at different temperatures are shown in **Fig.3.19**. In this set of experiments, the chlorination time was always equal to 1 hour. The threshold for observable transformation is around 800°C. The thickest converted layer is about 40µm thick, obtained for the highest temperature (T=1320°C). An Arrhenius plot of the converted thickness t_{conv} as a function of the reciprocal temperature indicates that the experimental value of the activation energy E_A controlling the transformation is around 42.63kJ/mol (0.44eV) (**Fig.3.20a**). This can be favorably compared with the activation energy corresponding to the chlorination of chromium oxide Cr_2O_3, around 86kJ/mol (0.891eV) [62].

Chemical composition of the transformed layer was studied by measuring Raman spectroscopy at the top surface of the chlorinated samples (**Fig.3.21**). To identify the nature of the chromium carbide (Cr_3C_2 or Cr_7C_3), we compared the measured spectra with two reference spectras acquired from pure Cr_3C_2 and Cr_7C_3 bulk phases synthesized as described in section 3.3.4. The characteristic peaks of Cr_3C_2 are found to lie at 208, 259, 307, 340, 432 and 536 cm^{-1}, whereas the peak positions of Cr_7C_3 are 155, 275, 469 and 497cm^{-1}. The results obtained for chlorination at various T's have been plotted in Fig.3.21, where the Cr_3C_2, Cr_7C_3 and Cr_2AlC [63] reference spectra are also inserted for the sake of comparison. At 500°C, Cr_2AlC is the only detected phase at the top surface. Cr_7C_3 is prevailing at the onset of phase conversion, for T=800°C. For all temperatures above 800°C, the peaks detected in the 150-600 cm^{-1} range can all be attributed to Cr_3C_2 (Fig.3.21a).

For the highest temperature (T=1300°C), peaks appearing in the high wavenumber part of the spectra indicate the presence of carbon (see Fig.3.21b, D and G bands at 1352 and 1580 cm^{-1}, resp.). Following the analysis of Ferrari *et al.* [64,65], the lack of any noticeable double-component in the 2D peak found around 2700 cm^{-1} could indicate the presence of monolayer graphene, as opposed to that of multilayer graphene or crystalline graphite, which exhibit a

double component. However, the full width at half maximum (FWHM) of the 2D peak is of order 60 cm^{-1}, not compatible with that of monolayer graphene, of order 20-25 cm^{-1} [64]. It is rather in agreement with low quality graphite, such as pyrolytic graphite or cokes processed at low temperature [66,67]. This observation, added to the consideration that in our case graphitization also occurs at a moderate temperature and takes place in a disordered material, makes highly defective graphite as the most probable carbon phase present in our structures. The intensity ratio between the G and 2D peaks widely fluctuates from one sample to another. This could also indicate that the detected graphite phase is highly defective. The formation of graphite is the last expected transformation, and the one which was put to good use to synthesize CDC's from various carbides [19-22]. In our case, XRD results indicate that it is never the prevailing phase.

The results of Raman spectroscopy seem therefore to indicate that although an initial formation of Cr_7C_3 may occur, this phase is eliminated later on in favor of Cr_3C_2. Besides, after one hour, graphite can be detected at the highest T. In the next section, we show that studying the nature of the phases in presence as a function of chlorination time and as a function of depth allows us to shed light about those two processes.

In the initial chlorination stage, pore size at the top surface tends to increase with T, as shown by the plot of pore size versus T in Fig.3.20b (pore size was estimated from sampling and averaging all pore sizes in a given SEM image), or as indicated by a plot of the surface porosity assessed using the image treatment method (Fig.3.20c). Porosity can reach 75% at 1300°C. The weighing method leads to a similar temperature threshold, but also exhibits a trend toward saturation at the highest T's (not shown here). As shown in the next section plotting the estimated porosity as a function of depth inside the converted part also shows that the porosity of a partially converted sample decreases with depth, which might explain the difference between the two methods used for assessing the porosity.

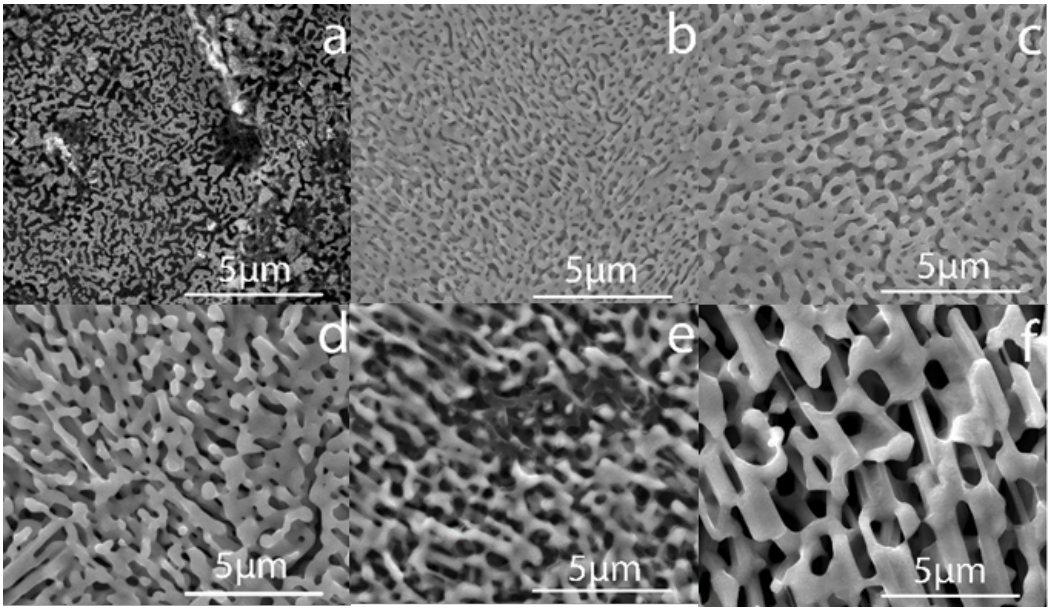

Figure 3.19. Surface morphology of porous Cr_3C_2 obtained by chlorinating Cr_2AlC crystals during one hour with pressure p=13.26mbar. Each image is for a different temperature: (a) 800 C° (b) 900 C° (c) 1000 C° (d) 1100 C° (e) 1200 C° (f) 1300 C°.

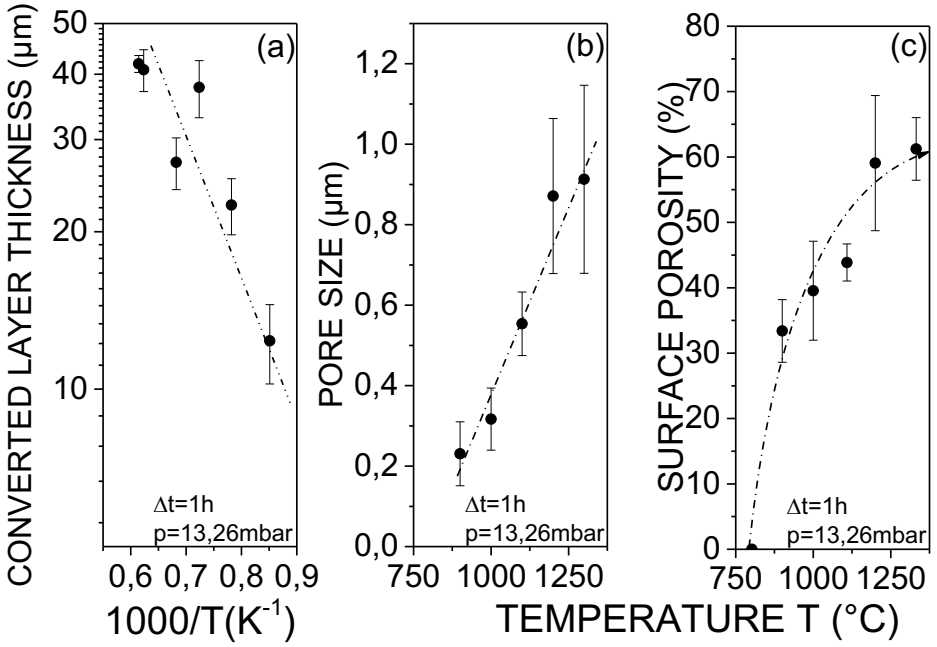

Figure 3.20. (a) Converted layer thickness versus reciprocal temperature, (b) pore size versus temperature and (c) surface porosity versus temperature (each point is for a different sample, chlorination time Δt=1h). Solid lines are guides to the eye.

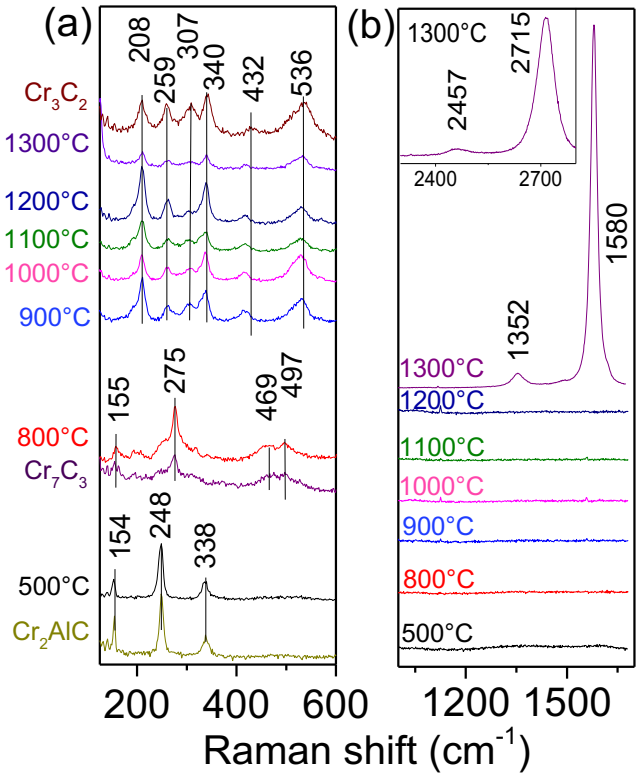

Figure 3.21. Raman spectra of porous Cr_3C_2 obtained at different temperatures and an exposition time Δt=1h (a) 125-600 cm^{-1} (b) 1000-1700 cm^{-1}.

3.4.3.6 Chlorination at 1200C with variable time

A set of chlorination experiments has been conducted as a function of time, with a fixed temperature T=1200°C. In all the data shown below, each time corresponds to a different sample and experiment. The variation of the converted Cr_3C_2 layer thickness is plotted as a function of chlorination time in **Fig.3.22a**. The dependence is neither totally linear (which would indicate that the kinetics is entirely controlled by the chemical reaction taking place at the interface), nor proportional to the square root of time (which would indicate that the transformation kinetics is controlled by the gas diffusion to or the evacuation of byproducts from the Cr_3C_2/Cr_2AlC interface). The empirical power exponent rather seems to indicate that the overall conversion process is limited by both reaction and diffusion processes for most of the investigated chlorination times. This is to be connected with the results of Presser *et al.* concerning the CDC formation from SiC fibers [20]. They found that the evolution with time can be described as a linear-parabolic law: Initially, the thickness of the formed layer increases linearly with time, because it is limited by the reaction kinetics. Then, above some critical time the diffusion of reactants and products through the porous layer progressively dominates and

shifts the reaction kinetics to a parabolic-like law. In our case, the deviation from an ideal parabolic law might be due either to the fact that the investigated times still lie in between the two regimes, or to the existence of a porosity gradient across the converted depth (see Fig.3.22c).

Fig.3.22b shows the variation of the overall porosity (as determined by weighing) as a function of chlorination time (surface porosity, as determined by SEM image processing, exhibits a quite similar trend). Although a linear plot would seem to indicate a stabilization and a saturation of porosity, plotting porosity as done in **Fig.3.22b** demonstrates that porosity proceeds logarithmically in time. This means that porosity still evolves very slowly and does not totally saturate even after several hours of chlorination. A possible explanation can be found by studying the dependence of porosity as a function of depth. This is roughly estimated by selecting a restricted area of the SEM image of a cross section and plotting the porosity of this area as a function of its average depth inside the converted layer, as determined by image processing (Fig.22 c shows the variation of the porosity as a function of the depth from the top surface in the case of a non-fully converted sample). Porosity turns out not to be constant as a function of depth but increases as one gets closer to the sample surface. This implies that the overall porosity change with time does not only result from the Cr_2AlC conversion but is also due to a layer transformation still occurring through the whole converted depth. It is thus quite reasonable to expect different reaction rates, depending on whether the porosity change takes place close to the surface or close to the Cr_3C_2/Cr_2AlC interface. Under some general conditions, a logarithmic time process may result from the sum of elementary processes with different time constants or reaction rates [68]. Here it could thus be due to this variable evolution of porosity as a function of thickness, in qualitative agreement with our empirical findings about the growth kinetics.

Observation of the Raman spectra corresponding to each chlorination time allows us to confirm that after an initial stage where Cr_2AlC is partially converted into both Cr_3C_2 and Cr_7C_3, this latter phase is eliminated in favor of Cr_3C_2 (Fig.3.25). As already noticed in section 3.4.3.6, after some time, peaks characteristics of the presence of carbon are systematically detected, but the fluctuations in their relative intensity makes difficult to assess whether the graphite proportion substantially increases with time, or whether it remains negligible with respect to that of Cr_3C_2. Avoiding graphite formation would require using chlorination times below 1h. Chlorination of Ti_2AlC has been thoroughly studied by Hoffman et al. [22] with the aim of producing CDC materials. In those experiments, chlorination was conducted under a large excess of pure Cl_2. The reaction was thus fast and complete, leading to full conversion into

CDC's. It has also been reported that during CDC formation, the dilution of Cl_2 in H_2 drastically decreases the conversion rate [63]. To understand the chemical evolution of the system, we have to consider the respective flux of Al, Cr and C leaving the Cr_2AlC crystals as a function of etching conditions. Al and Cr can vaporize through the formation of $AlCl_X$ and $CrCl_Y$ gaseous species respectively, C via the formation of hydrocarbons such as methane. From the thermodynamic calculations reported by Hoffman *et al.* for Ti_2AlC [22], we can infer that at low Cl_2 concentration (our case), vaporization of Al dominates. As a consequence, close to the Cr_2AlC interface, an initial loss of Al shifts the composition of the system to the Cr_2AlC-Cr_7C_3-Cr_3C_2 three-phase domain identified by Hallstedt *et al.* [69]. For longer times, Cr_7C_3, which contains a higher Cr/C ratio than Cr_3C_2, is converted into this latter carbide by vaporization of Cr under the effect of chlorine. For even longer time, Cr of Cr_3C_2 vaporizes, producing free carbon identified as graphite at the surface of the porous sample. The chlorination path described above can be roughly illustrated by the path drawn in the cross section of the ternary phase diagram shown in Figure 3.24. Although Cr_7C_3 is not detected at the top surface for times exceeding a few min, it should nevertheless be always present at the reaction front, located at the Cr_2AlC interface. We checked this scenario by measuring Raman spectra as a function of depth in a 340 µm-thick single-crystalline Cr_2AlC layer partially converted at 1200°C during 3h. As expected, Cr_7C_3 is still present close to the interface and, as one gets closer to the top surface, its transformation into Cr_3C_2 can be put on a quantitative footing by plotting the variation of the intensity ratio between the Cr_7C_3 Raman peak at 275 cm^{-1} and the Cr_3C_2 Raman peak at 208 cm^{-1} as a function of the distance from the Cr_2AlC interface (Fig.3.25). As demonstrated in Fig.3.25, this ratio continuously decreases until it vanishes for distances larger than roughly 30 µm. According to the investigation above, the scenario of the sample in chlorination can be shown in Fig. 3.26. The pore size will decrease when one gets closer to the interface between porous section and MAX phase compounds because the top surface suffer the chlorination longer than the inner section. Meanwhile phase Cr_7C_3 still exist in slightly porous section because that section is in the early stage of the chromium-removing period.

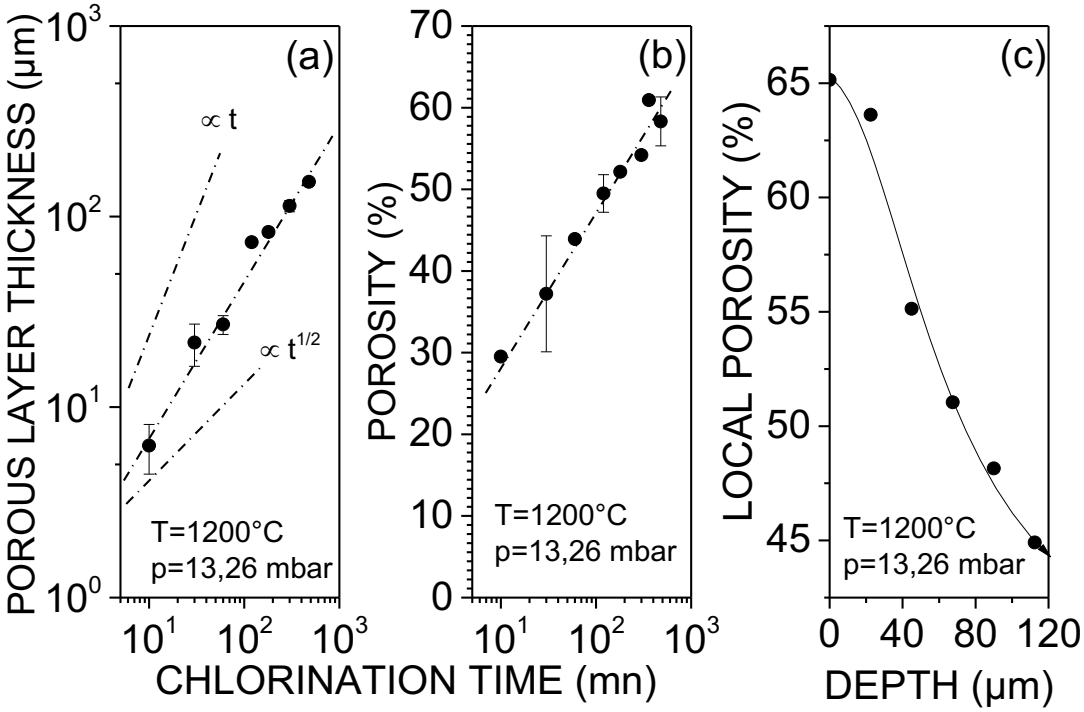

Figure 3.22. (a) Converted layer thickness *versus* time, (b) porosity as a function of time and (c) local porosity as a function of depth for an exposition Δt=5h. In all experiments T=1200°C. Solid lines are guides to the eye.

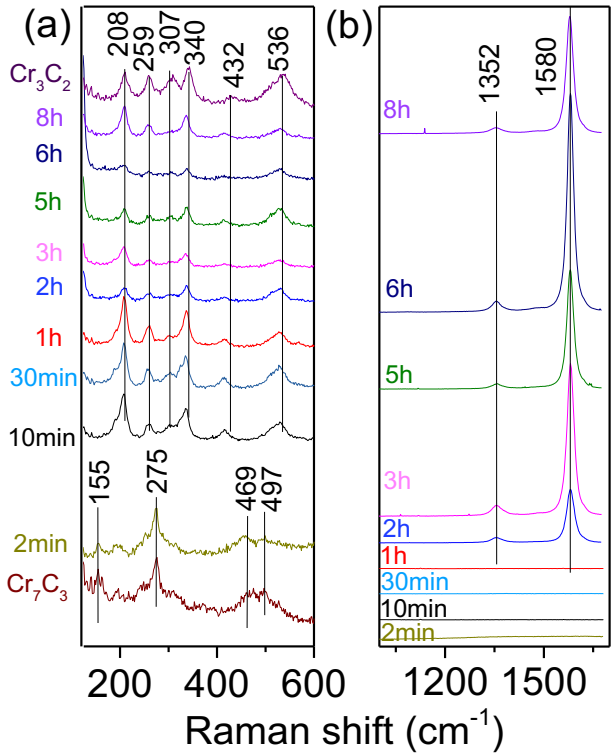

Figure 3.23. Raman spectra measured from samples chlorinated at 1200°C during different exposition times.

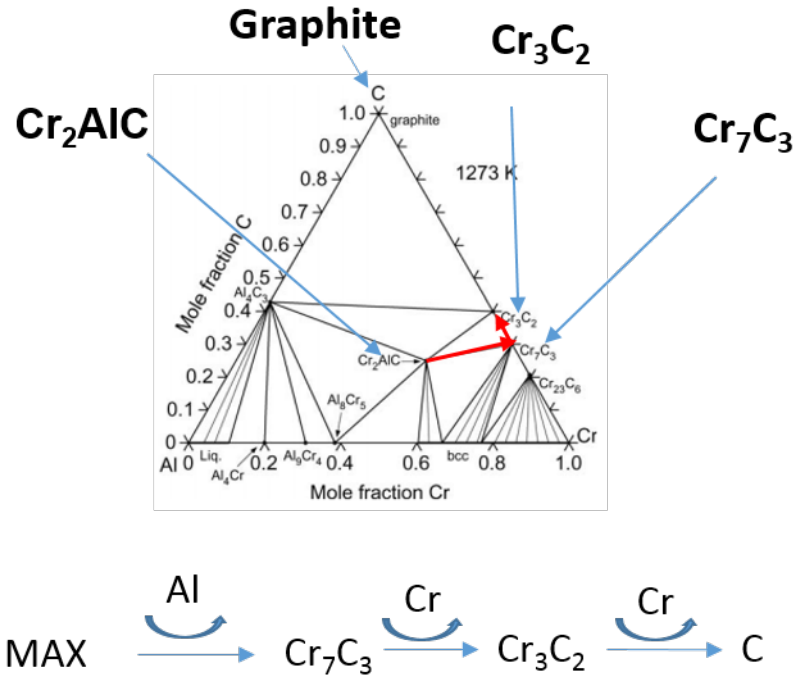

Figure 3.24. Phase diagram and chlorination path of the conversion from MAX phase Cr_2AlC to final product graphite [69].

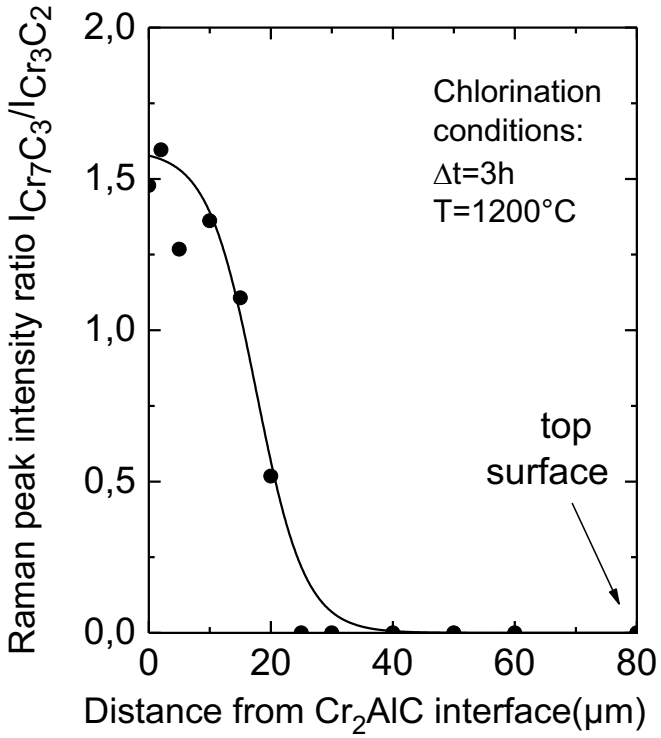

Figure 3.25. Ratio between the Cr_7C_3 Raman peak at 275cm^{-1} and the Cr_3C_2 Raman peak at 208cm^{-1} as a function of the distance from the Cr_2AlC interface. Chlorination temperature T=1200°C and time Δt=3h. The solid line is a guide to the eye.

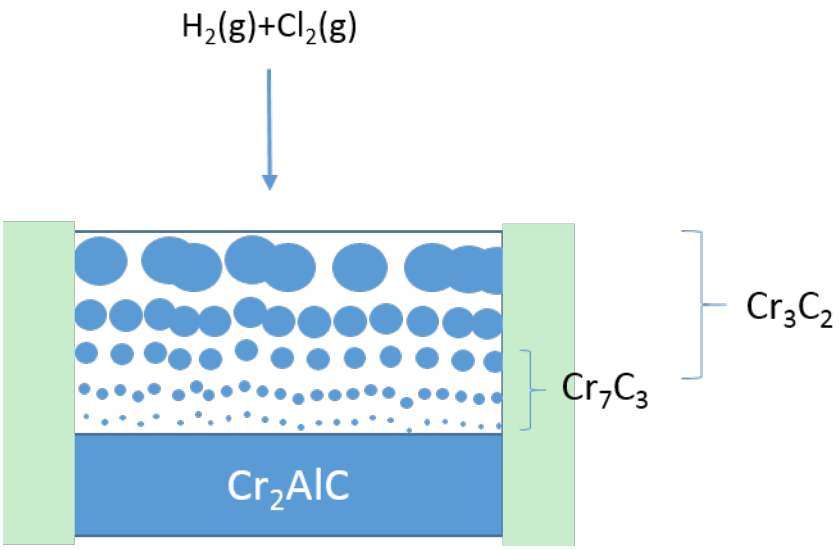

Figure 3.26. Sketch of cross section of incompletely chlorinated sample.

3.4.3.7 Role of the hydrogen

As previously noticed for Silicon Carbide (SiC) chlorination [70], the use of an additional hydrogen flow considerably slows down the transformation into CDC's. The slowing down principle is not only physical dilution, but also reaction with chlorine to form a less reactive reagent. A comparison of the sample chlorinated surface in the H_2/Cl_2 and that in Ar/Cl_2 is shown in Figure 3.27. The reaction conditions are the same except that one experiment corresponds to the addition of H_2 and the other to that of Argon. The different surface color indicates that the samples do not see the same chlorination conditions, the darker one (Fig.3.27a) being much more graphitized than the other (Fig.3.27b). If we only consider the physical dilution of the hydrogen and argon, the conversion thickness with hydrogen should be the same. However, in H_2/Cl_2, the converted thickness is about 29.8µm. and the one in Ar/Cl_2 is about 151.7 µm (**Fig.28**). Besides, the graphitized layer (the black layer about 37 µm at the right in **Fig.28 b**) appearing in the cross section corresponding to the use of Ar cannot be seen in the cross-section of the sample chlorinated with hydrogen. Chemical dilution of hydrogen makes the chlorination much slower. Therefore, addition of hydrogen allows us to convert the starting MAX phases into carbides.

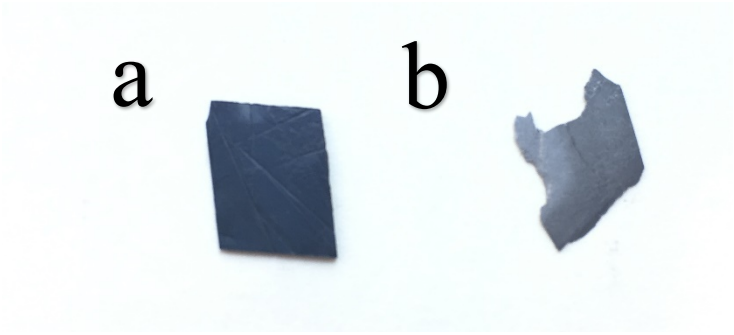

Figure 3.27. comparison between Cr_2AlC chlorinated in (a) Ar and Cl_2 (b) H_2 and Cl_2

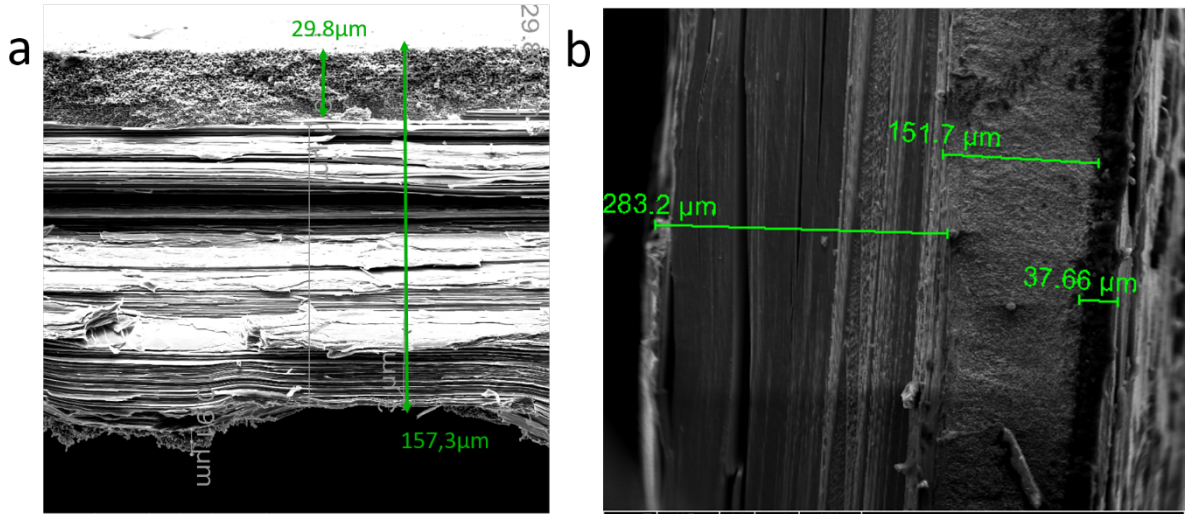

Figure 3.28. Cross-section of sample chlorinated in (a) H_2 and Cl_2 (b) Ar and Cl_2

3.5 Conclusion

We have synthesized various electrically conducting, highly porous carbides by using high temperature chlorination of MAX phase single crystals. In this section we focused more particularly on the case of the transformation of Cr_2AlC. After a very short initial stage where both Cr_7C_3 and Cr_3C_2 are present at the interface front, the porous layer is converted into porous Cr_3C_2 until, for very high processing temperatures and/or chlorination times, a gradual transformation of Cr_3C_2 into graphite also takes place. The porous layer is preferentially oriented. Typical pore sizes are sub-micrometric, and porosity typically ranges between 40 to 75%. The layers are electrically conducting and keep an overall resistivity value of the same order as that of bulk Cr_3C_2, demonstrating that an acceptable continuity is ensured throughout the porous medium. The magnetoresistance data present an interesting linear dependence with

the magnetic field at low T, with a negative component saturating at high field values. These quite specific signatures could be attributed either to the contribution of the graphite materials present after some hours of chlorination, or to the porous morphology of the Cr_3C_2 material itself. Our data seem to indicate that it is more reasonable to attribute the linear MR to the porous Cr_3C_2 layer. As already stated above, the linear MR component observed in our system might therefore constitute an original illustration of an old theoretical problem.

Reference

[1]. R.N. Pease, G.F. Walz, Kinetics of the thermal chlorination of methane, J. Am. Chem. Soc. 53 (1931) 3728–3737. doi:10.1021/ja01361a016.

[2]. J.C.B.E. V Ngton, L. Rattl, THE PHOTO-CHLORINATION OF POLYSTYRENE, 8 (1972) 1105–1111.

[3]. J.J. Kucera, D.C. Carpenter, The Catalytic Chlorination of Dioxane [1], J. Am. Chem. Soc. 57 (1935) 2346–2347. doi:10.1021/ja01315a003.

[4] Beck, U., 1986. Chlorobenzenes. In: Gerhartz, W. (Ed.), Ullman's Encyclopedia of Industrial Chemistry, vol. A6, p. 338

[5]. K. MacKenzie, J. Battke, F.D. Kopinke, Catalytic effects of activated carbon on hydrolysis reactions of chlorinated organic compounds: Part 1. γ-Hexachlorocyclohexane, Catal. Today. 102–103 (2005) 148–153. doi:10.1016/j.cattod.2005.02.038.

[6]. Greenwood, Norman N.; Earnshaw, Alan (1997). Chemistry of the Elements (2nd ed.). Butterworth-Heinemann. ISBN 0-08-037941-9

[7]. B.Y.P. Gross, D.L. Levi, The heats of formation of metallic halides, (1954) 626–629.

[8]. P.K. Jena, E.A. Brocchi, Metal Extraction Through Chlorine Metallurgy, Miner. Process. Extr. Metall. Rev. 16 (1997) 211–237. doi:10.1080/08827509708914136.

[9]. Korshunov BG, Georgievich B. Applications and potential uses of chlorination methods in metallurgy of non-common metals. Metall Rev Min Metall Inst Jpn. 8(1992)1–34.

[10]. F.N. Tebbe, J.Y. Becker, D.B. Chase, L.E. Firment, E.R. Holler, B.S. Malone, P.J. Krusic, E. Wasserman, J.Y. Becker, Multiple, Reversible Chlorination of C60, J. Am. Chem. Soc. 113 (1991) 9900–9901. doi:10.1021/ja00026a052.

[11]. S. Zhang, L. Shi, F. Mercier, O. Chaix-Pluchery, D. Chaussende, I. Gélard, B. Hackens, T. Ouisse, Conversion of MAX phase single crystals in highly porous carbides by high temperature chlorination, Ceram. Int. 43 (2017) 8246–8254. doi:10.1016/j.ceramint.2017.03.153.

[12]. S.A. Sisson, Y. Fan, M.M. Tanaka, A. Rogers, Y. Huang, B. Njegic, L. Wayne, M.S. Gordon, D. Dabdub, R.B. Gerber, B.J. Finlayson-pitts, Correction for Sisson et al., Sequential Monte Carlo without likelihoods, Proc. Natl. Acad. Sci. 106 (2009) 16889–16889. doi:10.1073/pnas.0908847106.

[13]. R. Tesser, E. Santacesaria, M. Di Serios, G. Di Nuzzi, V. Fiandra, Kinetics of glycerol chlorination with hydrochloric acid: A new route to α,γ-dichlorohydrin, Ind. Eng. Chem. Res. 46 (2007) 6456–6465. doi:10.1021/ie070708n.

[14]. T. Moritani, K. Kuchitsu, Y. Morino, Molecular Structures of Phosphoryl Fluoride, Phosphoryl Chloride, and Thiophosphoryl Chloride Studied by Gas Electron Diffraction, Inorg. Chem. 10 (1971) 344–350. doi:10.1021/ic50096a025.

[15]. W.E. Truce, G.H. Birum, E.T. McBee, Chlorination of Dimethyl Sulfide and Some of Its Derivatives with Sulfuryl Chloride and Thionyl Chloride, J. Am. Chem. Soc. 74 (1952) 3594–3599. doi:10.1021/ja01134a037.

[16]. R. Appel, Tertiary Phosphane/Tetrachloromethane, a Versatile Reagent for Chlorination, Dehydration, and P-N Linkage, Angew. Chemie - Int. Ed. 14 (1975) 801–811.

[17]. K. Araki, J.W. Halloran, Porous ceramic bodies with interconnected pore channels by a novel freeze casting technique, J. Am. Ceram. Soc. 88 (2005) 1108–1114.

[18]. S. Hashimoto, A. Yamaguchi, Growth of Hollow Cr_3C_2 Polycrystals with Cr_2O_3, J. Am. Ceram. Soc. 78 (1995) 1985–1988.

[19]. Y. Gogotsi, S. Welz, D.A. Ersoy, M.J. McNallan, Conversion of silicon carbide to crystalline diamond-structured carbon at ambient pressure, Nature 411 (2001) 283–287.

[20]. V. Presser, M. Heon, Y. Gogotsi, Carbide-derived carbons - from porous networks to nanotubes and graphene, Adv. Funct. Mater. 21 (2011) 810–833.

[21]. G.N. Yushin, E.N. Hoffman, A. Nikitin, H. Ye, M.W. Barsoum, Y. Gogotsi, Synthesis of nanoporous carbide-derived carbon by chlorination of titanium silicon carbide, Carbon 43 (2005) 2075–2082.

[22]. E.N. Hoffman, G. Yushin, M.W. Barsoum, Y. Gogotsi, Synthesis of Carbide-Derived Carbon by Chlorination of Ti_2AlC, Chem. Mater. 17 (2005) 2317–2322.

[23]. Lide, David R. (1998), Handbook of Chemistry and Physics (87 ed.), Boca Raton, FL: CRC Press, pp. 4–52, ISBN 0-8493-0594-2

[24]. A. Aubert, J. Danroc, A. Gaucher, J.P. Terrat, Hard chrome and molybdenum coatings produced by physical vapour deposition, Thin Solid Films. 126 (1985) 61–67. doi:10.1016/0040-6090(85)90175-0.

[25]. Chromium carbide description from http://www.us-nano.com/inc/sdetail/1023

[26]. J. Zackrisson, B. Jansson, G.S. Uphadyaya, H.-O. Andr´en, WC-Co based cemented carbides with large Cr3C2 additions, Int. J. Refract. Met. Hard Mater. 16 (1998) 417–422. doi:10.1016/S0263-4368(98)00048-1.

[27]. Henjered, Hellsing, Andrén, Nordén, 1986 A. Henjered, M. Hellsing, H.-O. Andrén, H. Nordén Quantitative microanalysis of carbide/carbide interfaces in WC–Co-base cemented carbides Mater. Sci. Technol., 2 (8) (1986), pp. 847-855

[28]. Chromium carbide powder product advantages from: http://www.langfengmetallic.com/news-in-company/chromium-carbide-powder-product-advantages.html

[29]. Chromium carbide powder product from http://fr.made-in-china.com/co_langfeng/image_Cr3c2-Chromium-Carbide-Powder-Has-High-Surface-Activity_egunooung_KSwTBMdhpNqG.html

[30]. Y.G.Wu, K.Wang, M.Q.Wang, M.Li, Chinese patent, Production method of chrome carbide powder, CN 102060296 A

[31]. http://www.amtecwelding.com/amtec-63-chromium-carbide/

[32]. S.-L. Zhang, M. Östling, Metal Silicides in CMOS Technology: Past, Present, and Future Trends, Crit. Rev. Solid State Mater. Sci. 28 (2003) 1–129. doi:10.1080/10408430390802431.

[33]. W.P. Leroy, C. Detavernier, R.L. Van Meirhaeghe, C. Lavoie, Thin film solid-state reactions forming carbides as contact materials for carbon-containing semiconductors, J. Appl. Phys. 101 (2007). doi:10.1063/1.2561173.

[34]. Jonathan Ellis and Michael Haw Materials World, Vol. 5 No. 11, pp. 136-37, November 1997.

[35]. M. Mohanty, R.W. Smith, M. De Bonte, J.P. Celis, E. Lugscheider, Sliding wear behavior of thermally sprayed 75/25 Cr3C2/NiCr wear resistant coatings, Wear. 198 (1996) 251–266. doi:10.1016/0043-1648(96)06983-9.

[36]. J.R. Davis, Thermal Spray Technology Edited by, Technology. (2004).

[37]. Bu Qian Wang, K. Luer, The erosion-oxidation behavior of HVOF Cr3C2-NiCr cermet coating, Wear. 174 (1994) 177–185. doi:10.1016/0043-1648(94)90100-7.

[38]. P. Colombo, In Praise of Pores, Science 322 (2008) 381–383.

[39]. S. Hashimoto, A. Yamaguchi, Preparation of porous Cr_3C_2 grains with Cr_2O_3, J. Am. Ceram. Soc. 79 (1996) 2503.

[40]. L. Zhang, K. Gao, A. Elias, Z. Dong, W. Chen, Porosity dependence of elastic modulus of porous Cr_3C_2 ceramics, Ceram. Int. 40 (2014) 191–198.

[41]. Z. Dong, Q. Zhang, W. Chen, Fabrication of highly porous chromium carbide with multiple pore structure, J. Am. Ceram. Soc. 97 (2014) 1317–1325.

[42]. L. Zhang, A. Elias, W. Chen, K. Gao, Electrical conductivity and wear behavior of bi-continuous Cr_3C_2–Cu composites, Ceram. Int. 41 (2015) 11075–11079.

[43]. S.H. Cui, J.H. Li, J.L. Luo, K.T. Chuang, L.J. Qiao, Co-generation of energy and ethylene in hydrocarbon fueled SOFCs with Cr_3C_2 and WC anode catalysts, Ceram. Int. 40 (2014) 11781–11786.

[44]. A.A. Edigaryan, V.A. Safonov, E.N. Lubnin, L.N. Vykhodtseva, G.E. Chusova, Y.M. Polukarov, Properties and preparation of amorphous chromium carbide electroplates, Electrochim. Acta 47 (2002) 2775–2786.

[45]. M. Wu, X. Lin, Y. Wang, L. Wang, W. Guo, D. Qi, X. Peng, A. Hagfeldt, M. Grätzel, T. Ma, Economical Pt-free catalysts for counter electrodes of dye-sensitized solar cells, J. Am. Chem. Soc. 134 (2012) 3419–3428.

[46]. Z. Dong, Q. Zhang, W. Chen, Fabrication of highly porous chromium carbide with multiple pore structure, J. Am. Ceram. Soc. 97 (2014) 1317–1325.

[47]. V.G. Grebenkina, Yu. P. Yusov and V.N. Sorokin, Low-resistance carbide resistors, Soviet Powder Metallurgy and Metal Ceramics 12 (1973) 345.

[48]. S.N. L'vov, V.F. Nemchenko, P.S. Kislyi, T.S. Verkhoglyadova, T.Y. Kosolapova, The electrical properties of chromium borides, carbides, and nitrides, Sov. Powder Metall. Met. Ceram. 1 (1964) 243–247.

[49]. Y.Kaburagi, H. Ishiyama, Linear dependence of transverse magnetoresistance on magnetic field in kish graphite, Carbon 33 (1995) 1505.

[50]. Y. Kaburagi, Y. Hishiyama, Electronic properties of kish graphite crystals with low values of residual resistivity ratio, Carbon 36 (1998) 1671–1676.

[51]. T. Osada, Negative Interlayer Magnetoresistance and Zero-Mode Landau Level in Multilayer Dirac Electron Systems, J. Phys. Soc. Jpn 77 (2008) 084711.

[52]. Y. Kopelevich, R.R. da Silva, J.C.M. Pantoja, A.M. Bratkovsky, Negative c-axis magnetoresistance in graphite, Phys. Lett. A374 (2010) 4629.

[53]. L. Wang, M. Yin, J. Jaroszynski, J.-H. Park, G. Mbamalu, T. Datta, Geometric dependence of transport and universal behavior in three dimensional carbon nanostructures, Appl. Phys. Lett. 109 (2016) 123104.

[54]. X. Zhang, Q.Z. Xue, D.D. Zhu, Positive and negative linear magnetoresistance of graphite, Phys. Lett. A 320 (2004) 471–477.

[55]. H.G. Johnson, S.P. Bennett, R. Barua, L.H. Lewis, D. Heiman, Universal properties of linear magnetoresistance in strongly disordered MnAs-GaAs composite semiconductors, Phys. Rev. B 82 (2010) 085202.

[56]. D. Stroud, F.P. Pan, Effect of isolated inhomogeneities on the galvanomagnetic properties of solids, Phys. Rev. B 13 (1976) 1434–1438.

[57]. M.M. Parish, P.B. Littlewood, Classical magnetotransport of inhomogeneous conductors, Phys. Rev. B 72 (2005) 094417.

[58]. S. Brunauer, P.H. Emmett, The use of van der Waals adsorption isotherms in determining the surface area of iron synthetic ammonia catalysts, J. Am. Chem. Soc. 57 (1935) 1754.

[59]. B.P. Flannery, H.W. Deckman, W.G. Roberge, K.L. D'Amico, Three-Dimensional X-ray Microtomography, Science 237 (1987) 1439.

[60]. G. B. Harris, X. Quantitative measurement of preferred orientation in rolled uranium bars, Philos. Mag. 43 (1952) 113.

[61]. V. Consonni, G. Rey, H. Roussel, D. Bellet, Thickness effects on the texture development of fluorine-doped SnO_2 thin films: The role of surface and strain energy, J. Appl. Phys. 111 (2012) 33523.

[62]. I. Gaballah, N. Kanari, S. Ivanaj, Kinetics of chlorination and oxychlorination of chromium (III) oxide, Metall. Mater. Trans. A 29 (1998) 1299–1308.

[63]. T. Ouisse, E. Sarigiannidou, O. Chaix-Pluchery, H. Roussel, B. Doisneau, D. Chaussende, High temperature solution growth and characterization of Cr_2AlC single crystals, J. Cryst. Growth 384 (2013) 88–95.

[64]. A.C. Ferrari, J.C. Meyer, V. Scardaci, C. Casiraghi, M. Lazzeri, F. Mauri, S. Piscanec, D. Jiang, K.S. Novoselov, S. Roth, A.K. Geim, Raman spectrum of graphene and graphene layers, Phys. Rev. Lett. 97 (2006) 187401.

[65]. A.C. Ferrari, Raman spectroscopy of graphene and graphite: Disorder, electron-phonon coupling, doping and nonadiabatic effects, Solid State Commun. 143 (2007) 47–57.

[66]. L.G. Cançado, K. Takai, T. Enoki, M. Endo, Y.A. Kim, H. Mizusaki, N.L. Speziali, A. Jorio, M.A. Pimenta, Measuring the degree of stacking order in graphite by Raman spectroscopy, Carbon 46 (2008) 272–275.

[67]. P. Lespade, A. Marchand, M. Couzi, F. Cruege, Caracterisation de materiaux carbones par microspectrometrie Raman, Carbon 22 (1984) 375–385.

[68]. P. Roura, The general relaxation time distribution of a logarithmic capacitance transient, J. Appl. Phys. 67 (1990) 3529–3530.

[69]. B. Hallstedt, D. Music, Z. Sun, Thermodynamic evaluation of the Al–Cr–C system, Int. J. Mat. Res. 97 (2006) 539.

[70]. V. Presser, M. Heon, Y. Gogotsi, Carbide-derived carbons - from porous networks to nanotubes and graphene, Adv. Funct. Mater. 21 (2011) 810–833.

Chapter 4

Electrochemical anisotropy of MAX phase Cr_2AlC

In this chapter, after a brief review of the literature on MAX phase corrosion resistance and anisotropy, we discuss the dependence of the electrochemical corrosion of Cr_2AlC single crystals on crystal orientation. Those crystals are sealed and dipped in 1M H_2SO_4 solution at room temperature. They are investigated by anodic polarization, electrochemical impedance spectroscopy (EIS) and corrosion morphology characterization. Polarization and EIS show significant differences between ab-plane and c-plane, either with respect to the corrosion current density or to the equivalent circuit required to fit the EIS data. We relate the corrosion mechanism to the Aluminum atom sensitivity and to the surface energy. In addition, we study the morphology of the patterns revealed at the sample surface by electrochemical etching. We show that these patterns are compatible with the existence of ripplocations, a family of defects which, as we argue, might be responsible for many deformation mechanisms in layered solids.

4.1 Introduction

4.1.1 Electrochemical method

Electrochemical methods are extensively used for a better control of some specific chemical reactions, for the study of reactivity in general and, more specifically, for assessing the corrosion properties of materials. They generally involve the use of a potentiostat system which allows one to control the voltage and current, thereby giving a better control of the redox scale and chemical valence of the elements involved in the reaction than by using "conventional" chemical reactions and chemical reagents. In particular, some special valence states can only be reached by these methods. They often permit a better characterization and/or control of properties like the valence, the reaction stoichiometry and reaction formula. It may allow one to avoid the formation of unwanted byproducts and reversible reaction, which makes the studied reaction more selective.

In this chapter, we use such electrochemical methods in order to investigate the corrosion resistance of MAX phase single crystals as well as its dependence of crystal orientation. This is achieved by selecting the crystal surfaces in contact with the electrolyte and by maintaining well defined potentiostatic conditions, either as a function of sweep rate, voltage or exposition time: Potential-dynamic polarization and Electrochemical Impedance Spectroscopy (EIS) have been put to good use in order to evidence the strong anisotropy in chemical reactivity which prevails in the case of Cr_2AlC.

4.1.2 State of the art and summary of previous work.

In 1999, three years after Barsoum et al. developed efficient synthesis methods for MAX phases [1], the first electrochemical evaluations of the corrosion potential and current density were conducted on Ti_3SiC_2 in variable conditions [2]. It was shown that Ti_3SiC_2 possesses a corrosion resistance around two times better than that of titanium metal, showing the potential of MAX phases for superseding the corresponding transition metals in some applications. From then on, the study of electrochemical corrosion resistance has been extended to many other phases. At present, the investigation of corrosion is further explored, but work has also been done in the field of the simulation of the reaction mechanisms, through the choice of equivalent

impedance circuits permitting to reproduce the EIS data. Three typical equivalent circuits involving two time-constants, as shown in Fig. 4.1, were chosen for fitting the experimental data of MAX phase compounds [3]. The majority of the available data in the literature deals with titanium containing MAX phases [2-9]. According to the published investigations, the early discovered MAX phases demonstrate excellent corrosion resistance in different harsh conditions, and therefore fulfill many of the requirements for potential applications in corrosive environments.

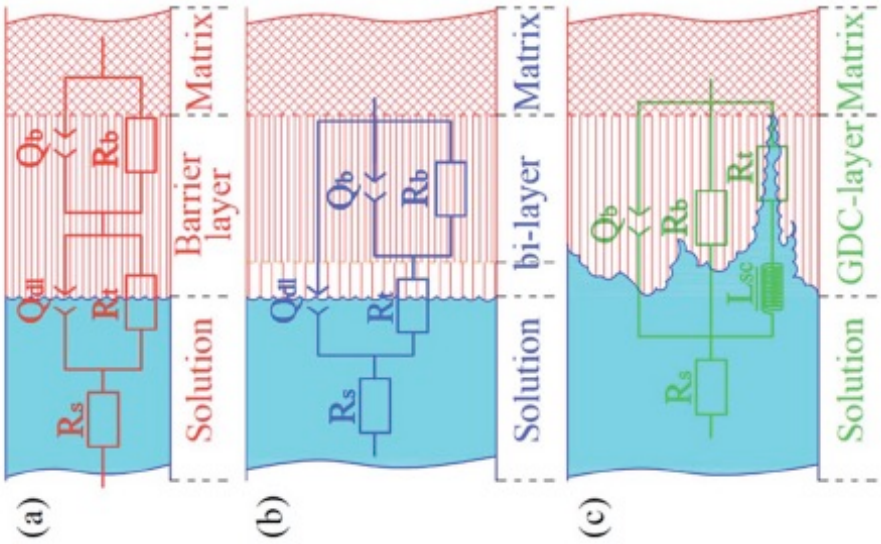

Figure 4.1. Typical Equivalent circuit (ECC) used for fitting the experimental data, (a) schematic and ECC used for nearly monolayer passivation film. (b) Schematic and ECC used for bi-layer structure. (c) schematic and ECC used for film growth dissolution-coupling (GDC) situation. Rs denotes solution resistance, Qdl and Rt represent the electrical double-layer capacitor and charge transfer resistance, and Qb and Rb are the barrier layer capacitor and resistance [3].

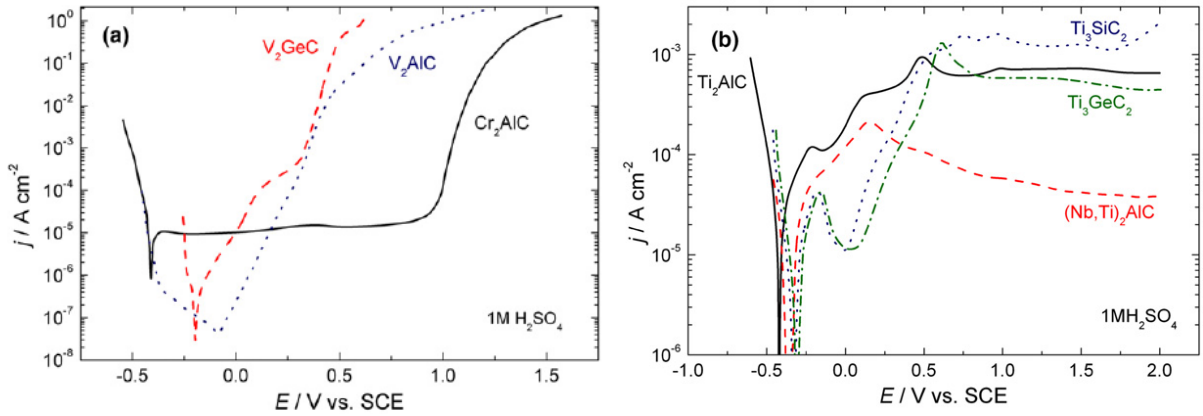

Figure 4.2. Polarization diagrams of (a) Cr_2AlC V_2GeC and V_2AlC (b) Ti_3SiC_2, $Ti3GeC_2$ and (Nc,Ti)AlC in 1M H_2SO_4[4]

In a corrosive environment, the chemical stability strongly depends on the nano-laminated structure including the atoms types and the number n. Accordingly, MAX phase compounds perform differently. According to Xie et al.[10], the corrosion of MAX phase compound resistance in 3.5M HCl solution heated at 200°C is connected to the MX layer thickness. For both carbides and nitrides, the resistance has a positive correlation with this thickness. In addition, another crucial factor is the passivation effect of the M and A elements, which is considered as the main determining factor of the different electrochemical behaviors [2-10]. In some highly corrosive conditions, M and A atoms are vulnerable to the etching and could form the corresponding oxides, a phenomenon which determines in turn the corrosion performance. Among the oxides and in the case of Ti_3SiC_2, both TiO_2 and SiO_2 are can be formed [5-9]. Fig.4.2 represents the polarization plot of some MAX phases in 1M H_2SO_4 [4]. Trans-passivation effect and passivation effect can be observed, respectively. As all the Ti-containing MAX phases possess passivation effect, we can assume that they perform better than no Ti-containing ones. Furthermore, the oxides protective performance varies on the corrosive conditions. As most of the ceramic compounds, they are more stable in base and salt solutions than in acids, because surface protective oxides cannot withstand long-term corrosion in acid.

No-Ti or Si-containing MAX phase compounds were relatively less studied. Although many other physical properties have already been dealt with in the literature, the electrochemical corrosion of Cr_2AlC has not been thoroughly studied. Jovic et al. published an investigation of polycrystalline Cr_2AlC polarization experiments in NaOH, HCl and H_2SO_4 solutions, showing corrosion trans-passivation phenomena [4]. Obviously, the passivation effect of Cr_2AlC is not sufficient to allow this material to withstand a high corrosion potential. Hence, at high potential, the performance is not comparable with those of Ti- or Si-containing MAX phase compounds. However, at low potential, Cr_2AlC could exhibit a better performance, since the corrosion current is the lowest of all the investigated phases [4]. Moreover, and although not comparable to that of the Ti-bases MAX phases, the corrosion potential of Cr_2AlC is nevertheless interesting for applications. Hence, in not too harsh an environment, Cr_2AlC could reveal to be outstanding for some applications.

4.1.3 Anisotropic properties and resistance to corrosion

Due to the Nano-lamellar structure and high lattice parameter ratio c/a, the MAX phase compounds are expected to present highly anisotropic features [11-13]. Most studies focused

on aspects such as magneto-transport and elasticity properties. Until the availability of single crystals and/or single-crystalline thin layers, the anisotropy of these properties had to rely on indirect considerations of oriented, polycrystalline bulk samples.

Magneto-transport anisotropies are ascribed both to anisotropies in the electronic structure and to anisotropic electron-phonon coupling, as indicated by Density Functional Theory (DFT) electronic structure calculations [11]. Band structure anisotropy leads in turn to Fermi surface and scattering mechanism anisotropies. In Cr_2AlC, the use of single crystals produced at LMGP demonstrated that the conductivity ratio between ab-plane and c-plane may exceed several hundred [12]. It is therefore quite natural to ask oneself whether the structural anisotropy can also lead to anisotropies in the electrochemical properties. This forms the main purpose of this chapter.

Du *et al.* [14] tested the corrosion resistance dependency on crystalline orientation. In supercritical water, the c-plane is widely covered by a thick layer of Al_2O_3 and has more cracks than other orientations. The discussion is focused on the reactive Al atom, which is vulnerable to the corrosion. The authors ascribe the high reactivity to the weakly bonded Al interlayers. Herein, we attempt to explore in more detail the anisotropic electrochemical behavior, benefiting for the first time from the availability of cm-sized single crystals. This makes possible a direct measurement of the in-plane and out-of-plane corrosion properties.

Surface energy considerations are often very useful for explaining the anti-corrosion performance on quantitative grounds [15]. For MAX phase compounds, several theoretical calculations conducted for the MAX phase (0001) ab-plane have already been published [16–19]. However, the surface energy cannot be directly measured directly, and most of the time is only evaluated by simulation. Due to their structural complexity, other crystalline planes have not yet been assessed, so that we cannot rely on such values for helping us to make comparisons and to understand possible differences between planes. Yet, a high reactivity of the Al atoms is a predominant feature noticed by all researchers studying the Al containing MAX phases. Hence, it is reasonable to think of this factor seriously for explaining an anisotropic anti-corrosion behavior. Owing to the low vacancy energy and vacancy migration energy [20], Al atom is the most reactive site during chemical reactions, and is easier to remove than the transition elements in the system. In the past decade, it was shown to be responsible for many potential transformations of MAX phases. The most exciting product is Mxene [21–23]. The aluminum elements present at the surface of c-planes make this orientation more vulnerable than that defined by the ab-plane, because in the latter configuration, etching an Al hcp layer

then leaves a surface totally devoid of Al atoms, whereas they are always present in the former configuration.

4.1.4 Evidence of ripplocations by electrochemical etching

Layered solids are ubiquitous in nature and span many orders of magnitude; from geological mountain ranges to single graphene layers. It has long been established that microscopic defects are a necessary condition for mechanical deformation. It has also long been assumed, implicitly or explicitly, that in layered solids basal dislocations (BDs) were that defect (**Fig.4.3a and b**).[24-28] As pointed out recently, however, BDs cannot explain many characteristic observations associated with the deformation of layered solids in general and kink band, KB, in particular for the simple reason that to form KBs, c-axis strain is required(**Fig.4.3c**)[29]. Since, in **Fig.4.3a and b**, the direction of dislocation and stress are parallel to the L axis, basal dislocations cannot result in or accommodate c-axis strain. The same is true of delamination of layered solids; BDs - that are confined to the basal planes – simply cannot result in the delaminations that are very often observed in layered solids, especially weakly bonded ones like graphite or transition metal dichalcogenides, as the delamination usually has a rotation angle between the basal plane and dislocation band(Fig.4.3d). Said otherwise the current conventional wisdom is simply incompatible with the some of the most basic characteristics of layered solids

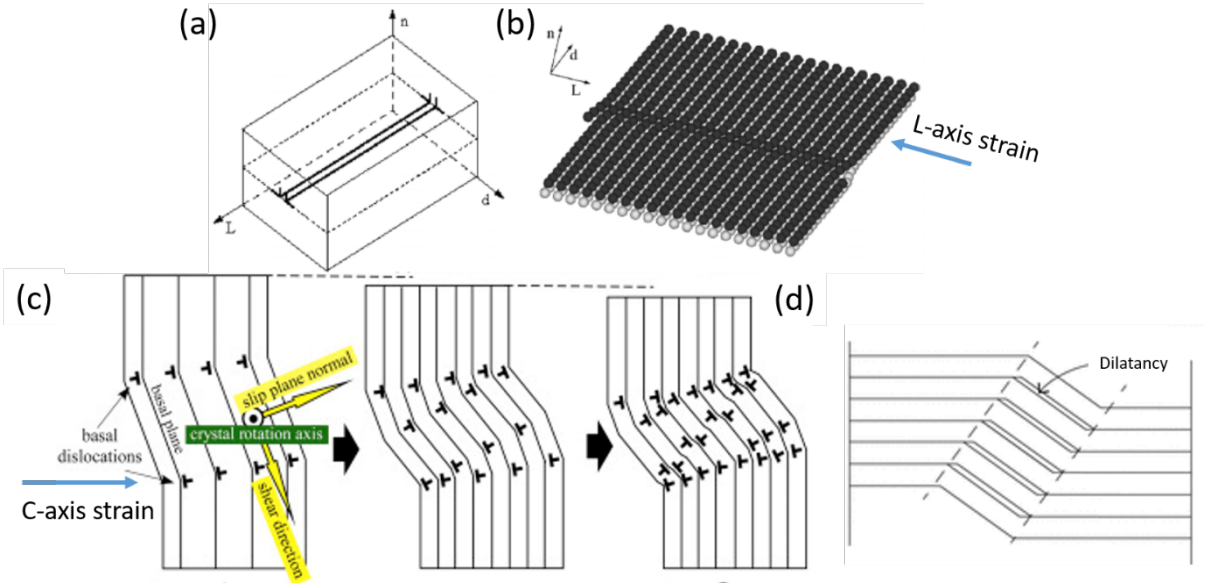

Figure 4.3. (a) Sketch of the simulation Mg crystal cell demonstrating a dislocation lying on a slip plane [30] (b) sketch of the slip plane after introduction of a screw dislocation along the *L*-direction. Dark and

light gray spheres indicate atoms above and below the dislocation line, respectively [30] (c) Mechanical model of kink band in the Zn single crystal under c-axis strain [31].(d) schematic explanation of the delamination in kink band[32]

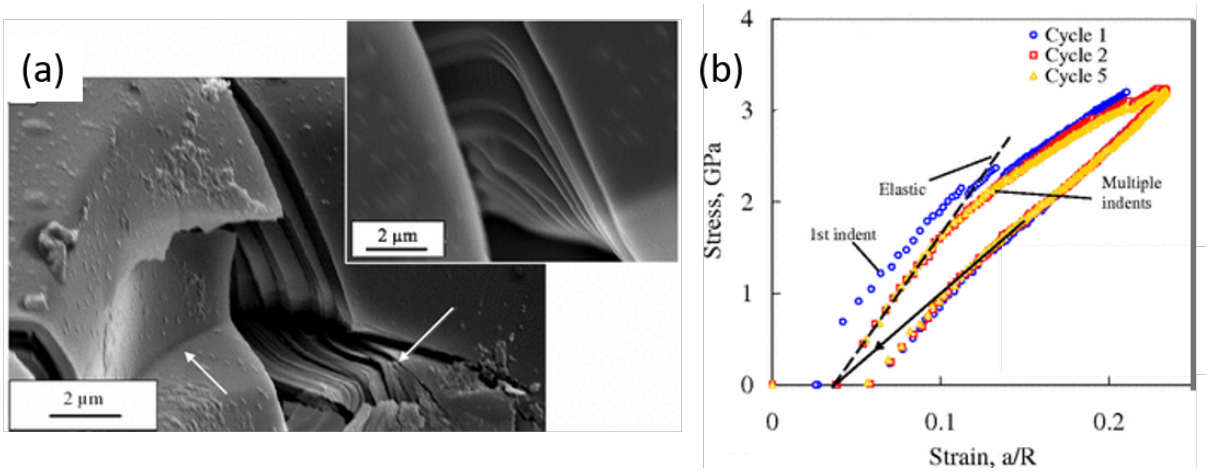

Fig. 4.4. (a)FESEM image of kinks (denoted by arrows) by massive indentation on muscovite single crystal(inset demonstrates delaminations).(b)strain/stress plot of indentation on muscovite single crystal. The strain is the ratio of contact area a to the indenter radius R. [33]

In 2004, Prof. Barsoum et al. tested indentation on muscovite single crystal and observed the incipient kink bands deformation (Fig.4.4a) They described this mechanism as kinking nonlinear elasticity, since the deformation caused by indentation is reversible and follows a non-linear response to the strain(Fig.4.4b) [33]. In particular, the plots (Fig.4.4b) are similar to those of tests on the layered solids such as Ti_3SiC_2 and graphite. In 2015, Kushima et al. postulated the existence of a new defect they termed a surface ripplocation to explain near surface deformation features observed in the van Der Waals bonded solid, MoS_2.(Fig.4.5a) [34]. In a structure of two 2D layers, one layer, slipped by shear strain, could be regarded as being locally insert an extra-line relative to the other (Fig.4.5b). Due to the weakly bonded layer structure like van Der Waals bonded solid, it is called ripplocation, exhibiting distinction with conventional dislocation. The same authors also used density function theory, DFT, to show that two ripplocations of the same sign were attracted to each other in sharp contrast to two dislocations of the same sign that repel, establishing that ripplocations as fundamentally different from dislocations(Fig.4.5c)[34]. In 2016, Gruber et al. used molecular dynamic calculations on graphite (Fig.4.6a)and experimental results on a MAX phase, Ti_3SiC_2(Fig.4.6b), to extend the idea of surface ripplocations to the bulk and as importantly show that such bulk ripplocations, BRs, defects are not just applicable to van Der Waals bonded solids, but rather

were the operative mechanism in all layered solids that do not twin.[35]. Ripplocations are simply a ripple in the atomic layers induced by buckling. Gruber et al. also showed that BRs, have no Burgers vector or polarities.[35]

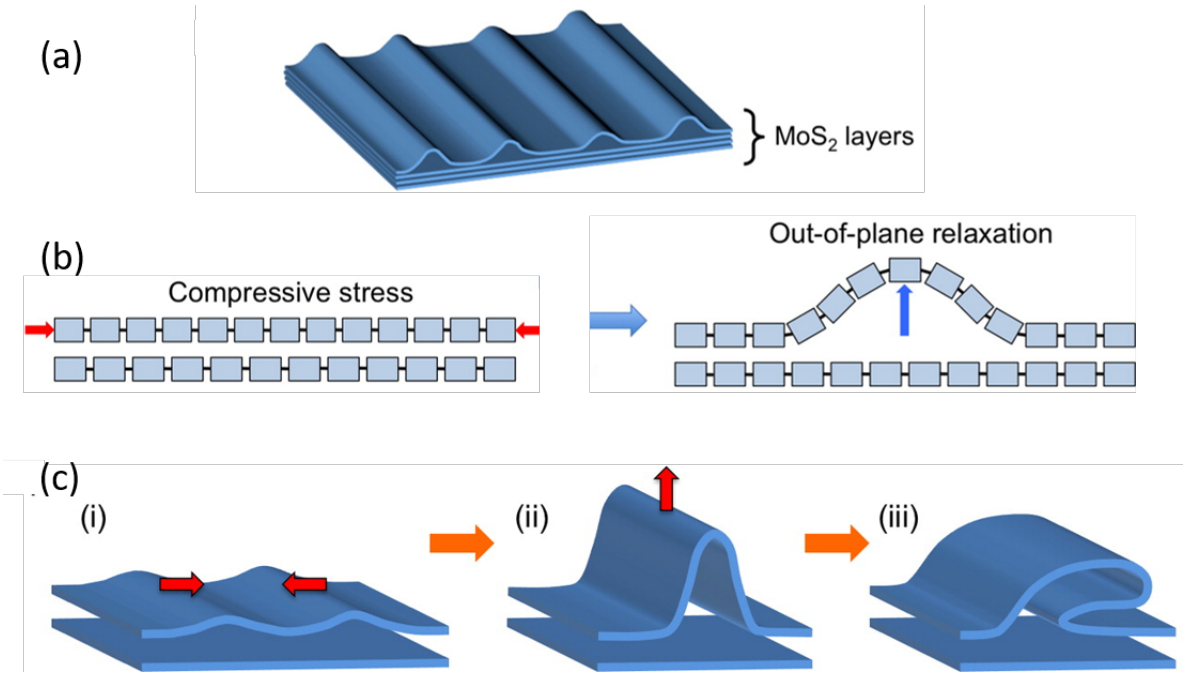

Figure 4.5. (a)schema of surface ripplocation of MOS_2 layer[34](b)schematic explanation of the formation of ripplocation ,simulated by DFT, by inserting an extra-line of layer in the MoS_2 bi-layer structure (c) schematic DFT simulation of the aggregation and self-folding of the ripplocations.

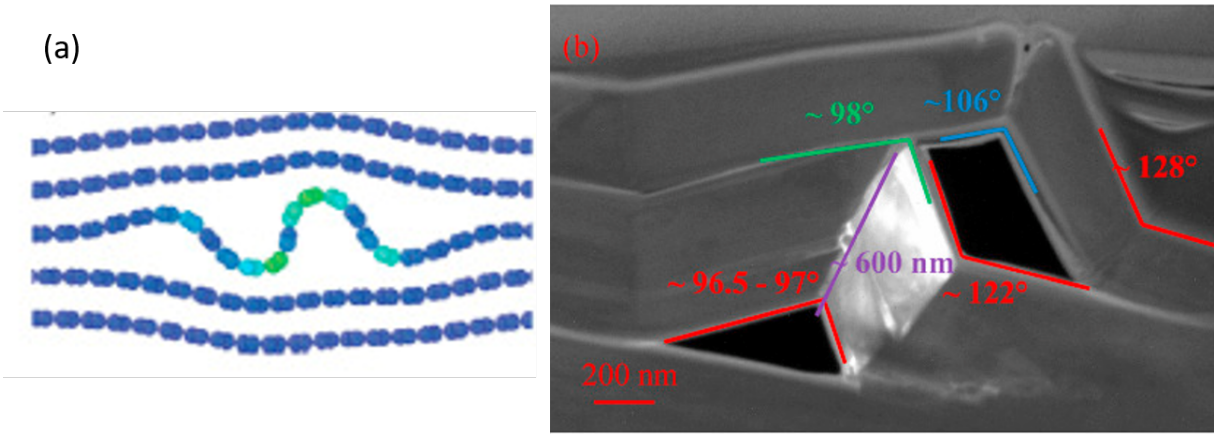

Figure 4.6. (a)schematic illustration of bulk ripplocation in graphite(b) TEM image of bulk ripplocation formed in Ti_3SiC_2 by indentation [35].

Before the polarization, the fine polished surface is rather smooth without visible trenches. Herein, through the electrochemical polarization on Cr_2AlC single crystals in sulphuric acid, we show that large, deep, narrow trenches parallel to the basal planes are formed.

These detectable trenches are not initial ones, but are amplified ones. The shape size and depths of these trenches are found to be a function of polishing grit size and etching time. Non-polished samples did not form trenches, but etched more or less uniformly. Since basal dislocations and stacking faults cannot explain these results and ripplocations can, we take these results as indirect evidence for the latter.

4.1.5 Objectives and content of this chapter

Until now, limited by the specimen scale, the chromium MAX phases anisotropic anti-corrosion behavior has not been extensively studied. Due to the development of MAX single-crystal size by Ouisse et al.[36], the investigation of the intrinsic electrochemical corrosion mechanisms in single crystals becomes feasible. This is of great importance in order to better assess the anti-corrosion performance of such materials. In this chapter, we report for the first time direct measurements of the anisotropic electrochemical behavior of single crystals of Cr_2AlC. Two different kinds of sealed single crystal faces, ab-plane and c-plane, respectively, are analyzed through the determination of open circuit potentials (OCP), DC potentiodynamic polarization curves and AC electrochemical spectroscopy impedance (EIS) techniques in 1M H_2SO4 solution. Effect of the crystalline orientation is sufficiently compared through the analysis of the corrosion current density and EIS data, and several mechanisms are also proposed. The study of the surface morphology after anodic corrosion on c-plane reveals the presence of interesting patterns, which have never been observed before. Hence a set of experiments are carried out to acquire the evolution and to determine the deformation type. All the proof demonstrates the existence of ripplocations.

4.2 Methodology

4.2.1 Raw material:

We used Cr_2AlC single crystals synthesized by high temperature solution growth following the process described in detail in the introduction chapter and in previous articles (see ref. [36] for Cr_2AlC).

4.2.2 Electrode sample preparation

According to the objectives, two patterns of sample preparation are used. One is aimed to measure the corrosion current and resistance by EIS. In this case, three types of Cr_2AlC single-crystalline working electrodes are prepared. The "raw" Cr_2AlC single crystal (Fig.4.7 a) combines ab-plane (platelet surfaces) and c-plane (platelet edges) structures, so that it is expected to possess intermediate properties between those two orientations. The other two types are sealed in resin to expose either the ab-plane or the c-plane, respectively (Fig.4.7b and c). In the latter cases, raw Cr_2AlC crystals were connected to a Cu wire on the back side using silver paste and bi-component epoxy resin for electrical contact and sample holding, respectively. Then, after resin solidification, the exposed surface of ab-plane and c-plane were successively polished with 320, 600, 1200, 2400 and 4000 grades SiC emery paper with grinder polisher. The samples were sonicated in distilled water and ethanol to remove residual particles from the surface.

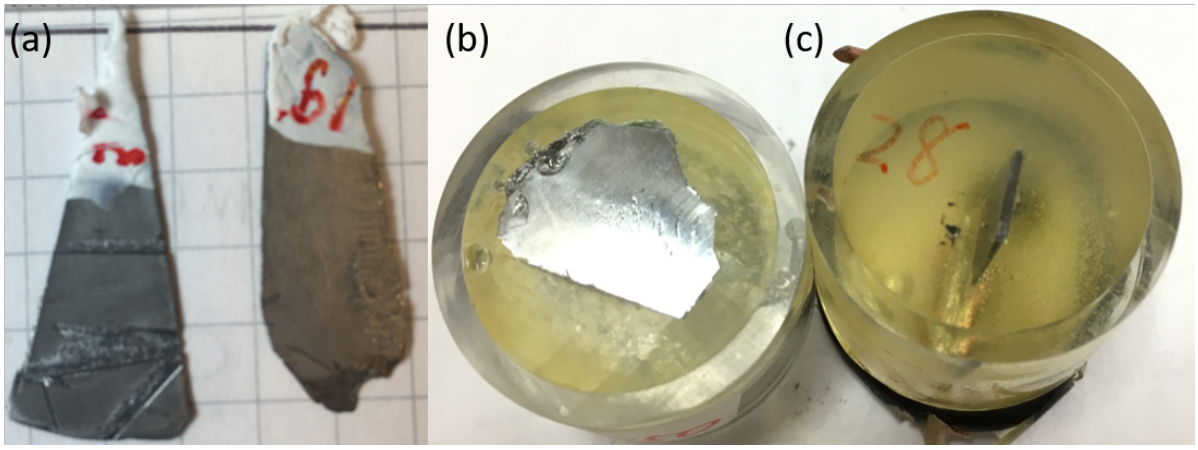

Figure 4.7. Cr_2AlC working electrodes (a) raw (b) ab-plane (c) c-plane

4.2.3 Electrochemical tests

All experiments were carried out in a three-electrode standard electrochemical cell at room temperature (Fig.4.8a). The platinum grid counter electrode, saturated calomel electrode (SCE) and Cr_2AlC working electrode are placed vertically with the same distance between each other in the electrolyte. A 1M H_2SO_4 solution which was made from analytical grade H_2SO_4 98% (**EMSURE®**) and distilled water. In comparison with inert gas protected systems, in our

case the oxygen in the air can dissolve in the electrolyte. However, the H_2SO_4 acid solution limits the effect of exposure to air and restricts the oxide layer to a few nm [37].

A Gamry REF600 potentiostat was used to record polarization and EIS curves. This potentiostat was monitored and controlled using the electrochemistry measurement software supplied by Gamry DigiElch.

(a) (b)

Figure 4.8. (a) three-electrode standard electrochemical cell (b) Potentiostat Gamry REF600 used for electrochemical test.

Samples were usually kept at open circuit potential (OCP) for 30 mn in the solution 1M H_2SO_4. Then, after the EIS, polarization curve was recorded in 100 mL of 1M H_2SO_4, from -50 mV to +1.5 V versus OCP at the sweep rate of 1mV/s. Impedance measurements were acquired at the voltage amplitude of 10 mV around OCP and a frequency range from 0.05Hz to 50 kHz (8 points for each frequency decade were acquired).

The second pattern is aimed to observe the edge(c-plane) of the polished and raw crystals. It is inspired by the polarization of sample through first pattern, where large trenches could be observed in the end of the etching. Hence, fine polishing is required to maximally hold the initial structure. The sealed edge(c-plane) was subjected to the same process of the first pattern with an additional polishing protocol, using successively diamond suspension with grain sizes of 6um, 3um, 1um, and 0.03um.

In order to acquire the evolution of the trenches, the voltage was ramped at a rate of 1 mV/s - from the open circuit voltage, OCV to -0.25 V, -0.1 V, 0 V, 0.6 V, 0.75 V, 0.85 V, 1 V and 1.2V vs. SCE. After reaching each potential, the sample was removed from the electrochemical cell, washed and observed under a scanning electron microscope, SEM, after

which it was placed back in the electrochemical cell and the voltage was ramped to the next level.

4.2.4 Characterization technics

All the samples are observed before and after electrochemical test by SEM using a Philips XL-30 field-emission gun (FEG) and a JEOL JSM 6300. Meanwhile, energy dispersive X-ray analyses (EDX) were performed.

EIS measurements were analyzed with the EC-Lab software in order to fit the data with the selected equivalent circuits and corresponding EIS parameters.

Optical micro-spectroscopy (Reichert MeF2) was performed to measure the etching depth after polarization.

4.3 Results and discussion

4.3.1 Indirect evidence for ripplocations

Since the mounted and exposed edges were polished down to different final grit sizes in the two patterns, according to the final size 9 μm and 0.03 μm, these c-plane electrodes are henceforth referred to as C-9μ and C-0.03μ, respectively.

When the C-9 c-plane is polarized to 1.5V vs. SCE, the large trenches were observed and some were regularly arranged with similar widths. Hence, the second preparation pattern was used to eliminate the mechanical exfoliation formation in the polishing progress and maximally hold the initial structure. Meanwhile, another set of unpolished c-plane electrodes are taken as reference.

Preliminary results showed that below a voltage of 0.6 V vs. SCE, there was no corrosion and in most experiments the voltage was thus ramped to 0.6 V before starting the SEM observations. In a few runs, when the voltage reached 0.85V, the cell was placed back in the electrochemical cell and held at that voltage for 3 mins, removed from the electrolyte and imaged in the SEM.

Fig. 4.9 shows a typical polarization curve for the Cr_2AlC single crystal. Here we just note that below 0.6 V vs. SCE, the corrosion current is low, due to the trans-passivation. As the

voltage surpass 0.6V vs. SCE, the corrosion current increases dramatically and significant morphology change could be acquired.

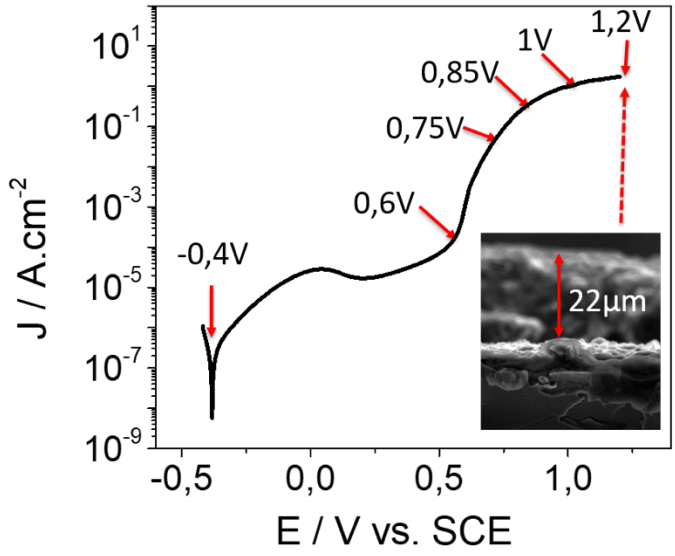

Figure 4.9. Typical polarization diagram for the Cr_2AlC single crystal in 1M H_2SO_4 from OCV to 1.2V vs. SCE with sweep rate of 1mV/s. The voltages, where the sample cross-section is observed by SEM, are indicated. Inset: SEM micrograph for a side view of a fine polished sample (C-0.03 µm) polarized from OCV to 1.2V vs. SCE with sweep rate of 1mV/s in 1M H_2SO_4

Before proceeding further, it is important to appreciate that the corrosion current simultaneously etches the samples uniformly and, in the case of polished samples, by the formation of narrow long trenches that are parallel to the basal planes. Longer etching times and higher voltages result in deeper material erosion. For example, inset in Fig. 4.9 shows a SEM micrograph that shows a side view of a C-0.03µ sample after etching up to 1.2 V, where it is clear that the recession of the sample, relative to that of the mounting material is ≈ 20 µm. Etching a similar sample up to 1.2 V, and holding at that voltage for 0.5 h, results in a recession of ≈ 7 mm (not shown).

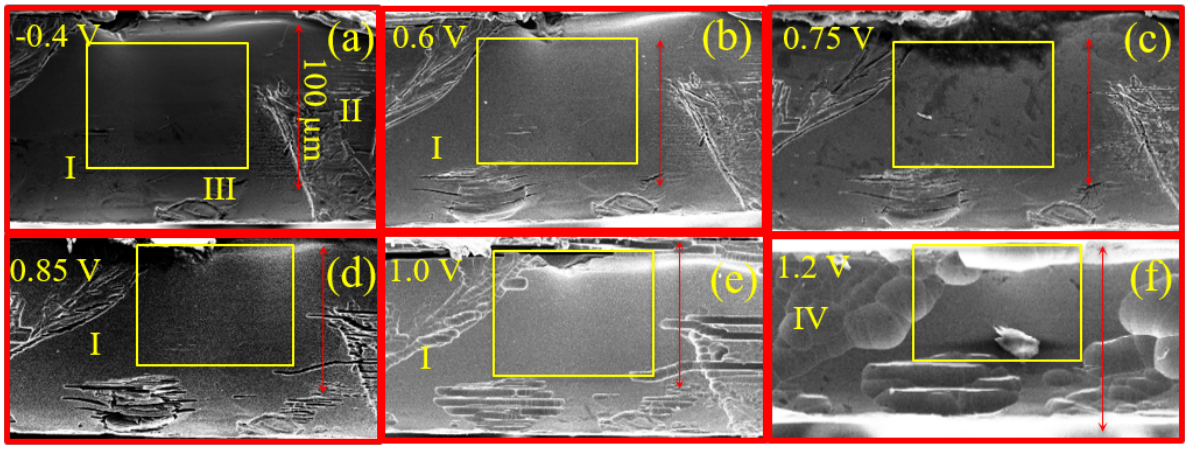

Figure 4.10. (a) SEM micrograph of raw crystal polarized from OCV to 0.6V with sweep rate of 1mV/s in 1M H_2SO_4. (b) SEM micrograph of sample in (a) polarized from 0.6V to 0.75V vs.SCE with sweep rate of 1mV/s in 1M H_2SO_4 (c) SEM micrograph of sample in (b) polarized from 0.75V to 0.85V vs.SCE with sweep rate of 1mV/s in 1M H_2SO_4 (d) SEM micrograph of sample in (c) polarized at 0.85V vs.SCE for 3mn in 1M H_2SO_4 (e) SEM micrograph of sample in (d) polarized from 0.85V to 1V vs.SCE with sweep rate of 1mV/s in 1M H_2SO_4 (f) SEM micrograph of sample in (e) polarized from 1V to 1.2V vs.SCE with sweep rate of 1mV/s in 1M H_2SO_4

As importantly, the uniform and non-uniform etching results in two distinctly different morphologies. In the unpolished samples (Fig.4.10), the etch pits appear as more or less equiaxed "grains" with what appears to be shallow ridges between. In sharp contradistinction, the etch pits in the polished samples initially appear as deep trenches that, in some cases, extend from one side of the sample to the other (see below).

Figures 4.10a shows a typical cross-sectional scanning electron microscope, SEM, micrograph of an *as-received* Cr_2AlC single crystal that is roughly 100 μm thick. The cross-section shows the presence of a more or less defect-free central region (outlined by a yellow square), surrounded by 4 defective regions labeled I, II, III and Ⅳ. Figures 10b to f show the same sample but after the voltage on the sample was successively ramped to 0.6 V, 0.75 V, 0.85 V, 1 V and 1.2 V, respectively. A perusal of these micrographs makes it clear that the central region – denoted by the square - was etched uniformly. The non-uniformly etched areas (regions I, II, III and IV), on the other hand, are all associated with growth defects. Said otherwise, in the absence of growth defects, the etching is more or less uniform. Region I in Fig.4.10d is noteworthy. Here defects, parallel to the basal planes, were introduced during growth or handling. These defects etch by the formation of deep trenches (region I in Fig.4.10e), that give way to a "brick wall", rounded morphology with deeper etching (region I in Fig.4.10f). It

follows that this rounded morphology is a signature of more or less uniform etching but only below defective areas.

The correlation between the polishing – or lack thereof - and the morphology and depth of the trenches – or lack thereof – is the most important result of this work for the simple reason that it unambiguously shows that polishing introduces defects in Cr_2AlC that are parallel to the basal planes. Not only are defects introduced, but as discussed below, the widths of the trenches and the extent by which they penetrate into the bulk is a function of polishing grit size.

Figures 4.11a to e, shows a series of typical cross-sectional SEM micrographs of a C-0.03μ sample as a function of corrosion potential. The microstructure of the sample for which a corrosion potential of 0.75V was reached (Fig. 4.11a) is quite smooth and indistinguishable from the initial polished surface (not shown). When the corrosion potential reaches 0.85 V, multiple (≈ one every 10 μm) deep and narrow trenches parallel to the basal planes are visible (Fig. 4.11b). Holding the sample for 3 min. at 0.85 V resulted in a significant widening of trenches and in some cases the merging of adjacent trenches to form large deep canyons denoted by vertical arrows in Figs. 4.11c. Note that not all fine horizontal cracks in Fig. 11b merge into deep canyons. Some are shallow and simply transform into shallow rounded brick shaped cavities (horizontal arrows in Fig. 4.11c). By the time the corrosion voltage is 1V (Fig. 4.11d) a noticeable general coarsening of the microstructure is evidenced. When the corrosion voltage is 1.2 V (Fig. 4.11e) the trenches have more or less disappeared and are replaced by the typical rounded features characteristic of more uniform etching. Post-etching optical micrographs established that the depth of the crater formed was ≈ 20 μm. It follows that polishing down to 0.03 μm creates defects parallel to the basal planes that penetrate roughly 20 μm into the bulk of the sample.

The SEM micrographs of a second sample are shown in Figs. 4.11f to j that correspond to those shown in Fig. 4.11a to e. Comparing the two sets of micrographs, it is reasonable to conclude that they share most features. The only possible difference is the fact that the defects in the second sample were slightly deeper than in the first since even after 1.2 V (Fig. 4.11j) some deep trenches are still visible.

To this point the results have been qualitative. In attempt to quantify some of the etching parameters, we carefully measured the lengths and width of some the defects as a function of time and as a function of polishing grit size. Figures 4.12a and b, respectively, compare the microstructures obtained when the corrosion voltage reached 0.85 V and after holding at that voltage for 3 min. Here again the longer etching time led to a general coarsening of the microstructure. In Fig. 4.12a, in addition to the large trench labeled T1, a relatively large

number of seemingly identical smaller, trench-like defects are visible. Of these only one set, denoted by short vertical arrows, near the bottom of Fig. 12a, transforms to a deep trench labeled T2 in Fig. 4.12d. The rest – some of which are denoted by horizontal arrows - appear to be shallower and do not transform into trenches, but into the rounded shallow features seen elsewhere.

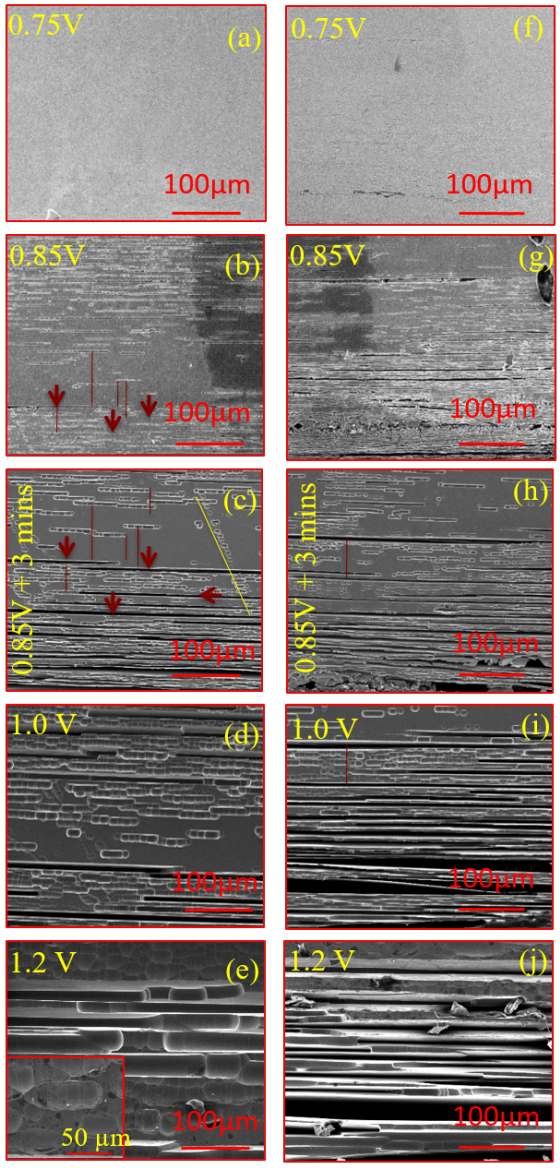

Figure 4.11. Two series of typical cross-sectional SEM micrographs of a C-0.03µ sample, successively passed following polarizations respectively (a) and (f) from OCC to 0.75V vs. SCE in 1M H_2SO_4 with sweep rate of 1mV/s (b) and (g) polarized from 0.75V to 0.85V vs. SCE in 1M H_2SO_4 with sweep rate of 1mV/s, large deep canyons are denoted by vertical arrows (c) and (h) polarized at 0.85V for 3mn. shallow rounded brick shaped cavities are indicated with horizontal arrows (d) and (i) polarized from 0.85V to 1V vs. SCE in 1M $H_2SO_4$with sweep rate of 1mV/s (e) and (j) polarized from 1 V to 1.2V vs. SCE in 1M H_2SO_4 with sweep rate of 1mV/s.

Figures 4.12c and d compare SEM micrographs of a C-0.03µ and a C-9µ sample, respectively, that were both etched to a voltage of 1.2 V. Careful measurement of the widths of the trenches yielded the following results 7.5±2.0µm and 12.5±3 µm for the C-0.03µ and a C-9µ samples respectively. In other words, the trenches created for the samples polished with the rougher sand paper were roughly 70% times wider than the ones polished with the finer grade. This result again establishes a relationship between the severity of polishing and the size of the canyons or trenches created. This comment notwithstanding the relationship between the width of trenches observed herein and the polishing medium is unclear. How and why the trenches that form appear to be more or less of the same width after a given etching

protocol is unclear at this time. This aspect, which is beyond the scope of this work, could be a very fruitful area of research.

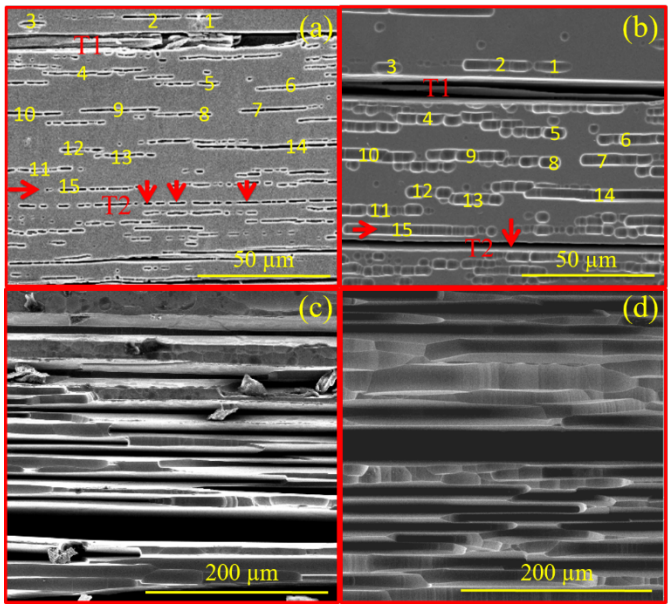

Figure 4.12. (a) The microstructures of the sample polarized from OCV to 0.85V vs.SCE with sweep rate of 1mV/s in 1M H_2SO_4. Smaller, trench-like defects, which transform to deep trenches, are denoted by short vertical arrows. Those, which transform to be shallower, are denoted by horizontal arrows (b) the same sample in (a) holding at the voltage of 0.85V for 3 min(c) The microstructures of the fine polished sample(C-0.03 µm) polarized to 1.2V in 1M H_2SO_4 with sweep rate of 1mV/s (d) The microstructures of the coarse polished sample(C-9 µm) polarized from to 1.2V in 1M H_2SO_4 with sweep rate of 1mV/s

A total of 8 different samples were explored, and over 100 individual SEM micrographs were taken and analyzed. In most cases no evidence for corrosion at a voltage of 0.75 V was observed (Fig. 4.11a). One of the samples, however, showed very fine lines at a voltage of 0.75 V (Fig. 4.13). Another showed small etch pits parallel to the basal planes and to each other (Fig. 4.11f). The uniformity of the etch pits and their ordering is noteworthy. From these micrographs it is clear that the canyons formed start off as very thin cracks (Fig. 4.11b) that develop into small parallel etch pits (Fig. 4.11c) that then merge together to form the larger/deeper canyons. Note that most of these parallel etch pits are quite shallow and disappear with increasing voltage.

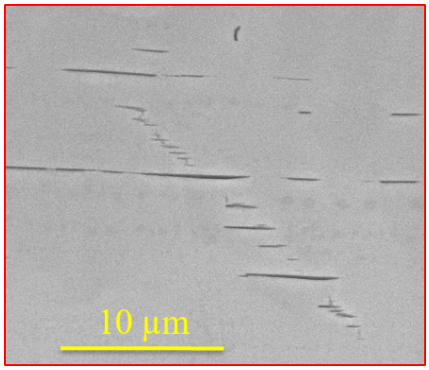

Figure 4.13. Fine polished Cr_2AlC sample(C-0.03µ) polarized from OCV to 0.75V vs. SCE in 1M H_2SO_4 with sweep rate of 1mV/s

A direct relationship between polishing and the size/existence of the canyons or trenches created is established. The only question remaining then is: What is the nature of these defects? Stacking faults can be eliminated because they would extend across the entire crystal, whereas the defects induced by the fine polishing only penetrate roughly 20 µm into the bulk. In other words, the defects are near surface defects. Basal dislocations can also be eliminated since, if they had any signature at all, they would appear as thin parallel slip lines (see inset in Fig. 4.9a, taken from deformed ZnO single crystals [38]).

The simplest explanation for the defects observed is that the polishing introduces ripplocations into the bulk. The mechanism envisioned is not unlike the one shown in Fig. 4.14a. In order to obtain more evidence concerning what occurs in the bulk of the sample, the edges of a few large single crystals were hand polished down to 25 µm for 3 mins. The samples were then placed in a SEM and their polished surfaces and, more importantly, the sides of the crystals adjacent – or sharing a corner – to the polished surfaces were imaged by SEM. The images of the sides of single crystals that were polished (Figs. 4.14b and c) clearly demonstrate the relationship between kinking, kink band formation and delaminations. Figure 4.14d also shows a side view of a single crystal where a long delamination crack was followed from the polished surface on the right to its end, roughly 1 mm into the single crystal. Barousm et al. previously argued [35], and this work confirms, that it is the buckling/kinking of the basal planes that result in the delaminations typically observed when layered solids are mechanically deformed, especially if they are not confined during the deformation process. Note that basal dislocations *per se* cannot cause delaminations.

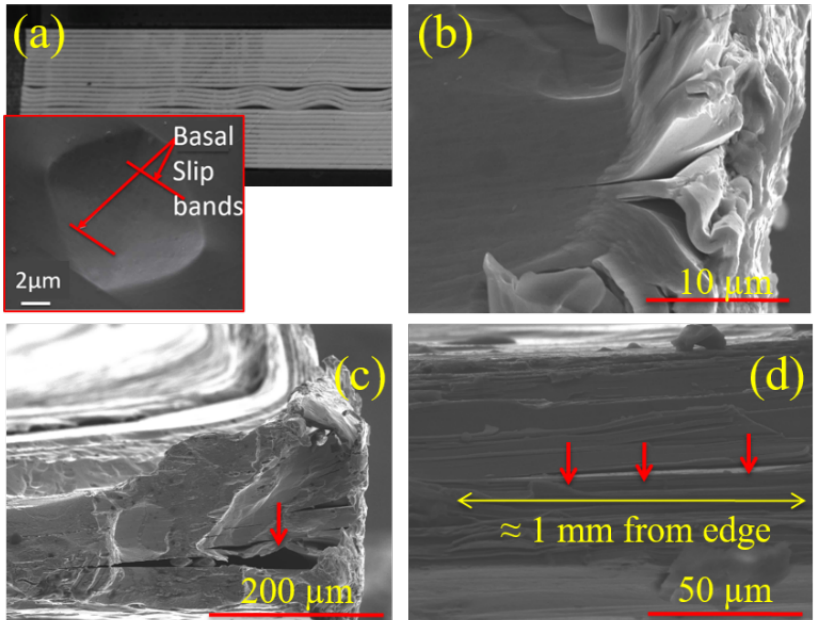

Figure 4.14. (a) Mechanism of deformation caused by pressing stress[38] (b) and (c) kink band formation and delaminations on the c-plane, caused by polishing on sand paper (P 600=25 μm) for 3min (d) long delamination crack from the polished surface on the right to its end, roughly 1 mm

Gruber et al. [35] showed that the energy of required to nucleate bulk ripplocations in graphite – the quintessential van der Waals bonded solid – was quite high. In the MAX phases, in which the bonds between the layers is a strong primary bond, it is reasonable to assume that the energy needed to nucleate bulk ripplocations would be at least several times higher. We thus hypothesized that only very confined basal planes that were loaded to several GPa would buckle and create bulk ripplocations. This indeed was found to be the case in a recent paper by Griigs et al [39] who presented evidence that indeed ripplocations were nucleated when spherical nanoindenters were indented in another MAX phase, Ti_3SiC_2.[39] What is thus fascinating herein and unexpected is relative ease by which the bulk ripplocations nucleated and grew as a result of polishing down to 0.03 μm. This comment notwithstanding it is hereby acknowledged that quite high stresses can be generated during polishing, but nevertheless, we find the results obtained quite intriguing. Based on the results of this work, it is reasonable to argue that any contact mechanics of layered solids that assumed dislocations to be the operative micromechanism needs to be revisited. It is important to note that the differences is not cosmetic, but fundamental. Gruber at al. have shown that once nucleated, bulk ripplocations – at least in graphite - are very mobile indeed even at 10 K.

One important axiom of dislocation-based contact mechanics has been that the extent of damage, of say an indenter of radius R, is of the order of R. The atomic modeling of Gruber et al. has shown that is not the case for bulk ripplocations. Because of their wave-like nature

bulk ripplocations tend to extend much further into a solid than dislocations. It is for this reason for example that a surface polished with 25 μm coarse SiC paper can result in a crack that extends 1 mm into the bulk (Fig. 4.14d). At this point it is important to note the features observed herein are clearly *not* Griffith cracks that propagated from the surface into the material. And while the features shown in Fig. 8 are reminiscent of small brittle cracks, the way these evolve into parallel etch pits (Fig. 4.12b), the bridges between them (inset in Fig. 4.12b) categorically rules out that they were cracks.

Figure 4.15 is a SEM micrographs of the top surface – vis. the basal planes - of a Cr_2AlC single crystal after etching. In general, in this orientation, the etching is quite uniform. Most polishing-induced scratch lines - present before etching - are eliminated during the sweep, from OCV to 1.2V vs. SCE, leading to flat surfaces. Heavy scratches, on the other hand, sometimes result in the characteristic patterns as shown in Fig. 4.15. The structure of these patterns, appearing along the polishing grain track are reminiscent of Shallamach waves, usually observed in soft materials such as polymers. [40]. In such materials, the stick-slip-like motion of the indenting object leads to the dilation of materials inside shear bands and subsurface voiding, as observed in much detail by Tang and Martin in the case of polymer blends with lamellar structures [40]. In our case, we postulate that the deformation-induced ripplocations and buckling lead to a periodic rotation of the *ab* planes from the horizontal towards the vertical. Figure 9c is a schematic of how that can occur. To do so, KB, or regions of sharper radii of curvatures, must form. And since it is reasonable to assume the atoms in the latter are higher in energy, then it is not unreasonable to assume that when exposed to the etching solution, they would etch faster resulting in the chevron repeated pattern shown in Figs. 9a and b. At this junction, it is worth noting that when mica or graphite single crystals were indented with a spherical indenter, massive basal plane rotations – in some cases as high as 90° - were clearly observed in post-indentation SEM micrographs.[41,42]

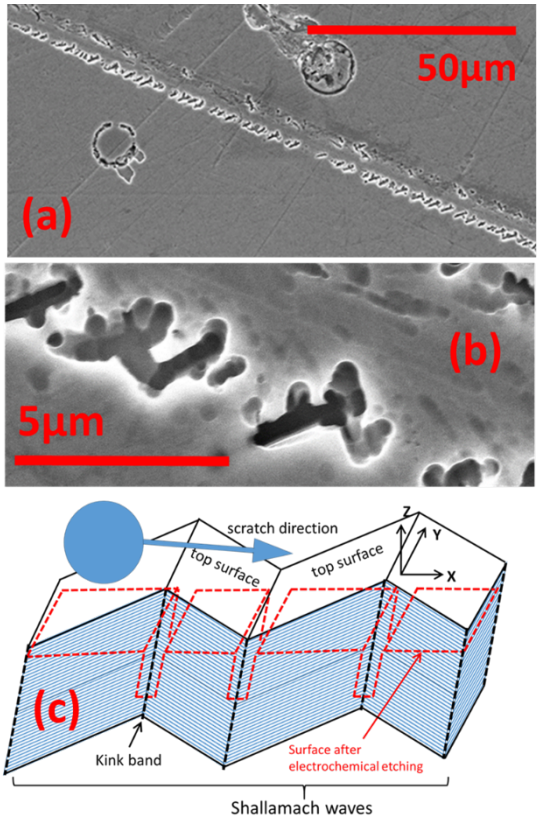

Figure 4.15. (a) and (b) SEM micrographs acquired after the electrochemical etching of a heavy scratch induced during the polishing of the top surface of a Cr_2AlC crystal (*i.e.* parallel to the *ab* planes). (c) proposed mechanism leading to the etching pattern along the polishing-induced defective track.

Observation of scratch-induced defects in harder and isotropic inorganic crystals – in which presumably the deformation is mediated by dislocations - lead to totally different defective structures [43]. In our case, the transformation of ripplocations and buckling induced in the subsurface lead to the formation of KBs, leading in turn to the characteristic pattern of Fig.4.15. These comments notwithstanding, it is hereby acknowledged that much more work is needed to understand the intricacies of how ripplocations nucleate and deform in the bulk in general and near surfaces in particular. Here we but scratched the surface of this fascinating, universal mechanism in the deformation of layered solids.

4.3.2 Electrochemical measurements

4.3.2.1 Anodic polarization

Quantitative anodic polarization was carried out on “ab-plane”, “raw crystal” (regarded as combining ab-planes and c-planes as the whole sample is exposed to the solution) and “c-plane” type electrodes respectively. As the polarization curves of the same electrode type are repeatable, one sample is selected for each type (Fig.4.16). Anodic polarization starts from -0.05V (vs OCP) and ends at 1.5V vs OCP. Corrosion potentials (E_{corr}) of all samples types lie around -0.4V (vs. SCE). After a rapid rise, current density reaches a plateau at around 0V due to a passivation effect (oxide film) on the exposed surface. As in the literature [4], this effect consists in trans-passivation, which is not sufficient to completely stop the corrosion. With the potential going on increasing, a presumably thicker and denser film protects the electrode that holds the current constant. Then at around 0.6V vs SCE, the protective passivation effect cannot protect the sample anymore and a second sharp current increase occurs. Subsequently, the working electrode starts to release orange Cr^{6+} compound into solution, indicating high dissolution rate of material and oxidation of M element. Corrosion current densities are obtained by dividing the corrosion current (I_{corr}) by the geometric area of surface in contact with the electrolyte. In Table 4.1, current densities of c-plane, raw crystal and ab-plane electrodes are around $7*10^{-7}$, $2*10^{-7}$ and $4*10^{-8}$ $A.cm^{-2}$ respectively. The corrosion current density of ab-plane significantly differs from that of c-plane. The value of c-plane corrosion current density is about 15 times higher than that of the ab-plane, suggesting that the ab-plane possesses a better corrosion resistance. Furthermore, comparing all the three curves, especially the trans-passivation section, the order of the current density value is c-plane> raw crystal> ab-plane(Table 4.1). Consequently, during the whole polarization process, ab-plane exhibits better performance than c-plane. Furthermore, polycrystals of Cr_2AlC [4] exhibit a corrosion current density similar to that of the raw Cr_2AlC electrode measured in this work, whose corrosion current density value was found to be in the middle between those of ab-plane and c-plane.

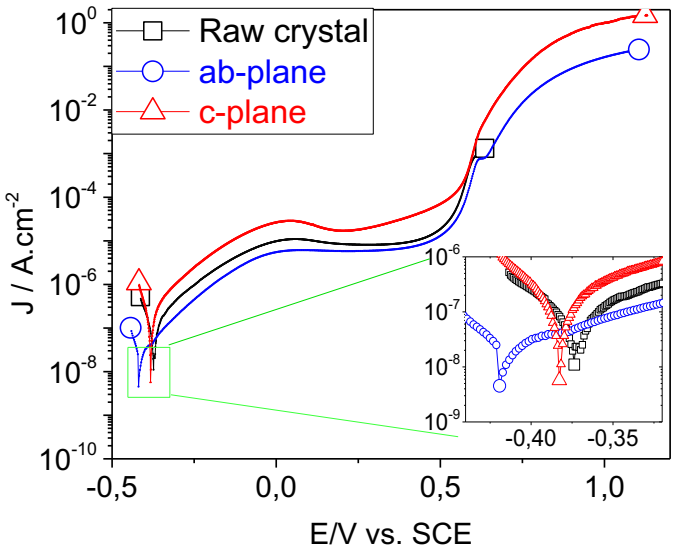

Figure 4.16. Polarization curve of Cr_2AlC sample in 1M H_2SO_4 from OCP to +1.5V vs OCP: c-plane (triangle) ab-plane (round) raw crystal (square).

Table 1. Corrosion current and trans-passivation current for the three types of electrode form OCP to 1.5V vs OCP in 1 M H_2SO_4

Electrode	$I_{corr}(A.cm^{-2})$	$I_{passiv}(A.cm^{-2})$
ab-plane	$4*10^{-8}$	$4*10^{-6}$
Raw	$7*10^{-7}$	$6*10^{-6}$
c-plane	$2*10^{-7}$	$2*10^{-5}$

As discussed in the previous section, ripplocations are created during the polishing. It is reasonable that c-plane with numerous nanometric ripplocations could lead to an overestimated value of the corrosion current, because it could be locally (in the trenches) higher than that expected from a flat surface.

4.3.2.2 Determination of corrosion current

The corrosion current is an important indicator for assessing the potential of a given material for some industrial applications. The common method of determination is to use a Tafel plot, or I-V curve in a semilogarithmic scale, in the polarization domain where the corrosion current logarithm is expected to show a linear dependence on V [44]. In most

situations, the value can be given automatically by the analysis software. However, according to theoretical definition, it needs both cathodic and anodic polarization curves. In our experiment, high reduction or oxidation potential could irreversibly change the condition and make the expected value to deviate. Hence, it is not feasible to measure both on the same electrode. Furthermore, the obtained anodization plot doesn't have a strictly linear region. This forced us to define a protocol for assessing the corrosion current. We decided to keep the experimental points for which the derivative was relatively constant, and then to extrapolate the best linear fit of this domain to the OCV in order to extract the corresponding value of the corrosion current, as detailed below.

We first smooth the experimental data to eliminate noise (Fig.4.17). After smoothing, the current density is differentiated to find a constant value which could correspond to Tafel theory. In Fig.18, the section between -0.307V and -0.265V is the closest to a horizontal line. Then, extrapolating a linear fit in this area to the OCV voltage value gives us our "best" estimation of the corrosion current. For example, the current density value of a c-plane electrode is $2.69*10^{-6}A.cm^{-2}$(Fig.4.19).

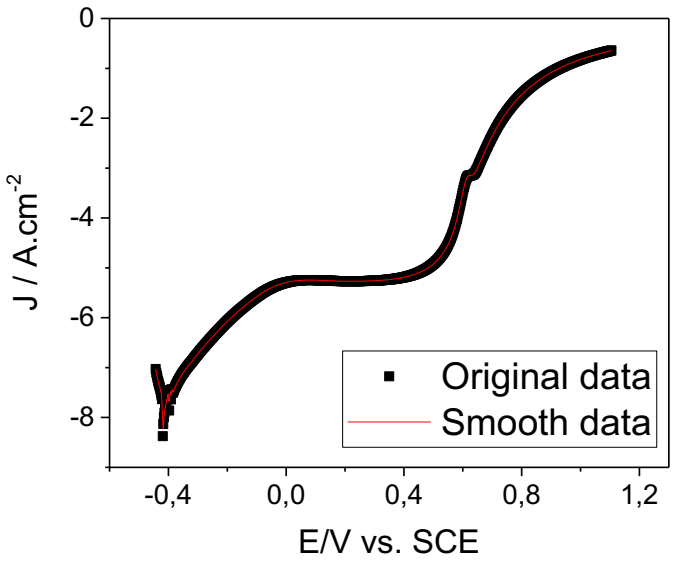

Figure 4.17. Smoothed polarization curve of Cr_2AlC c-plane working electrode in H_2SO_4 from OCV (-0.4V) to 1.2V vs SCE with sweep rate of 1mV/s.

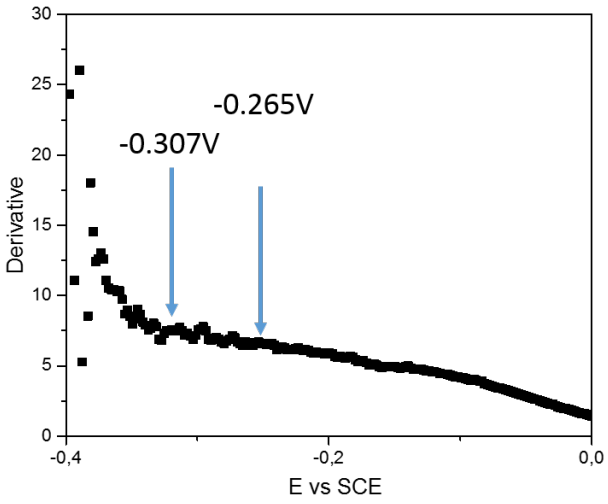

Figure 4.18. Derivation of current density of Cr_2AlC c-plane working electrode in H_2SO_4 from OCV (-0.4V) to 1.2V vs SCE with sweep rate of 1mV/s. The section from OCP to 0V vs SCE is exhibited.

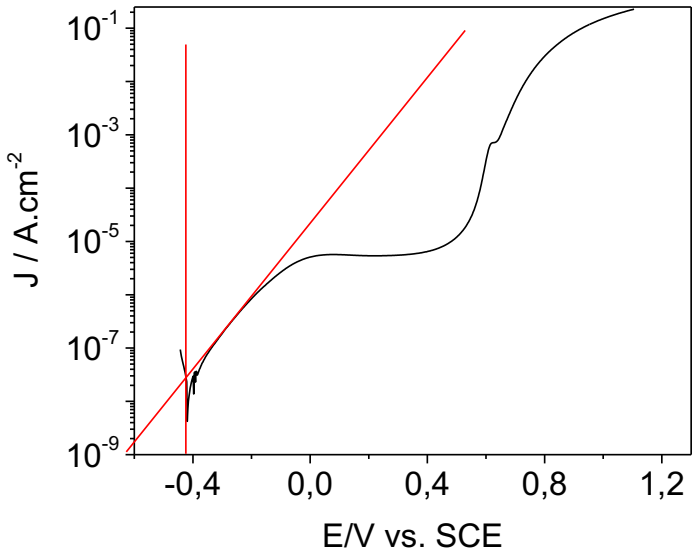

Figure 4.19. Determination of the corrosion current density value of sample in Fig.4.11 after derivation

4.3.2.3 EIS measurements

The electrochemical impedance spectroscopy (EIS) could provide further information on the anti-corrosion behavior. EIS measurements are presented as Nyquist plots (Fig.4.20 a), where imaginary part (Z``) of the impedance is plotted vs its real part (Z`), and Bode plots (Fig.4.14b), which present the impedance modulus |Z| and shift phase versus frequency. Experimental points are presented with symbols (black square, red round and blue triangle) corresponding to raw crystal, c-plane and ab-plane respectively. Nyquist plots recorded around OCP exhibit apparent semi-circles (Fig.4.20a). In particular, the Nyquist plot of c-plane shows depressed semi-circle, indicating that there is more than one time-constant. The Bode plots

(Fig.4.20b) correspond to the results of Nyquist plot that it appears two time-constant in the plot of c-plane. At low frequency, all the three type electrodes have the shift phase around 85°, which correspond to the typical value of CPE. Comparing the impedance modules |Z| at low frequency (e.g.0.03Hz) (Fig.20b), the ab-plane electrode presents a value of 100KΩ while the c-plane has a value of 5KΩ. It is similar to the ratio of the corrosion current density between the two types. At high frequency, ab-plane and raw crystal exhibit a constant phase shift while that of c-plane decreases to 68°. The constant phase shift indicates only one time constant in the equivalent circuit. For c-plane, the second phase shift value reveals the existence of a second time constant, which could be ascribed to diffusion and surface heterogeneity.

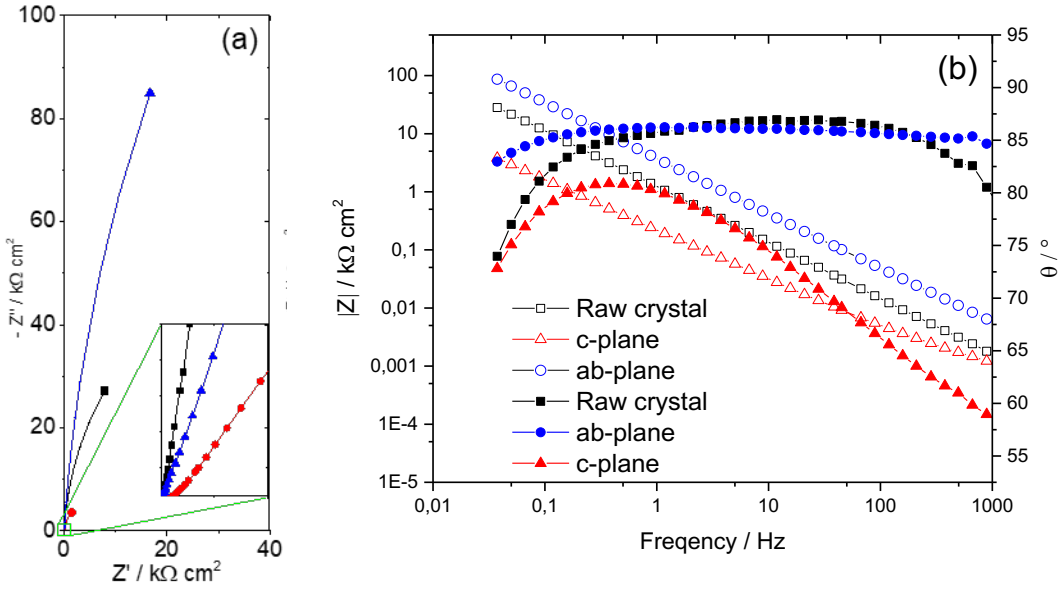

Figure 4.20. Electrochemical Impedance spectra recorded from 0.03 Hz to 1 KHz around Ecorr (-0.4V) from 0.03Hz to 1 kHz in 1M H_2SO_4: c-plane (triangle) ab-plane (round) raw crystal (square). (a) Nyquist plot (b) Bode representation (modulus |Z| and shift phase)

EIS data are usually interpreted using electrical equivalent circuits representing physical processes occurring in the real system. However, the analysis of EIS spectra by equivalent circuit is complex, mostly due to the overlapping of phenomena. Equivalent circuits are proposed in Fig.4.21. The best values of the respective elements forming those circuits were determined by fitting (Table 4.2). The effective capacitance is obtained through the module Brug.

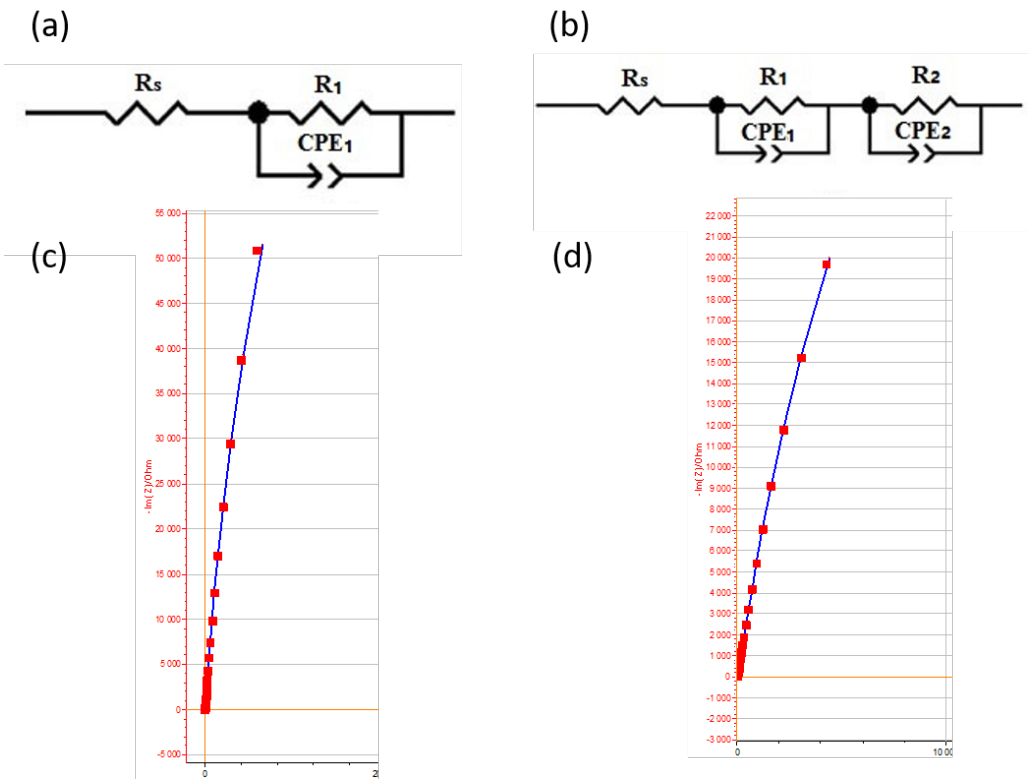

Figure 4.21. Fitting equivalent of (a) ab-plane (b) c-plane. R_s representing the resistance of the solution, a pseudo-capacitance called constant phase angle element and denoted as CPE_1 in parallel with a resistance R_1, which describes the capacitance of the electrical double layer formed between the electrolyte and MAX phases and resistive behavior of charged space respectively. R_2 and CPE_2 represent the resistance and pseudo-capacitance elements of the oxides respectively. (c) and (d) fit diagrams for correspondent (a) and(b) respectively. Red symbols denote the experimental data and blue lines represent fitting result.

According to the results in Nyquist and bode plot, a simple equivalent circuit is satisfying enough for fitting the ab-plane impedance(Fig.4.21c). This circuit (Fig.4.21a) consists in an electrolyte resistance R_s related to the resistance resulting from all electrical contacts in the measuring system, including contribution of the solution. A second element is a pseudo-capacitance called constant phase angle element and denoted as CPE_1 in parallel with a resistance R_1, which describes the capacitance of the electrical double layer formed between the electrolyte and the MAX phases and resistive behavior of charge space, respectively. As the ratio of area between ab-plane and c-plane is extremely large in the raw crystal, the equivalent circuit of raw crystal follows that of ab-plane. Besides, we did not take into account the possible existence of defects, which could considerably complicate the analysis. For that reason, here we decided not to comment this sample in detail. According to the analysis of the plots, a two time-constant circuit is proposed for c-plane(Fig.4.21b and d). In addition to R_1 and CPE_1, R_2

and CPE_2 represent the resistance and pseudo-capacitance elements of the oxides, respectively. A CPE element is used rather than an ideal capacitance in order to take into account the heterogeneous character of the solution/Max phase interface that cannot behave as an ideal capacitor.

The impedance of a CPE is given by the following equation,

$$Z_{CPE} = {}^{1}/_{Q(j\omega)^{\alpha}}$$

Where **ω** is radial frequency, **α** is the exponential factor (0<n<1) and $j=\sqrt{-1}$ is the imaginary number.

In Table 4.2, the solution resistance, R_s, for raw crystal electrode is significantly larger than those for the other two electrodes. This could be ascribed to the different electrode contact area, since the raw crystal is connected by alligator clip and sealed electrodes are connected with Cu wire by silver paste. Fig.4.20b illustrates the variation of the impedance module as a function of frequency. The curve slopes are linked to the α value. The straight curve reveals that in the equivalent circuit there is only one CPE. By EIS analysis, the parameter α was around 0.95. The factor α is an indicator of the substrate interface heterogeneity [45]. When α=1, the equation can reduce to an ideal capacitor with capacitance C while α=0 corresponds to a resistor. In all cases, the basal ab-plane α values around 0.95（Table 4.2）indicate that the surface is slightly heterogeneous. The second element for c-plane is ascribed to the oxide film, which contributes little to the system resistance. As straight line with angle around 60º appeared at high frequency in the Bode plot (Fig.4.20b), the CPE_2 with the α value around 0.5 (Table 4.2) could be considered as a diffusive element. As the micrographs demonstrated in the ripplocation section, one can find many trenches for the fine polished c-plane. Due to the material nature and nanoscale size, these trenches are not detectable by SEM, which could increase the complexity of the electrode surface. In particular, this increased complexity could in turn increase the c-plane electrode geometric area and lead to overestimate the capacitance.

Table 4.2. Equivalent circuit alpha constant of raw crystal, ab-plane and c-plane in 1M H_2SO4, obtained by fitting the EIS diagrams presented in **Fig.4.21**

Electrode type	Surface area cm^2	Rs ohm cm^2	R_1 ohm cm^2	α_1	Q_1 $\mu F/cm^2$	C_{eff1} $\mu F/cm^2$	R_2 ohm cm^2	α_2	Q_2 $\mu F/cm^2$	C_{eff2} $\mu F/cm^2$
Raw	2,67	2,1	$2.2*10^5$	0.94	128,18	83.27				
c-plane	0,076	0.71	$4.6*10^4$	0.93	410	196	56	0.49	8319	7.13
ab-plane	1,81	0,507	$2.85*10^6$	0.95	33.71	19.68				

For electrode resistance, as the property is not intrinsical to the material and is also related to ion/electron conductivity, electrochemical reaction, diffusion of gases, etc. Hence, in electrochemistry, the meaningful unit, ohm.cm^2, is used to exhibit the material property for a given surface. In Table 4.2, the total resistance of c-plane (R_s+R_1+R_2=4.6*10^4 ohm cm^2) is much less than that of ab-plane (R_s+R_1=2.85*10^6 ohm cm^2). Due to the complexity, the ratio is much larger that the obtained value in polarization and Nyquist plot, but it still exhibits the significant advantage of ab-plane. As noted above, the different circuits reveal different electrochemical behaviors. In the aqueous solution, at OCP, the c-plane is easily oxidized, as reflected by the EIS analysis and an equivalent circuit involving a second parallel connection. Such a phenomenon is associated with the corrosion mechanism that will be discussed in the next section. Moreover, defective structure and atomic arrangement makes the c-plane less resistant.

4.4 Corrosion mechanism analysis

Electrochemical measurements exhibit significant differences in corrosion resistance between ab-plane and c-plane. It is no surprise that this anisotropy has been proved in other properties of MAX phases. Owing to the large size single crystals, we demonstrate, the first time, the direct electrochemical results. In addition to the large current ratio between c-plane and ab-plane, at Ecorr, although the EDX analysis cannot give a convincing confirmation, EIS measurements suggested the existence of an oxide film on the c-plane. Previously, it has been proved that MAX phases can provide the A element to form nanoscale nitrides and oxides with the presence of impurity elements (i.e. O and N)[20,46,47]. Consequently, the chemical sensitivity of c-plane is generally attributed to the presence of atom A. The investigation of Liao et al. gives us the theoretical explanation [20]. Through a first-principle calculation, it reveals that the vacancy formation energy of Al is lower than those of M and C, and the vacancy formation energy with impurity is lower than those without impurity at 1600K. It is linked to the intrinsic property of Al and, most importantly, to the weak bonds between Al layer and MX slabs. In Fig.4.22, the water green zone denotes the open space region in Ti_2AlC structure, involving almost all intrinsic defects. I(tri) ,I(pri)and I(oct) represent the interstitial sites with high symmetry in Al plane, respectively (smallest atoms in Fig.4.22). The defective structure

stability calculation shows that the energy sum of the vacancy formation in these three sites is the lowest among all the elements in MAX phase. Hence, it could give a convincing explanation to the higher reactivity of Al than other elements in MAX phases in most of the reactions, such as in molten salt[48]. In our case, the electrochemical polarization increases the reactivity of the whole structure, with similar effect to that of the high temperature [20], while the oxygen in the solution could serve as inducing factor to reduce the Al vacancy formation energy to form aluminum oxides. This could theoretically explain the role of Al in the reaction.

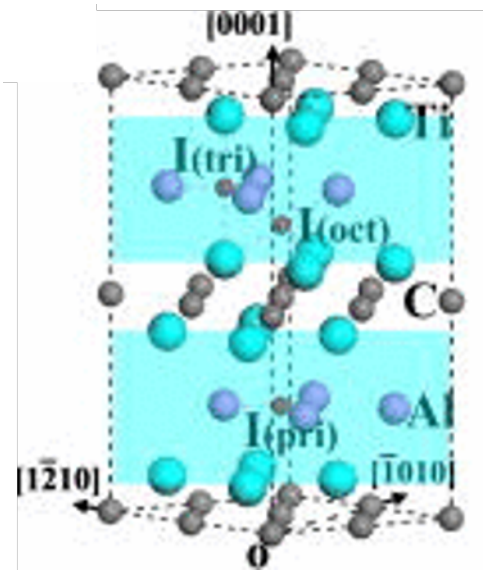

Figure 4.22. (a) Schematic defect-in-supercell model of possible interstitial sites (smallest atoms) in Ti_2AlC

However, this significant argument could not satisfy our exploration of the anisotropy. Other theories, typically explaining the anisotropic behavior, also attract our attention. According to the electrode potential table [49], the potential from Al^{3+} to Al is lower than that from Cr^{3+} to Cr. Hence Al is easier to be oxidized than Cr in the polarization, which could not explain the presence of the aluminum oxides at E_{corr} but can explain the current difference.

Another theory, Surface energy, is typically referred to explain the anisotropy behavior of hexagonal close compacted structure [15,50,51]. Despite the absence of available methods to calculate the surface energy of any plane except (0001) in MAX phase, a preliminary estimation might still be useful in order to compare the various orientations and to understand the anisotropic behavior. Surface energy is of great importance to characterize metal surface energy, defined as the additional free energy per unit area for given crystalline plane. It is expressed as below [50]:

$$\gamma = \frac{\Delta E}{\Delta S} = \frac{\sum_\alpha I_\alpha^d E_\alpha}{2S}$$

where ΔE denotes additional energy to form new surface, and S is the surface area of related plane.α indicates the bond type. E_α is bond energy. I^d_α represents the number of bond α obtained by simulation DBAM(dangling bond analysis method).

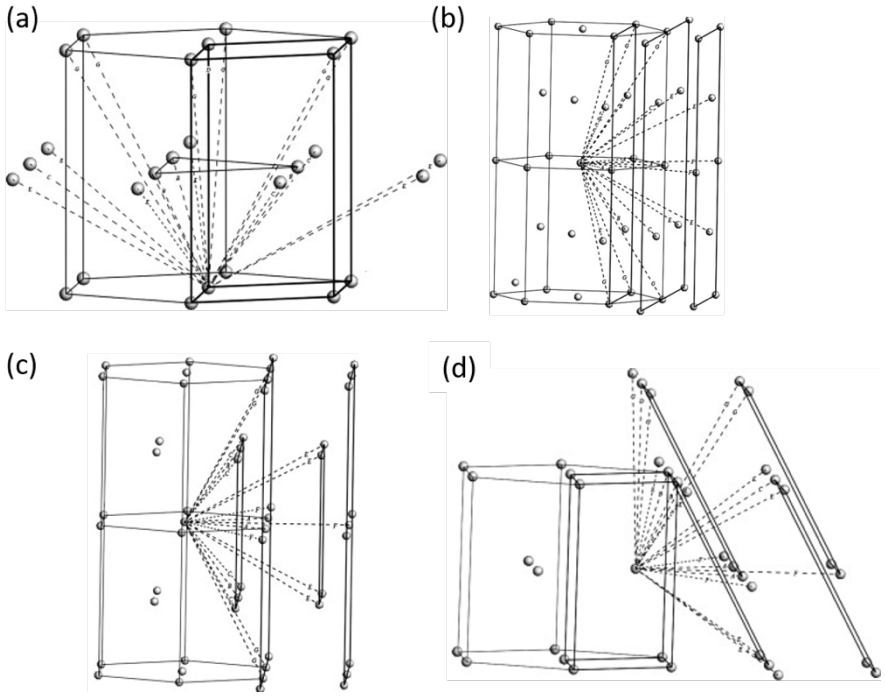

Figure 4.23. Spatial distribution of dangling bonds of hcp structure on (a)(001) plane(b) (100)plane(c)(110) plane(d)(011)[50]

Fig.4.23 shows the spatial distribution of dangling bonds of hcp structure on the four compared planes, where the type and number of bonds are defined. Calculated results in the literature demonstrate a strong anisotropy and the surface energy order of planes is importantly linked to the c/a ratio[50].For metals with c/a larger than 1.624, the energy result is $\gamma_{(001)} < \gamma_{(011)} < \gamma_{(010)} < \gamma_{(110)}$. In our case, since MAX phase c/a (i.e. 4.4[36]) is much larger than 1.624, the anisotropy of MAX phase is definitely much stronger than that of a typical hcp structure. Other simulations give the similar arguments that high atom density planes offer higher corrosion resistance than lower density ones [52]. With the high ratio of c/a, reasonably, the long bonding and fewer neighbor atoms in other planes (e.g.(10-10)) could result in lower surface energy. Consequently, the resistance of **ab**-plane (0001) is expected to be much higher than that of a c-plane.

4.5 Conclusion

We show that the shape and morphology of defects created my mechanically polishing large Cr_2AlC single crystals are consistent with the nucleation of bulk ripplocations. It is difficult to reconcile the deep trenches - that are always parallel to the basal planes - with the nucleation and growth of basal dislocations or stacking faults. Given that in the MAX phases the only defects that have been linked to their mechanical deformation have, incorrectly, been basal dislocations, it follows that the fact that the results presented here are totally incompatible with their existence is one more piece of evidence that anybody advocating their existence and role would have to contend with and explain. This is especially true given that the evidence presented herein is consistent with the existence of bulk ripplocations.

The anisotropic anti-corrosion behavior of Cr_2AlC single crystals was investigated by electrochemical methods for the first time. A substantially anisotropic behavior has been evidenced by recording polarization curves, studying the morphology by SEM and investigating the possible impedance structure by fitting EIS data. Indeed, the ab-plane (000l) exhibits higher anti-corrosion properties due to compact Cr_2C layers, no sensitive Al atoms and a lower surface energy. In other words, the c-plane is more vulnerable, due to the continuous presence of easily removable Al atoms and a corresponding higher surface energy. Concrete results can be summarized as follows: (1) the corrosion current density of the c-plane is about 15 times higher than that of the ab-plane. (2) Furthermore, the ab-plane impedance modulus is almost more than 20 times higher than that of c-plane. (4) At last, for c-plane orientation, the presence of an oxide film was also assumed in order to explain the equivalent circuit required for fitting the data. The surface energy and other crucial elements play important roles in corrosion resistance of different crystalline orientations. Further studies are certainly required in order to complete the electrochemical investigation of Cr_2AlC crystals as well as that of other single crystals of the MAX phase family. A reliable determination of the surface energies should also greatly help one to put our qualitative remarks and conclusions on a firmer quantitative footing.

Reference

[1]. M.W. Barsoum, T. El-Raghy, Synthesis and characterization of a remarkable ceramic: Ti_3SiC_2, J. Am. Ceram. Soc. 79, 1953(1996)

[2]. Waheed, A. F. & Barsoum, M. W. Preliminary report on the electrochemical behavior of Ti_3SiC_2. J. Mat. Sci. Lett. 8, 9–10(1999).

[3]. Zhu, M., Wang, R., Chen, C., Zhang, H. B. & Zhang, G. J. Comparison of corrosion behavior of Ti_3SiC_2 and Ti_3AlC_2 in NaCl solutions with Ti. *Ceram. Int.* 43 (2017) 5708–5714.

[4]. Jovic, V. D., Jovic, B. M., Gupta, S. & El-raghy, T. Corrosion behavior of select MAX phases in NaOH , HCl and H_2SO_4. *Corros. Sci.* 48 (2006)4274–4282.

[5]. Jovic, V. D., Barsoum, M. W., Jovic, B. M., Ganguly, A. & El-raghy, T. Corrosion Behavior of Ti_3GeC_2 and Ti_2AlN in 1M NaOH. *J. Electrochem. Soc.* 153 (2006) B238–243

[6]. Travaglini, J., Barsoum, M. W., Jovic, V. & El-Raghy, T. The corrosion behaviour of Ti_3SiC_2 in common acids and dilute NaOH. *Corros. Sci.* 45, 1313–1327(2003).

[7]. Jović, B. M. *et al.* Ru layers electrodeposited onto highly stable Ti2AlC substrates as cathodes for hydrogen evolution in sulfuric acid solutions. *J. Electroanal. Chem.* 766, 78–86 (2016).

[8]. Li, D., Liang, Y., Liu, X. & Zhou, Y. Corrosion behavior of Ti_3AlC_2 in NaOH and H2SO4. *J. Eur. Ceram. Soc.* 30, 3227–3234 (2010).

[9] Jovic, V. D. & Barsoum, M. W. Corrosion Behavior and Passive Film Characteristics Formed on Ti , Ti_3SiC_2 , and Ti_4AlN_3 in H_2SO_4 and HCl. 2–7 (2004).

[10]. Xie, J., Wang, X., Li, A., Li, F. & Zhou, Y. Corrosion behavior of selected $M_{n+1}AXn$ phases in hot concentrated HCl solution : Effect of A element and MX layer. *Corros. Sci.* 60, 129–135(2012).

[11]. P. Eklund, M. Bugnet, V. Mauchamp, S. Dubois, C. Tromas, J. Jensen, L. Piraux, L. Gence, M. Jaouen, T. Cabioch. Epitaxial growth and electrical transport properties of Cr2GeC thin films. *Phys. Rev. B - Condens. Matter Mater. Phys.* 84, 1–9 (2011).

[12]. Ouisse, T. *et al.* Magnetotransport properties of nearly-free electrons in two-dimensional hexagonal metals and application to the $M_{n+1}AX_n$ phases. *Phys. Rev. B - Condens. Matter Mater. Phys.* 92, 1–12 (2015).

[13]. V. Mauchamp, W. Yu, L. Gence, L. Piraux, T. Cabioc'h, V. Gauthier, P. Eklund and S. Dubois. Anisotropy of the resistivity and charge-carrier sign in nanolaminated Ti_2AlC: Experiment and ab initio calculations. *Phys. Rev. B - Condens. Matter Mater. Phys.* 87, 1–7 (2013).

[14]. Du, Y. *et al.* Anisotropic corrosion of Ti_2AlC and Ti_3AlC_2 in supercritical water at 500°C. *Ceram. Int.* 43, 7166–7171 (2017).

[15]. Bland, L. G., Gusieva, K. & Scully, J. R. Effect of Crystallographic Orientation on the Corrosion of Magnesium: Comparison of Film Forming and Bare Crystal Facets using Electrochemical Impedance and Raman Spectroscopy. *Electrochim. Acta* 227, 136–151 (2017).

[16] . Music, D., Sun, Z., Ahuja, R. & Schneider, J. M. Surface energy of $M_2AC(0001)$ determined by density functional theory (M=Ti,V,Cr; A=Al,Ga,Ge). *Surf. Sci.* 601, 896–899 (2007).

[17]. N. Li, R. Sakidja, W.-Y. Ching, Oxidation of Cr_2AlC (0001): Insights From Ab Initio Calculations. JOM. 65, 1487 (2013)

[18]. Sun ZM, Ahuja R. Ab initio study of the Cr_2AlC (0001) surface. Appl. Phys. Lett. 88, 161913(2006).

[19]. Wang, L. *et al.* density functional study Stable M_2AlC (0001) surfaces (M = Ti , V and Cr) by first-principles investigation. J. Phys. Condens. Matter. 20, 225006(2008).

[20]. T. Liao, J.Y. Wang, Y.C. Zhou, First-principles investigation of intrinsic defects and (N, O) impurity atom stimulated Al vacancy in Ti_2AlC, Appl Phys. Lett. 93 (2008).

[21]. Ghidiu, M., Lukatskaya, M. R., Zhao, M.-Q., Gogotsi, Y. & Barsoum, M. W. Conductive two-dimensional titanium carbide `clay' with high volumetric capacitance. *Nature* 516, 78–81 (2014).

[22]. Naguib, M. *et al.* Two-dimensional transition metal carbides. *ACS Nano* 6, 1322–1331 (2012).

[23]. Naguib, M. *et al.* Two-dimensional nanocrystals produced by exfoliation of Ti_3AlC_2. *Adv. Mater.* 23, 4248–4253 (2011).

[24]. Christoffersen, R. & Kronenberg, A. K. Dislocation interactions in experimentally deformed biotite. *J. Struct. Geol.* 15, 1077–1095 (1993).

[25]. Kronenberg, A. K., Kirby, S. H. & Pinkston, J. Basal slip and mechanical anisotropy of biotite. *J. Geophys. Res.* 95, 19257 (1990).

[26]. Mares, V. M. & Kronenberg, A. K. Experimental deformation of muscovite. *J. Struct. Geol.* 15, 1061–1075 (1993).

[27]. Barsoum, M. W., Zhen, T., Kalidindi, S. R., Radovic, M. & Murugaiah, A. Fully reversible, dislocation-based compressive deformation of Ti_3SiC_2 to 1GPa. *Nat. Mater.* 2, 107–111 (2003).

[28]. Freise EJ, Kelly A. Twinning in graphite. *Proc. Phys. Soc. A*. 264,269-276(1961).

[29]. Barsoum, M. W. & Tucker, G. J. Deformation of layered solids: Ripplocations not basal dislocations. *Scr. Mater.* 139, 166–172 (2017).

[30]. S. Groh, E.B. Marin, M.F. Horstemeyer, D.J. Bammann, Dislocation motion in magnesium: a study by molecular statics and molecular dynamics, Model. Simul. Mater. Sci. Eng. 17 (2009) 75009. doi:10.1088/0965-0393/17/7/075009.

[31]. Hess, J.B., Barrett, C.S.. Structure and nature of kink bands in zinc. Met. Trans. 185, (1949)599-606.

[32]. J. W. Cosgrove, The association of folds and fractures and the link between folding, fracturing and fluid flow during the evolution of a fold–thrust belt: a brief review. Geological Society, London, Special Publications, 421, 41-68, 12 May 2015,

[33]. M.W. Barsoum, A. Murugaiah, S.R. Kalidindi, T. Zhen, Kinking nonlinear elastic solids, nanoindentations, and geology, Phys. Rev. Lett. 92 (2004) 255508–1. doi:10.1103/PhysRevLett.92.255508.

[34]. Kushima, A., Qian, X., Zhao, P., Zhang, S. & Li, J. Ripplocations in van der Waals layers. *Nano Lett.* 15, 1302–1308 (2015).

[35]. Gruber, J. *et al.* Evidence for Bulk Ripplocations in Layered Solids. *Sci. Rep.* 6, 33451 (2016).

[36]. Ouisse, T. *et al.* High temperature solution growth and characterization of Cr_2AlC single crystals. *J. Cryst. Growth* 384, 88–95 (2013).

[37]. X. Liu, P.K. Chu, C. Ding, Surface modification of titanium, titanium alloys, and related materials for biomedical applications, Mater. Sci. Eng. R Reports 47, 49–121(2004)

[38]. Basu, S. & Barsoum, M. W. Deformation micromechanisms of ZnO single crystals as determined from spherical nanoindentation stress–strain curves. *J. Mater. Res.* 22, 2470–2477 (2007).

[39]. Griggs J, Lang A, Gruber J, Tucker G, Taheri M, Barsoum MW. *Acta Mater.* 2017,131 141-155.

[40]. H. Tang and D.C. Martin, J. Mat. Sci. **38** (2003) 803– 815

[41]. Basu S, Barsoum MW. On Spherical Nanoindentations, Kinking Nonlinear Elasticity of Mica Single Crystals and Their Geological Implications. J Struct Geology. 2009;31 791–801.

[42]. Barsoum MW, Murugaiah A, Kalidindi SR, Gogotsi Y. Kink Bands, Nonlinear Elasticity and Nanoindentations in Graphite. Carbon. 2004;42:1435-45.

[43]. R. Gassilloud, J. Michler, C. Ballif, Ph. Gasser and P. Schmuki, Electrochimica Acta **51** (2006) 2182–2187

[44]. A.J. Bard, L.R. Faulkner, Fundamentals and applications, Electrochemical Methods, John Wiley and Sons, Inc., New York, 2001, pp. 92-132.

[45]. B. Hirschorn, M.E. Orazem, B. Tribollet, V. Vivier, I. Frateur, M. Musiani, Determination of effective capacitance and film thickness from constantphase-element parameters, Electrochimica Acta. 55, 6218–6227(2010).

[46]. T. Liao, J. Wang, Y. Zhou, Ab initio modeling of the formation and migration of monovacancies in Ti2AlC, Scr. Mater. 59 (2008) 854–857.

[47]. J. Rosen, P.O.Å. Persson, M. Ionescu, A. Kondyurin, D.R. McKenzie, M.M.M. Bilek, Oxygen incorporation in Ti2AlC thin films, Appl. Phys. Lett. 92 (2008) 64102.

[48]. Naguib, M. et al. On the topotactic transformation of Ti_2AlC into a Ti–C–O–F cubic phase by heating in molten lithium fluoride in air. J. Am. Ceram. Soc. 94 (2011). 4556–4561

[49]. Lide, David R., ed. (2006). CRC Handbook of Chemistry and Physics (87th ed.). Boca Raton, FL: CRC Press. ISBN 0-8493-0487-3.

[50]. B.Q. Fu, W. Liu, Z.L. Li, Calculation of the surface energy of hcp-metals with the empirical electron theory, Appl. Surf. Sci. 255 (2009) 9348–9357. doi:10.1016/j.apsusc.2009.07.034.

[51]. J.-M. Zhang, D.-D. Wang, K.-W. Xu, Calculation of the surface energy of hcp metals by using the modified embedded atom method, Appl. Surf. Sci. 253 (2006) 2018–2024.

[52]. M. Hoseini, A. Shahryari, S. Omanovic, J.A. Szpunar, Comparative effect of grain size and texture on the corrosion behaviour of commercially pure titanium processed by equal channel angular pressing, Corros. Sci. 51, 3064–3067 (2009)

General conclusion and perspectives

In the present thesis, we reported our investigation of the chemical reactivity of MAX phase single crystals. As discussed in all chapters, the unique features displayed by such crystals are strongly connected to their highly anisotropic structure and the weak bonding between the A layers and the $M_{n+1}X_n$ layers. Chemical reactivity is dominated by the reactivity of the A atoms. The availability of large size single crystals made possible to directly assess the anisotropy of this chemical reactivity for the first time. We also showed that the prominent role played by the A element in initiating chemical transformations could lead to the synthesis of original materials.

One objective of this work was to synthesize large-scale MXenes from MAX phase single crystals by selectively removing the A atoms. Experiments were carried out in HF, HF-based solutions, in electrochemical etching conditions, etc. The most effective approach is proven to rely on the use of HF-based solutions. Our study indicates that the H^+ ions break the bonds and the F^- ions serve as the complexing agent during extraction. We used DRX and Raman spectroscopy to gain insight into the etching process mechanisms. As expected, the latter starts from the surface to the bulk. DRX reveals that the M-A interlayer bonds are broken and substituted by functional groups. This process results in the in-plane rotation of MX layers around the c-axis, leading to a disorder which increases with time. This leads in turn to the disaggregation of the surface structural order and makes difficult to produce large-area MXenes.

In order to find an alternative route for synthesizing MXenes, we studied high-temperature chlorination. We focused on finding conditions avoiding the carbonization which was achieved in previous published work. It turns out that under exposition to chlorine and hydrogen, Cr_2AlC, V_2AlC and Ti_3SiC_2 single crystals are not converted into MXenes but into highly porous chromium, vanadium or titanium carbides. We focused on porous Cr_3C_2 and showed that we can attain a porosity not obtained in the previous work, the latter involving a totally different fabrication process and not relying on the use of MAX phases. Our results show that the chlorination process could etch the MAX phases, starting from a loss of the A element to form chromium carbides, and then forms graphite after a longer exposition time or/and at a higher temperature. Porosity strongly depends on the reaction temperature, and the converted layer thickness is dominated by the reaction time. Eventually, we found that the resistivity of our porous layers still exhibits the same order of magnitude as previous data on bulk materials,

and we measured a magnetoresistance linear component which we attribute to the porosity itself.

Our last reactivity study deals with electrochemical etching in H_2SO_4 solution. Sealed Cr_2AlC electrodes with different exposed surfaces show significant differences. We systematically investigated the anisotropic behavior of corrosion resistance through electrochemical polarization and impedance spectroscopy. We evidenced the strongly anisotropic reactivity, corrosion being less effective when exposing an ab-plane rather than a c-plane. Moreover, we proposed adapted equivalent circuits in order to simulate the electrochemical reaction and to explain the corrosion mechanism. A simple circuit with one time constant was applied to reproduce the MAX phase data on the ab-plane. More complex equivalent circuits were required for the c-plane. We attribute these differences to the reactivity of the A element and to the way it is inserted in the anisotropic MAX phase structure. This results in orientation-dependent corrosion mechanisms. Furthermore, we show that the shape and morphology of defects created by mechanically polishing large Cr_2AlC single crystals are revealed by the electrochemical etching and are consistent with the nucleation of recently discovered defects called ripplocations. Our electrochemical polarization results are thus used as indirect evidence for the existence of these defects, which are not dislocations and which are specific to lamellar compounds.

Chemical reactivity of materials as particular as MAX phases has already attracted a lot of interest. Our motivation for working on single crystals was that many aspects, and most of all the anisotropy, could be better grasped that way than by relying on the usual powders and polycrystalline samples. The panel of experiments that we chose to carry on was necessarily limited. However, it did not only reveal the specificity of the A element (here mainly Al), but the combined roles played by this element and the structure into which it is embedded in order to determine the overall chemical reactivity and possible transformations. Our hope is that our results will motivate future and systematic investigations, extending our own attempts to the use of other acids, other electrochemical conditions, etc., so as to establish a bulk of knowledge which should in turn have a useful impact on applications. In the synthesis of MXenes, using large surface areas but thin layers instead of large size single crystals could probably be more suited to selective exfoliation. Besides, our crystals were not defect-free, so that data obtained from imperfect platelet edges could certainly be improved by using faces not affected by surface defects, and lead to anisotropy parameters closer to the theoretical ones. It is also clear that improving the equivalent circuits proposed in this work might give a more physical insight into the mechanisms responsible for the corrosion process of MAX phase single crystals. Data about

the surface energy dependence on orientation are lacking, and they could be helpful for better understanding the anisotropy of some MAX phase properties, including the chemical reactivity.

Résumé de la thèse en français

Etudes de la réactivité chimique des monocristaux de phase MAX

1. Introduction

A ce jour, les dispositifs électroniques s`inscrivent toujours dans des besoins croissants. Les conducteurs sont massivement employés tels que or, argent et des matériaux coûteux et rares, etc. Parmi les candidats potentiels, en particulier, les phases MAX sont considérées prometteuses. De formule $M_{n+1}AX_n$ (n= 1, 2 ou 3), elles forment une famille de carbures et nitrures ternaires nano-lamellaires où M est un métal de transition, A est généralement un élément du groupe 13-16 et X est le carbone ou l'azote ou tous les deux [1]. Elles possèdent une combinaison excellente de propriétés des métaux et céramiques, par exemple stabilité chimique, élasticité mécanique, conductivité thermique et électrique, usinabilité, etc [2-4]. Elles ont suscité un intérêt croissant dans le domaine scientifique de la science des matériaux. Leurs propriétés exceptionnelles laissent augurer de nombreuses applications dans le futur [5-9]. Certaines sont déjà appliquées dans l`industrie [5,10].

1.1 Objectifs et contribution

Cette thèse est centrée sur la réactivité chimique des monocristaux de phase MAX et met à profit la méthode de synthèse développée au LMGP. Elle apporte quelques points de vue originaux sur la stabilité chimique et les possibilités de conversion de ces phases en nouveaux composés. L'étude de la réactivité chimique des phases MAX constitue en effet le sujet principal de la présente thèse. La sensibilité chimique des atomes A domine la réactivité chimique générale des phases MAX en raison sa haute réactivité par rapport aux autres éléments. En conséquence, la réactivité des phases MAX est fortement liée à la stabilité chimique des atomes A. Les travaux réalisés concernent précisément les problématiques liées aux aspects de réactivité chimique: Comment les monocristaux de Cr_2AlC se comportent-ils dans les acides et les bases communs? Comment les mêmes cristaux se comportent-ils dans des environnements agressifs à haute température, telles que la chloruration à haute T? Quel est le rôle joué par la structure nano-lamellaire et les atomes Al des phases MAX dans chacune des réactions chimiques impliquées dans de telles conditions?

Afin de trouver les réponses, les sujets qui ont été abordés sont 1) Synthèse de MXenes à partir de monocristaux de phases MAX basée sur la réactivité chimique des atomes A. Le but est de synthétiser des MXenes de grande surface en profitant de monocristaux de grande taille. Cela nous donne une étude approfondie des connaissances de la sélection et du mécanisme de l'agent de gravure. 2) Réactivité chimique lors de la chloruration: le but initial est d'obtenir le MXene en tant que produit intermédiaire dans la réaction. Toutefois, nous présentons un autre dérivé attractif des phases MAX, les carbures de chrome poreux qui présentent plusieurs propriétés intéressantes. 3) Résistance anisotropique en électrochimie. Les monocristaux de grande taille sont utilisés pour la première fois comme électrode pour les tests électrochimiques. Une anisotropie significative est démontrée par polarisation électrochimique et EIS.

1.2 La structure

Les phases $M_{n+1}AX_n$ ont une structure symétrique et hexagonale, qui appartient au groupe spatial D^4_{6h} (P^6_3 / mmc), avec la répétition de deux unités de formule par unité de cellule MX et A. Dans chaque cas, des couches $M_{n+1}X_n$ compactes adjacentes et fermées sont séparées par une couche de groupe A pure, et les atomes X occupent des sites octaédriques entre les couches M [1]. La structure en couches de ces composés est montrée à la Fig.1. Les unités M_6X partagent leurs bords et sont les mêmes que celles observées dans la structure de sel gemme. Les atomes du groupe A sont situés au centre des prismes trigonaux qui sont plus grands que les sites octaédriques et permettent ainsi de loger de grands atomes A. La structure montre une forte anisotropie où le rapport entre paramètre de maille c/a est plus que 4. Les liaisons MA sont plus longs que ceux de MX qui rend les atomes A plus réactifs. En conséquence, la réactivité chimique des phases MAX est principalement dominée par la sensibilité chimique des atomes A.

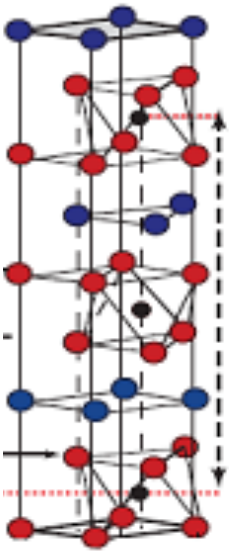

Figure 1. Structure de phase M_2AX[1]

1.3 MXenes

Les MXenes sont des composés bidimensionnels transformés des phases MAX. La méthode générale de synthèse est la gravure dans HF concentré (Fig.2a). Cette méthode a été proposée par le groupe de Michel Barsoum à Drexel [11]. La Fig.2b montre la morphologie des Mxenes [12]. Les feuillets de MXenes sont entrelacés avec des liaisons Van der Waals ou des liaisons hydrogène au lieu des liaisons M-A dans les phases MAX. ils ont la même structure que les couches MX dans les phases MAX. Des feuillets MX de quelques nanomètres d'épaisseur (caractère bidimensionnel), à structure hexagonale, comportent ainsi les atomes X situés sur les sites octaédriques du maillage formé par l'élément M. Il est important de noter qu'une fois que les feuillets MX sont séparés, ils ont à la surface des éléments de terminaison T qui occupent les sites vides laissés par l'élément A.

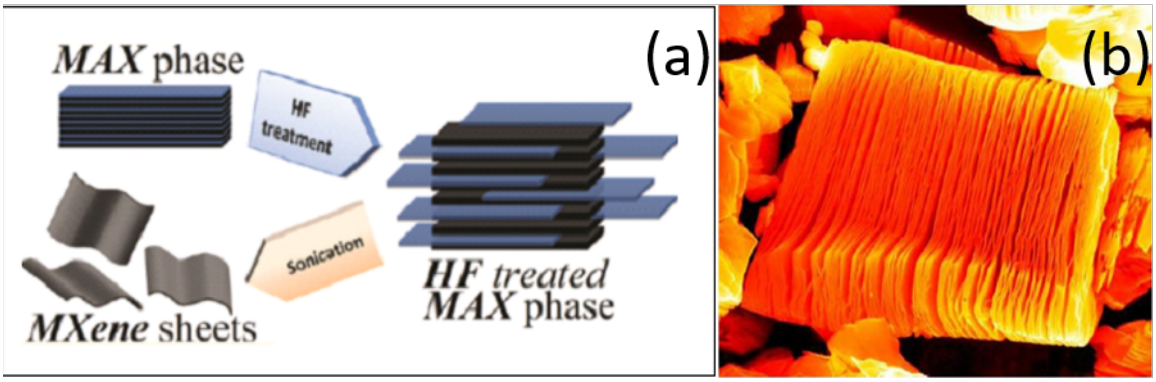

Figure 2.(a) Processus de synthèse des Mxenes à aprtor de phases MAX en attaquant dans HF et ensuite en utilisant des ultra-sons [11] (b) image MEB de Ti_2C obtenu par gravure HF [12]

Les couches 2D présentent d'excellentes caractéristiques en termes de conductivité électrique et thermique et présentent parfois de meilleures propriétés que leurs phases mères. En outre, les MXenes ont un caractère hydrophile. Ils sont promis à des applications dans le domaine de stockage d`énergie et des dispositifs électroniques.

1.4 Croissance de monocristaux de phases MAX

Les phases MAX employées dans la thèse sont sous forme massive et monocristalline. Les monocristaux au LMGP sont tous synthétisés par la méthode de croissance en solution à haute température. Ici nous prenons l'exemple de la synthèse de Cr_2AlC, qui est le composé principal étudié dans cette thèse. Les appareillages expérimentaux sont montrés dessous.

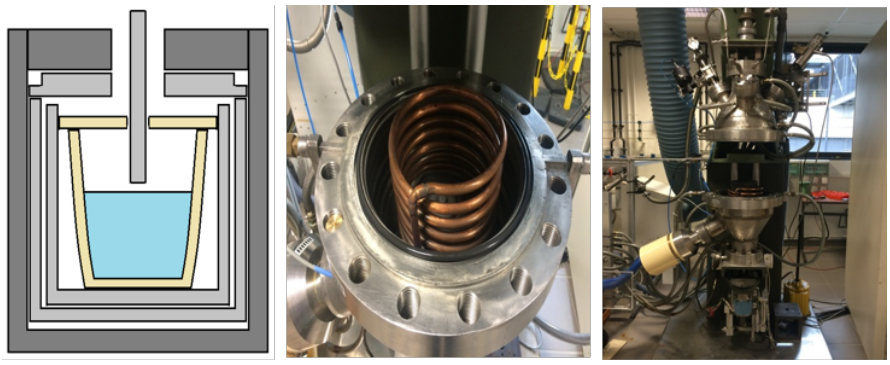

Figure 3. Appareil expérimental: a) Schéma de montage du creuset, b) bobine inductive pour le chauffage, c) vue complète du réacteur de croissance.

Les poudres de Cr et Al sont d'abord fondues dans un creuset en alumine qui est positionné à l'intérieur des creusets en graphite double, pour former la solution de croissance, avec un rapport atomique x_{Al} / x_{Cr} d'environ 8/13. Un couvercle de graphite isolant protecteur est réglé pour réduire le rayonnement thermique (Fig.3a). Le creuset est chauffé par un courant d'induction fourni par une bobine de cuivre (Fig.3b). Et toutes les étapes ont lieu dans le réacteur montré dans la Fig.3c. Ensuite, le mélange binaire est chauffé rapidement à 1000°C sous vide. Selon la vitesse de chauffage, cette étape est maintenue pendant environ 30 minutes. À 1000°C, le gaz protecteur Argon est introduit pour réduire l'évaporation.

Ensuite, le creuset est chauffé à 1600 °C lentement pendant 2 heures. La croissance commence à partir des mélanges binaires de granulés de Cr et Al avec la composition proche de Al_8Cr_5. Au-delà du point de fusion d'Al, dans le diagramme Cr-Al-C ternaire, une surface liquide se forme le long de la ligne Cr-Al dans la section isotherme [13]. Dans la gamme de température autour de 1400 ° C, à partir d'un rapport de fraction x_{Cr} = 0,4 dans le binaire de Cr-Al, une petite quantité de C pourrait entraîner une phase liquide d'équilibre avec Al_4C_3 seul, Al_4C_3 et Cr_2AlC,

Cr_2AlC seul ou Cr_2AlC et Cr_7C_3 [13]. Il offre la possibilité d'obtenir Cr_2AlC à partir de la phase liquide. Ici, la source de carbone est une tige de graphite. A une température supérieure à 1600 ° C qui favorise la dissolution du carbone dans la solution, la tige de graphite rotative motorisée est trempée dans la solution pour diffuser le carbone dans le système jusqu'à obtention d'une fraction atomique x_C légèrement inférieure à 0,1. Par la suite, la température diminue lentement pour éviter la nucléation de nombreux cristaux de Cr_2AlC en favorisant les phénomènes de mûrissement d'Ostwald [14]. L'ensemble du processus de croissance est illustré à la Fig.4. La vitesse de refroidissement habituelle est de 2-3°C par heure. Le processus de refroidissement lent est arrêté à 1250°C, puis l'échantillon retourne à la température ambiante avec un refroidissement naturel.

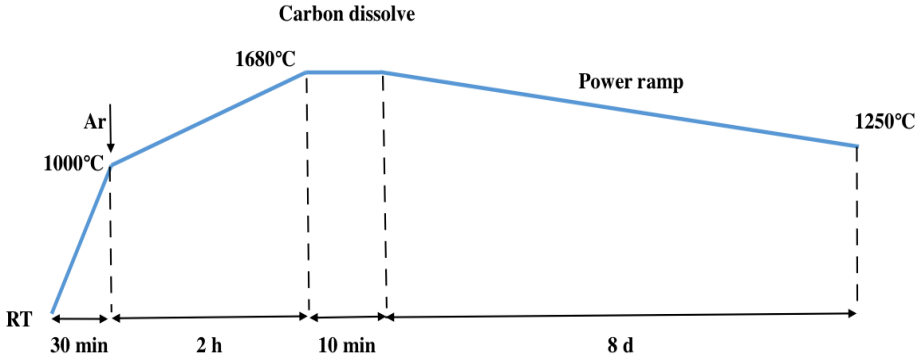

Figure 4. Processus entier de la croissance en solution à haute température.

La Figure 5 montre la masse de Cr_2AlC retirée du creuset d'alumine après refroidissement. Un gros bloc est formé par le flux solidifié (Fig.5a), avec des cristaux piégés à l'intérieur. Du fait de la nucléation spontanée et de la croissance cristalline, après une attaque chimique dans du HCl dilué, les cristaux sont régulièrement imbriqués (Fig.5b) et peuvent ensuite être extraits du flux solidifié dissous.

Enfin, les cristaux sont passés aux ultra-sons dans de l'eau distillée et de l'éthanol. La surface des monocristaux est de quelques cm^2 (Fig.5c). Les épaisseurs des cristaux varient principalement de 100µm à 1000µm.

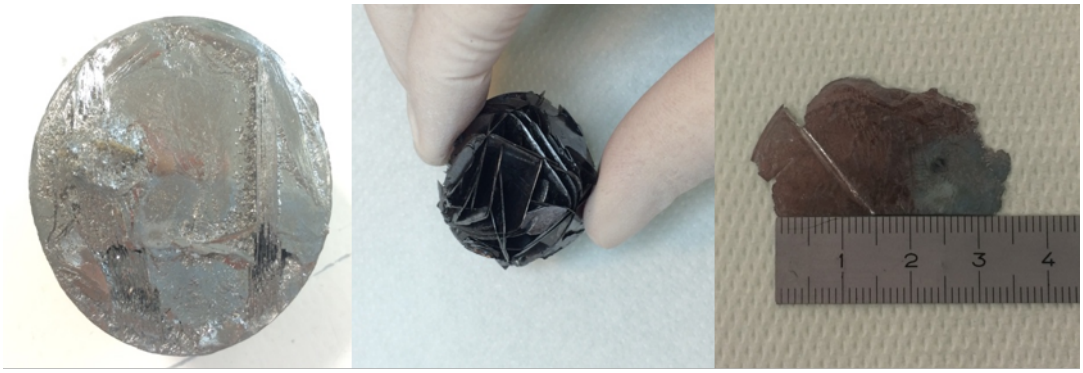

Figure 5. Différentes étapes après le refroidissement (Cr_2AlC): a) en masse b) après la gravure au HCl c) un échantillon typique après passage aux ultra-sons.

2. Exfoliation de la phase MAX en Mxene

2.1 Introduction

A température élevée, du fait que les liaisons M-A sont plus faibles que les liaisons M-X, les phases MAX perdent sélectivement l'élément A. La température élevée induit la transformation de la structure de la couche MX en structure de type sel gemme 3D MX [15,16]. Dans cette décomposition à haute température, les couches MX perdent leur structure lamellaire pour adopter celle des pierres précieuses, ce qui les rend inutilisables. Dans cette section, nous avons essayé d'exfolier des monocristaux des phases MAX pour former des Mxenes de grande surface. En plus de la méthode par gravure d'HF, nous avons testé d'autres solutions chimiques pour atteindre ce but.

2.2 Détails expérimentaux

Les essaies sont réalisés dans les solutions chimiques. Nous avons trempé les phases MAX V_2AlC dans HF à différents concentrations, acides classiques (ex. HCl, H_2SO_4 et HNO_3), base classique NaOH sans et avec tampon ammoniaque. Les échantillons traités sont analysés par la méthode DRX Laue (diffractomètre Bruker D8 Advance avec rayonnement Cu Kα1 (λ= 1.540598 nm) en configuration Bragg-Brentano), Spectroscopie Raman (spectromètre Jobin Yvon / Horiba Labram), ICP (ICP-MS), et MEB (FEG-SEM, ZEISS ULTRA 55) afin d'étudier le processus de réaction et sa sélectivité de gravure vis-à-vis de l'élément A.

2.3 Résultats et discussion

Les résultats sont démontrés dans Figure 6.

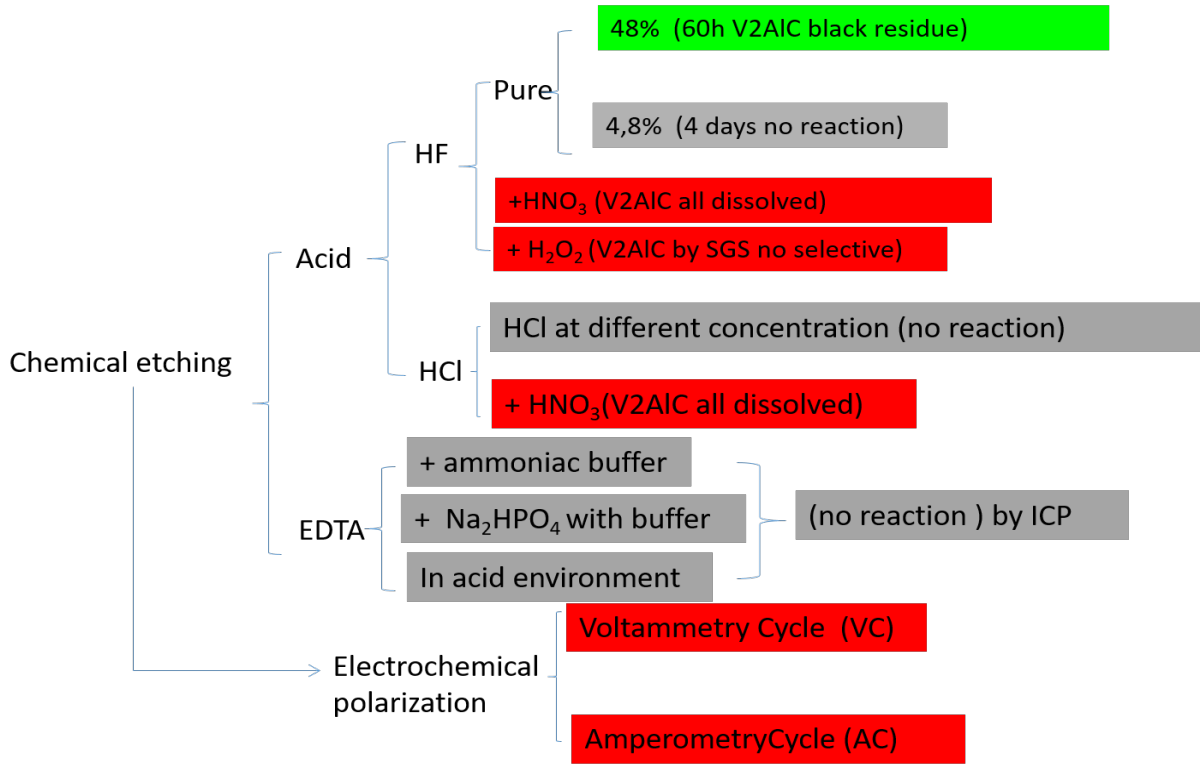

Figure 6. Schéma des différentes méthodes chimiques utilisées pour la gravure de V_2AlC et les résultats associés

HF et autres solutions corrosives sont testés pour la faisabilité d'une attaque chimique sélective de l'élément A. Les composés de V_2AlC sont stables dans HCl, H_2SO_4 et d'autres solutions corrosives conventionnelles. Le réactif oxydant, tel que HNO_3 et H_2O_2, peut réagir avec V_2AlC, mais conduire à un processus incontrôlé. Parmi les différentes solutions, HF se révèle être l'approche la plus efficace. En particulier, la gravure efficace dépend des éléments essentiels suivants : l'agent qui coupe les liaisons M-A et l'agent complexant. Dans cette section, les représentants sont H^+ et F^-, ce qui s'est apparu la seule combinaison efficace jusqu'à présente. En outre, le temps, la température et la concentration, même l'agitation pourraient grandement influencer le processus de gravure.

Les monocristaux V_2AlC conservent une brillance métallique pendant une durée de 24 heures. La Figure 7 montre la morphologie de la surface des monocristaux de V_2AlC après un traitement de 16h dans HF. Les échantillons conservent toujours la forme initiale. Cependant, le bord du cristal perd sa brillance et le centre maintient un brillant métallique. L'intégrité de la surface n'est plus complète, cette dernière est généralement fissurée.

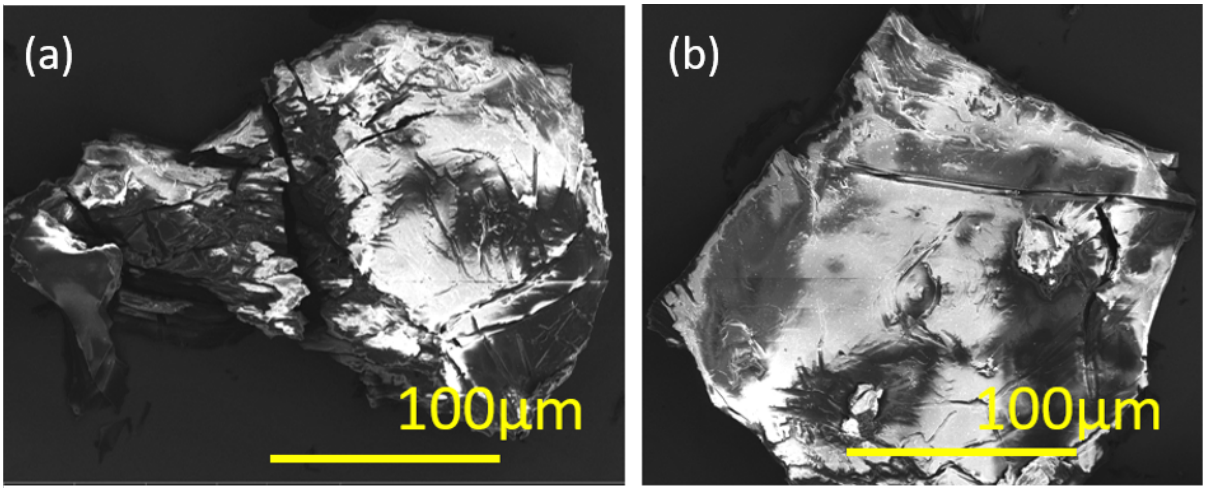

Figure 7. Observation au MEB du monocristal de V_2AlC après 16h de traitement HF 48% (a) et (b) sont des différents échantillons sous même condition de réaction.

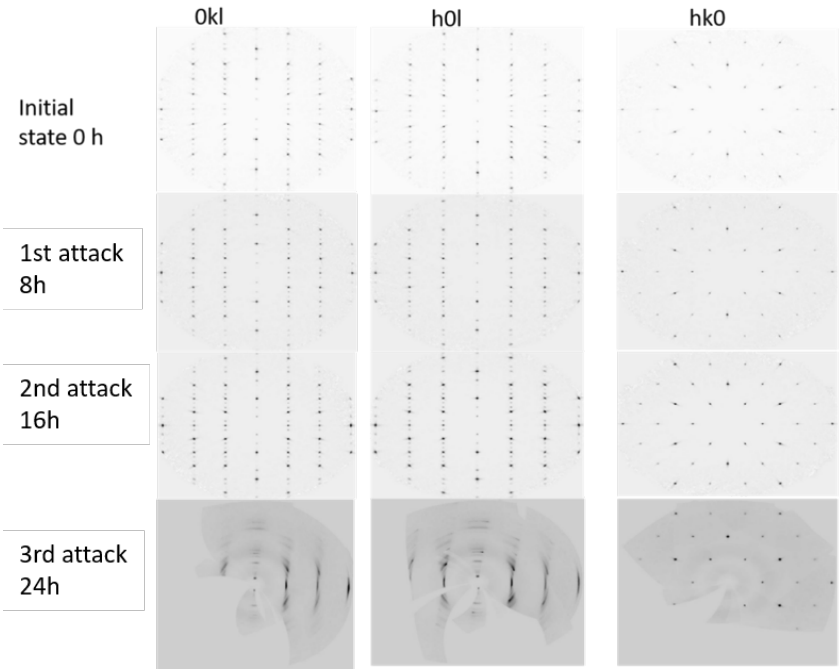

Figure 8. Diagramme XRD de V_2AlC à partir de l'état initial, gravure 8h, gravure 16h et 24h de gravure.

La Figure 8 montre les résultats du diagramme DRX Laue sur le même monocristal de V_2AlC lors de l'état initial et après une durée comprise entre 8h à 24h. A l'état initial et pendant les premières 16 heures, il révèle une structure parfaite, où les taches de diffraction sont parfaitement rondes et symétriques. Et à partir de 16 heures, la structure suivant les axes x et y devient visiblement désordonnée. Les taches de diffraction sont nettement élargies asymétriquement et tendent à former des taches en forme de banane, ce qui montre la variété des paramètres du réseau structural. Il est donc raisonnable d'évaluer que l'orientation cristalline

originale d'a et b (x et y) tourne et produit plus de nouvelles orientations. En d'autres termes, le monocristal est transformé en poly-cristal. On remarque que la diffraction le long de l'axe z (direction c) garde l'état initial. Nous supposons que l'ordre suivant l'axe c reste constant. Cela nous indique que la structure n'est plus complète mais divisée en petites pièce, c'est la raison pour laquelle les MXenes obtenu sont sous forme de petits morceaux.

De plus, nous avons effectué des multi-exfoliations sur l`échantillon V_2AlC dans HF pendant 60h. Les exfoliations sont réalisées par la résine et faits sur le même côté du cristal original. La première couche est dénommée numéro 1. De cette manière, toutes les couches exfoliées sont dénommées et analysées par spectroscopie Raman. Les spectres Raman des couches exfoliées sont résumés sur Figure 9. La première couche a une forte intensité typique du graphène et les signaux associés aux MXenes sont extrêmement faibles. Lorsque la mesure sonde une partie plus profonde à partir de la surface, le rapport d'intensité entre le graphène et MXene diminue. Pour l'échantillon à nombre modéré, le pourcentage de chaque composition est probablement proche. L'image du graphène disparaît jusqu'à l`interface entre section exfoliable et non-exfoliable de l'échantillon. Cela pourrait expliquer pourquoi le MXene obtenu est toujours en peu de couches, parce que le cristal MAX épais gravé serait finalement composé de phase MAX, MXenes et graphène dans la même structure.

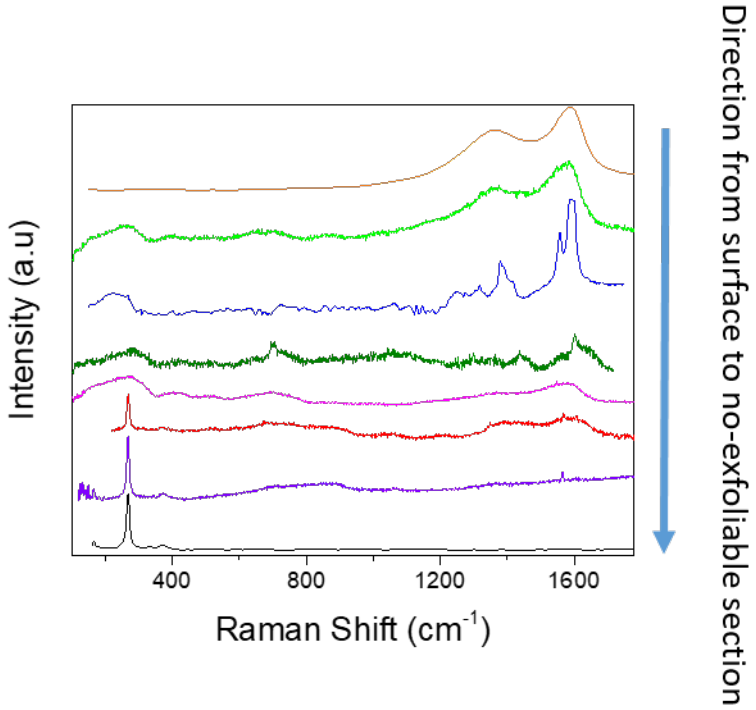

Figure 9. Résumé des spectres Raman de différentes couches exfoliées de V_2AlC après 60h de gravure.

Selon les essais précédents, il montre que les Mxenes obtenus ne dépassent pas le centimètre. Selon les résultats de Raman et DRX, en cours de réaction, la structure est abimée et le cristal est brisé. Sur les bords du cristal, la gravure de HF a créé une fissure entre deux couches de MXenes. Comme les intervalles sont nanométriques, la diffusion de HF est limitée et introduit la formation d`un espace s`appelant corrosion Crevice [17]. Cet espace implique que la solution corrosive dans cette zone est indépendante de la solution de mère. Les paramètres de la solution dans cet espace sont caractéristiques de conditions de confinement, sans aucun échange avec l`extérieur. En conséquence, la taille de MXenes synthétisés est limitée par l`effet de Crevice. En outre, selon la réaction par HF, se forment le gaz H_2 et fluor d`aluminium. Dans la zone Crevice, les produits sont confinés dans cette zone et aucun échange pour les permettre de sortir. En conséquence, des explosion nanométriques ont lieu, qui brisent la structure. Selon ce mécanisme, nous avons essayé d'autres agents chimique pout résoudre ce problème et augmenter l`espace confiné.  EDTA et des réactif d`ion chlorure sont employés afin que les éléments puissent pénétrer dans la structure et l`effet de Crevice puisse être diminuée. Toutefois, selon les résultats, il semble que les éléments ne peuvent pas entrer dans la structure efficacement. En conséquence, F ion est l`agent le plus efficace jusqu'à maintenant.

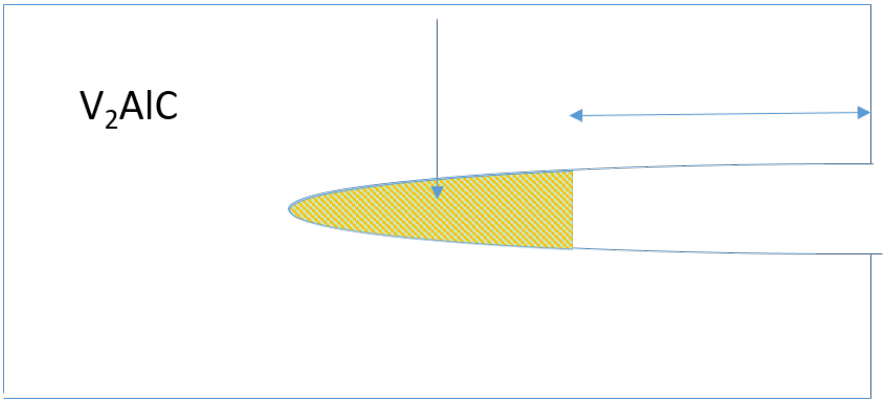

Figure 10. Schéma de corrosion Grevice dans la gravure de phase MAX dans HF

3. Polarisation électrochimique pour enlèvement d'Al

3.1 Introduction

Dans la deuxième section, nous testons la réactivité chimique des Phases MAX et essayons d`enlever l`élément A par méthode électrochimique. Par comparaison des résistances électrochimiques des plans contenant l`élément A et ceux ne contenant pas l`élément A, nous nous attendons à relever des différences significatives.

Dans cette section, nous utilisons les méthodes électrochimiques afin d'étudier la résistance à la corrosion des monocristaux de phase MAX ainsi que sa dépendance avec l'orientation cristalline. Ceci est obtenu en sélectionnant des plans cristallins en contact avec l'électrolyte et en maintenant des conditions potentiostatiques bien définies. Polarisation dynamique et spectroscopie d'impédance électrochimique (EIS) sont utilisées pour démontrer l'anisotropie forte de la réactivité chimique qui est prévue dans le cas de Cr_2AlC.

3.2 Détails expérimentaux

Pour les expériences, nous avons préparé trois types de électrodes, monocristaux brut, électrodes avec orientation unique exposant plans ab et c. Les électrodes de travail monocristallines Cr_2AlC avec orientation unique sont préparées par enrobage dans de la résine puis polissage.

Les polarisations anodiques quantitative ont été effectuées sur les électrodes "plan ab", cristaux bruts et des "plan c" respectivement. La polarisation anodique commence à partir de -0.05V (par rapport à OCV) et se termine à 1.5V par rapport à OCV à la vitesse 1mV/s.

Les échantillons ont généralement été maintenus au potentiel du circuit ouvert (OCP) pendant 30 mn dans la solution H_2SO_4 1M antérieur aux tests. . Les mesures d'impédance ont été acquises à l'amplitude de tension de 10 mV autour d'OCP et à une gamme de fréquence de 0,05 Hz à 50 kHz. Puis, après l'EIS, la courbe de polarisation a été enregistrée dans 100 mL de H_2SO_4 1 M, de -50 mV à +1,5 V par rapport à l'OCP à la vitesse de balayage de 1 mV/s

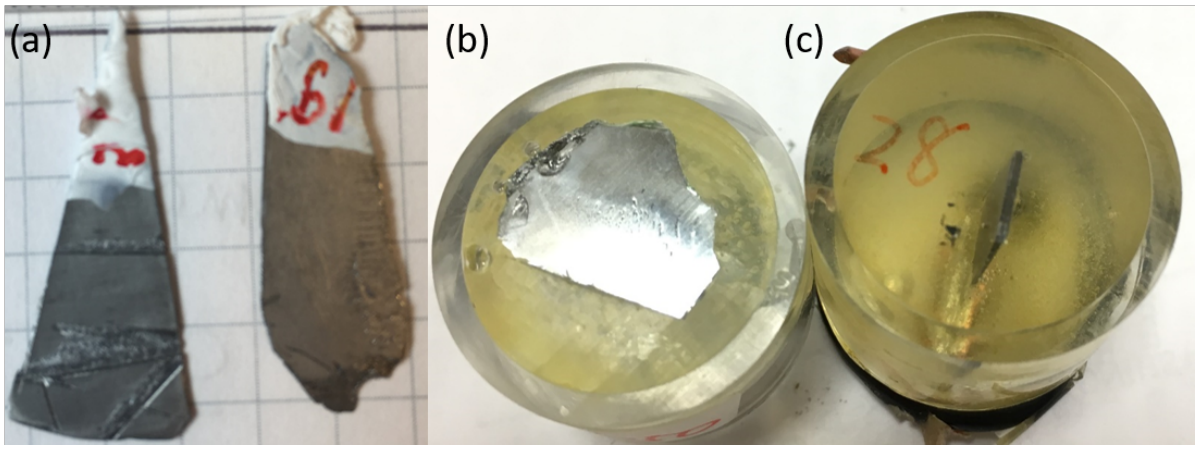

Figure 11. Cr_2AlC électrodes de travail (a) cristaux brut (b) plane ab(c) plane c

Figure 12. (a) Cellule électrochimique standard à trois électrodes (b) Potentiostat Gamry REF600 utilisé pour le test électrochimique.

3.3 Résultats et discussion

Les potentiels de corrosion (Ecorr) de tous les types d'échantillons se situent autour de -0,4V (vs. SCE). Tenant compte d'incertitudes liées à l`appareil, il peuvent être considérés comme similaires. Les formes de courbes des polarisations des trois types des électrodes sont similaires. A partir du potentiel d'auto-corrosion, les courants de polarisations montent rapidement puis sont freinés par l`effet de trans-passivation. Du 0V aux environs de 0,6 V vs SCE, les courants ont une valeur relativement constante. Enfin, en franchissant le zone de l`effet trans-passivation effective, une augmentation rapide du courant apparait et l`électrode se dissout rapidement. Dans Tableau 1, les densités de courant en moyen des électrodes du plan c, du cristal brut et du plan ab sont d'environ $7*10^{-7}$, $2*10^{-7}$ et $4*10^{-8}$ $A.cm^{-2}$ respectivement. La valeur de la densité de courant de corrosion du plan est environ 15 fois plus élevée que celle du plan ab, montrant que le plan ab possède une meilleure résistance à la corrosion. En outre, dans la section de trans-passivation, l'ordre de la valeur de densité de courant est c-plan> cristal brut> ab-plan (Tableau 1).

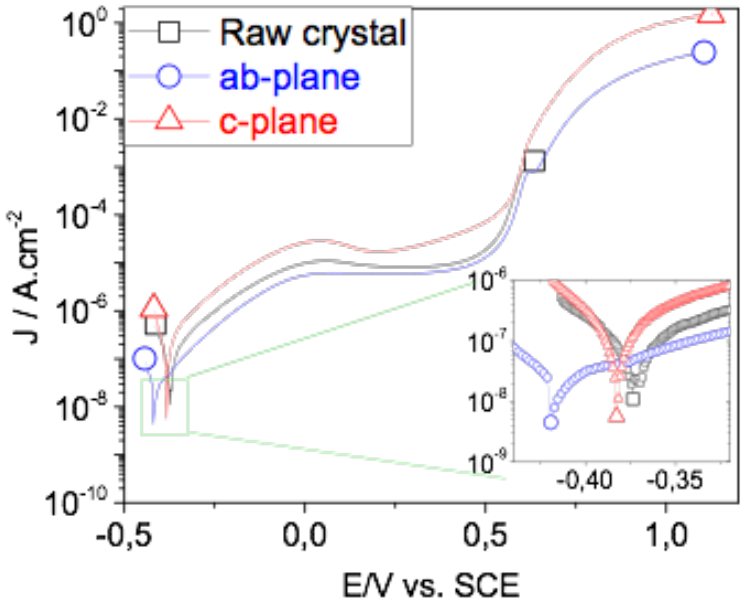

Figure 13. Courbes de polarisation de l'échantillon Cr_2AlC dans 1M H_2SO_4 d'OCP à + 1.5V par rapport à l'OCP: plan-c (triangle) plan ab (rond) cristal brut (carré).

Tableau 1. Courant de corrosion et courant de passivation pour les trois types d'électrodes d'OCP à 1.5V vs OCP dans 1 M H_2SO_4

Electrode	$I_{corr}(A.cm^{-2})$	$I_{passiv}(A.cm^{-2})$
ab-plane	$4*10^{-8}$	$4*10^{-6}$
Raw	$7*10^{-7}$	$6*10^{-6}$
c-plane	$2*10^{-7}$	$2*10^{-5}$

La spectroscopie d'impédance électrochimique (EIS) pourrait fournir des informations supplémentaires sur le comportement anticorrosion. Les mesures d'EIS sont présentées sous la forme de diagrammes de Nyquist (Fig.14a) et de Bode (Fig.14b). Le diagramme de Nyquist montre un demi-cercle déprimé sur plane-c différent que ce du plane ab qui a un demi-cercle lisse, indiquant qu'il y a plus d'une constante de temps pour plane c. Les diagrammes de Bode (Fig.14b) correspondent bien aux résultats de Nyquist avec deux constantes de temps dans la courbe du plan-c. En comparaison des modules d'impédance à basse fréquence (par exemple 0,1 Hz) (figure 14b), l'électrode du plan ab présente une valeur de 5000 KΩ tandis que le plan c a une valeur de 300 KΩ. Il est similaire au rapport de la densité de courant de corrosion entre

les deux types. À haute fréquence, le plan ab et le cristal brut présentent un décalage de phase constant tandis que celui du plan c diminue jusqu'à 58 °. Le déphasage constant indique une seule constante de temps dans le circuit équivalent. Mais pour le plan c, la deuxième valeur de déphasage révèle l'existence d'une seconde constante de temps, qui pourrait être attribuée à la diffusion et à l'hétérogénéité de surface.

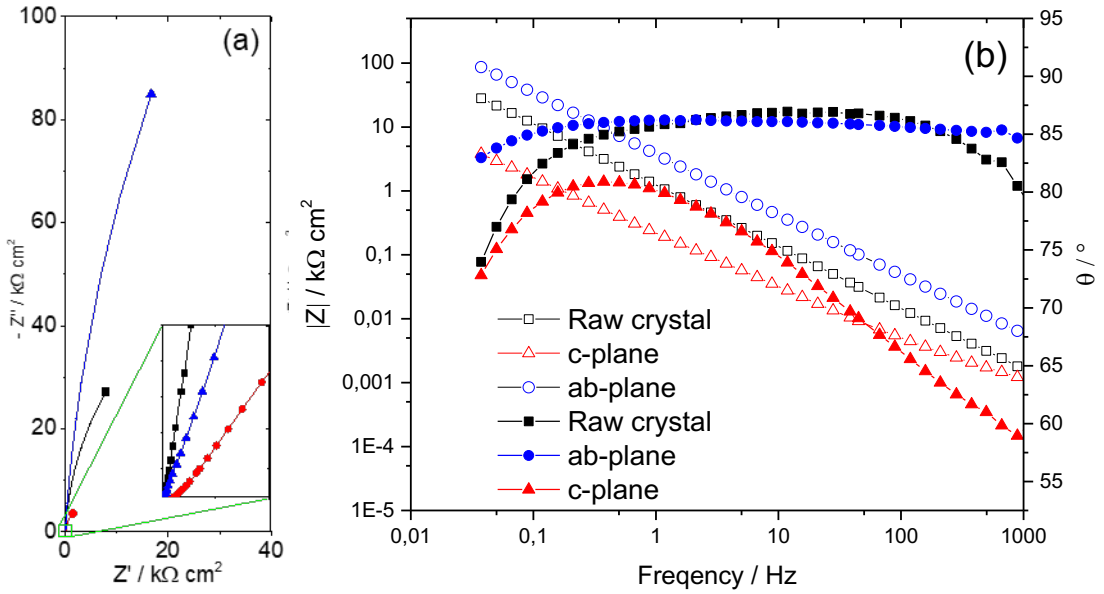

Figure 14. Spectre d'impédance électrochimique enregistré de 0,03 Hz à 1 KHz autour de Ecorr (-0,4V) de 0,03Hz à 1 kHz dans H_2SO_4 1M: plan brut (rond) du plan c (triangle) cristal brut (carré). (a) Tracé de Nyquist (b) Représentation de Bode (module | Z | et phase de décalage)

L'anisotropie a été prouvée dans d'autres propriétés des phases MAX. En raison de la grande taille des monocristaux, nous démontrons, la première fois, l`anisotropie électrochimiques directement.

En premier, le plus important est que sur le plan c, les éléments A contactent directement les agents chimiques. La réactivité chimique de l`élément A réduit la résistance globale. En conséquence, comme les résultats dans la section précédente, les éléments A sont les facteurs dominants pour la réactivité chimique de phase MAX. En outre, le potentiel d'électrode d'élément A est plus bas et l'énergie de surface des plans ab est plus petite, la rendant plus résistante et contribuant à l'effet d'anisotropie mesuré.

4. Chloruration

4.1 Introduction

La chloruration des composés de la phase MAX n'est pas étudiée ici pour la première fois. Mais nous l'utilisons ici pour la première fois pour enlever les éléments A et transformer la phase

Cr_2AlC en carbures de chrome très poreux, et montrer certaines propriétés originales de ces matériaux.

4.2 Détails expérimentaux

Les chlorurations ont lieu dans un réacteur à quartz CVD avec des gaz de chlore et d'hydrogène. En comparant les morphologies cristallines avant et après la chloruration (Figure 15), nous pouvons facilement observer que les échantillons perdent leur brillance métallique. Les principales raisons sont que le matériau dense est converti en un matériau poreux et se transforme de monocristallin en polycristallin brut.

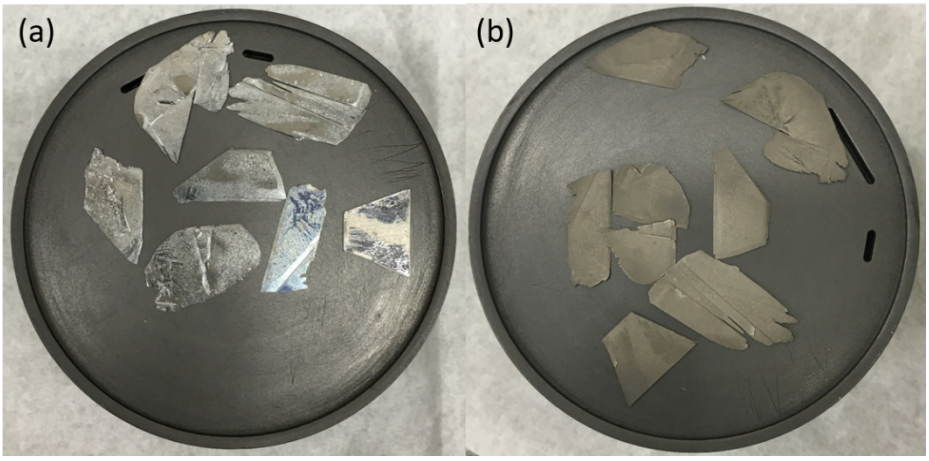

Figure 15. Plaquettes cristallines Cr_2AlC (a) avant et (b) après chloration

Nous nous concentrons ici sur l'analyse de la transformation subie par Cr_2AlC. Le milieu poreux est clairement continu. Les diamètres des pores typiques sont de taille submicronique. En raison de notre processus de synthèse, nous observons une seule échelle typique, contrairement à la structure poreuse multi-taille (Figure 16).

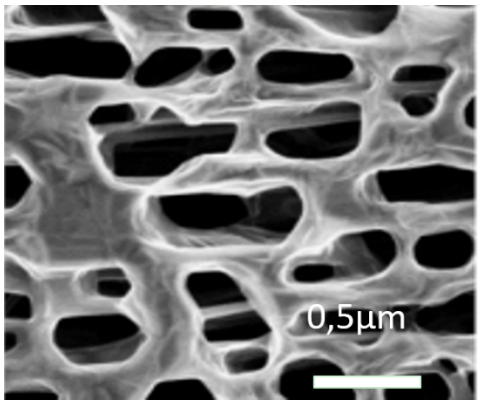

Figure 16. Image MEB de la surface supérieure de couches poreuses obtenues après chloruration à haute température des monocristaux de phase MAX Cr_2AlC transformés en Cr_3C_2 poreux.

Des échantillons totalement convertis ont été mesurés ainsi que leurs propriétés de transport électrique. La résistivité $\rho 0$ pour le champ magnétique nul B et la magnétorésistance

transversale (MR) $\Delta\rho/\rho 0$ a été mesurée en fonction de la température de 300K à 4K. La dépendance de Résistivité $\rho 0$ sur T est sur la Figure 17. Il est intéressant de noter que malgré une porosité de l'ordre de 60%, la résistivité reste du même ordre de grandeur que Cr_3C_2 massif [18], également similaire à la résistivité d'autres carbures de chrome [19].

La mesure de la magnétorésistance en fonction du champ magnétique nous permet de mettre en évidence certaines caractéristiques spécifiques. Les Figures 18 a et b montrent la dépendance de la magnétorésistance avec B et T.

À des températures inférieures à 5K et à un champ magnétique faible, une composante MR négative peut clairement être observée. Cette composante MR négative est seulement observable pour T à peu près en dessous de 100K. Cela pourrait être attribué à la localisation faible (WL). Selon la mécanique quantique, dans un système désordonné cohérent, la résistivité dépend de la probabilité pour qu'un électron passe d'un site donné à un autre. La somme des amplitudes de probabilité contient tous les chemins possibles et impliquent donc des phénomènes d'interférence d'ondes complexes. Puisqu'un chemin de retour vers le site de départ peut être suivi dans deux directions opposées, en l'absence de champ magnétique, ces deux voies similaires interfèrent de manière constructive et augmentent la résistivité. C'est le phénomène de localisation faible. Avec la présence d'un champ magnétique, un déphasage est introduit suivant le sens avec lequel une onde parcout un même chemin, et l'effet de localisation faible va diminuer. Une MR négative peut donc être observée.

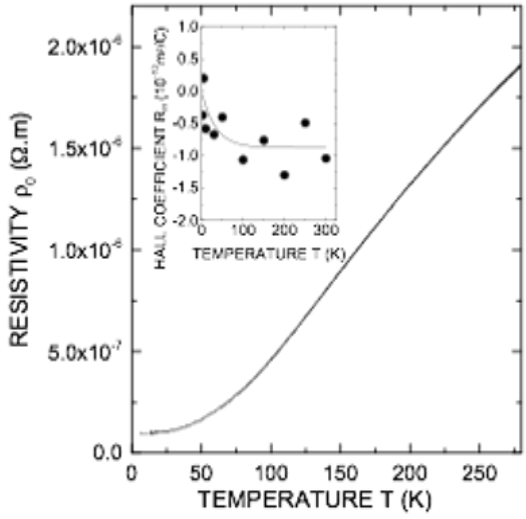

Figure 17. Résistivité électrique $\rho 0$ en fonction de la température d'un échantillon totalement converti. L'insert montre le coefficient de Hall R_H en fonction de la température T. Dans l'insert, la ligne continue est un guide pour l'œil.

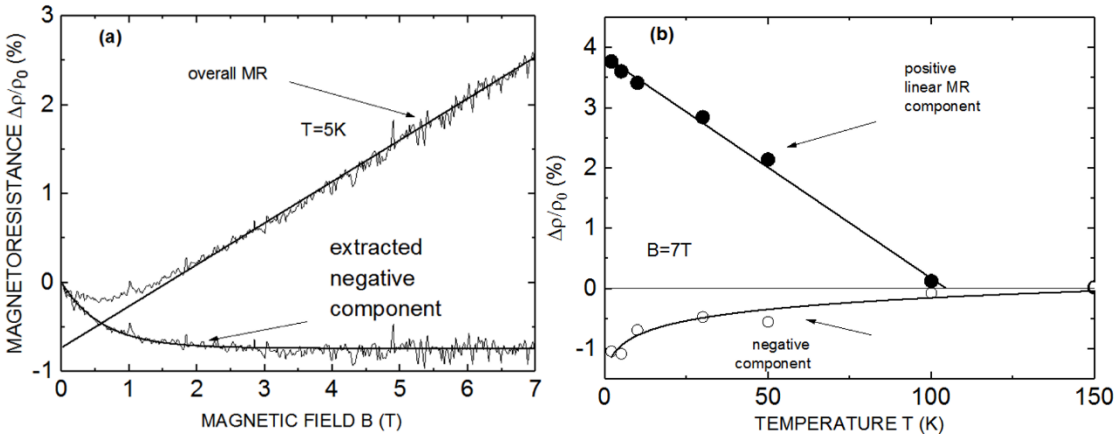

Figure 18. Magnétorésistance (MR) du même échantillon que sur la Fig.17. (a) RM par rapport au champ magnétique à T = 5K, (b) composante MR linéaire positive à B = 7T et composante MR négative saturée à B = 7T en fonction de T

En outre, Le plus remarquable est le comportement particulier de la MR apparaissant à T au-dessous de 100K et des champs supérieurs, pour lesquels une contribution linéaire et positive à la MR prédomine (Fig.18a). l'analyse quantitative des données montre que cette MR linéaire est linéaire provient très probablement du Cr_3C_2 poreux. Par un ajustement approprié de la courbe expérimentale dans le régime de champ élevé, il est possible d'extraire le coefficient de la contribution linéaire. Le composant négatif peut ensuite être extrait en retirant la composante linéaire des valeurs de magnétorésistance globales. Ici, pour des inclusions totalement isolantes (un cas plus proche du nôtre), si le libre parcours moyen du transport reste beaucoup plus petit que la dimension linéaire typique des inclusions et si la fraction volumique f des inclusions reste faible, il a été démontré que la MR est linéaire, proportionnelle à f et à la mobilité [20]. Des conclusions théoriques anciennes pourraient donc s'appliquer au milieu poreux Cr_3C_2.

Afin d`étudier le processus et mécanisme de la chloruration, nous avons effectué deux séries d`expériences. En premier, les chlorurations sont réalisées à différentes températures pendant 1 heure. La Figure 19 montre des images MEB typiques de la surface après chloruration pendant une durée comprise entre 900°C et 1300°C. La couche convertie la plus épaisse a une épaisseur d'environ 40 µm, obtenue à la température la plus élevée (Fig.20a). Un tracé d'Arrhenius de l'épaisseur convertie t_{conv} en fonction de la température réciproque indique que la valeur expérimentale de l'énergie d'activation E_A est d'environ 42,63 kJ/mol. Ceci peut être favorablement comparé à l'énergie d'activation correspondant à la chloruration de l'oxyde de chrome Cr_2O_3, autour de 86kJ / mol (0,891eV) [21].

Dans l'étape de chloruration initiale, la taille des pores à la surface supérieure tend à augmenter avec T (Fig.20b). La porosité de surface présente également une tendance vers la saturation à

T la plus élevée (Fig.20c). En conséquence, la densité des pores à haut température diminue relativement.

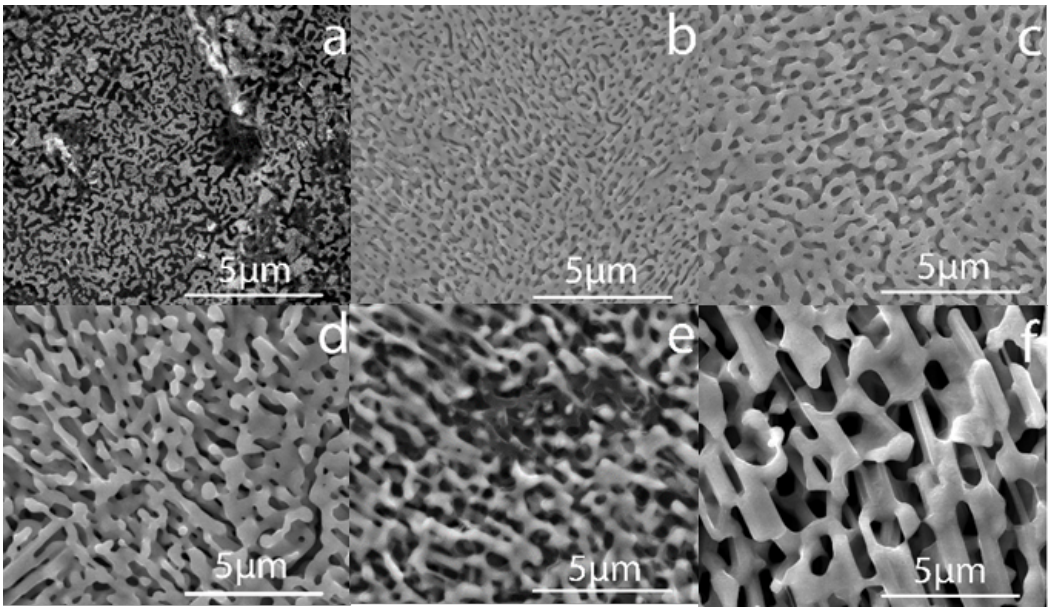

Figure 19. Morphologie de surface du Cr_3C_2 poreux obtenu par chloruration des cristaux de Cr_2AlC pendant une heure avec une pression p = 13,26 mbars. Chaque image est pour une température différente: (a) 800C° (b) 900C° (c) 1000C° (d) 1100C° (e) 1200C° (f) 1300C°.

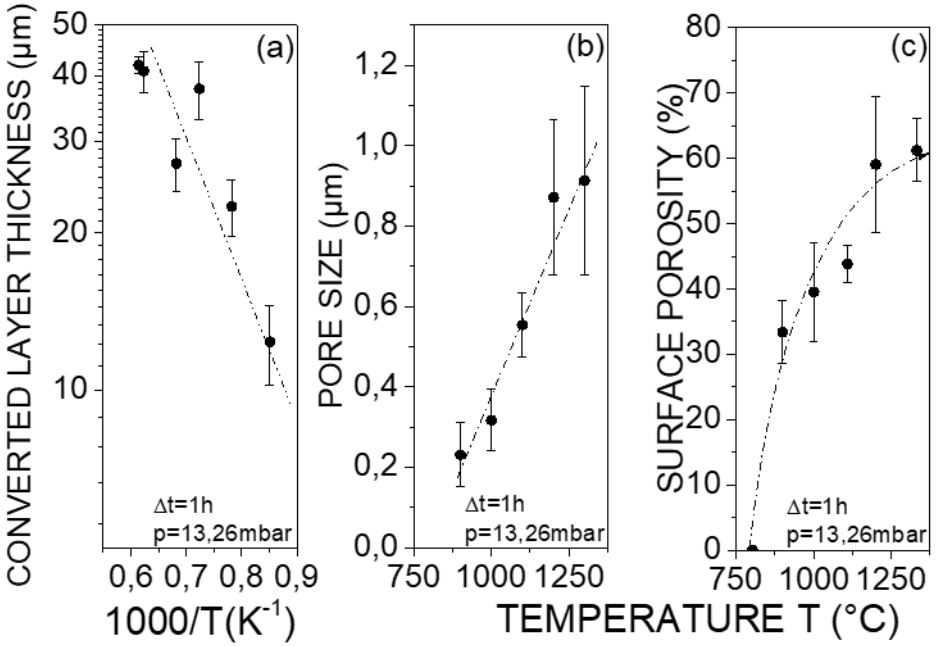

Figure 20. (a) Épaisseur de couche convertie en fonction de la température réciproque, (b) taille des pores en fonction de la température et (c) porosité de surface en fonction de la température (chaque point correspond à un échantillon différent, temps de chloruration = 1h). Les lignes continues sont des guides pour l'œil.

Une autre série d'expériences de chloruration a été réalisée en fonction du temps, avec une température fixe 1200°C. La variation de l'épaisseur de la couche Cr_3C_2 convertie est tracée en fonction du temps de chloruration (Figure 21a). La dépendance n'est ni totalement linéaire ni proportionnelle à la racine carrée du temps. L'exposant de puissance empirique semble plutôt indiquer que le processus de conversion global est limité par les processus de réaction et de diffusion pour la plupart des temps de chloruration étudiés.

La Figure 21 b montre la variation de la porosité globale en fonction du temps de chloruration. Nous pouvons observer que la porosité évolue encore très lentement et ne sature pas complètement même si après plusieurs heures de chloruration. Une explication possible peut être trouvée en étudiant la dépendance de la porosité en fonction de la profondeur. La Figure 21c montre la variation de la porosité en fonction de la profondeur de la surface dans un échantillon non entièrement converti. La porosité n'est pas constante en fonction de la profondeur, mais augmente au fur et à mesure qu'on se rapproche de la surface. Cela implique que le changement global de la porosité avec le temps ne peut être seulement attribué à la conversion de Cr_2AlC, mais est également dû à une transformation de couche qui se produit encore à travers toute la structure convertie. Il est donc tout à fait raisonnable de s'attendre à des vitesses de réaction différentes, selon que le changement de porosité se produit près de la surface ou à proximité de l'interface Cr_3C_2/Cr_2AlC.

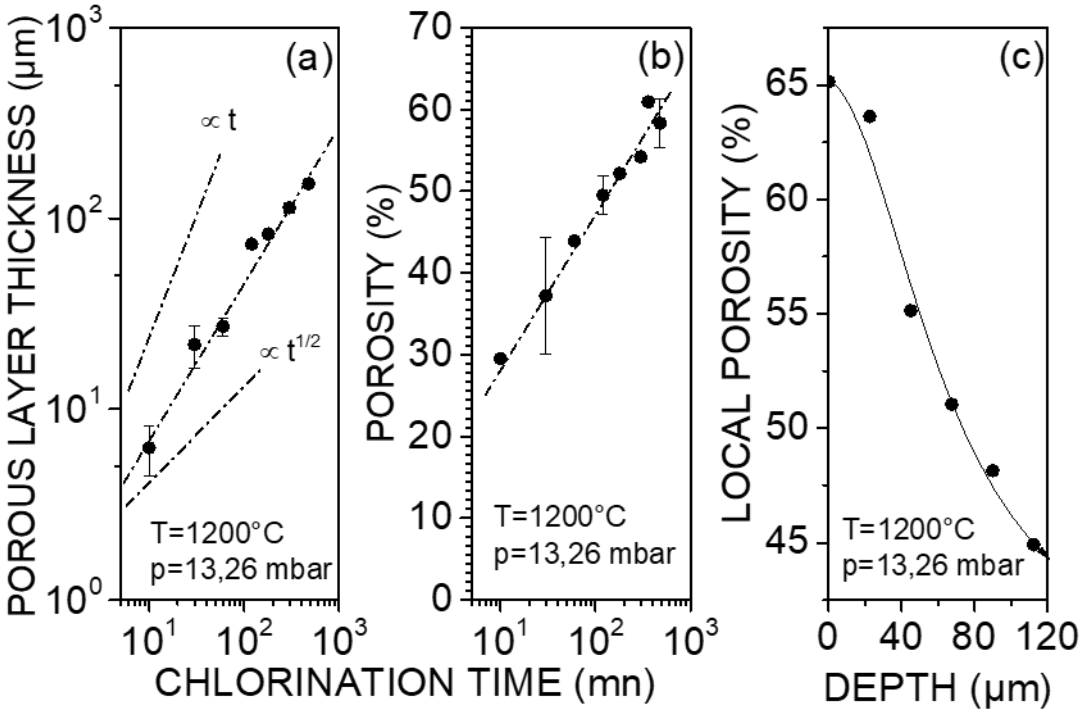

Figure 21. (a) Epaisseur de couche convertie en fonction du temps, (b) porosité en fonction du temps et (c) porosité locale en fonction de la profondeur pour une exposition Δt = 5h. Dans toutes les expériences T = 1200°C. Les lignes solides sont des guides pour l'œil.

Nous avons vérifié ce schéma en mesurant les spectres Raman en fonction de la profondeur dans une couche de Cr_2AlC monocristallin de 340 µm d'épaisseur partiellement convertie (Fig.22). Comme prévu, Cr_7C_3 est toujours présent à proximité de l'interface et, à mesure qu'on se rapproche de la surface, sa transformation en Cr_3C_2 peut être quantifiée en traçant la variation du rapport d'intensité entre le pic Raman Cr_7C_3 à 275 cm^{-1} et le pic Raman Cr_3C_2 à 208 cm^{-1} en fonction de la distance à l'interface Cr_2AlC. Comme démontré, ce rapport diminue continuellement jusqu'à disparaître pour des distances supérieures à environ 30µm.

La voie de chloruration décrite ci-dessus peut être grossièrement illustrée par le trajet tracé dans la section transversale de la section isotherme du diagramme de phase ternaire représentée Fig.23. Dans la réaction, le long de la ligne jaune, les éléments A sont éliminés d`abord pour former des phases binaires de carbures de chrome. Cette procédure est accompagnée par une perte de chrome, en conséquence, la première phase de carbure de chrome est $Cr_7C_3$. Avec l`élimination de chrome, la phase Cr_7C_3 est transformé en Cr_3C_2. Avec une température assez haute et une durée plus longue, Cr_3C_2 peut être transformé en graphite.

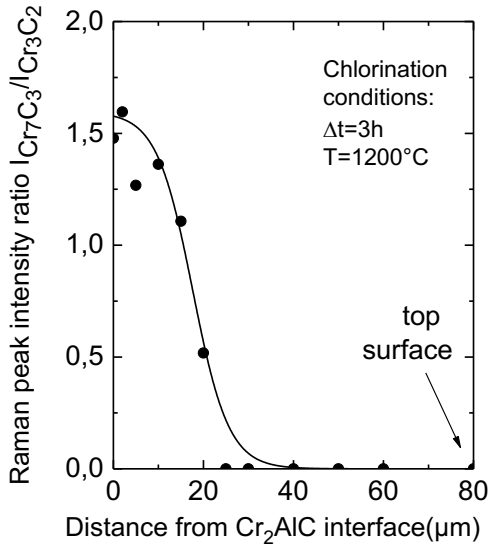

Figure 22. Rapport entre le pic Raman Cr_7C_3 à 275 cm^{-1} et le pic Raman Cr_3C_2 à 208 cm^{-1} en fonction de la distance de l'interface Cr_2AlC. Température de chloration T = 1200°C et temps Δt = 3h. La ligne continue est un guide aux yeux.

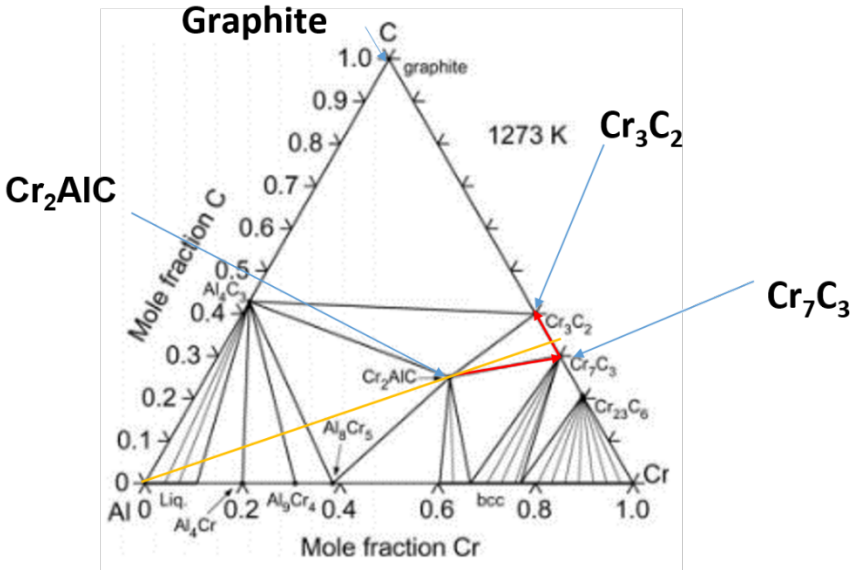

Figure 23. Section isotherme du diagramme de phase ternaire et trajectoire de chloruration de la conversion de la phase MAX Cr_2AlC en produit final graphite [22].

5. Conclusion générale et perspective

Dans la thèse présentée, nous avons rapporté nos études de la réactivité chimique des monocristaux de phases MAX. Comme expliqué dans tous les chapitres, les caractéristiques uniques affichées par de tels cristaux sont fortement liés à leur structure hautement anisotrope et à la faible liaison entre les couches A et les couches $M_{n+1}X_n$. La réactivité chimique est dominée par la réactivité des atomes A. La disponibilité de monocristaux de grande taille a permis d'évaluer directement l'anisotropie de cette réactivité chimique, et ce pour la première fois. Nous avons également montré que le rôle important joué par l'élément A dans l'initiation des transformations chimiques pouvait conduire à la synthèse de matériaux originaux.

Un objectif de ce travail était de synthétiser des MXenes à grande échelle à partir de monocristaux de phase MAX en éliminant sélectivement les atomes A. Des expériences ont été réalisées dans des solutions à base d'HF, dans des conditions de gravure électrochimique, etc. Il a été démontré que l'approche la plus efficace repose sur l'emploi de solutions à base d'HF. Notre étude indique que les ions H^+ cassent les liaisons et que les ions F^- servent d'agent complexant pendant l'extraction. Nous avons utilisé la spectroscopie DRX et Raman pour mieux comprendre les mécanismes du processus de gravure. Comme prévu, ce dernier commence de la surface pour progresser en volume. La gravure par HF induit la formation de l`espace Crevice qui confine la solution dans la structure. Par conséquent, ceci conduit

également à la désagrégation de l'ordre structurel de surface et rend difficile la production de Mxenes de grande surface.

Afin de trouver une voie alternative pour synthétiser les MXenes, nous avons étudié la chloruration à haute température. Nous nous sommes concentrés sur la recherche de conditions évitant la carbonisation réalisée dans les travaux publiés précédemment. Il s'avère qu'en maintenant une sous exposition au chlore et à l'hydrogène, les monocristaux de Cr_2AlC, V_2AlC et Ti_3SiC_2 ne sont pas convertis en MXenes mais en carbures de chrome, de vanadium ou de titane très poreux. Nous nous sommes concentrés sur le Cr_3C_2 poreux et avons montré que nous pouvions atteindre une porosité non obtenue dans les travaux publiés précédemment, qui faisaient appel à des phases de départ et des procédés de conversion complètement différents. Nos résultats montrent que le processus de chloruration permet de graver les phases MAX, à partir d'une perte de l'élément A pour former des carbures de chrome, puis former du graphite après un temps d'exposition plus long et / ou à plus haute température. La porosité dépend fortement de la température de réaction, et l'épaisseur de la couche convertie est dominée par le temps de réaction. Finalement, nous avons constaté que la résistivité de nos couches poreuses présente toujours le même ordre de grandeur que les données publiés pour des matériaux massifs, et nous avons mesuré une composante linéaire de magnétorésistance que nous attribuons à la porosité elle-même.

Notre dernière étude de réactivité porte sur la gravure électrochimique en solution H_2SO_4. Les électrodes Cr_2AlC scellées avec différentes surfaces exposées présentent des différences significatives. Nous avons étudié systématiquement le comportement anisotrope de la résistance à la corrosion par polarisation électrochimique et spectroscopie d'impédance(EIS). Nous avons mis en évidence une réactivité fortement anisotrope, la corrosion étant moins efficace lors de l'exposition d'un plan ab plutôt que d'un plan c. De plus, nous avons proposé des circuits équivalents adaptés afin de simuler la réaction électrochimique et d'expliquer le mécanisme de corrosion. Un circuit simple avec une constante de temps a été appliqué pour reproduire les données de phase MAX sur le plan ab. Des circuits équivalents plus complexes étaient nécessaires pour le plan-c. Nous attribuons ces différences à la réactivité de l'élément A et à son insertion dans la structure de phases MAX anisotropes. Cela entraîne des mécanismes de corrosion dépendant de l'orientation.

La réactivité chimique de matériaux aussi particuliers que les phases MAX a déjà suscité beaucoup d'intérêt. Notre motivation pour travailler sur les monocristaux était que de nombreux aspects, et surtout l'anisotropie, pouvaient être mieux compris de cette façon, plutôt qu'en s'appuyant sur les poudres et les échantillons poly-cristallins habituels. Le panel d'expériences

que nous avons choisi de mener était nécessairement limité. Cependant, il n'a pas seulement révélé la spécificité de l'élément A (ici principalement Al), mais les rôles combinés joués par cet élément et la structure dans laquelle il est intégré afin de déterminer la réactivité chimique globale et les transformations possibles. Notre espoir est que nos résultats motiveront des investigations futures et systématiques, en étendant nos propres idées à l'utilisation d'autres acides, d'autres conditions électrochimiques, etc., afin d'établir une masse de connaissance qui devrait avoir un impact utile sur les applications. Dans la synthèse des MXenes, dans le futur, de nouvelles phases et agents chimiques devront être testés pour réaliser l'exfoliation de MXenes de grande taille, et des techniques appropriées pour augmenter la distance inter-feuillets et éviter de briser la structure. En outre, nos cristaux n'étaient pas exempts de défauts, de sorte que les données obtenues à partir de bords de plaquettes imparfaites pourraient certainement être améliorées en utilisant des faces non affectées par des défauts de surface, et conduire à des paramètres d'anisotropie plus proches des paramètres intrinsèques. Il est également clair que l'amélioration des circuits équivalents proposés dans ce travail pourrait donner un aperçu plus physique des mécanismes responsables du processus de corrosion des monocristaux de phases MAX. Les données sur la dépendance de l'énergie de surface par rapport à l'orientation font défaut, et elles pourraient être utiles pour mieux comprendre l'anisotropie de certaines propriétés de la phase MAX, y compris la réactivité chimique. Dans les études de chloruration, les caractéristiques particulières en terme de taille de pores pourraient être appliquées ou exploitées dans des applications spécifiques (filtration, catalyse, etc.).

Références

[1]. M.W. Barsoum, The $M_{N+1}AX_N$ phases: a new class of solids: thermodynamically stable nanolaminates, Prog. Solid State Chem. 28 (2000) 201-281.

[2]. Nickl JJ, Schweitzer KK, Luxenberg P. Gasphasenabscheidung im Systeme Ti-C-Si. J Less-Common Met, 26(3) (1972)335–53.

[3]. Barsoum MW, El-Raghy T, Radovic M. Ti_3SiC_2: a layeredmachinable ductile ceramic. Interceram Int Ceram Rev .2000; 49:226-233.

[4]. Naguib, M. et al. On the topotactic transformation of Ti_2AlC into a Ti–C–O–F cubic phase by heating in molten lithium fluoride in air. J. Am. Ceram. Soc. 94 (2011). 4556–4561

[5]. M. Barsoum, MAX phases: Properties of Machinable Ternary Carbides and Nitrides, Wiley-VCH, Weinheim, 2013.

[6]. Sundberg M, Malmqvist G, Magnusson A, et al. Alumina forming high temperature silicides and carbides. Ceram Int., 30(7)(2004) 1899–1904.

[7]. S. Gupta, D. Filimonov, T. Palanisamy, T. El-Raghy, M.W. Barsoum, Ta_2AlC and Cr_2AlC Ag-based composites—new solid lubricant materials for use over a wide temperature range against Ni-based superalloys and alumina, Wear 262 (2007) 1479–1489.

[8]. Gromelski, S.j., Caciolo, P., and Cox, R.L.(2007) Carbide and nitride ternary ceramic glove and condom formers. US Patent 7, 235, 505, P.Office,ed(US).

Technology, 206(4) (2011) 591

[9]. G. L. Harris, *Properties of Silicon Carbide*, EMIS Datareviews Series, no. 13, INSPEC, IEE, UK, 1995.

[10]. Markus Diebel. Portable electronic device case, (2010) USD623180 S1.

[11].Naguib, M. et al. On the topotactic transformation of Ti_2AlC into a Ti–C–O–F cubic phase by heating in molten lithium fluoride in air. J. Am. Ceram. Soc. 94 (2011). 4556–4561

[12]. Naguib, M.; Kurtoglu, M.; Presser, V.; Lu, J.; Niu, J.; Heon, M.; Hultman, L.; Gogotsi, Y.; Barsoum, M. W. Two-Dimensional Nanocrystals Produced by Exfoliation of Ti_3AlC_2. Adv. Mater., 23 (2011)4248−4253.

[13]. B. Hallstedt, D. Music and Z. M. Sun, Thermodynamic evaluation of the Al-Cr-C system, *Int. J. Mat. Res*., 97, 539-42 (2006).

[14]. T. Ouisse, E. Sarigiannidou, O. Chaix-Pluchery, H. Roussel, B. Doisneau, D. Chaussende, High temperature solution growth and characterization of Cr_2AlC single crystals, J. Cryst. Growth 384 (2013) 88–95.

[15]. W. Jeitschko, H. Nowotny, F. Benesovsky, Ti_2AlN, eine stickstoffhaltige H-phase, Mon. Chem. 94 (6) (1963) 1198–1200.

[16]. W. Jeitschko, H. Nowotny, Die Kristallstructur von Ti_3SiC_2-Ein Neuer Komplexcarbid-Typ, Monatsh Chem. 98 (1967) 329-337.

[17]. Corrosion at pipe supports: causes and solutions, James N.Britton,2002. https://stoprust.com/technical-library-items/06-pipe-supports/

[18]. V.G. Grebenkina, Yu. P. Yusov and V.N. Sorokin, Low-resistance carbide resistors, Soviet Powder Metallurgy and Metal Ceramics 12 (1973) 345.

[19]. S.N. L'vov, V.F. Nemchenko, P.S. Kislyi, T.S. Verkhoglyadova, T.Y. Kosolapova, The electrical properties of chromium borides, carbides, and nitrides, Sov. Powder Metall. Met. Ceram. 1 (1964) 243–247.

[20]. D. Stroud, F.P. Pan, Effect of isolated inhomogeneities on the galvanomagnetic properties of solids, Phys. Rev. B 13 (1976) 1434–1438.

[21]. I. Gaballah, N. Kanari, S. Ivanaj, Kinetics of chlorination and oxychlorination of chromium (III) oxide, Metall. Mater. Trans. A 29 (1998) 1299–1308.

[22]. B. Hallstedt, D. Music, Z. Sun, Thermodynamic evaluation of the Al–Cr–C system, Int. J. Mat. Res. 97 (2006) 539.